Baryon Chiral Perturbation Theory in its manifestly covariant forms and the study of the πN dynamics
&
On the $Y(2175)$ resonance

Jose Manuel Alarcón Soriano

Departamento de Física

Universidad de Murcia

Tesis Doctoral

Director: Prof. José Antonio Oller Berber

Dedicado a todos aquellos
que siempre confiaron en mí.

Contents

Chapter 1

Introduction

The word "hadron" was introduced in the sixties to name particles that interact strongly. Nowadays it is known that these particles are part of two different groups: mesons and baryons, which have integer and semi-integer spin, respectively. In 1961, Murray Gell-Mann [1] and, independently, Yuval Ne'eman [2] proposed a model to explain the properties of these hadrons. According to this model, the hadrons were composed by more fundamental particles called *quarks* and their antiparticles. This model was very successful in explaining properties as the relations between the masses of different hadrons as well as to predict the existence of new ones. It also allowed to group the large amount of discovered hadrons into multiplets of defined spin and parity. This model was known as the *Eightfold-Way* or, in more technical terms, $SU(3)$ *flavor symmetry* ($SU(3)_F$). Quarks also need to have an extra degree of freedom called *color charge*. This is so because in the quark model the Δ^{++} baryon is composed by only one type of quark (the up quark) with parallel spins, so as to to have total spin equal to 3/2. The quarks need an additional degree of freedom in order to build from them an antisymmetric wave function [3]. That additional degree of freedom was proposed via an additional $SU(3)$ gauge symmetry associated with a conserved charge called color.[♯1] This gauge symmetry associated with color predicts the existence of an octet of gauge bosons that are known as *gluons*, which carry the strong interaction.

Despite the great success of the quark model, the existence of quarks was a mere hypothesis since they had not been experimentally observed before. It was not until 1968 that deep inelastic scattering experiments at the Stanford Linear Accelerator Center (SLAC) showed that the proton contained much

[♯1] From now on we will refer to this gauge group as $SU(3)_C$.

smaller point-like particles that could be identified with the hypothesized quarks. However, this experiment showed puzzling results since while many theorists of that time suspected that field theory became infinitely strong at short distances (Landau pole), the SLAC results showed that the strong interaction was weaker at high energies. The puzzle was solved in 1973 with the discovery by Gross, Wilczek and Politzer that non-Abelian gauge theories like $SU(3)_C$ exhibit a property known as *asymptotic freedom*.[♯2] This property implies that at high energies the quarks behave as free particles, explaining the deep inelastic scattering results obtained at the SLAC. On the other hand it also pointed out a possible reason of why quarks were not observed as isolated states, because the same calculation lead to a stronger interaction in the low energy regime. This is known as the *confinement hypothesis*.[♯3]

A Lagrangian formulation that deals with quarks as the fundamental degrees of freedom describing their interaction through their $SU(N_c)$[♯4] gauge symmetry exist and is known as *Quantum Chromodynamics* (QCD). The Lagrangian of QCD can be written in the following compact form:

$$\mathcal{L}_{QCD} = \sum_{u,d,\ldots} \bar{q}_i \left(i\not{D} - m_{q_i} \right) q_i - \frac{1}{4} G^a_{\mu\nu} G^{\mu\nu}_a \tag{1.1}$$

Where q_i denotes the N_c-multiplet corresponding to the quark u,d,..., D_μ is the covariant derivative in the colour space, m_{q_i} is the mass of the quark q_i (the same in the N_c-multiplet) and $G_{\mu\nu}$ is the gluon field.

In order to study the symmetries of the strong interaction we will take the following part of the QCD Lagrangian:

$$\mathcal{L}^0_{QCD} = \sum_{u,d} i\bar{q}_i \not{D} q_i = i\bar{u}\not{D}u + i\bar{d}\not{D}d \tag{1.2}$$

It was pointed by Heisenberg [4] in the thirties than protons and neutrons (also called nucleons) have almost the same mass, and the strength of the strong interaction between them is the same, independently of whether they are protons or neutrons. Because the quark content of the proton and neutron was determined to be uud and udd respectively, at the quark level it means that the u and d quarks are almost identical from the strong interaction point of view. In the massless limit because of $\mathcal{L}^0_{QCD}$ they behave in the same way. Due to this fact, is a good idea to group them in a doublet, called

[♯2] This discovery led them to win the Nobel Price in Physics in 2004.

[♯3] Confinement is an hypothesis since there is no formal proof nowadays.

[♯4] $SU(N_c)$ is the generalization of the $SU(3)_C$ symmetry to an arbitrary number of colors N_c.

in the literature *isospin-doublet* or *isodoublet*, and rewrite (1.2) in terms of this isodoublet:

$$\mathcal{L}^0_{QCD} = i\bar{\psi}\not{D}\psi \tag{1.3}$$

Where $\psi = \begin{pmatrix} u \\ d \end{pmatrix}$ is the isospin-doublet.[♯5] The Lagrangian (1.2) is invariant under rotations in the space defined by the quarks that constitute the isodoublet, also called *isospin space*. Mathematically, the transformation can be defined by:

$$\begin{pmatrix} u \\ d \end{pmatrix} \to \exp\left(i\theta_i^V \tau^i + i\gamma_5 \theta_i^A \tau^i\right) \begin{pmatrix} u \\ d \end{pmatrix} \tag{1.4}$$

Where the τ^i are the so-called *isospin matrices* (Pauli matrices divided by two) and obey the isospin algebra of $SU(2)$ $[\tau_i, \tau_j] = i\epsilon_{ijk}\tau_k$. One can check easily that (1.3) is invariant under (1.4).

We can take τ_i and $\gamma_5\tau_i \equiv \tilde{\tau}_i$ as the generators of these transformations, satisfying the following algebra:

$$\begin{aligned} [\tau_i, \tau_j] &= i\epsilon_{ijk}\tau_k \\ [\tau_i, \tilde{\tau}_j] &= i\epsilon_{ijk}\tilde{\tau}_k \\ [\tilde{\tau}_i, \tilde{\tau}_j] &= i\epsilon_{ijk}\tau_k \end{aligned} \tag{1.5}$$

This Lie algebra can be decoupled into two commuting $SU(2)$ subalgebras that act independently on the left- and right-handed part of the quark fields.This is the so called *chiral symmetry*.

The generators of this $SU(2)_L \times SU(2)_R$ algebra are:

$$\tau^i_L = \frac{1}{2}(1+\gamma_5)\tau^i, \qquad \tau^i_R = \frac{1}{2}(1-\gamma_5)\tau^i \tag{1.6}$$

And satisfy:

$$[\tau_{Li}, \tau_{Lj}] = i\epsilon_{ijk}\tau_{Lk} \tag{1.7}$$
$$[\tau_{Ri}, \tau_{Rj}] = i\epsilon_{ijk}\tau_{Rk} \tag{1.8}$$
$$[\tau_{Li}, \tau_{Rj}] = 0 \tag{1.9}$$

As we argue later, this $SU(2)_L \times SU(2)_R$ symmetry is spontaneously broken into the isospin $SU(2)_V$ subgroup, that remains unbroken, according to

[♯5] This procedure can be generalized to N_f-multiplet, where N_f is the number of quark flavours. We would have for (1.2) a sum over the s,c,... quarks.

the Vafa-Witten theorem [5]. On the other hand, an insertion of a mass term in (1.2), like the one of Eq.(1.1), explicitly breaks the symmetry generated by axial transformations associated to the generators $\tilde{\tau}_i = \gamma_5 \tau_i$, but this will be considered later.

According to Noether's theorem, we can derive from (1.3) the conserved currents at the classical level from $\mathcal{L}^0_{QCD}$, Eq.(1.2):

$$\vec{V}^\mu = i\bar{\psi}\gamma^\mu\vec{\tau}\psi, \qquad \vec{A}^\mu = i\bar{\psi}\gamma^\mu\vec{\tilde{\tau}}\psi = i\bar{\psi}\gamma^\mu\gamma_5\vec{\tau}\psi \tag{1.10}$$

$$\partial_\mu\vec{V}^\mu = 0, \qquad \partial_\mu\vec{A}^\mu = 0 \tag{1.11}$$

Where $\vec{\tau} = (\tau_1, \tau_2, \tau_3)$, $\vec{\tilde{\tau}} = (\tilde{\tau}_1, \tilde{\tau}_2, \tilde{\tau}_3)$.
The charges associated to these currents are:

$$\vec{Q}_V = \int d^3x \vec{V}^0, \qquad \vec{Q}_A = \int d^3x \vec{A}^0 \tag{1.12}$$

The vector and axial charges, $\vec{Q}_V$ and $\vec{Q}_A$ respectively, satisfies the same commutation relations as the matrices τ and $\tilde{\tau}$:

$$[Q_{Vi}, Q_{Vj}] = i\epsilon_{ijk}Q_{Vk} \tag{1.13}$$

$$[Q_{Vi}, Q_{Aj}] = i\epsilon_{ijk}Q_{Ak} \tag{1.14}$$

$$[Q_{Ai}, Q_{Aj}] = i\epsilon_{ijk}Q_{Vk} \tag{1.15}$$

Acting on the isodoublet of quantum fields ψ, these charges induce the transformation (1.4) that, at infinitesimal order can be written as:

$$\left[\vec{Q}_V, \psi\right] = -\vec{\tau}\psi \tag{1.16}$$

$$\left[\vec{Q}_A, \psi\right] = -\vec{\tilde{\tau}}\psi = -\gamma_5\vec{\tau}\psi \tag{1.17}$$

If the symmetry represented by (1.4) were exact, for each hadronic state $|h\rangle$ we would have another hadronic state $\vec{Q}_A|h\rangle$ with the same quantum numbers except parity, that would be opposite to $|h\rangle$.[♯6] However, no such parity doubling is observed in the hadron spectrum (see Fig. 1.1). So, if we want to use the *chiral symmetry* $SU(2)_L \times SU(2)_R$[♯7] as an approximation to

[♯6] Though $\vec{Q}_A|h\rangle$ is not normalized for $|h\rangle$ being a plane wave, it is so for a wave package.
[♯7] One can extend this idea to $SU(N_f)_L \times SU(N_f)_R$.

hadronic interactions, we must assume that this symmetry is spontaneously broken into its isospin subgroup $SU(2)_V$ [5], that is $SU(2)_L \times SU(2)_R \to SU(2)_V$.

On the other hand, a spontaneously broken chiral symmetry entails the existence of massless Goldstone bosons [6, 7] with the same quantum numbers as the broken symmetry generators $\vec{Q}_A$. Hence, they must have zero spin, negative parity, unit isospin, zero baryon number and zero strangeness.[‡8]

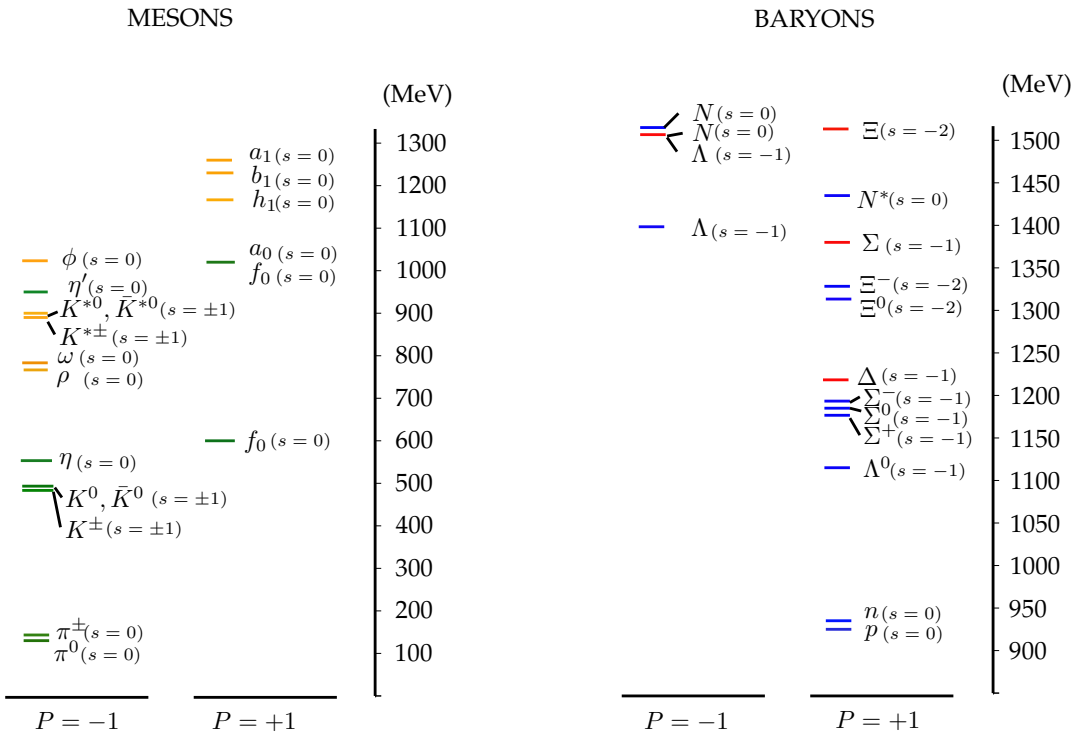

Figure 1.1: Hadron spectrum up to 1.3 and 1.5 GeV for mesons and baryons respectively, distinguishing between hadrons with positive parity ($P=+1$) and negative parity ($P=-1$). Blue (red) lines refer to baryons with $J=1/2$ ($J=3/2$), green (yellow) lines refer to mesons with $J=0$ ($J=1$), and s refers to their strangeness content.

Taking a look on Fig. 1.1, one realizes that the lightest of all hadrons is the pion, which has these quantum numbers precisely. That fact leads us to consider the *pions as the Goldstone bosons associated with the spontaneous breaking of the chiral symmetry.*[‡9] The pion has finally a finite, albeit small,

[‡8]The zero strangeness is a requirement for the case $N_f = 2$ only.
[‡9]The Goldstone theorem is explained in the Appendix A.

mass because of the explicit chiral symmetry breaking in $\mathcal{L}_{QCD}$ due to the quark masses.

The fact that $Q_A^a|0\rangle \neq 0$ and the consideration of the pion (π) as the Goldstone boson of the broken axial symmetry allow us to deduce $\langle 0|Q_A^a|\pi_a\rangle \neq 0$. Considering that Q_A^a is the spatial integral of the time component of the four-vector A_a^μ and assuming Lorentz covariance, we can extrapolate this result to the axial current: $\langle 0|A_a^\mu|\pi_a\rangle \neq 0$. Considering the four-vector transformation properties of this matrix element, it is usually parameterized in the literature as:

$$\langle 0|A_a^\mu|\pi_b(p)\rangle = if_\pi p^\mu \delta_{ab} \tag{1.18}$$

Where the constant f_π is the so-called weak decay constant of the pion, because tell us the strength of the pion weak decay. Taking the divergence of the axial current, which is equivalent to multiply the right hand side of Eq.(1.18) times $-ip_\mu$, gives:

$$\langle 0|\partial_\mu A_a^\mu|\pi_b(p)\rangle = f_\pi p^2 \delta_{ab} \tag{1.19}$$

One sees clearly from this relation that the *exact* spontaneously broken chiral symmetry leads to a vanishing mass for the pions (Goldstone bosons) and any difference from zero must come form a non-vanishing mass. Eq.(1.19) also allow us to parameterize the divergence of the axial current as a term proportional to the pion mass squared and a single pion operator, what would lead us to the celebrated *partially conserved axial-vector currents* (PCAC) [8]. From PCAC is straightforward to deduce the successful Goldberger-Treiman relation [9]:

$$g_{\pi N} = \frac{g_A m_N}{f_\pi} \tag{1.20}$$

Which, besides the nucleon mass m_N, relates strong interaction quantities as the pion-nucleon coupling $g_{\pi N}$ with weak interaction quantities as the nucleon axial coupling g_A and the pion weak decay constant f_π.

From the historical point of view, the development of these ideas started with the Goldberger-Treiman relation in 1957 on the basis of a dynamical calculation of the pion decay. In order to explain the surprising success of this approximate calculation, the idea of PCAC was introduced. Later, Nambu and Jona-Lasinio [10] recognized that the appearance of this massless or nearly massless pion was a symptom of a broken exact or approximate

symmetry. Subsequently, Goldstone [6] remarked that broken symmetries always entail massless bosons, and this was proved in 1962 by Goldstone, Salam and Weinberg [7]. The nature of the broken symmetry group became important only with the consideration of processes involving more than one pion, starting with the Adler-Weisberger sum rule in 1965 [11], whose success showed that the broken symmetry is indeed $SU(2)_L \times SU(2)_R$.

As we will see in the next chapter, the existence of an spontaneously broken chiral symmetry in the low energy region of the strong sector provide us powerful tools to treat *systematically* and *perturbatively* low energy process involving the strong interacting Goldstone bosons. These tools are included in what is nowadays known as *Chiral Perturbation Theory* (ChPT). In this thesis we will use this theory to study the elastic πN scattering and the S-wave scattering of $\phi(1020)f_0(980)$ and $\phi(1020)a_0(980)$.

Studying πN scattering is interesting because is a hadronic reaction that gives access to some of the most prominent and fundamental questions related to the strong interactions [12]. At low energies, it allows to test the dynamical constraints imposed by the chiral symmetry of QCD in one of the simplest processes involving a nucleon [13]. It is also essential to understand πN scattering for a first-principle approach to the nuclear structure, as the long-range part of the NN interactions is given by the exchange of pions [14]. As such, it is also a remarkable process to study the role played by isospin violation in nuclear phenomena [15]. At higher energies, πN scattering provides a probe to explore the baryonic spectrum of QCD or to study the properties of these states [16, 17]. Experimental data on differential cross sections and polarization observables have been collected in the last 50 years, and more intensively in the last decade thanks to fully dedicated experiments at meson factories. The usual way to organize the experimental information is by means of energy-dependent parameterizations of the scattering amplitude projected in partial waves (PW), fitted to the data and supplemented with unitarity and analyticity constraints. These analyses provide an accurate representation in PWs of the data included in the parameterizations, which can be used to extract values of scattering parameters and strong coupling constants or to identify the effect of resonances in the different isospin-angular momentum channels.[♯10]

In spite of the very long and sustained effort in studying the πN scattering amplitude, there are fundamental questions concerning this process that have not been satisfactorily answered yet. For instance, it is still unclear the exact

[♯10] See the classical treatise of Höhler [12] for an exhaustive review on the πN scattering amplitude. For updated descriptions of the current experimental situation and data see Refs.[17, 18].

value of the pion-nucleon coupling constant $g_{\pi N}$ and, therefore, the amount of violation of the Goldberger-Treiman (GT) relation [9], though it is known that it should be smaller than around 4% [19]. Another open question in the low-energy regime is the extraction of an accurate value of the pion-nucleon sigma term, $\sigma_{\pi N}$. This quantity and the isoscalar scattering amplitude can be related in the unphysical region of the Mandelstam plane, namely at the soft (Weinberg) point and at Cheng-Dashen (CD) points [20]. The latter is specially appropriate for determining $\sigma_{\pi N}$ since it can be reached by analytic continuation of the scattering amplitude. However, there still exists a sizable discrepancy between the values obtained from different PW analyses [21]. Given the importance that the sigma terms have in our understanding of the origin of the mass of the ordinary matter and in constraining supersymmetric models from direct searches of dark matter [22, 23], there is an intensive campaign for obtaining these observables using model-independent methods [21, 24]. Besides that, it is important to determine accurately the πN scattering parameters. The scattering lengths ought to be compared with those obtained from the analysis of the accurately measured $1S$ level shift in pionic hydrogen and deuterium [25]. An alternative source of phenomenological information on the scattering parameters is given by the analyses of the NN interaction [14].

On the other hand, it remains a challenge for the theory to understand hadronic processes directly from the parameters and dynamics of the underlying QCD. Important progress in the computation of meson-meson, meson-baryon and baryon-baryon scattering lengths in unquenched lattice QCD (LQCD) has been reported [26], although those of the πN system are still computationally prohibitive. Nevertheless, results were obtained in a pioneering quenched calculation [27] and, more recently in an unquenched calculation, an S-wave scattering phase shift in the $I = 1/2$ channel has been extracted from the negative-parity single nucleon correlation function [28]. The LQCD simulations are often run with quark masses heavier than the physical ones and their results require a careful chiral extrapolation to the physical point.

Chiral Perturbation Theory (ChPT), as the effective field theory of QCD at low energies [29, 30, 31], is a suitable framework to build a model-independent representation of the πN scattering amplitude and to tackle some of these problems.[♯11] An interesting feature of ChPT is that, regardless of the specific values of the LECs, it inherits the chiral Ward-Takashi (WT) identities of QCD among different Green functions [31]. Some of these identities at leading order in the chiral expansion were obtained using PCAC and Current-

[♯11] For comprehensive reviews on ChPT see Ref.[32, 33, 34].

Algebra methods in the fifties and sixties, conforming what has been known as low-energy theorems since then [35]. Remarkable examples of these theorems in the πN system are the above-mentioned GT relation and the one at the CD point between $\sigma_{\pi N}$ and the scattering amplitude. Another interesting examples are the Weinberg predictions for the scattering lengths [36] or the Adler condition for the isovector πN scattering amplitude [8]. Then, ChPT is a suitable framework to investigate up to which extent the low-energy theorems apply since it allows to compute systematically the higher-orders in the chiral expansions of the corresponding WT identities.

However, the one-baryon sector of ChPT has some specific problems that complicates its treatment respect the mesonic sector. Namely, on the contrary to the mesons (identified with the Goldstone bosons), the baryons cannot be considered as soft particles and introduce a new heavy scale in the theory. This heavy scale (of the order of the baryon mass m_B) breaks the homogeneity of the chiral amplitude since $m_B/\Lambda_{\chi SB}$ is not a small quantity. This becomes a problem if one wants to compute the quantum corrections to a given process or magnitude. In this case the contribution of the loop diagrams with baryon loops do not follow the hierarchy of the perturbative expansion and one finds that loop diagrams including baryonic propagators can contribute to any order. This is certainly a major problem for any perturbative theory since invalidates the reliability of a perturbative calculation up to a given order. Fortunately, this problem has solution. One possibility is to integrate out the heavy degrees of freedom of the baryon through a non-relativistic Foldy-Wouthuysen transformation [37]. In this way one only has to deal with the soft components, that follow the standard power counting of ChPT. This is the so-called *Heavy Baryon Chiral Perturbation Theory* (HBChPT). However, the radius of convergence of the HB expansion is limited and insufficient in many cases, so it is desirable to retain the good analytical properties of a relativistic calculation. In this thesis we study deeply the properties and convergence of two methods that allow us to recover the standard power counting of BChPT keeping its covariant formulation. These are the Infrared Regularization scheme (IR), that we present in Chapter 4, and the Extended-On-Mass-Shell scheme (EOMS), in Chapter 5. The success of covariant BChPT could provide answers to the still open questions regarding πN interaction as well as to give model-independent predictions to related quantities as the scattering lengths, the pion-nucleon coupling, and the pion-nucleon sigma term, which are still subject of great controversy, specially the latter.

A more phenomenological application of ChPT is presented in Chapter 6. There, we study the scattering $\phi(1020) f_0(980)$ and $\phi(1020) a_0(980)$ and the

relation of the former with the resonance $\phi(2170)$ (or $Y(2175)$, as we will refer to it from now on). This is a resonance with quantum numbers $J^{PC} = 1^{--}$ and mass around 2.15 GeV that was observed by the BABAR Collaboration for fist time in the reaction $e^+e^- \to \phi(1020)f_0(980)$ [38]. These experimental findings have renewed the theoretical interest in the region of the $Y(2175)$.

Several proposals trying to address the nature and properties of this resonance have been done. Among them, it was suggested in [39] that the $Y(2175)$ could be a tetraquark state or, as Ref.[40] proposed, a $\phi(1020)K\bar{K}$ molecular state. Our investigations, reported in [41] and included in Chapter 6, indicates that the $Y(2175)$ has at least a large $\phi(1020)f_0(980)$ component.

The organization of this thesis is as follows: In Chapter 2 we explain how to exploit the spontaneously broken chiral symmetry of the strong interactions to construct an effective field theory that allow us to apply perturbation theory to low energy strong interacting processes that involve the Goldstone bosons. In order to do so, we follow the seminar papers of Coleman, Wess, Zumino together with Callan for the second one [42]. In Chapter 3 we introduce the reader to the fascinating world of πN scattering. We present the importance that the study of this reaction has for different fields in physics and how it has been studied using different approaches. Apart from ChPT, we pay special attention to the partial wave analyses because they have been the main method used to extract information from πN scattering data. In this chapter we mention the problems that ChPT has when one baryon field is included in the theory and present the current approaches of ChPT with baryons (BChPT) to treat them. We also comment the advantages and limitations of every approach and the interesting results obtained in each one. In Chapter 4 we present our calculation of the πN scattering amplitude using the Infrared Regularization scheme (IR) [21] where we also, for the first time in the literature, unitarize the resulting πN partial waves in IR. We study the phase shifts provided by different partial wave analyses and overcome the difficulties that [43] encountered to fit them. We prove that the IR description of the phase shifts is of the same quality as those of HBChPT, being able to reproduce them up to energies of $\sqrt{s} \approx 1.14$ GeV. But the most striking results concerns to the deviation to the Goldberger-Treiman relation (Δ_{GT}) that IR obtains. In this case, a value of $\Delta_{GT} \approx$ 20–30% is obtained, what is in clear contradiction to theoretical and experimental bounds that point to a value of $\lesssim 4\%$. This puzzle triggered our calculation in the other covariant scheme, Extended-On-Mass-Shell (EOMS) [44]. This calculation is presented in Chapter 5 where first, we compare our IR results of [21] with our EOMS [44] ones. Later, we introduce the $\Delta(1232)$ resonance as an explicit degree of freedom and achieve an excellent convergence in the

low energy region that lies below the $\Delta(1232)$ region. Thanks to that excellent convergence, we could extrapolate our chiral amplitude fitted in the physical region to the subthreshold domain and extract the values of different subthreshold quantities. We show that these extracted values are in good agreement with the values obtained using dispersive methods. We conclude that, contrary to what is obtained in HBChPT or IR, the EOMS amplitude with the $\Delta(1232)$ as an explicit degree of freedom can connect both the physical region with the subthreshold one. As we show in the same Chapter, the good convergence of the EOMS calculation allows us to extract from PWAs a reliable value of the pion-nucleon sigma term [45]. We also study the behavior of the EOMS amplitude under unitarization methods and show that the unitarized EOMS amplitude achieves a much better description than the one obtained in IR. In Chapter 6 we study the $\phi(1020)f_0(980)$ scattering in S-wave near threshold determining the $\phi K\bar{K}$ scattering amplitude from chiral Lagrangians. Then we construct the $f_0(980)$ as a bound state from the rescattering of two kaons in an $I = 0$, S-wave state, and determine the amplitude by resuming the unitary loops or right-hand cut. We find resonant peaks with mass and width in agreement with those of the $Y(2175)$ and describe the $e^+e^- \to \phi(1020)f_0(980)$ scattering data. The results obtained from our approach show that the $Y(2175)$ has at least a large a $\phi(1020)f_0(980)$ component. Later, we extrapolate these results to the $I = 1$ case to study the $\phi(1020)a_0(980)$ S-wave scattering. We show that if the properties of the $a_0(980)$ are taken from the N/D method, a visible peak is clearly observed around 2.03 GeV, that would imply the presence of a dynamically generated isovector 1^{--} resonance [46]. This supports the idea that a study of the $e^+e^- \to \phi(1020)a_0(980)$ reaction might provide novel relevant information about hadronic structure and interactions around the 2 GeV region. Finally, in Chapter 7 we summarize briefly the subjects studied in this thesis and present the most relevant conclusions, with the prospects of apply them to forthcoming researches.

Chapter 2

Chiral Perturbation Theory

From the previous chapter is clear that the chiral symmetry is spontaneously broken and according to the Goldstone theorem we have massless, spin zero, pseudoscalar bosons in the hadron spectrum identified with the pions.[♯1] In this chapter we will deal with the problem of studying the dynamics of these particles. The aim is to obtain a Lagrangian describing the dynamics of these Goldstone bosons and its transformation properties, which should be invariant under a variety of inner symmetry transformation groups and on the group of Poincaré. One example of such kind of Lagrangians is the $SO(4)$ invariant σ-model:

$$\mathcal{L} = \frac{1}{2}\partial_\mu \phi_n \partial^\mu \phi_n - \frac{M^2}{2}\phi_n \phi_n - \frac{\lambda}{4}(\phi_n \phi_n)^2 \tag{2.1}$$

Where n is summed over the values $0, 1, 2, 3$, and ϕ_0 and $\vec{\phi}$ are an isoscalar and isovector scalar fields, respectively. However, we do not have any reason to consider λ as a small parameter in order to apply perturbation theory. For such kind of theories we would need either to include all Feynman diagrams of all orders of perturbation theory or find a criterion to drop higher-order diagrams. For this reason is convenient to write the Lagrangian describing the Goldstone bosons interactions by means of derivative couplings since, due to the Goldstone boson nature of the pions, the interactions weaken along with the energy of the process. In that case, we can establish a hierarchy between all the possible Feynman diagrams and expand the scattering amplitudes by means of a perturbative expansion in powers of Goldstone bosons energies

[♯1] Pions are not massless in the real world because of the explicit breaking of chiral symmetry due to the quark masses.

If the fields transform linearly under the symmetry group, the classification of all possible field-transformations reduces to the standard problem of representation theory. However, for phenomenological applications the situation is often more complicated since the fields only transform linearly under a certain subgroup that leaves the vacuum invariant. Fortunately, it is possible to classify all possible nonlinear realizations of an internal symmetry group which become linear when restricted to a given subgroup and construct in a systematic way nonlinear Lagrange densities which are invariant under the nonlinear field transformations [42]. In this realization the Lagrangian is suited for perturbative theory since the Goldstone bosons appear accompained by space-time derivatives. On the other hand, these Goldstone bosons operators generate higher order divergences from loops corrections, that need to be absorbed by new higher order operators, that is, the theory is non-renormalizable.

The range of validity of the perturbative description will be limited within a range of energies, whose upper limit will be denoted by $\Lambda_{\chi SB}$. The value of $\Lambda_{\chi SB}$ can be established in two ways. First, we can take into account that a perturbative expansion has no sense in a resonance region, where non-perturbative effects are crucial. If one looks at the hadron spectrum one sees that the first resonance is the ρ, that has a mass of $M_\rho = 700$ MeV, so one could establish $\Lambda_{\chi SB} = M_\rho = 700$ MeV. On the other hand, $\Lambda_{\chi SB}$ can be associated with the characteristic scale that fixes the size of the loop corrections. Under changes of the renormalization scale μ of $\mathcal{O}(1)$ one obtains that $\Lambda_{\chi SB} \simeq 4\pi f_\pi \simeq 1.2$ GeV [47]. So, the perturbative expansion makes sense only for a range of energies below $\Lambda_{\chi SB} \in 0.7$–$1.2 \sim 1$ GeV.

In this chapter we will show how to construct an invariant Lagrangian under a symmetry group G which transforms linearly under a certain subgroup $H \subset G$ that leaves invariant the vacuum. In Sec. 2.1 we set a equivalence criterion between different nonlinear realizations based on a property of local field theory. Later, in Sec. 2.2 we study the transformation properties under G and H of the fields used in our phenomenological approach. Section 2.3 is dedicated to classify all the nonlinear realizations based on the transformation properties obtained in Sec. 2.2. We also present there a theorem which allow us to write the phenomenological Lagrangians in terms of the fields that transform linearly, leaving the nonlinearly transforming fields as the coordinates of the G/H group. In Sec. 2.4 we study the relations between linear and nonlinear transformations. In Sec. 2.5 we calculate the covariant derivatives associated with the group G using the transformation properties of the different fields and from the definition of the standard coordinates. We specify this calculation to the chiral group in Sec. 2.6 and extend these

ideas to a gauge group in Sec. 2.7. Finally, in Sec. 2.8 we establish a hierarchy between the different Feynman diagrams of a perturbative calculation by introducing a power counting, and in Sec. 2.9 we construct effective Lagrangians based in the results of Sec. 2.6 and applying the power counting of Sec. 2.8. The set of the techniques described in this chapter form what is called *Chiral Perturbation Theory*.

2.1 Properties of nonlinear Lagrangians*

In order to have an equivalence criterion between different nonlinear realization, we will consider equivalent the transformations that leave unchanged the on-shell S-matrix elements.

Suppose we have a Lagrangian written in terms of the field ϕ:

$$\mathcal{L}[\phi] = \mathcal{L}_0[\phi] + \mathcal{L}_1[\phi] \tag{2.2}$$

Where $\mathcal{L}_0[\phi]$ is the free part of the Lagrangian and $\mathcal{L}_1[\phi]$ is the interacting part. If we make a local, nonlinear change of variables:

$$\phi = \chi F[\chi] \quad , \quad F[0] = 1 \tag{2.3}$$

We will have, in terms of χ, the following Lagrangian:

$$\mathcal{L}[\chi F[\chi]] \equiv \mathcal{L}_0[\chi] + \mathcal{L}_2[\chi] \tag{2.4}$$

With $\mathcal{L}_0[\chi]$ the same as $\mathcal{L}_0[\phi]$ but substituting $\phi \to \chi$. In this way we have the new interaction $\mathcal{L}_2[\chi]$. Because $F[0] = 1$, both ϕ and χ creates/annihilates the same particle, and we can compare:

$$\mathcal{L}[\phi] = \mathcal{L}_0[\phi] + \mathcal{L}_1[\phi] \quad \text{with} \quad \mathcal{L}'[\phi] = \mathcal{L}_0[\phi] + \mathcal{L}_2[\phi] \tag{2.5}$$

Where we have made the replacement $\chi \to \phi$ in $\mathcal{L}_2[\chi]$.

A theorem of relativistic quantum field theory states that, with weak restrictions on $\mathcal{L}$ and F, the on-shell S-matrix elements coincide in both cases. The proof is based in the fact that only linear terms in χ contribute to one-particle state and the higher orders in χ (the different terms) do not contain one-particle singularities. In other words, it is irrelevant the choice of a particular set of interpolating fields.

This theorem applies to the exact solution, but it is easy to see that it can be applied to a loop expansion. From the original Lagrangian $\mathcal{L}[\phi]$, we define the new Lagrangian $\mathcal{L}[\phi, a]$ as:

*Taken from [42] and several lecture notes delivered by J. A. Oller.

$$\mathcal{L}[\phi, a] = a^{-2}\mathcal{L}[a\phi] \Rightarrow \mathcal{L}[\phi, 1] = \mathcal{L}[\phi] \tag{2.6}$$

Since we are expressing the solution in a power series of the parameter a, that is equivalent to a loop expansion with the relation [42]:

$$a^P \to P = E + 2L - 2 \tag{2.7}$$
$$a\phi = a\chi F[a\chi] \tag{2.8}$$
$$\mathcal{L}[\phi, a] = \mathcal{L}[a\chi F[a\chi]] \tag{2.9}$$

With L the number of loops and E the number of external lines.

From (2.8) we obtain the same expression for counting the powers of a for χ and ϕ so, order by order in a (which is the same as in the number of loops), the on-shell S-matrix elements must be the same. As a result we consider that two nonlinear realizations are equivalent if they are related by the fixed nonlinear transformation of Eq.(2.3).

2.2 Standard form of nonlinear realizations*

Let G a compact, connected, semisimple Lie group of dimension n, and be $H \subset G$ a continuous subgroup of G. Let V_i $(i = 1, \ldots, n-d)$ be the generators of H and A_ℓ $(\ell = 1, \ldots, d)$ the rest of the generators chosen in such a way that they form a complete subset of generators of G, being orthonormal with respect the Cartan inner product. In a neighborhood of the identity, every element of $g \in G$ can be uniquely decomposed in the following way:

$$g = e^{\xi \cdot A} e^{u \cdot V} \quad , \quad \xi \cdot A = \sum_\ell \xi_\ell A_\ell \quad , \quad u \cdot V = \sum_i u_i V_i \tag{2.10}$$

Because, if H is an invariant subgroup:

$$\begin{aligned} g = e^{\xi \cdot A + u \cdot V} &= \lim_{N\to\infty} \left(1 + \frac{\xi \cdot A}{N} + \frac{u \cdot V}{N}\right)^N \\ &= \lim_{N\to\infty} (g_A h_V)^N = \lim_{N\to\infty} \underbrace{g_A h_V \ldots g_A h_V}_{N} \\ &= \lim_{N\to\infty} \underbrace{(g_A h_V g_A^{-1})}_{\in H} \underbrace{(g_A^2 h_V g_A^{-2})}_{\in H} \cdots \underbrace{(g_A^N h_V g_A^{-N})}_{\in H} g_A^N \\ &= h e^{\xi \cdot A} = h e^{\xi \cdot A} h^{-1} h = e^{\xi' \cdot A} h = e^{\xi' \cdot A} e^{u \cdot V} \end{aligned} \tag{2.11}$$

*Taken from [42].

So, for every element $g_0 \in G$, we can write:

$$g_0 e^{\xi \cdot A} = e^{\xi' \cdot A} e^{u' \cdot V} \quad \text{with} \quad \xi' = \xi'(\xi, g_0) \ , \ u' = u'(\xi, g_0) \tag{2.12}$$

If $h : \ \psi \to \mathcal{D}(h)\psi$ is an unitary and linear representation of the subgroup $H \subset G$, we can assign to every element $g_0 \in G$ a pair of transformations:

$$g_0 : \quad \xi \to \xi' \quad , \quad \psi \to \mathcal{D}(e^{u' \cdot V})\psi \tag{2.13}$$

The first one corresponds to the left-coset and the second one is the linear representation $\mathcal{D}$ of H. This application is a nonlinear realization of G, because:

$$\xi \overset{g_0}{\to} \xi' \overset{g_1}{\to} \xi'' \tag{2.14}$$

$$g_0 e^{\xi \cdot A} = e^{\xi' \cdot A} e^{u' \cdot V} \tag{2.15}$$

$$g_1 e^{\xi' \cdot A} = e^{\xi'' \cdot A} e^{u'' \cdot V} \tag{2.16}$$

$$g_0 g_1 e^{\xi \cdot A} = g_1 e^{\xi' \cdot A} e^{u' \cdot V} = e^{\xi'' \cdot A} e^{u'' \cdot V} e^{u' \cdot V} \tag{2.17}$$

$$g_0 g_1 e^{\xi \cdot A} = e^{\xi'' \cdot A} e^{u''' \cdot V} = e^{\xi'' \cdot A} e^{u'' \cdot V} e^{u' \cdot V} \tag{2.18}$$

$$\Rightarrow e^{u''' \cdot V} = e^{u'' \cdot V} e^{u' \cdot V} \tag{2.19}$$

Because $\mathcal{D}$ is a representation, if $u' = u'(\xi, g_0)$ and $u'' = u''(\xi', g_1)$, then:

$$\mathcal{D}(e^{u''' \cdot V}) = \mathcal{D}(e^{u'' \cdot V}) \mathcal{D}(e^{u' \cdot V}) \tag{2.20}$$

We take $\mathcal{D}$ in (2.13) as an irreducible representation and designate this equation as our standard form of the realization of G.

It is easy to see that this realization is linear when is restricted to the subgroup H, because if $g_0 = h \in H$:

$$h e^{\xi \cdot A} = h e^{\xi \cdot A} h^{-1} h = e^{\xi' \cdot A} h \tag{2.21}$$

And, therefore, $h = e^{u' \cdot V}$. So the transformation of ξ under $h \in H$ is the linear transformation:

$$\xi' = \mathcal{D}^{(b)}(h)\xi \tag{2.22}$$

Where $\mathcal{D}^{(b)}(h)$ is a linear representation of H determined uniquely by G.[♯2] Moreover, in this particular case where u' is independent of ξ, the field ψ transforms also linearly, that is $\mathcal{D}(e^{u' \cdot V}) = \mathcal{D}(h)$. Summarizing:

[♯2]For the case where $G = SU(N_f)_L \times SU(N_f)_R$ and $H = SU(N_f)_V$, $\mathcal{D}^{(b)}(h)$ is the adjoint representation of $SU(N_f)_V$.

$$h \in H: \quad \xi \to \mathcal{D}^{(b)}(h)\xi \quad , \quad \psi \to \mathcal{D}(e^{u'\cdot V})\psi \tag{2.23}$$

To conclude this section we apply the ideas presented here to the special case where G has an automorphism $\mathcal{R}: g \to R(g)$ such that:

$$V_i \to V_i \qquad\qquad A_\ell \to -A_\ell \tag{2.24}$$

As is the case for the chiral groups, where the parity operator induces an automorphism that changes the sign of the axial generators A_ℓ. Applying the automorphism to:

$$g_0 e^{\xi\cdot A} = e^{\xi'\cdot A} e^{u'\cdot V} \to e^{u'\cdot V} = e^{-\xi'\cdot A} g_0 e^{\xi\cdot A} \tag{2.25}$$

One obtains:

$$R(g_0) e^{-\xi\cdot A} = e^{-\xi'\cdot A} e^{u'\cdot V} \to e^{u'\cdot V} = e^{\xi'\cdot A} R(g_0) e^{-\xi\cdot A} \tag{2.26}$$

From Eqs.(2.25) and (2.27), one obtains:

$$e^{-\xi'\cdot A} g_0 e^{\xi\cdot A} = e^{\xi'\cdot A} R(g_0) e^{-\xi\cdot A} \Rightarrow e^{2\xi'\cdot A} = g_0 e^{2\xi\cdot A} R(g_0^{-1}) \tag{2.27}$$

For chiral groups, $g \in G = SU(N_f)_L \times SU(N_f)_R$ can be decomposed in $g = g_L g_R$ with $g_L \in SU(N_f)_L$ and $g_R \in SU(N_f)_R$ and, if R is a parity transformation:

$$g_L = e^{\theta_L \lambda_L}, \qquad g_R = e^{\theta_R \lambda_R}, \qquad R(g) = e^{\theta_L \lambda_R} e^{\theta_R \lambda_L} \tag{2.28}$$

Where λ_L and λ_R are the generators of the $SU(N_f)_L$ and $SU(N_f)_R$ Lie algebra, respectively. If we apply this decomposition to the results of Eq.(2.28) we obtain:

$$e^{2\xi\cdot A} = e^{2\xi\cdot\lambda_R} e^{-2\xi\cdot\lambda_L} \tag{2.29}$$

$$\begin{aligned} e^{2\xi'\cdot A} &= e^{\theta_L\lambda_L} e^{\theta_R\lambda_R} e^{2\xi\cdot A} e^{-\theta_L\lambda_R} e^{-\theta_R\lambda_L} \\ &= e^{\theta_L\lambda_L} e^{-2\xi\lambda_L} e^{-\theta_R\lambda_L} e^{\theta_R\lambda_R} e^{2\xi\lambda_R} e^{-\theta_L\lambda_R} \end{aligned} \tag{2.30}$$

Then:

$$e^{-2\xi'\lambda_L} = e^{\theta_L\lambda_L}e^{-2\xi\lambda_L}e^{-\theta_R\lambda_L} \tag{2.31}$$

$$e^{2\xi'\lambda_R} = e^{\theta_R\lambda_R}e^{2\xi\lambda_R}e^{-\theta_L\lambda_R} \tag{2.32}$$

We also have that, for chiral symmetries, Eq.(2.12) can be recast as [48]:

$$\begin{aligned}\exp\big[i\sum_a(\theta_a^V\lambda_a+\theta_a^V\lambda_a\gamma_5)\big]\exp\big(-i\gamma_5\sum_a\xi_a(x)\lambda_a\big)\\ =\exp\big(-i\gamma_5\sum_a\xi'_a(x)\lambda_a\big)\exp\big(i\sum_a\theta_a(x)\lambda_a\big)\end{aligned} \tag{2.33}$$

Where the first exponential is just the chiral rotation of Eq.1.4 (Chapter 1) generalized to a the $SU(N_f)\times SU(N_f)$ thorough the generalized Gell-Mann matrices λ_a. The decoupling of the left- and right-hand algebras allow us to write the terms proportional to $(1+\gamma_5)$ and $(1-\gamma_5)$ separately, obtaining:

$$\begin{aligned}\exp\big[i\sum_a\theta_a^L\lambda_a\big]\exp\big(-i\sum_a\xi_a(x)\lambda_a\big)\\ =\exp\big(-i\sum_a\xi'_a(x)\lambda_a\big)\exp\big(i\sum_a\theta_a(x)\lambda_a\big)\end{aligned} \tag{2.34}$$

$$\begin{aligned}\exp\big[i\sum_a\theta_a^R\lambda_a\big]\exp\big(-i\sum_a\xi_a(x)\lambda_a\big)\\ =\exp\big(-i\sum_a\xi'_a(x)\lambda_a\big)\exp\big(i\sum_a\theta_a(x)\lambda_a\big)\end{aligned} \tag{2.35}$$

Where $\theta_a^L\equiv\theta_a^V+\theta_a^A$ and $\theta_a^R\equiv\theta_a^V-\theta_a^A$. Multiplying Eq.(2.34) by the inverse of Eq.(2.35) one can eliminate the right-hand side both equations and isolate $U'(x)\equiv\exp\big(-2i\sum_a\xi'_a(x)\lambda_a\big)$ to obtain the transformation law of $U(x)\equiv\exp\big(-2i\sum_a\xi_a(x)\lambda_a\big)$:

$$U'(x)=\exp\big[i\sum_a\theta_a^R\lambda_a\big]U(x)\exp\big[-i\sum_a\theta_a^L\lambda_a\big] \tag{2.36}$$

Or, equivalently:

$$U'(x)=R\,U(x)\,L^\dagger \tag{2.37}$$

Where $R\in SU(N_f)_R$ and $L\in SU(N_f)_L$.

2.3 Classification of all nonlinear realizations*

In this section we show that Eq.(2.13) gives the standard form form the classification of all realizations of nonlinear field transformations under a group. To study this classification, we consider an n-dimensional real differentiable manifold M on which G acts, with G a compact, semisimple and connected Lie group.

$$g : x \to T_g x, \qquad x \in M, \quad g \in G \tag{2.38}$$

Let $T_g x$ be an analytic function of g and x.[♯3] We can identify the set of coordinates $x \in M$ with the fields used in effective theories. The problem concerning to all the possible transformation laws of fields under the action of a group G translates in finding all the possible realizations of the same group on M that fulfill Eq.(2.3). Let us recall that the latter guarantees the on-shell equivalence of of the S-matrix elements under field redefinitions. Then we have an special point, the origin, that should be preserved for all the sets of coordinates. Because the fields are employed in Taylor series, we do not need to characterize the group action globally, is enough to consider a neighborhood around the origin. Regarding to G, we restrict ourselves to the neighborhood of the identity, due to the properties of the compact, connected Lie groups.

We have elements of G that leave invariant the origin, and those elements constitute a subgroup $H \subset G$[♯4] called *stability group of the origin*. So, to construct the most general Lagrangian compatible with the symmetry group G, with a subgroup H which leaves invariant the ground state, we have to find the most general way to realize G and H on a manifold M. As we shall see immediately, this problem is equivalent to find all the nonlinear realizations of G that become linear when are restricted to H.

Theorem 1. ***(Theorem of linearization):*** *Let $H \subset G$ be a subset of G (compact, connected, semisimple Lie group) formed by all the elements of G that leave invariant the origin in such a way that, for this coordinate system:*

$$T_h 0 = 0 \quad , \quad \forall h \in H \tag{2.39}$$

Then, there exists a set of coordinates in a neighborhood of the origin that, in this new coordinate system, we have:

*Taken from [42].

♯3This assumption is necessary for the Taylor series used in field theories.

♯4This subgroup is formed, at least, by the identity.

$$T_h y = \mathcal{D}(h) y \quad , \quad \forall h \in H. \tag{2.40}$$

Being $\mathcal{D}(h)$ a linear representation of H.

Proof: Since $T_g x$ is continuous in x and $T_h 0 = 0$, it follows that around the origin it must exist a neighborhood that stays invariant under the action of the group H, because H is continuous, bounded and compact. Expanding $T_h x$ in a Taylor series:

$$T_h x = \mathcal{D}(h) x + \mathcal{O}(x^2) \quad , \quad \forall h \in H \tag{2.41}$$

Being $\mathcal{D}(h)$ a linear realization of H.

We can define a new set of coordinates in the following way:

$$y = \int_H dh\, \mathcal{D}^{-1}(h) T_h x \tag{2.42}$$

Where dh is the invariant measure and the group integral is normalized in such a way that $\int_H dh = 1$. The new coordinates y are analytical functions of x. Actually, the Taylor series of y as a function of x is:

$$y = x + \mathcal{O}(x^2) \tag{2.43}$$

So, the determinant of the Jacobian matrix is equal to one in the origin, and we can use the new coordinates y as a new coordinate system. Under the action of an element $h_0 \in H$ we have:

$$\begin{aligned} h_0 : \quad y \to & \int_H dh \mathcal{D}^{-1}(h) T_h T_{h_0} x = \int_H dh \mathcal{D}^{-1}(h) T_{hh_0} x = \\ & = \int_H d(hh_0) \mathcal{D}^{-1}(hh_0 h_0^{-1}) T_{hh_0} x = \mathcal{D}(h_0) y \end{aligned} \tag{2.44}$$

As we wanted to prove. ■

This theorem is useful by itself. On the one hand, Eq.(2.42) is a simple test for linearizability. On the other hand, if a transformation law can be linearized, the formula (2.42) gives an explicit formula for the new fields that transform linearly.

Now we continue with the problem of finding the most general way for the nonlinear realizations of a symmetry group G, that become linear when are restricted to a subgroup $H \subset G$. As before, let V_i the generator of H and A_ℓ the rest of the generators of G. In the following we will use gx instead of $T_g x$ for shortening.

Let us define the submanifold $N \subset M$ consisting in all the points obtained by the application of $g \in G$ on the origin, that is $g0$. The points in N will have the form $e^{\xi \cdot A}0$, because every transformation can be written in a neighborhood around the identity as $g = e^{\xi \cdot A}e^{u \cdot V}$, Eq.(2.3), and $g0 = e^{\xi \cdot A}e^{u \cdot V}0 = e^{\xi \cdot A}0$, because $e^{u \cdot V}0 = 0$. So, in this neighborhood, the ξ_ℓ characterize the point $g0$ and works like the coordinates of this point. If we had two sets of coordinates satisfying $e^{\xi_1 \cdot A}0 = e^{\xi_2 \cdot A}0$ then $e^{-\xi_2 \cdot A}e^{\xi_1 \cdot A}0 = 0 \Rightarrow e^{-\xi_2 \cdot A}e^{\xi_1 \cdot A} = e^{u \cdot V}$. But the generators V can only be obtained as a product of at least two A_ℓ's so, at fist order, $\xi_1 = \xi_2$ and the jacobian of the function $\xi_2(\xi_1)$ will be distinct to zero, and we will have a one-to-one correspondence between ξ_1 and ξ_2. Since $\xi_1 = \xi_2$ is a solution, this is the *only* solution. So, the transformation properties of every point in N are entirely determined because:

$$g(e^{\xi \cdot A}0) = e^{\xi' \cdot A}e^{u' \cdot V}0 = e^{\xi' \cdot A}0 \tag{2.45}$$

Where we have taken into account Eq.(2.12). We introduce the $n - d$ remaining coordinates to describe any point in M and group it in the real vector ψ, so that any point in M will have, in a neighborhood of the origin, the coordinates (ξ, ψ), and any point in N will have the form $(\xi, 0)$ and will transform as:

$$g(\xi, 0) = (\xi'(\xi, g), 0) \tag{2.46}$$

From the theorem of linearization we know we can choose the coordinates (ξ, ψ) in such a way that the subgroup H (the stability group of the origin) acts linearly. According to (2.46) the representation is reducible and since H is a compact group and the representation can be made orthogonal choosing a convenient set of coordinates ψ, it can always be written in the fully reduced form.

$$e^{u \cdot V}(\xi, \psi) = (\mathcal{D}^{(b)}(e^{u \cdot V})\xi, \mathcal{D}(e^{u \cdot V})\psi) \tag{2.47}$$

Here, $\mathcal{D}$ is a linear (orthogonal) representation of H of dimension $n - d$ and $\mathcal{D}^{(b)}$ is the representation induced on ξ by:

$$e^{\xi' \cdot A} = e^{u \cdot V}e^{\xi \cdot A}e^{-u \cdot V} \tag{2.48}$$

We introduce a new set of coordinates that we will call *standard coordinates* defined by:

$$(\xi, \psi)^* = e^{\xi \cdot A}(0, \psi) \tag{2.49}$$

Which results in:

$$(\xi, 0)^* = (\xi, 0) \tag{2.50}$$
$$(0, \psi)^* = (0, \psi) \tag{2.51}$$

This definition is a map of the pair $(\xi, \psi)^*$ into M whose Jacobian determinant does not vanish at he origin, so its an allowed set of coordinates near the origin.

But now, taking into account Eq.(2.12) we know everything about the action of $g \in G$ in a neighborhood of the origin, because:

$$\begin{aligned} g(\xi, \psi)^* &= g e^{\xi \cdot A}(0, \psi)^* = e^{\xi' \cdot A} e^{u' \cdot V}(0, \psi)^* \\ &= e^{\xi' \cdot A}(0, \mathcal{D}(e^{u' \cdot V})\psi)^* = (\xi', \mathcal{D}(e^{u' \cdot V})\psi)^* \end{aligned} \tag{2.52}$$

Where ξ' and u' are given by Eq.(2.12). So, the new coordinates transform as the standard representation,[♯5] Eq.(2.23). We see then that *the most general nonlinear realization of a group G with a subgroup H that leaves unchanged the origin, reduces to the standard form after a convenient change of coordinates in a neighborhood of the origin.*[♯6]

2.4 Relations between linear and nonlinear transformations*

We consider the differential manifold (ξ, Ξ) with the fields Ξ_α transforming according an irreducible and unitary representation of the group G, and ξ according to (2.13):

$$g_0 : \xi \to \xi' \quad \text{and} \quad \Xi_\alpha \to \Xi'_\alpha = \sum_\beta \mathcal{D}_{\alpha\beta}(g)\Xi_\beta \tag{2.53}$$

Now, let us see how to generate fields that transform under $g \in G$ according to the standard form. First, we define:

[♯5] That is the reason of calling them standard coordinates.

[♯6] In the practice, we usually require an unitary representation of the subgroup H. In that case is necessary to combine the real fields (coordinates) in a complex field.

*Taken from [42].

$$\Psi_\alpha = \sum_\beta \mathcal{D}_{\alpha\beta}(e^{-\xi\cdot A})\Xi_\beta \tag{2.54}$$

This definition is an allowed change of fields in the sense of Eq.(2.3). The field Ψ_α, under the action of $g \in G$, transforms into:

$$\begin{aligned}\Psi'_\alpha &= \sum_\beta \mathcal{D}_{\alpha\beta}(e^{-\xi'\cdot A})\Xi'_\beta = \sum_\beta \mathcal{D}_{\alpha\beta}(e^{-\xi'\cdot A}g)\Xi_\beta = \\ &= \sum_\beta \mathcal{D}_{\alpha\beta}(e^{-\xi'\cdot A}ge^{\xi\cdot A})\Psi_\beta = \sum_\beta \mathcal{D}_{\alpha\beta}(e^{u\cdot V})\Psi_\beta\end{aligned} \tag{2.55}$$

And, if it is restricted to H, $\mathcal{D}(g) = \mathcal{D}(h)$. Notice that the previous equation corresponds to the standard form given in Eq.(2.23). On the other hand, $\mathcal{D}(h)$ can be reducible but, in that case, Ψ_α can be decomposed in a set of fields $\psi^{(a)}_\alpha$ with a lower number of components:

$$(\xi, \Psi) \sim (\xi, \sum_a \oplus \psi^{(a)}) \tag{2.56}$$

In that case, the apparent additional physical information due to the connection between a higher number of coordinates is illusory since, as seen in Sec. 2.1, a theory with ξ and Ξ has the same physical consequences than a theory with ξ and $\psi^{(a)}$. In any case, the dimension of the multiplets is the one of the irreducible linear representation of the subgroup H and not the one of the irreducible linear representation of G. One should also emphasize that in a Lagrangian theory one could use the fields Ξ but this more constraint theory is not the most general one according to group-theoretic considerations.

The previous construction can be inverted to give rise to fields that transform linearly like Ξ_α as function of the fields ξ_l and the fields $\psi^{(a)}_\alpha$. Our task translates now in finding a function f_α of ξ and ψ which transform according to a linear representation of the group G:

$$g_0 : f_\alpha(\xi, \psi) \to f_\alpha(\xi', \psi') = \sum_\beta \mathcal{D}_{\alpha\beta}(g_0) f_\beta(\xi, \psi) \tag{2.57}$$

If we assume we can expand $f_\alpha(\xi, \psi)$ in a Taylor series on the variable ψ, is enough to consider the linear term in ψ:

$$f_\alpha(\xi,\psi)=\sum_r F_{\alpha r}(\xi)\psi_r \tag{2.58}$$

This is so because the general problem can be reduced to this one by solving the Clebsch-Gordan problem for the subgroup H and the tensor products of the ψ's. We have then:

$$g_0:\sum_r F_{\alpha r}(\xi')\psi'_r=\sum_{\beta,s}\mathcal{D}_{\alpha\beta}(g_0)F_{\beta s}(\xi)\psi_s \tag{2.59}$$

The representation $\mathcal{D}$ is not arbitrary, because when its reduced to the subgroup H, $\mathcal{D}$ must be reducible and contain, as one of its components, the representation $R(h)$ under which ψ transforms linearly under the action of the subgroup H. To see this, for $g_0=h$ one has the result:

$$h:\sum_r F_{\alpha r}(\xi')\psi'_r=\sum_{r,s}F_{\alpha r}(\xi')R_{rs}(h)\psi_s=\sum_{\beta,s}\mathcal{D}_{\alpha\beta}(h)F_{\beta s}(\xi)\psi_s \tag{2.60}$$

Taking $\xi=0$,[♯7] we have:

$$\sum_{r,s}F_{\alpha r}(0)R_{rs}(h)\psi_s=\sum_{\beta,s}\mathcal{D}_{\alpha\beta}(h)F_{\beta s}(0)\psi_s \tag{2.61}$$

From the Schur's lemma, it follows that either $F_{\alpha r}=0$ or $\mathcal{D}(h)$ contains the irreducible representation $R(h)$. But we cannot have $F_{\alpha r}(0)=0$ because this would invalidate Eq.(2.57) as a proper change of fields according to Sec. 2.1. Vice versa, if $\mathcal{D}$ is reducible and contains the irreducible representation $R(h)$, when is restricted to the subgroup H, then there exist a set of functions $F_{\alpha r}(\xi)$ such that $f_\alpha(\xi,\psi)=\sum_r F_{\alpha r}(\xi)\psi_r$ transforms linearly according to the representation $\mathcal{D}$. We can see this if we decompose $g\in G$ in the unique form:

$$g=e^{\xi\cdot A}e^{u\cdot V} \tag{2.62}$$

That we can write, in a convenient basis:

$$\mathcal{D}(g)=\mathcal{D}(e^{\xi\cdot A})\mathcal{D}(e^{u\cdot V})=\mathcal{D}(e^{\xi\cdot A})\begin{pmatrix}R(e^{u\cdot V}) & 0\\ 0 & \tilde{\mathcal{D}}(e^{u\cdot V})\end{pmatrix} \tag{2.63}$$

[♯7] That means $\xi'=0$ according to the transformation laws of ξ under $h\in H$.

And, under composition:

$$\begin{aligned}\mathcal{D}(g_0)\mathcal{D}(g) &= \mathcal{D}(g_0 g) = \mathcal{D}(g_0 e^{\xi\cdot A} e^{u\cdot V}) \\ &= \mathcal{D}(e^{\xi'\cdot A} e^{u'\cdot V} e^{u\cdot V}) = \mathcal{D}(e^{\xi'\cdot A})\mathcal{D}(e^{u'\cdot V} e^{u\cdot V}) \\ &= \mathcal{D}(e^{\xi'\cdot A}) \begin{pmatrix} R(e^{u'\cdot V} e^{u\cdot V}) & 0 \\ 0 & \tilde{\mathcal{D}}(e^{u'\cdot V} e^{u\cdot V}) \end{pmatrix} \end{aligned} \tag{2.64}$$

From these equations we have:

$$\sum_\beta \mathcal{D}_{\alpha\beta}(g_0)\mathcal{D}_{\beta r}(e^{\xi\cdot A}) = \sum_s \mathcal{D}_{\alpha s}(e^{\xi'\cdot A}) R_{sr}(e^{u'\cdot V}) \tag{2.65}$$

And we can identify:

$$F_{\alpha s}(\xi) = \mathcal{D}_{\alpha s}(e^{\xi\cdot A}) \tag{2.66}$$

Because they have the desired property:

$$\begin{aligned}\sum_s \mathcal{D}_{\alpha s}(e^{\xi'\cdot A})\psi'_s &= \sum_{s,r} \mathcal{D}_{\alpha s}(e^{\xi'\cdot A}) R_{sr}(e^{u'\cdot V})\psi_r \\ &= \sum_{\beta,r} \mathcal{D}_{\alpha\beta}(g_0)\mathcal{D}_{\beta r}(e^{\xi\cdot A})\psi_r \end{aligned} \tag{2.67}$$

As special case, we consider $R(h)$ to be the trivial representation and replace ψ by a constant. Then, the previous theorem gives us a way to find representations of G for which we can find functions of ξ that transform according to that representation. We can use these results on $SU(N)_L \times SU(N)_R$. These representations containing the identity when are restricted to $SU(N)_V$ are of the form $(v, \bar{v})$, where v refers to an irreducible representation of $SU(N)_V$. Functions of ξ_ℓ only cannot transform linearly by any other representation of $SU(N)_L \times SU(N)_R$.

We saw how we can build up fields that transform linearly by taking linear combinations of field that transform nonlinearly.[‡8] This means that, by using a similar construction, we can obtain a field that transforms according to a linear representation form another field that transforms according to another different linear representation. Specifically, we suppose that Ξ_α transforms under $g \in G$ in the following way:

$$g : \Xi_\alpha \to \Xi'_\alpha = R^{(1)}_{\alpha\beta}(g)\Xi_\beta \tag{2.68}$$

[‡8]These linear combinations have ξ-dependent coefficients.

We seek necessary and sufficient conditions for the existence of functions $F_{\mu\beta}(\xi)$ such that the field:

$$X_\mu = F_{\mu\beta}(\xi)\Xi_\beta \tag{2.69}$$

Transforms according to:

$$g : X_\mu \to X'_\mu = R^{(2)}_{\mu\nu}(g)X_\nu \tag{2.70}$$

Being $R^{(1)}$ and $R^{(2)}$ two linear and irreducible representations of G. As we show, this problem has solution only when the reduction of $\bar{R}^{(1)} \times R^{(2)}$ contains one of the representations that can be realized as a function of the fields ξ, in the way that we already characterized them.

First, we see that it is a necessary condition:

$$R^{(2)}_{\mu\nu}(g)X_\nu = R^{(2)}_{\mu\nu}(g)F_{\nu\beta}(\xi)\Xi_\beta = F_{\mu\alpha}(\xi')R^{(1)}_{\alpha\beta}(g)\Xi_\beta \tag{2.71}$$

$$\Rightarrow F_{\mu\alpha}(\xi') = R^{(2)}_{\mu\nu}(g)F_{\nu\beta}\left[R^{(1)}(g)\right]^{-1}_{\beta\alpha} = R^{(2)}_{\mu\nu}(g)\bar{R}^{(1)}_{\alpha\beta}(g)F_{\nu\beta}(\xi) \tag{2.72}$$

And also sufficient, because if we reduce the product $\bar{R}^{(1)} \times R^{(2)}$ as:

$$\langle\alpha, \bar{1}|\langle\nu, 2| = \sum_{\sigma,r}\langle\alpha, \bar{1}; \nu, 2|\sigma, r\rangle\langle\sigma, r| \tag{2.73}$$

By assumption, for at least one value r_0 of r, there exist a set of functions $f_\sigma(\xi)$ such that:

$$f_\sigma(\xi') = R^{(r_0)}_{\sigma\rho}f_\rho(\xi) \tag{2.74}$$

Due to the completeness of the Clebsch-Gordan coefficients, we have:

$$\bar{R}^{(1)}_{\alpha\beta}R^{(2)}_{\mu\nu}\langle\beta, \bar{1}; \nu, 2|\rho, r\rangle = \langle\alpha, \bar{1}; \mu, 2|\sigma, r\rangle R^{(r)}_{\sigma\rho} \tag{2.75}$$

If we define:

$$F_{\mu\alpha}(\xi) = \langle\alpha, \bar{1}; \mu, 2|\sigma, r\rangle f_\sigma(\xi) \tag{2.76}$$

we see that

$$\begin{aligned} F_{\mu\alpha}(\xi') &= \langle\alpha, \bar{1}; \mu, 2|\sigma, r_0\rangle R^{(r_0)}_{\sigma\rho}f_\rho(\xi) = \bar{R}^{(1)}_{\alpha\beta}R^{(2)}_{\mu\nu}\langle\beta, \bar{1}; \nu, 2|\rho, r_0\rangle f_\rho(\xi) = \\ &= \bar{R}^{(1)}_{\alpha\beta}R^{(2)}_{\mu\nu}F_{\nu\beta}(\xi) = R^{(2)}_{\mu\nu}F_{\nu\beta}(\xi)\left[R^{(1)}\right]^{-1}_{\beta\alpha} \end{aligned} \tag{2.77}$$

So, equation (2.70) follows form equations (2.68) and (2.69).

2.5 Covariant derivatives and invariant Lagrangians*

The main results of the previous sections is that by using an appropriate redefinition of the coordinates, every nonlinear realization of G that becomes linear when is restricted to the subgroup $H \subset G$ can be written in the standard form, Eq.(2.13), by means of the following procedure:

- First we introduce the coordinates (ξ, Ψ) that transforms linearly under the subgroup H.
- The standard coordinates of the point (ξ, Ψ) are defined as (ξ, ψ), where ψ is defined by the relation $e^{-\xi \cdot A}(\xi, \Psi) = (0, \psi)$.

The Lagrangian density is a function of the fields and gradients, where the transformation properties of the gradients are determined by the transformation properties of the fields. Therefore the group is realized through the transformation of the differentiable manifold $(\xi, \psi, \partial_\mu \xi, \partial_\mu \psi)$ (see Sec. 2.4). These transformations are not in the standard form, but can be also written in this form because the gradients transform linearly under H. We extend the definition of the standard coordinates to include the gradients:

$$(0, \psi, D_\mu \psi, D_\mu \xi) = e^{-\xi \cdot A}(\xi, \psi, \partial_\mu \psi, \partial_\mu \xi) \tag{2.78}$$

Where $D_\mu \psi$ and $D_\mu \xi$ are the covariant derivatives in the sense that they are constructed so that they have the same transformation properties as the fields:

$$D_\mu \psi \to \mathcal{D}(e^{u \cdot V}) D_\mu \psi \tag{2.79}$$

$$D_\mu \xi \to \mathcal{D}^{(b)}(e^{u \cdot V}) D_\mu \xi \tag{2.80}$$

Now we proceed to obtain explicit expressions for the covariant derivatives. Under infinitesimal space-time displacement we have form (2.12):

$$g(de^{\xi \cdot A}) = (de^{\xi' \cdot A}) e^{u' \cdot V} + e^{\xi \cdot A}(de^{u' \cdot V}) \tag{2.81}$$

According to (2.23), if T_i are the matrices that represent the generators V_i:

*Taken from [42].

$$d\psi' = e^{u'\cdot T} d\psi + (de^{u'\cdot T})\psi \tag{2.82}$$

These equations can be used to obtain the transformation laws of the gradients. If we take $g = e^{-\xi\cdot A}$, that corresponds to the "standardization" of the coordinates, Eq.(2.78), and recall the transformation laws of Eq.(2.12), one deduces easily that $\xi' = 0$ and $u' = 0$ and, form Eq.(2.13) $\psi' = \psi$. At this point:

$$de^{\xi'\cdot A} \equiv e^{(\xi'+d\xi')\cdot A} - e^{\xi'\cdot A} = e^{d\xi'\cdot A} - 1 = d\xi'\cdot A \tag{2.83}$$

$$de^{u'\cdot V} \equiv e^{(u'+du')\cdot V} - e^{u'\cdot V} = e^{du'\cdot V} - 1 = du'\cdot V \tag{2.84}$$

For this particular point (or choice of coordinates) Eq.(2.81) takes the form:

$$e^{-\xi\cdot A} de^{\xi\cdot A} = du'\cdot V + d\xi'\cdot A \tag{2.85}$$

Equation (2.85) can be used to calculate du' and $d\xi'$. On the other hand using (2.84) on (2.82) we obtain:

$$d\psi' = d\psi + du'\cdot T\,\psi \tag{2.86}$$

And the covariant derivatives are then:

$$D_\mu \xi = p_\mu \tag{2.87}$$

$$D_\mu \psi = \partial_\mu \psi + v_\mu \cdot T\,\psi \tag{2.88}$$

Where p_μ and v_μ are defined from:

$$e^{-\xi\cdot A}\partial_\mu e^{\xi\cdot A} = v_\mu\cdot V + p_\mu\cdot A \tag{2.89}$$

It is easy to see that (2.87) and (2.88) transform as covariant derivatives (Eqs.(2.79) and (2.80)) if we use (2.12) and its derivative to obtain:

$$\underbrace{e^{-\xi'\cdot A}\partial_\mu e^{\xi'\cdot A}}_{v'_\mu\cdot V + p'_\mu\cdot A} = e^{u'\cdot V}\,\underbrace{e^{-\xi\cdot A}(\partial_\mu e^{\xi\cdot A})}_{v_\mu\cdot V + p_\mu\cdot A}\,e^{-u'\cdot V} + e^{u'\cdot V}(\partial_\mu e^{-u'\cdot V}) \tag{2.90}$$

Therefore:

$$p'_\mu \cdot A = e^{u'\cdot V} p_\mu \cdot A\, e^{-u'\cdot V} \Rightarrow p'_\mu = \mathcal{D}^{(b)}(e^{u'\cdot V}) p_\mu \tag{2.91}$$

$$v'_\mu \cdot V = e^{u'\cdot V} v_\mu \cdot V e^{-u'\cdot V} - e^{-u'\cdot V}(\partial_\mu e^{u'\cdot V}) \Rightarrow D_\mu \psi' = e^{u'\cdot T} D_\mu \psi \tag{2.92}$$

As we wanted to prove.

The crucial result of this section is that by constructing a Lagrangian using ψ, $D_\mu\psi$ and $D_\mu\xi$, which is superficially invariant under the subgroup H we have have, as a result, that this Lagrangian is also invariant under G.[♯9] A far reach result is that once an invariant Lagrangian $\mathcal{L}(\xi, \psi, \partial_\mu\xi, \partial_\mu\psi)$ is written, then:

$$\mathcal{L}(\xi, \psi, \partial_\mu\xi, \partial_\mu\psi) = \mathcal{L}\big(e^{\xi\cdot A}(0, \psi, D_\mu\xi, D_\mu\psi)\big) = \mathcal{L}(0, \psi, D_\mu\xi, D_\mu\psi) \tag{2.93}$$

And the fields ξ only appear through the covariant derivatives. This is why the interactions of the Goldstone bosons vanish when their momentum is zero.

2.6 Application to the chiral group*

For some groups, as the chiral group, the commutator of two generators of type A_ℓ is proportional to a generator of type V_i. Whenever this happens, one can compute v_μ and p_μ from Eq.(2.89) easily because one can separate the odd from even multiple commutators. For example, using the formula:

$$e^{-\xi\cdot A}\partial_\mu e^{\xi\cdot A} = \frac{1 - e^{-\Delta_{\xi\cdot A}}}{\Delta_{\xi\cdot A}} \partial_\mu \xi \cdot A \tag{2.94}$$

Where the operator $\Delta_{\xi\cdot A}$ is defined as,

$$\Delta_{\xi\cdot A} X = [\xi \cdot A, X] \tag{2.95}$$

One obtains, from Eq.(2.85):

[♯9] The same statement is also true in the opposite direction.

*Taken from [42].

$$v_\mu \cdot V = \frac{1-\cosh \Delta_{\xi\cdot A}}{\Delta_{\xi\cdot A}} \partial_\mu \xi \cdot A \tag{2.96}$$

$$p_\mu \cdot A = \frac{\sinh \Delta_{\xi\cdot A}}{\Delta_{\xi\cdot A}} \partial_\mu \xi \cdot A \tag{2.97}$$

If we consider the chiral group $G = SU(N_f)_L \times SU(N_f)_R$ and identify A_ℓ with the N_f-axial generators and V_i with the N_f-vector generators, the above inequality may be further transformed. Let f_{ijk} be the totally antisymmetric structure constants for $SU(N_f)_V$ in a canonical basis where the Cartan inner product is given by $g_{ij} = -c\,\delta_{ij}$, with $c > 0$. The matrices $(t_i)_{jk} = -f_{ijk}$ furnish the adjoint representation:

$$[t_i, t_j] = f_{ijk} t_k \tag{2.98}$$

Treating ξ, $\partial_\mu \xi$, v_μ and p_μ as N_f-component vectors, we deduce:

$$v_\mu = \frac{1-\cosh(\xi \cdot t)}{\xi \cdot t} \partial_\mu \xi \tag{2.99}$$

$$D_\mu \xi = p_\mu = \frac{\sinh \xi \cdot t}{\xi \cdot t} \partial_\mu \xi \tag{2.100}$$

$$D_\mu \psi = \partial_\mu \psi + T \cdot \left(\frac{1-\cosh(\xi \cdot t)}{\xi \cdot t} \partial_\mu \xi \right) \psi \tag{2.101}$$

For $N_f = 2$ ($T = -\frac{1}{2} i\tau$), we have from (2.99)-(2.101):

$$D_\mu \xi = \partial_\mu \xi + \frac{1}{3!}(\partial_\mu \xi \times \xi) \times \xi + \frac{1}{5!} \ldots \tag{2.102}$$

$$D_\mu N = \partial_\mu N - \frac{1}{2} i\tau \cdot (\frac{1}{2!} \partial_\mu \xi \times \xi + \frac{1}{4!}[(\partial_\mu \xi \times \xi) \times \xi] \times \xi + \ldots) N \tag{2.103}$$

Where N is the nucleon doublet. For $N_f = 3$, denoting with B the traceless baryon octet and with λ_i the Gell-Mann matrices:

$$\xi = \frac{1}{2} \sum_{i=1}^{8} \xi_i \lambda_i, \qquad p_\mu = \frac{1}{2} \sum_{i=1}^{8} p_{\mu i} \lambda_i, \qquad v_\mu = \frac{1}{2} \sum_{i=1}^{8} v_{\mu i} \lambda_i. \tag{2.104}$$

In this notation, Eqs.(2.87)-(2.89) take the form:

$$D_\mu \xi = p_\mu = \partial_\mu \xi + \dots \tag{2.105}$$
$$D_\mu B = \partial_\mu B - i[v_\mu, B] \tag{2.106}$$
$$e^{i\gamma_5 \xi} \partial_\mu e^{-i\gamma_5 \xi} = -i v_\mu - i\gamma_5 p_\mu \tag{2.107}$$

Where, in this case:

$$v_\mu = \frac{i}{2}[\xi, \partial_\mu \xi] + \dots \tag{2.108}$$

As pointed out in the previous section, we can obtain a $G = SU(N_f)_R \times SU(N_f)_L$ invariant Lagrangian if we build it up from $H = SU(N_f)_V$ invariant terms. For $N_f = 3$ we can take the building blocks of Eqs.(2.104) and (2.105)-(2.107), and construct the simple $SU(3)_V$ invariant Lagrangian:

$$\begin{aligned}\mathcal{L} &= \mathrm{Tr}\{-a^{-2} D_\mu \xi D^\mu \xi + i\bar{B}\gamma^\mu D_\mu B + i\bar{B} M B + b_1 \bar{B}\gamma^\mu \gamma_5 p_\mu B + b_2 \bar{B}\gamma^\mu \gamma_5 B p_\mu\} = \\ &= \mathrm{Tr}\{-a^{-2} p_\mu p^\mu + i\bar{B}(\gamma^\mu \partial_\mu + M)B + \bar{B}\gamma^\mu [v_\mu, B] + \bar{B}\gamma^\mu \gamma_5 (b_1 p_\mu B + b_2 B p_\mu)\}\end{aligned} \tag{2.109}$$

That describe the interaction between the pseudoscalar and baryon octets ruled by the broken symmetry group $G = SU(N_f)_L \times SU(N_f)_R \to H = SU(N_f)_V$. The term $-a^{-2} p_\mu p^\mu$ indicates that the normalized pseudoscalar matrix (Φ) is:

$$\Phi = \frac{\xi}{a} \tag{2.110}$$

If we express Eq.(2.109) in terms of the matrix Φ, and neglect higher nonlinearities, we find a pseudovector meson-baryon interaction with independent coefficients (F and D):

$$\begin{aligned}&a\mathrm{Tr}\{\bar{B}\gamma^\mu \gamma_5 (b_1 (\partial_\mu \Phi) B + b_2 B \partial_\mu \Phi)\} \\ &\quad \propto F\,\mathrm{Tr}\left(\bar{B}\gamma^\mu \gamma_5 [\partial_\mu \Phi, B]\right) + D\,\mathrm{Tr}\left(\bar{B}\gamma^\mu \gamma_5 \{\partial_\mu \Phi, B\}\right)\end{aligned} \tag{2.111}$$

As well as a current-current coupling:

$$\frac{i}{2} a^2 \mathrm{Tr}\{B\gamma_\mu [[\Phi, \partial_\mu \Phi], B]\} \tag{2.112}$$

In a meson-baryon scattering calculation one must include the second-order effect of the trilinear pseudovector interaction as well as the first-order effect of the quadrilinear current-current interaction. Only this total contribution has an invariant dynamical meaning, i.e., independent of the particular choice of fields.

2.7 Gauge Fields*

The construction of a Lagrangian invariant under coordinate-dependent group transformations requires (in order to keep the invariance) the introduction of a set of gauge fields $\rho_{\mu i}$ and $a_{\mu \ell}$, associated with the generators V_i and A_ℓ, respectively. Let their transformation law be given by:

$$\rho'_\mu \cdot V + a'_\mu \cdot A = g(\rho_\mu \cdot V + a_\mu \cdot A)g^{-1} - f^{-1}(\partial_\mu g)g^{-1} \tag{2.113}$$

Where f is a constant that gives the strength of the universal coupling of the gauge fields to all other fields. Instead of defining $v_{\mu i}$ and $p_{\mu \ell}$ by Eq.(2.89), we now define them by:

$$e^{-\xi \cdot A}[\partial_\mu + f(\rho_\mu \cdot V + a_\mu \cdot A)]e^{\xi \cdot A} = v_\mu \cdot V + p_\mu \cdot A \tag{2.114}$$

As we did in the previous section, we can use the Eq.(2.114) to compute v_μ and p_μ as functions of ξ, $\partial_\mu \xi$, ρ_μ, and a_μ. With this new definition, p_μ and a_μ satisfies the new space-time transformation, since the additional terms which arise from the differentiation of g are compensated by corresponding terms in the transformation law of the gauge fields. The covariant derivative can therefore be defined, as before, by:

$$D_\mu \xi = p_\mu \qquad \text{and} \qquad D_\mu \psi = \partial_\mu \psi + v_\mu \cdot T\psi \tag{2.115}$$

And, from Eq.(2.114), we obtain: $D_\mu \xi = \partial_\mu \xi + f a_\mu + \ldots$.

The most general Lagrangian invariant under coordinate-dependent group transformations can be obtained by adding to the generalized Yang-Mills Lagrangian for the fields ρ_μ and a_μ any local function of ψ, ξ, v_μ and their derivatives which is superficially invariant under the coordinate-dependent subgroup H. If we add to this Lagrangian a mass term for the gauge fields:

*Taken from [42].

$$\mathcal{L}_{mass} = -\frac{1}{2}m^2[\sum_i \rho_{\mu\, i}\rho_i^\mu + \sum_l a_{\mu\, l}a_l^\mu] \tag{2.116}$$

The invariance is restricted to coordinate-independent group transformations.[♯10] With the mass term, the gauge field satisfy the conservation equations:[♯11]

$$\partial_\mu \rho_i^\mu = 0, \qquad \partial_\mu a_i^\mu = 0 \tag{2.117}$$

Observe that, while the fields $\rho_{\mu\, i}$ have bare mass m, the mass of the fields $a_{\mu\,\ell}$ differs from m. This is because the invariant kinetic term for the field ξ has the form:

$$\mathcal{L}_\xi^{kin} = -\frac{1}{2}\eta^2 \sum_\ell D_\mu \xi_\ell D^\mu \xi_\ell = -\frac{1}{2}\eta^2 \sum_\ell (\partial_\mu \xi_\ell + f a_{\mu\,\ell} + \dots)^2 \tag{2.118}$$

Where η is a normalization parameter. This introduces in the Lagrangian an additional term proportional to $\sum_\ell (a_{\mu\,\ell})^2$ as well as a term proportional to $\sum_\ell \partial_\mu \xi_\ell a_\ell^\mu$. When this bilinear coupling is transformed away by introducing the field:

$$\hat{a}_{\mu\,\ell} = a_{\mu\,\ell} + \frac{\eta^2 f}{\eta^2 f^2 + m^2}\partial_\mu \xi_\ell \tag{2.119}$$

The associated mass is seen to be given by

$$\hat{m}^2 = m^2 + \eta^2 f^2 \tag{2.120}$$

[♯10] Observe that, without this mass term, the field ξ, that appears in Eq.(2.114) as a gauge parameter, could be completely eliminated from the Lagrangian.

[♯11] Or corresponding partial conservation equations if a term which break the coordinate-independent group invariance is added to the Lagrangian.

2.8 The Power Counting

In the previous sections, we saw how to construct a Lagrangian invariant under a group G spontaneously broken into a a subgroup H where the Goldstone bosons appear as the coordinates (ξ) of the broken symmetry generators. Despite the apparent complexity of this nonlinear realization, this form will allow us to establish a hierarchy between the infinite possible terms that we can construct through the method described above and, therefore, apply perturbation theory. More concretely, since the Lagrangian is invariant under space-time *independent* symmetry transformations, it cannot have any dependence on the new Goldstone boson fields when they are constant, so every term in the Lagrangian that contains these new Goldstone bosons fields must contain at least a spacetime derivative of the Goldstone boson fields. These derivatives introduce kinematic factors, which are of the size of the Goldstone boson energy, when we calculate a process for Goldstone bosons reactions. This means that for low energies, the main contribution of a process involving the Goldstone bosons will be given by terms involving the lower number of derivatives. Taking into account that the number of derivatives is bounded from below, one can deduce that as the number of derivatives increases for a term in the Lagrangian, its contribution at low energies will be less important. For a pseudo-Goldstone[♯12] boson, the approximate symmetry is still a good one if the mass of the Goldstone particle is much smaller than the typical scale associated with the higher energy degrees of freedom that have been integrated out. This means that, in this case, we can treat the Goldstone boson masses as a small quantity, along with the derivatives of the Goldstone bosons fields, and apply perturbation theory. The hierarchy of each Feynman diagram that followed from the expansion over the Goldstone bosons momenta and masses was studied systematically by Weinberg [49, 48]. He deduced that the order (importance) ν of a diagram involving pseudo-Goldstone bosons in a low energy process was given by:

$$\nu = \sum_i V_i(d_i + M_i - 2) + 2L + 2 \tag{2.121}$$

Where V_i is the number of interaction vertices of type i in the diagram, d_i and M_i are the number of derivatives and the number of factors of pseudo-Goldstone masses, respectively, in the interaction of type i, and L is the number of loops in the diagram.

[♯12]The name pseudo-Goldstone boson is used in the literature for a Goldstone boson which finally acquires mass due to small explicit symmetry breaking terms in the Lagrangian.

When one wants to incorporate nucleons in the process, one has to take into account that the nucleon is not a "soft" particle. This is so because its mass (and hence, the temporal component of the derivative) is not a small quantity that increases the order of a given diagram. However, if one nucleon with momentum p interacts with a soft pion of momentum q, the nucleon propagator scales as $1/q$, as we see form expanding the quadratic term in the nucleon propagator:

$$\frac{-i(\not{p}+\not{q})+m_N}{(p+q)^2-m_N^2} \underset{q\to 0}{\longrightarrow} \frac{-i\not{p}+m_N}{2(p\cdot q)} \tag{2.122}$$

Lowering a diagram order one unit per internal nucleon line (propagator). The internal nucleon lines, along with the internal pionic lines, can be written in terms of the external nucleon lines (E_N) and the number of loops, giving as a final result:

$$\nu = \sum_i V_i(d_i + M_i - 2 + \frac{n_i}{2}) + 2L - \frac{E_N}{2} + 2 \tag{2.123}$$

Where n_i is the number of nucleon fields in the interaction of type i. The point here is that the coefficient $(d_i + M_i - 2 + \frac{n_i}{2})$ is always positive or zero and E_N is a fixed number for a given process. So Eq.(2.123) *establishes a hierarchy* between the infinite number of Feynman diagrams allowed by the symmetry and *allow us to calculate systematically*, from a finite number thereof, *a given process ruled by that symmetry.*

2.9 Construction of Effective Lagrangians

In order to construct effective Lagrangians where the symmetry is realized in a nonlinear manner, we list below the building blocks that have well defined transformation properties under the chiral group as well as well defined properties under charge conjugation (C), parity transformation (P) and time reversal transformation (T). From Sec. 2.6 we know that the elements that we have for construction the chiral invariant Lagrangians are the baryon field ψ, its covariant derivative $D_\mu\psi$ and the covariant derivatives of the coordinates ξ (the Goldstone bosons).

In order to take into account the mass of the Goldstone bosons, we have to include a mass term which breaks explicitly the chiral symmetry of the Lagrangian. Such type of terms is usually called in the literature symmetry

breakers. One can construct this mass term from the quark mass term of QCD:

$$\mathcal{L}_{QCD}^{Mass} = -\bar{q}_R M q_L - \bar{q}_L M^\dagger q_R, \qquad M = diag(m_u, m_d, m_s, \dots) \tag{2.124}$$

Where $q_{L,R} = \frac{1}{2}(1 \mp \gamma_5)q$, which transforms under $SU(N_f)_L \times SU(N_f)_R$ as $q_L \to L q_L$ and $q_R \to R q_R$, with $L \in SU(N_f)_L$ and $R \in SU(N_f)_R$. Following the ideas of Ref.[50], although M is a constant matrix, $\mathcal{L}_{QCD}^{Mass}$ would be invariant if M were to be transformed as $M \to RML^\dagger$ where, as before, $L \in SU(N_f)_L$ and $R \in SU(N_f)_R$. One can then construct the mass term from the matrices U and M keeping "invariant"[♯13] the Lagrangian. Then, at lowest order one obtains:

$$\mathcal{L}_{Mass} \propto \mathrm{Tr}\{MU^\dagger + UM^\dagger\} \tag{2.125}$$

The combination $\mathrm{Tr}\{MU^\dagger + UM^\dagger\}$ is the only invariant combination since $\mathrm{Tr}\{MU^\dagger - UM^\dagger\}$ is not invariant under parity.[♯14] The term $\mathcal{L}_{Mass}$ can account for the masses because contains only even terms in the Goldstone bosons fields.[♯15] The chiral limit is defined as the point where we recover the chiral symmetry at the Lagrangian level, that is, $m_q \to 0$, which implies $M \to 0$.

Following the reasoning of Sec. 2.8, the building blocks ψ, $D_\mu\psi$, U, u_μ[♯16] and M scale with the Goldstone boson momenta q as:

$$\psi \sim \mathcal{O}(1), \qquad D_\mu\psi \sim \mathcal{O}(1), \qquad U \sim \mathcal{O}(1), \qquad u_\mu \sim \mathcal{O}(q), \qquad M \sim \mathcal{O}(q^2)$$

Where the last relation follows from the fact that the boson mass term is quadratic in the boson mass, not linear as in the fermionc case. That is the reason for the scaling relations $m_q \sim M_\phi^2 \sim \mathcal{O}(q^2)$, where M_ϕ corresponds to the masses of the Goldstone bosons.

Now we apply these ideas to construct the lowest order Lagrangians that describe the interaction between pions ($\mathcal{L}_{\pi\pi}$), identifying them as Goldstone

[♯13] As pointed before, this term is finally not invariant because, at the end, the mass matrix is not transformed. But in following this procedure one keeps track of the underlying QCD explicit way of breaking chiral symmetry.

[♯14] The transformation properties of U under the chiral group were deduced in Sec. 2.2, Eq.(2.37).

[♯15] This is because $M = M^\dagger$.

[♯16] From now on, we use u_μ instead of p_μ of Eq.(2.100) in order to avoid possible misunderstanding with the particles momenta.

bosons, and between pions and a nucleon ($\mathcal{L}_{\pi N}$). In this case $N_f = 2$ and the baryon field is the isodoublet:

$$\psi = \begin{pmatrix} p \\ n \end{pmatrix}$$

We choose to parameterize the pion fields through the so-called exponential parameterization:

$$U = \exp(i\Phi/f), \qquad \Phi = \begin{pmatrix} \frac{\pi^0}{\sqrt{2}} & \pi^+ \\ \pi^- & -\frac{\pi^0}{\sqrt{2}} \end{pmatrix} \tag{2.126}$$

Where f is the pion weak decay constant in the chiral limit.[♯17] For $\mathcal{L}_{\pi\pi}$ the building block u_μ is the only one that involves pion field derivatives, and can enter only through the Lorentz invariant combination $u_\mu u^\mu$. This monomial, together with the mass term, Eq.(2.125), forms the lowest order pionic Lagrangian, which is of order q^2:

$$\mathcal{L}^{(2)}_{\pi\pi} = \alpha_1 \langle u_\mu u^\mu \rangle + \alpha_2 \langle MU^\dagger + UM^\dagger \rangle \tag{2.127}$$

Where the superscript (2) refers to the (chiral) order of the vertices that this Lagrangian generates and $\langle \dots \rangle$ symbolizes the trace over the flavour space. Other monomials constructed with these building blocks are either not invariant over the desired symmetries or generate contributions of higher order. The unknown coefficients can be determined by requiring that this Lagrangian reproduce the kinetic term of a spin-0 particle and the result of Eq.(1.18).

For the leading πN interaction we only have to add to the spin-$\frac{1}{2}$ Lagrangian (using the covariant derivative), a piece that couple the fermionic currents to the pions. The fermionic currents can be vectorial ($\bar{\psi}\gamma^\mu\psi$) or axial vectorial ($\bar{\psi}\gamma^\mu\gamma_5\psi$). Taking into account that the lowest order pionic building block u_μ transforms as an axial vector, the only coupling allowed by symmetry that preserves Lorentz invariance is the coupling to the axial vector fermionic current. Then, the lowest order πN Lagrangian reads:

$$\mathcal{L}^{(1)}_{\pi N} = \bar{\psi}(i\not{D}_\mu - m)\psi + \beta\bar{\psi}\gamma^\mu\gamma_5\psi u_\mu \tag{2.128}$$

[♯17] The reason of this name can be directly deduced from Eq.(1.18).

Again, the superscript (1) refers to the chiral order. It is interesting to point out that, although ψ and $D_\mu\psi$ are both $\mathcal{O}(1)$, the operator $(i\not{D}_\mu - m)$ generates terms of $\mathcal{O}(q)$ because the heavy scale generated by the nucleon mass is eliminated. In this case β can be deduced from the coupling of the nucleon to axial currents.

For completeness we write the leading order Lagrangians with their coefficients deduced:

$$\mathcal{L}^{(2)}_{\pi\pi} = \frac{f^2}{4}\langle u_\mu u^\mu\rangle + \frac{f^2 B_0}{2}\langle MU^\dagger + UM^\dagger\rangle \tag{2.129}$$

$$\mathcal{L}^{(1)}_{\pi N} = \bar{\psi}(i\not{D}_\mu - m)\psi + \frac{g}{2}\bar{\psi}\not{u}\gamma_5\psi \tag{2.130}$$

Where B_0 is related to the pion mass through the relation $M_\pi^2 = (m_u + m_d)B_0$ [33] and g is the so-called axial coupling in the chiral limit. Notice that $\mathcal{L}^{(1)}_{\pi N}$ gives the right leading one-pion matrix elements between two nucleons. This could have been deduced uniquely from the fact that the global chiral symmetry is spontaneously broken, see Chapter 19.2 of Ref.[48] or Ref.[51]. E. g., there is no need to know the symmetry group to obtain this matrix element. For further details we refer the reader to Refs.[32, 33]. Other fields with scalar, pseudoscalar, vector and pseudovector transformation properties can be introduced within this formalism through the sources s, p, v_μ and a_μ [30]. For higher order contributions one has to construct new higher order monomials with undetermined coefficients not fixed by the symmetry. These coefficients, that can be determined by comparison with the experiment, sum rules or lattice QCD, are the so-called low-energy constants (LECs).

Chapter 3

πN Scattering

As commented in Chapter 1, the pion-nucleon (πN) scattering is an important hadronic process that allows for precise tests of the chiral QCD dynamics and contains experimental information on the internal structure of the nucleon. Historically, the study of this reaction has been performed by means of partial wave analyses (PWAs), which are based on unitarity and Mandelstam analyticity (see Ref.[12]). As we show in this chapter, these use the differential cross section and polarization data to reconstruct the different partial waves. However, Chiral Perturbation Theory, presented in Chapter 2, is an excellent tool to study this process in the low-energy region, and provides a model-independent approach to contrast the PWAs results. Moreover, ChPT also supplies a sensible way to estimate the theoretical errors committed in the perturbative treatment. This contrasts with the PWAs, where the magnitude of the resulting uncertainties are often estimated by repeating the analysis with reasonable modifications of the energy-dependent parametrizaton of the amplitudes. On the other hand, one has to take into account possible effects due to the violation of the isospin symmetry due to electromagnetic interactions and the quark masses difference. This is important because PWAs make use of isospin symmetry to resolve some ambiguities encountered within this method (see Sec. 3.1) and large violations could lead to sizeable effects.

In this chapter we will focus on two approaches to pion-nucleon scattering that have been historically the most important ones. First we review in Sec. 3.1 the methodology of PWAs that, on the other hand, have been used as input in ChPT studies of pion-nucleon scattering. We will pay special attention to the PWAs performed by three different groups: the Karlsruhe-Helsinki group, the George Washington University group and the Matsinos' group. We explain the methodology used by these PWAs and discuss their

differences and similarities. We highlight some phenomenological information extracted by these analyses and compare between them and with independent determinations. This information will be very important in Chapters 4 and 5 because provides us a method to check the reliability of the ChPT analysis performed there. We will also discuss the different data base used by these analyses and comment on some criticisms done on the experimental information included in these data and the phenomenology deduced from there. After introducing the reader to the partial wave analyses, the Sec. 3.2 will be dedicated to Chiral Perturbation Theory. There, we establish the formalism used in Chapters 4 and 5 to study the πN scattering process with ChPT, which is the main topic of this thesis. We set up the definitions and normalization of the different quantities employed in our calculations as well as the chiral Lagrangians used. We will also elaborate on the problem concerning the power counting that appears once baryons are included in ChPT and show explicitly that the origin of that problem is the non-vanishing nucleon mass in the chiral limit. The covariant solutions to this problem will be explained in Chapters 4 and 5. Later, in Sec. 3.3 we analyze the possible impact of isospin breaking corrections in the isospin symmetric study performed in Chapters 4 and 5. Finally, in Sec. 3.4 we present a set of techniques that allow us to resum the right-hand cut associated to unitarity corrections and extend the range of validity of the perturbative treatment.

3.1 Partial Wave Analyses

A partial wave analysis is an analysis of the available data of $\pi^+ p$ and $\pi^- p$ scattering together with the single charge exchange (SCX) reaction $\pi^- p \to \pi^0 n$, whose aim is determining the hadronic partial wave amplitudes from differential cross sections and polarization data. If isospin invariance is assumed, the elastic and SCX reactions can be described by four invariant amplitudes, for instance $A^{\pm}(s,t)$ and $B^{\pm}(s,t)$. At a given value of (s,t), one can construct two isospin triangle relations from differential cross section data and polarization parameters for the above mentioned reactions. However, there still remain three types of ambiguities:

- The relative angle between the two triangles.
- A reflection of each triangle at one of its sides.
- A common phase factor to all the amplitudes.

This lead us to require a theoretical input, in addition to unitarity, in order to determine uniquely the amplitude from experimental data[♯1] [12]. Such theoretical constraints are provided by fixed-t analyticity that, together with isospin invariance, are strong enough to resolve the ambiguities of PWAs. Both, the Karlsruhe-Helsinki analysis of Ref.[16] (KA85) and the George Washington University analysis of Ref.[17], that will be used in Chapters 4 and 5, have in common that use fixed-t analyticity as a constraint. They use one-dimensional dispersion relations along curves of constant t, which have the advantages of preserving the crossing symmetry and having enough experimental data up to very large momentum for $0 \geq t \gtrsim -1$ GeV^2. The basic input of these analyses are the forward amplitudes derived from total cross sections by means of the optical theorem. However, still remains the uncertainties resulting from experimental errors and discrepancies between different data sets (which are frequently more important). In fact, there are some criticisms concerning to the experimental data employed by the WI08 solution [52] which uses the data set [53], whereas the KA85 solution includes in its analysis some data [54] that nowadays is believed to be erroneous [55]. On the other hand, to obtain the pure hadronic amplitude is necessary to filter from the data the Coulomb and electromagnetic contributions. The common treatment to filter this contribution is due Tromborg *et al.* [57] which use dispersion theory to isolate the electromagnetic and Coulomb contributions of the amplitude. This treatment, used by the Karlsruhe-Helsinki (KH) and the George Washington (GW) groups, distinguishes between corrections of the phase shifts and of the absorption parameters. The phase shifts include a mixing term between an $I = 1/2$ and $I = 3/2$, and have the following corrections:

- Corrections due to Coulomb scattering of external particles, which include the exchange of a photon between a pion and a nucleon in πN intermediate states.
- Corrections due to the charged and neutral pions and nucleons mass differences.
- Corrections due to the different $\pi^- pn$, $\pi^0 pp$ and $\pi^0 nn$ coupling constants.
- Corrections due to the coupling of the γn channel to $\pi^- p$ scattering.
- Some corrections called in dispersion theory as "short range contributions", which include among other things the u-d quark mass difference.

[♯1] Except near the threshold, where further information is not needed.

It is important to point out that in the dispersion theory the only contribution from the t- and u-channel which is taken into account is that from u-channel nucleon exchange. The rest of the unphysical contributions are omitted, which cannot even being estimated. As recognized in Ref.[58], this is a serious drawback of the dispersive method, and prevents it from set any conclusion about isospin violation.

On the other hand, the analysis of Matsinos' group of Ref.[18], that will be used in Chapter 5, uses relativised Schrödinger equations (RSEs) that contain the sum of an long range electromagnetic potential and short range effective hadronic potential to estimate the electromagnetic corrections reliably. Though the use of a hadronic potential in a RSE is a weak point of this method, this potential is only used to calculate the corrections, not hadronic quantities themselves. According to their authors [59], the main reasons to use a potential model to calculate the electromagnetic corrections are the following:

- The results of the previous analyses need to be extended to lower energies, where is now a large amount of new data obtained at pion factories.

- To control the effects that a change of the hadronic input has on the electromagnetic corrections. This has not been done in the dispersive approach of Ref.[57].

- To check the effects of some fine details of the electromagnetic interactions which can become important an the present precision of the experimental data. This is not contained in [57] either.

- To use energy independent hadronic potentials, instead of the energy dependent ones used before, to calculate the electromagnetic corrections for $\sqrt{s} \lesssim 1.16$ GeV.

The implementation of this electromagnetic potential for $\pi^+ p$ and $\pi^- p$ together with their coupled channels is explained in Ref.[59]. In contrast with the methodology followed in [16] and [17], the authors analyze the elastic scattering data (listed in [18]) separately, and only perform the analysis up to energies of $\sqrt{s} \simeq 1.16$ GeV. However, both EM06 and WI08 have in common the inclusion of new data of high quality collected along the last 20 years in meson factories. The inclusion of these three different PWAs will provide us a mechanism to decouple our results (and therefore our conclusions), from the methodology employed in the PWAs.

3.2 Chiral Perturbation Theory

As explained before, Chiral Perturbation Theory is an appropriate tool to study the pion-nucleon scattering process. The main advantage of this approach is that it takes into account the relevant degrees of freedom of the process allowing us to apply perturbation theory thanks to the nonlinear realization of chiral symmetry. This provides us a more transparent (compared to PWAs) framework where physical observables are directly connected to the low energy constants of the chiral Lagrangian. This perturbative treatment also allows us to estimate, with some confidence, theoretical uncertainties coming from higher order contributions in the chiral expansion. This will be very important for quantities that require an accurate and reliable determination, as the pion-nucleon sigma term, studied in Sec. 5.6 of Chapter 5.

A first attempt to apply baryon ChPT (BChPT) to elastic πN scattering was undertaken by Gasser *et al.* in [13], where the *off-shell* amplitude was obtained up to $\mathcal{O}(q^3)$ in a manifestly Lorentz covariant formalism.[♯2] It was there where it was shown that the presence of the nucleon mass as a new large scale in the chiral limit invalidated naïve power counting arguments in the baryon sector. This problem was partially overcome in the heavy-baryon formalism (HBChPT) [62], in which one recovers a neat power-counting scheme at the cost of manifestly Lorentz covariance. Calculations of the πN scattering amplitude up to $\mathcal{O}(q^3)$ [63] and $\mathcal{O}(q^4)$ [64] accuracies have been performed in the HB formalism by Fettes *et al.*, showing a good description of the $S-$ and $P-$wave phase shifts of different PWs analyses at low energies. It was latter shown that the HB approach is not well suited for studying some of the low-energy theorems involving the πN scattering amplitude [19]. The problem is that the non-relativistic expansion implemented in HBChPT alters the analytical structure of the baryon propagator such that the chiral expansion of some Green functions does not converge in certain parts of the low-energy region [19, 65]. This problem shows up in the analytic continuation of the πN scattering amplitude onto the unphysical region or in the behavior of the form factors close to the two-pion threshold, $t = 4m_\pi^2$ [60]. Besides that, it has been shown that the non-relativistic expansion may have a problematic convergence in some other cases [66, 67, 68].

Based on the ideas previously discussed in Ref.[69], Becher *et al.* proposed the infrared scheme (IRChPT) [19] as a solution to the problems of the HB formalism. The IR scheme is a manifestly Lorentz covariant approach to BChPT that preserves the HB power counting at the same time as it resumms

[♯2]For reviews on BChPT see Refs. [60, 61].

the kinetic terms of the positive-energy part of the baryon propagators, curing the analyticity problems of the HB approach. The πN scattering amplitude has been also calculated at $\mathcal{O}(q^3)$ [43, 21] and $\mathcal{O}(q^4)$ [19] accuracies in the IR scheme. At $\mathcal{O}(q^4)$ the amplitude rapidly converges in the proximity of the CD point so one can investigate meticulously the corresponding low-energy theorems. However, and despite the $\mathcal{O}(q^3)$ representation describes the low energy phase-shifts as good as the HB approach (as we will see in Chapter 4), the convergence at $\mathcal{O}(q^4)$ comes out to be not rapid enough to connect the subthreshold and threshold regions. More importantly, the IR amplitude leads to an unphysically large violation (of about 20%) of the GT relation [43, 21]. These problems seriously question the range of applicability of ChPT in the baryon sector.

A serious drawback of the IR method is that, in curing the problems of the HB expansion, it runs into its own ones with the analytic properties of the loop integrals [70]. This is related to the fact that the IR resummation of kinetic terms performed on the HB propagators completely omits the inclusion of negative-energy pole or anti-nucleon contribution, violating charge conjugation symmetry and, therefore, causality [71]. The most striking consequence of this is the appearance of unphysical cuts. Despite lying outside the range of applicability of ChPT, these cuts can have sizable contributions to the Green functions at low-energies, disrupting the convergence of the respective chiral expansions. This has been indeed shown in different applications of ChPT in the baryon sector such as the chiral extrapolation of the nucleon magnetic moment [66], the $SU(3)_F$ breaking of the baryon magnetic moments [67] or the unitarized description of the πN scattering amplitude [21].

However, the Extended-On-Mass-Shell (EOMS) renormalization scheme [72, 73] allows one to use Lorentz covariant BChPT respecting the standard power counting of ChPT. The main advantage of EOMS over the HB and IR schemes is that it respects the analytic structure of the different terms in the chiral expansion in the sense that they satisfy dispersion relations [70]. With these improvements, we showed in [44] that the chiral representation of the πN scattering amplitude at $\mathcal{O}(q^3)$ gives an excellent description of the PW phase shifts up to the Δ resonance region at the same time as it provides stable values for the LECs and the associated observables. We found that this representation is also suitable to extrapolate, in the center-of-mass energy, the experimental data onto the the subthreshold region. All together, we developed a predictive framework that allows to investigate, in a model-independent fashion, the handful of low-energy theorems related to the elastic πN scattering. Two remarkable outcomes are the experimental

determination of $\sigma_{\pi N}$ [45] and of $g_{\pi N}$. A main conclusion is that the large GT discrepancy found in Refs. [43, 21] can be traced back to the analyticity issues of the IR method rather than to a breaking of the chiral convergence in the πN system. All these results will be presented in Chapter 5.

A completely different difficulty in the baryon sector of ChPT is related to the $\Delta(1232)$. Its contributions to the Green functions can be important at very low energies since this resonance is very close in mass to the nucleon. In the conventional chiral expansion, these effects are accounted for by the LECs but the radius of convergence in this case becomes drastically reduced. This problem is prominent in πN scattering as the threshold for this process is at a center-of mass energy $\delta W = M_\pi$ away from the soft-point, that is the point around which the chiral expansion is actually done. An improved convergence of the chiral series can be obtained including the Δ resonance as an explicit degree of freedom [74, 75, 76]. In this case, one introduces a power counting for the new scale $\epsilon = m_\Delta - m_N$ and computes the Δ contributions accordingly. The Δ corrections to the πN scattering amplitude has been calculated in the HB [77] and IR [43] schemes up to $\mathcal{O}(\epsilon^3)$ within the small-scale expansion (SSE), which considers $\epsilon \sim \mathcal{O}(q)$ [75]. In case of the HB calculation, the inclusion of the Δ increases the range of energies described as compared with the Δ-less case at $\mathcal{O}(q^3)$, although the values of the LECs strongly depended on the fitted data, blurring the conclusions on the extracted values of some observables. In the IR case, the Δ corrections notably worsen the description of the different PW phase-shifts [43]. However, as we will see in Chapter 5, within EOMS the inclusion of this resonance increases significatively the convergence of the chiral series, becoming an essential piece to achieve reliable predictions for important quantities as $g_{\pi N}$ and $\sigma_{\pi N}$.

In this section we discuss to the formalism of ChPT with baryons and comment some important related issues.

3.2.1 Miscellaneous

We consider the process $\pi^a(q)N(p,\sigma;\alpha) \to \pi^{a'}(q')N(p',\sigma';\alpha')$. Here a and a' denote the Cartesian coordinates in the isospin space of the initial and final pions with four-momentum q and q', respectively. Regarding the nucleons, $\sigma(\sigma')$ and $\alpha(\alpha')$ correspond to the third-components of spin and isospin of the initial (final) states, in order. The usual Mandelstam variables are defined as $s = (p+q)^2 = (p'+q')^2$, $t = (q-q')^2 = (p-p')^2$ and $u = (p-q')^2 = (p'-q)^2$, that fulfill $s+t+u = 2M_\pi^2 + 2m_N^2$ for on-shell scattering, with m_N and M_π the nucleon and pion mass, respectively. Exact isospin symmetry is assumed in the following, so that it is convenient to consider Lorentz- and isospin-invariant amplitudes. We then decompose the scattering amplitude as [12]:

$$T_{aa'} = \delta_{a'a}T^+ + \frac{1}{2}[\tau_a, \tau_{a'}]T^- \tag{3.1}$$

$$T^\pm = \bar{u}(p', \sigma')\left[A^\pm + \frac{1}{2}(\not{q} + \not{q}')B^\pm\right]u(p, \sigma) \tag{3.2}$$

Where the Pauli matrices are indicated by τ_c and the definitions of the indices and momenta are shown in the diagram of Fig. 3.1.

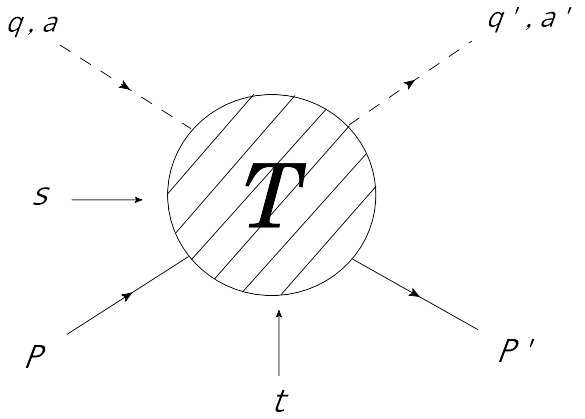

Figure 3.1: Diagrammatic representation of the Lorentz- and isospin-invariant amplitudes. In this figure, s and t correspond to the Mandelstam variables, while P and P' correspond to the momentum incoming and outgoing nucleon, respectively. On the other hand, q (q') corresponds to the momentum of an incoming (outgoing) pion with cartesian isospin index a (a').

The decomposition (3.2), however, is not transparent from the power counting point of view, since the leading order contributions of $A^\pm$ and $B^\pm$ cancel [19]. Therefore, for power counting issues is necessary to write the scattering amplitude in terms of $D \equiv A + \nu B$, where $\nu = \frac{s-u}{4m_N}$, so that the scattering amplitude takes the form:

$$T^\pm = \bar{u}(p', \sigma')\left[D^\pm - \frac{1}{4m_N}[\not{q}', \not{q}]B^\pm\right]u(p, \sigma) \tag{3.3}$$

On the other hand, the free one-particle states are normalized according to the Lorentz-invariant normalization:

$$\langle \mathbf{p}', \sigma'; \gamma | \mathbf{p}, \sigma; \gamma \rangle = 2E_p(2\pi)^3\delta(\mathbf{p}' - \mathbf{p})\delta_{\sigma\sigma'}\delta_{\gamma\gamma'} \tag{3.4}$$

Where E_p is the energy of the particle with three-momentum $\mathbf{p}$ and γ indicates any internal quantum number. A free two-particle state is normalized accordingly and it can be decomposed in states with well defined total spin S and total angular momentum J. In the center-of-mass (CM) frame one has:

$$|\pi(-\mathbf{p};a)N(\mathbf{p},\sigma;\alpha)\rangle = \sqrt{4\pi}\sum_{\ell,m,J}(m\sigma\mu|\ell SJ)Y_\ell^m(\hat{\mathbf{p}})^*|J\mu\ell;a\alpha\rangle \tag{3.5}$$

With $\hat{\mathbf{p}}$ the unit vector of the CM nucleon three-momentum $\mathbf{p}$, ℓ the orbital angular momentum, m its third component, $\mu = m + \sigma$ the third-component of the total angular momentum and $S = 1/2$ for πN scattering. The Clebsch-Gordan coefficient is denoted by $(m_1 m_2 m_3|j_1 j_2 j_3)$, corresponding to the composition of the spins j_1 and j_2 (with third-components m_1 and m_2, in order) to give the third spin j_3, with third-component m_3. The state with total angular momentum well-defined, $|J\mu\ell;a\alpha\rangle$, satisfies the normalization condition:

$$\langle J'\mu'\ell';a'\alpha'|J\mu\ell;a\alpha\rangle = \delta_{JJ'}\delta_{\mu'\mu}\delta_{\ell\ell'}\frac{4\pi\sqrt{s}}{|\mathbf{p}|}\delta_{a'a}\delta_{\alpha'\alpha} \tag{3.6}$$

The partial wave expansion of the πN scattering amplitude can be worked out straightforwardly from Eq.(3.5) (see Appendix G). By definition, $\mathbf{p}$ gives the positive direction of the $\mathbf{z}$-axis. Inserting the series of Eq.(3.5) one has for the scattering amplitude:

$$\begin{aligned}\langle\pi(-\mathbf{p}';a')N(\mathbf{p}',\sigma';\alpha')|T|\pi(-\mathbf{p};a)N(\mathbf{p},\sigma;\alpha)\rangle = \\ 4\pi\sum_{\ell,m,J}Y_\ell^0(\hat{\mathbf{z}})(m\sigma'\sigma|\ell\frac{1}{2}J)(0\sigma\sigma|\ell\frac{1}{2}J)Y_\ell^m(\hat{\mathbf{p}}')T_{J\ell}(s)\end{aligned} \tag{3.7}$$

Where T is the T-matrix operator and $T_{J\ell}$ is the partial wave amplitude with total angular momentum J and orbital angular momentum ℓ. Notice that in Eq.(3.7) we made use of the fact that $Y_\ell^m(\hat{\mathbf{z}})$ is non-zero only for $m = 0$. Recall also that because of parity conservation partial wave amplitudes with different orbital angular momentum do not mix. From Eq.(3.7) it is straightforward to isolate $T_{J\ell}$ with the result:

$$\begin{aligned}T_{J\ell}(a',\alpha';a,\alpha) = \frac{1}{\sqrt{4\pi(2\ell+1)}(0\sigma\sigma|\ell\frac{1}{2}J)} \\ \times\sum_{m,\sigma'}\int d\hat{\mathbf{p}}'\,\langle\pi(-\mathbf{p}';a')N(\mathbf{p}',\sigma';\alpha')|T|\pi(-\mathbf{p};a)N(\mathbf{p},\sigma;\alpha)\rangle(m\sigma'\sigma|\ell\frac{1}{2}J)Y_\ell^m(\hat{\mathbf{p}}')^*\end{aligned} \tag{3.8}$$

In the previous expression the resulting $T_{J\ell}$ is, of course, independent of the choice of σ.

The relation between the Cartesian and charge bases is given by:

$$\begin{aligned} |\pi^+\rangle &= \frac{1}{\sqrt{2}}(|\pi^1\rangle + i|\pi^2\rangle) \\ |\pi^-\rangle &= \frac{1}{\sqrt{2}}(|\pi^1\rangle - i|\pi^2\rangle) \\ |\pi^0\rangle &= |\pi^3\rangle \end{aligned} \tag{3.9}$$

According to the previous definition of states $|\pi^+\rangle = -|1,+1\rangle$, $|\pi^-\rangle = |1,-1\rangle$ and $|\pi^0\rangle = |\pi^3\rangle = |1,0\rangle$, where the states of the isospin basis are placed to the right of the equal sign. Notice the minus sign in the relationship for $|\pi^+\rangle$. Then, the amplitudes with well-defined isospin, $I = 3/2$ or $1/2$, are denoted by $T_{IJ\ell}$ and can be obtained employing the appropriate linear combinations of $T_{J\ell}(a', \alpha'; a, \alpha)$, Eq.(3.8), in terms of standard Clebsch-Gordan coefficients.

Due to the normalization of the states with well-defined total angular momentum, Eq.(3.6), the partial waves resulting from Eq.(3.8) with well defined isospin satisfy the unitarity relation:

$$\mathrm{Im}T_{IJ\ell} = \frac{|\mathbf{p}|}{8\pi\sqrt{s}}|T_{IJ\ell}|^2 \tag{3.10}$$

Which holds for $|\mathbf{p}| > 0$ and below the inelastic threshold due the one-pion production at $|\mathbf{p}| \simeq 210$ MeV. Given the previous equation, the S-matrix element with well defined I, J and ℓ, denoted by $S_{IJ\ell}$, corresponds to:

$$S_{IJ\ell} = 1 + i\frac{|\mathbf{p}|}{4\pi\sqrt{s}}T_{IJ\ell} \tag{3.11}$$

Satisfying $S_{IJ\ell}S^*_{IJ\ell} = 1$ in the elastic physical region. In the same region we can then write:

$$S_{IJ\ell} = e^{2i\delta_{IJ\ell}} \tag{3.12}$$

With $\delta_{IJ\ell}$ the corresponding phase shifts. And, form Eqs.(3.11) and (3.12) one has:

$$T_{IJ\ell} = \frac{8\pi\sqrt{s}}{|\mathbf{p}|} \sin\delta_{IJ\ell} e^{i\delta_{IJ\ell}} \tag{3.13}$$

However, if the calculation is perturbative, the S-matrix does not fulfill unitarity exactly and one cannot use Eq.(3.13) to calculate the phase shifts. Instead, is necessary to perform a perturbative expansion of the previous equation up to the order considered to find the relation between the perturbative amplitude and its corresponding phase shift. Following this procedure, we find that up to $\mathcal{O}(q^4)$ the different phase shifts can be obtained from the perturbative amplitudes by means of the equation:

$$\delta_{IJ\ell} = \frac{|\mathbf{p}|}{8\pi\sqrt{s}} \mathrm{Re} T_{IJ\ell} \tag{3.14}$$

3.2.2 Chiral Lagrangians

According to the chiral power counting discussed in Sec. 2.8 [49], for an $\mathcal{O}(q^3)$ calculation ($\nu = 3$) of the πN scattering amplitude we need to consider the following $\pi\pi$ and πN Lagrangians:[♯3]

$$\mathcal{L}_{ChPT} = \mathcal{L}^{(2)}_{\pi\pi} + \mathcal{L}^{(4)}_{\pi\pi} + \mathcal{L}^{(1)}_{\pi N} + \mathcal{L}^{(2)}_{\pi N} + \mathcal{L}^{(3)}_{\pi N} \tag{3.15}$$

Where the superscript indicates the chiral order ν. Here, $\mathcal{L}^{(n)}_{\pi\pi}$ refers to the purely mesonic Lagrangian (without baryons) and $\mathcal{L}^{(n)}_{\pi N}$ corresponds to the one bilinear in the baryon fields. The explicit form for the mesonic Lagrangians is:

$$\begin{aligned} \mathcal{L}^{(2)}_{\pi\pi} &= \frac{f^2}{4}\langle u_\mu u^\mu + \chi_+ \rangle \\ \mathcal{L}^{(4)}_{\pi\pi} &= \frac{1}{16}\ell_4 \left(2\langle u_\mu u^\mu \rangle \langle \chi_+ \rangle + \langle \chi_+ \rangle^2\right) + \dots \end{aligned} \tag{3.16}$$

Where the ellipsis indicate terms that are not needed in the calculations given here and $\langle \cdots \rangle$ denotes the trace of the resulting 2×2 matrix in the flavour space. For the different symbols, f is the pion weak decay constant in the chiral limit and:

[♯3] This is for the case in which we do not consider the Δ-isobar contribution.

$$u^2 = U \ , \ u_\mu = iu^\dagger \partial_\mu U \, u^\dagger \ , \ \chi_\pm = u^\dagger \chi u^\dagger \pm u \chi^\dagger u \tag{3.17}$$

The explicit chiral symmetry breaking due to the non-vanishing quark masses (in the isospin limit $m_u = m_d = \hat{m}$) is introduced through $\chi = 2B_0\hat{m}$. This is a generalization of Eq.(2.125). The constant B_0 is proportional to the quark condensate in the chiral limit $\langle 0|\bar{q}^j q^i|0\rangle = -B_0 f^2 \delta^{ij}$. In the following we employ the so-called sigma-parameterization, where:

$$U(x) = \sqrt{1 - \frac{\vec{\pi}(x)^2}{F^2}} + i\frac{\vec{\pi}(x)\cdot\vec{\tau}}{F} \tag{3.18}$$

For the pion-nucleon Lagrangian we have:

$$\mathcal{L}_{\pi N}^{(1)} = \bar{\psi}(i \not{D} - m)\psi + \frac{g}{2}\bar{\psi}\not{u}\gamma_5\psi \tag{3.19}$$

$$\begin{aligned}\mathcal{L}_{\pi N}^{(2)} = {} & c_1\langle\chi_+\rangle\bar{\psi}\psi - \frac{c_2}{4m^2}\langle u_\mu u_\nu\rangle(\bar{\psi}D^\mu D^\nu\psi + \text{h.c.}) + \frac{c_3}{2}\langle u_\mu u^\mu\rangle\bar{\psi}\psi \\ & - \frac{c_4}{4}\bar{\psi}\gamma^\mu\gamma^\nu[u_\mu, u_\nu]\psi + \ldots\end{aligned} \tag{3.20}$$

$$\begin{aligned}\mathcal{L}_{\pi N}^{(3)} = {} & \bar{\psi}\Bigg(-\frac{d_1+d_2}{4m}([u_\mu,[D_\nu,u^\mu]+[D^\mu,u_\nu]]D^\nu + \text{h.c.}) \\ & + \frac{d_3}{12m^3}([u_\mu,[D_\nu,u_\lambda]](D^\mu D^\nu D^\lambda + \text{sym.}) + \text{h.c.}) + i\frac{d_5}{2m}([\chi_-,u_\mu]D^\mu + \text{h.c.}) \\ & + i\frac{d_{14}-d_{15}}{8m}\left(\sigma^{\mu\nu}\langle[D_\lambda,u_\mu]u_\nu - u_\mu[D_\nu,u_\lambda]\rangle D^\lambda + \text{h.c.}\right) \\ & + \frac{d_{16}}{2}\gamma^\mu\gamma_5\langle\chi_+\rangle u_\mu + \frac{id_{18}}{2}\gamma^\mu\gamma_5[D_\mu,\chi_-]\Bigg)\psi + \ldots\end{aligned} \tag{3.21}$$

In the previous equation m is the nucleon mass in the chiral limit ($m_u = m_d = 0$) and the covariant derivative D_μ acting on the baryon fields is given by $\partial_\mu + \Gamma_\mu$ with $\Gamma_\mu = [u^\dagger, \partial_\mu u]/2$. As pointed before, the low-energy constants (c_i and d_i) are not fixed by chiral symmetry and, in this case, we extract their values by fitting them to πN scattering data. Again, only the terms needed for the present study are shown in Eq.(3.21). For further details on the definition and derivation of the different monomials we refer the reader to Refs.[63, 78]. Up to $\mathcal{O}(q^3)$, these Lagrangians generate the contributions displayed in Fig. 3.2.

The calculations presented in Chapters 4 and 5 are finally given in terms of m_N, f_π and g_A, which implies some reshuffling of pieces once m, f and g

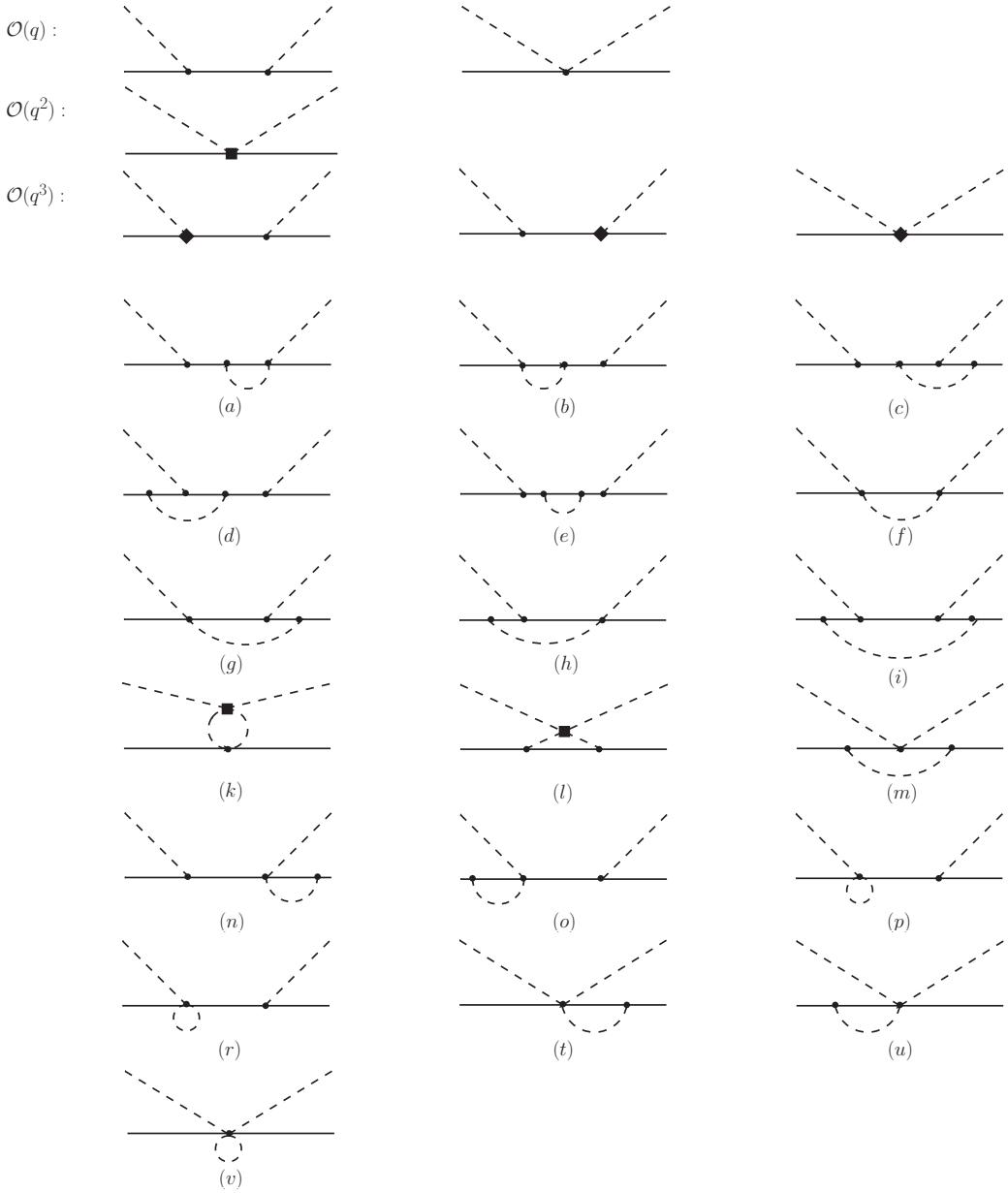

Figure 3.2: πN scattering diagrams (direct version) up to $\mathcal{O}(q^3)$. Filled circles: $\mathcal{O}(q)$ vertices. Filled squares: $\mathcal{O}(q^2)$. Filled diamonds: $\mathcal{O}(q^3)$ vertices.

are expressed in terms of their physical values making use of their expressions at $\mathcal{O}(q^3)$ [19]. In this work we employ the numerical values $f_\pi = 92.4$ MeV, $M_\pi = 139$ MeV, $m_N = 939$ MeV and $g_A = 1.267$.

The $\Delta(1232)$ resonance

As pointed out before, the $\Delta(1232)$ plays an important role in the πN scattering process. This is a spin-3/2 resonance that can be described by a Rarita-Schwinger field [79] $\psi_\mu^{(\sigma)}$, where μ and σ (which will be omitted in the following) are the vector and spin indices, respectively. The free Lagrangian of a massive Rarita-Schwinger field is given by:

$$\mathcal{L}_{3/2} = \bar{\psi_\mu}(i\gamma^{\mu\nu\alpha}\partial_\alpha - m\gamma^{\mu\nu})\psi_\nu \tag{3.22}$$

Where here m is the mass of the spin-3/2 particle, $\gamma^{\mu\nu\alpha} = \frac{1}{2}\{\gamma^{\mu\nu}, \gamma^\alpha\} = -i\epsilon^{\mu\nu\alpha\beta}\gamma_\beta\gamma_5$ and $\gamma^{\mu\nu} = \frac{1}{2}[\gamma^\mu, \gamma^\nu]$. However, the spin-3/2 particle described by Eq.(3.22) has unphysical spin-1/2 degrees of freedom that lead to some pathologies as negative-norm states [80] or acausal modes [81]. This spin-1/2 contribution can be eliminated if we impose the following gauge symmetry:

$$\psi_\mu(x) \to \psi_\mu(x) + \partial_\mu\epsilon(x) \tag{3.23}$$

Where $\epsilon(x)$ is a spinor field. This symmetry is satisfied by the massless Rarita-Schwinger Lagrangian, Eq.(3.22), but the interesting point is to apply this symmetry to the Rarita-Schwinger field couplings. This is because the gauge-invariant couplings have the important property of fulfill the transversality condition:

$$p_\mu\Gamma^\mu(p, \dots) = 0 \tag{3.24}$$

Where p is the momentum of the Rarita-Schwinger field and μ is its vector index. This property is crucial to filter the spin-1/2 contributions because the spin-3/2 propagator obtained from the Rarita-Schwinger Lagrangian (3.22) reads:

$$S_{\mu\nu}(p) = -\frac{1}{\not{p} - m}P_{\mu\nu}^{(3/2)} + \frac{2}{3m^2}(\not{p} + m)P_{22,\mu\nu}^{(1/2)} - \frac{1}{\sqrt{3}m}(P_{12,\mu\nu}^{(1/2)} - P_{21,\mu\nu}^{(1/2)}) \tag{3.25}$$

Where $P_{\mu\nu}^{(3/2)}$ projects onto the pure spin-3/2 state and $P_{22,\mu\nu}^{(1/2)}$, $P_{12,\mu\nu}^{(1/2)}$ and $P_{21,\mu\nu}^{(1/2)}$ are projection operators onto the spin-1/2 states. They have the following form:

$$P^{(3/2)}_{\mu\nu} = g_{\mu\nu} - \frac{1}{3}\gamma_\mu\gamma_\nu - \frac{1}{3p^2}(\not{p}\gamma_\mu p_\nu + p_\mu\gamma_\nu\not{p}) \tag{3.26}$$

$$P^{(1/2)}_{22,\mu\nu} = \frac{p_\mu p_\nu}{p^2} \tag{3.27}$$

$$P^{(1/2)}_{12,\mu\nu} = \frac{p^\rho p_\nu \gamma_{\mu\rho}}{\sqrt{3}p^2} \tag{3.28}$$

$$P^{(1/2)}_{21,\mu\nu} = \frac{p_\mu p^\rho \gamma_{\rho\nu}}{\sqrt{3}p^2} \tag{3.29}$$

It is easy to see that if a coupling satisfies the transversality condition (3.24), the spin-1/2 contributions decouple from observables, since:

$$\Gamma^\mu(p,\dots)S_{\mu\nu}(p)\Gamma^\nu(p,\dots) = -\Gamma^\mu(p,\dots)\frac{1}{\not{p}-m}P^{(3/2)}_{\mu\nu}\Gamma^\nu(p,\dots) \tag{3.30}$$

However, a chiral interaction for the Rarita-Schwinger field ψ_μ does not have the gauge symmetry (3.23). In this case, one can make use of the Euler-Lagrange equations on the Lagrangian (3.22):

$$i\gamma^{\mu\nu\alpha}\partial_\alpha\psi_\nu - m\gamma^{\mu\nu}\psi_\nu = (i\not{\partial} - m)\psi_\nu = 0 \tag{3.31}$$

$$\partial_\mu(i\gamma^{\mu\nu\alpha}\partial_\alpha - m\gamma^{\mu\nu})\psi_\nu = \gamma^{\mu\nu}\partial_\mu\psi_\nu = \partial\cdot\psi = 0 \tag{3.32}$$

$$\gamma_\mu(i\gamma^{\mu\nu\alpha}\partial_\alpha - m\gamma^{\mu\nu})\psi_\nu = -(2i\gamma^{\mu\nu}\partial_\mu + 3m\gamma^\nu)\psi_\nu = \gamma\cdot\psi = 0 \tag{3.33}$$

To write an on-shell equivalent chiral Lagrangian with couplings that satisfy the gauge condition (3.23) up to a given order[♯4], see Refs.[82, 76] for more details.

We use this *consistent* formulation of chiral Lagrangians, due to Pascalutsa, to filter the unphysical degrees of freedom of the Rarita-Schwinger spinor Δ_μ describing the $\Delta(1232)$-resonance. We obtain then the following consistent couplings to the nucleons and pions:

$$\mathcal{L}^{(1)}_{\pi N\Delta} = \frac{i\,h_A}{2f_\pi m_\Delta}\left(\partial_\rho\bar{\Delta}_\mu\right)T^{\dagger a}\gamma^{\rho\mu\nu}\psi\partial_\nu\pi^a + \text{h.c.} \tag{3.34}$$

[♯4]The inclusion of various different symmetries in a given interaction is not easy (whenever possible). However, the perturbative treatment of effective field theories allow us to reconcile the gauge symmetry of Eq.(3.23) and chiral symmetry up to a given order in the EFT expansion [76].

Where the T^a are the spin-3/2 $\longrightarrow$ spin-1/2 projectors, which verify $T^a T^{\dagger b} = \delta^{ab} - \tau^a \tau^b/3$, and h_A is the $N\Delta$ axial coupling, that is poorly determined but related with the $\pi N\Delta$ coupling through the off-diagonal Goldberger-Treiman relation. The latter is fixed by fitting the πN elastic scattering P_{33} phase shifts across the Δ region with a "dressed" Born term. This leads to $h_A = 2.90(2)$ for a Breit-Wigner width of $\Gamma_\Delta = 118(2)$ MeV [76], which value is taken from the PDG [83]. Alternatively we can use h_A it as a fitting parameter and use it to check the reliability of the PWA used to extract its value.

At $\mathcal{O}(q^2)$, we have the following $N\Delta$ Lagrangians correcting the Born-term contribution of the Δ to πN scattering:

$$\mathcal{L}^{(2)}_{N\Delta} = \frac{d_3^\Delta}{m_\Delta}\, \bar{N} T^a \omega^a_{\mu\nu} \gamma^\mu \gamma^{\nu\rho\sigma} D_\rho \Delta_\sigma - \frac{i d_4^\Delta}{m_\Delta^2}\, \bar{N} T^a \omega^a_{\mu\nu} \gamma^{\nu\rho\sigma} D^\mu D_\rho \Delta_\sigma + \text{h.c.} \tag{3.35}$$

Where $\omega^a_{\mu\nu} = \langle \tau^a [\partial_\mu, u_\nu] \rangle / 2$. These Lagrangians are consistent and the on-shell equivalent of them was presented in [84], which are al so equivalent to the ones of Fettes and Meißner [77]. Of course, before including the $\Delta(1232)$ contributions in the πN amplitude one has to assign a counting to the Δ interactions. Because the $\Delta(1232)$ is quite close to the πN threshold, we have to distinguish between two low energy regions: the region below the $\Delta(1232)$ and the $\Delta(1232)$-resonance region. In this thesis we only study energy regions up to $\sqrt{s} = 1.20$ GeV which belongs to the first one. Within this region the $\Delta(1232)$ propagator is suppressed with respect to the nucleon one by a factor $p^{1/2}$ [76] so, in this counting, we only needed $\mathcal{L}^{(1)}_{\pi N\Delta}$ and $\mathcal{L}^{(2)}_{\pi N\Delta}$ for an $\mathcal{O}(q^3)$ calculation.

3.2.3 The Power Counting in Covariant Baryon Chiral Perturbation Theory

While the techniques described in Chapter 2 are valid for both the mesonic and the baryonic sectors, there are important differences when our calculations include baryons. In the pure mesonic sector, the amplitudes are homogeneous functions of the meson energy and contributions from n-loop diagrams are suppressed in powers of q^{2n} (meson momenta), obtaining therefore the desired hierarchy to apply perturbation theory. Concretely, in the $SU(2)$ sector, the chiral order ν and the number of loops in the chiral expansion of the $\pi\pi$ scattering amplitude is as given in Eq.(2.123), and depicted in Fig. 3.3.

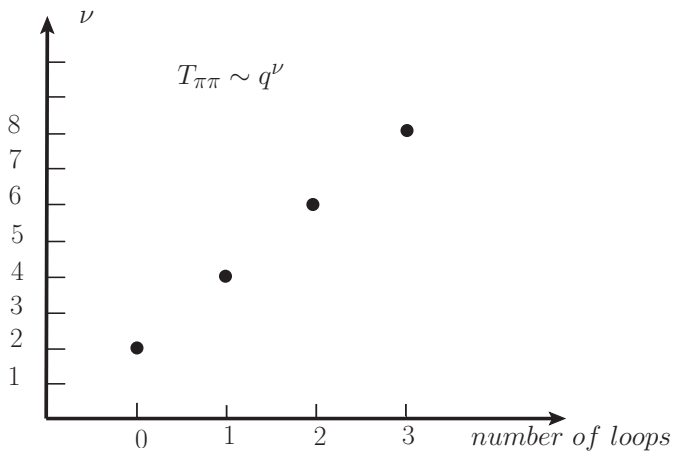

Figure 3.3: Scaling dependence of the $\pi\pi$ scattering amplitude, $T_{\pi\pi}$, with the pion momentum q.

For the case with baryons, one has to deal with a new heavy scale which does not vanishes in the chiral limit: the nucleon mass. The latter makes that the nucleon momenta scales as $p^{\mu} \sim \mathcal{O}(1)$ [13], spoiling the homogeneity of the amplitudes and breaking the power counting explained in Sec. 2.8. A visual description is shown in Fig. 3.4 [13].

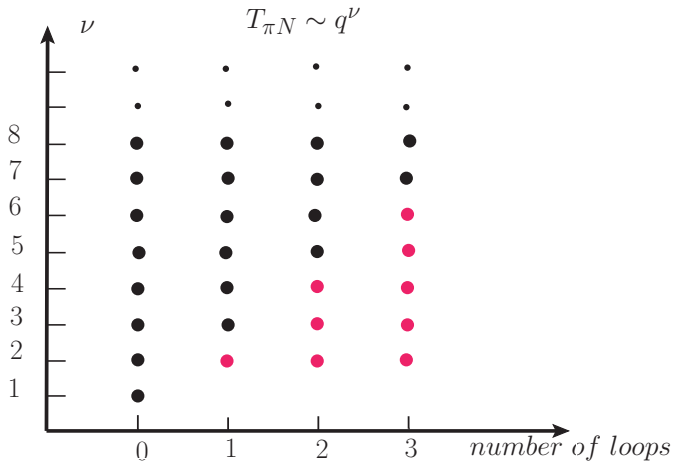

Figure 3.4: Scaling dependence of the πN scattering amplitude, $T_{\pi N}$, with the pion momentum q. Red points corresponds to contributions that break the power counting.

To illustrate the problem, we consider the one-loop correction to the nucleon mass which corresponds to the Feynman diagram displayed in Fig.3.5.

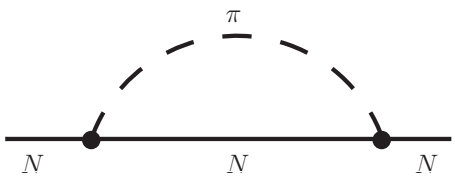

Figure 3.5: One-loop self-energy of the nucleon.

According to Eq.(2.123), this diagram should generate contributions of $\mathcal{O}(q^3)$ that correct the nucleon mass in the chiral limit. However, an explicit calculation shows that corrections are given by:

$$m_N = m - \frac{3g^2 m_N}{2f^2}(2\bar{\lambda}(m_N^2 + M^2)) + \frac{3g^2 m_N M^2}{32\pi^2 f^2}(1 - \log\left(\frac{m_N^2}{\mu^2}\right)) - \frac{3g^2 m_N^3}{32\pi^2 f^2}\log\left(\frac{m_N^2}{\mu^2}\right) + \mathcal{O}(q^3) \tag{3.36}$$

Where μ is the scale of renormalization and $2\bar{\lambda} = [-\Gamma(2-d/2)+\log(\mu^2/4\pi)-1]/(4\pi)^2$ with d the space-time dimension of the loop virtual momentum in the dimensional regularization method. So, as pointed before, it turns out that the non-vanish nucleon mass generates terms of $\mathcal{O}(1)$ and $\mathcal{O}(q^2)$ that break the power counting[♯5] and, in principle, could spoil the applicability of perturbation theory. However this complication can be overcome by a suitable renormalization procedure. Such kind of procedures will be explained in Chapters 4 and 5.

3.3 Isospin breaking corrections

Isospin symmetry implies a degenerate mass in the nucleon isospin doublet. However, the difference between the u and d quarks introduces a difference of 2.5 MeV in the the neutron mass respect to the proton one. This splitting due to the quark masses is compensated by electromagnetic interactions that rises the proton mass in 1.2 MeV. This leaves an overall correction of 1.3 MeV for the neutron mass over the proton one due to the isospin breaking

[♯5]Notice that if m_N would scale as $M \sim q$, all the terms would be $\mathcal{O}(q^3)$ and we would not have power counting breaking terms.

effects of electromagnetism and quark masses difference. This fact rises the question about the impact of isospin violation in strong interaction process like the one we are considering here. In fact, πN scattering is an excellent testground for studying this question, since modern meson factories allow us to have huge amount of very precise low-energy data. The availability of these high quality data opened the way to studying the isospin breaking corrections from the experimentally accessible reactions $\pi^+ p$ and $\pi^- p$ scattering and the single charge exchange (SCX) reaction $\pi^- p \to \pi^0 n$. A consistent study of these reactions within the framework of ChPT have been performed in Ref.[85] calculating the chiral amplitude taking into account the quark masses difference and including electromagnetic corrections valid for a pion momentum $\gtrsim 1$ MeV.[♯6] In this work the authors analyzed the isospin breaking corrections by studying the difference between the complete amplitude and the same amplitude in the isospin limit. This was done for pion momenta from 25 to 100 MeV, which corresponds to $\sqrt{s} \approx 1.08$ to ≈ 1.11 GeV. Its main conclusion was that the size of the isospin breaking effects in the S-wave is of $\approx -0.7\%$, whereas for the P-waves lies in the range from -4 to -1.5%.

On the other hand, Matsinos' group also studied the isospin breaking corrections within its potential model approach (explained in Sec. 3.1). In Ref.[18] the authors checked the isospin symmetry in the hadronic interactions by trying to reproduce the SCX reaction from their hadronic phase shifts extracted from $\pi^+ p$ and $\pi^- p$ scattering data and they found an important underestimation of the measured SCX cross sections. Namely, a previous analysis carried by E. Matsinos gives an estimation for the isospin breaking effects of $\approx 6\%$ [86], although no estimations for these effects are given by Ref.[18]. This conclusion was reinforced by the results of [87], where the same authors found a sizeable difference between the value of the S-wave scattering length for $\pi^+ p$ scattering and the value for the same quantity obtained from the S-wave scattering length for $\pi^- p$ and SCX reactions by means of isospin invariance. However, there exist some criticism to the potential model approach as well as to the dispersive one since they can introduce systematic errors due to a possible mismatch in the description of both interactions the strong and the electromagnetic ones. This could become very important when studying small quantities like isospin symmetry violation [85].

Nevertheless, since we use Chiral Perturbation Theory to calculate our amplitudes, we consider more consistent to take into account the results of [85], that uses the same approach and provides a consistent way to study

[♯6] For lower pion momenta the loop diagrams with virtual photons are not suppressed compared with the tree level, see Ref.[85] for further details.

together the strong and the electromagnetic interaction. The relative deviations obtained in that work will be taken into account during the fitting procedure of our amplitudes to the phase shifts provided by the different partial waves.

3.4 Unitarization Techniques

As pointed in Chapter 2, the S-matrix obtained in Chiral Perturbation Theory does not satisfy unitarity. However, there exists various techniques that allow to resum the Feynman diagrams that give rise to the right hand cut, Eq.(3.10). These unitarization techniques have proved to be very successful in the description of non-perturbative phenomena with ChPT [88, 89]. In this thesis we will follow the methodology of Ref.[90] that deduces, in terms of the N/D method [91], the most general structure of an elastic partial wave amplitude that fulfills elastic unitarity, Eq.(3.10). This representation is accomplished by means of the analytical properties of the scattering amplitudes combined with elastic unitarity, that provides an explicit form for the imaginary part of the inverse of the scattering amplitude for the different partial waves. Using the Cauchy's theorem to perform a dispersion relation for the inverse of a partial wave, whose discontinuity is known along the right hand cut, one obtains the following expression [90]:

$$T(s) = \frac{1}{\mathcal{T}(s)^{-1} + g(s)} \tag{3.37}$$

Where the $\mathcal{T}(s)$ amplitude corresponds to those other terms not generated by the right hand cut, e.g. crossed channel dynamics, and $g(s)$ is the so-called unitary loop function. The latter is obtained by integration of the phase space of the scattering process along the unitarity cut. As explained in Ref.[90], the $\mathcal{T}(s)$ amplitude (or interaction kernel) can be obtained from effective field theory as Chiral Perturbation Theory. In this way the unitarized amplitude T fulfills unitarity and embodies the underlying chiral symmetry. For the case of πN scattering, which is the case that we are interested in, the phase space is $|\mathbf{p}|/(8\pi\sqrt{s})$, so the unitary loop function reads:

$$
\begin{aligned}
g(s) &= g(s_0) - \frac{s-s_0}{\pi}\int_{s_{th}}^{\infty} ds' \frac{|\mathbf{p}|}{8\pi\sqrt{s'}}\frac{1}{(s'-s)(s'-s_0)} \\
&= \frac{1}{(4\pi)^2}\left\{a(\mu) + \log\left(\frac{m_N^2}{\mu^2}\right) - \frac{m_N^2 - M_\pi^2 + s}{2s}\log\left(\frac{M_\pi^2}{m_N^2}\right)\right. \\
&+ \frac{|\mathbf{p}|}{\sqrt{s}}\left[\log(s - m_N^2 + M_\pi^2 + 2\sqrt{s}|\mathbf{p}|) + \log(s + m_N^2 - M_\pi^2 + 2\sqrt{s}|\mathbf{p}|)\right. \\
&\left.\left. - \log(-s + m_N^2 - M_\pi^2 + 2\sqrt{s}|\mathbf{p}|) - \log(-s - m_N^2 + M_\pi^2 + 2\sqrt{s}|\mathbf{p}|)\right]\right\}
\end{aligned}
\tag{3.38}
$$

Where M_π and m_N are the pion and nucleon masses, respectively, and μ is the renormalization scale. On the other hand the subtraction constant $a(\mu)$ is just another way of rewriting $g(s_0)$. So, in order to apply this method we only need to determine $\mathcal{T}(s)$, which can be done from lowest order calculations within ChPT, as in Ref.[90]. However, it is interesting to generalize this procedure to any order calculation in the chiral expansion. This was achieved in Ref.[92] by matching order by order the chiral amplitude with the chiral expansion of Eq.(3.37). Namely, taking into account that $g(s) = \mathcal{O}(q)$:

$$
T^{(1)} + T^{(2)} + T^{(3)} = \mathcal{T}^{(1)} + \mathcal{T}^{(2)} + \mathcal{T}^{(3)} - g(s)\left(\mathcal{T}^{(1)}\right)^2 \tag{3.39}
$$

Where the superscript (n) refers to the chiral order of the amplitudes. Matching order by order we obtain the following relations between the chiral amplitude (that is, the expanded $T(s)$) and the expansion of the interaction kernel $\mathcal{T}(s)$:

$$
\begin{aligned}
\mathcal{T}^{(1)}(s) &= T^{(1)}(s) \\
\mathcal{T}^{(2)}(s) &= T^{(2)}(s) \\
\mathcal{T}^{(3)}(s) &= T^{(3)}(s) + g(s)\left(T^{(1)}(s)\right)^2
\end{aligned}
\tag{3.40}
$$

Where we see that, up to $\mathcal{O}(q^2)$, the interaction kernel and the chiral amplitude coincide but, from $\mathcal{O}(q^3)$ hereafter the chiral amplitude is corrected by the unitary loop function. This is easy to understand since the $\mathcal{O}(q^3)$ is the leading loop contribution (unitarity corrections) and this, and higher orders, need to be corrected in such a way that we do not overcount the the unitarity corrections that are being taken into account by the right hand cut resummation. It is interesting to point out that this method can be connected with other unitarization methods used in ChPT. One of these methods is the K-matrix formalism, which is based in writing the unitarity

amplitude by means of an interaction kernel $\mathcal{K}(s)$ and the phase space factor $\rho(s) = |\mathbf{p}|/(8\pi\sqrt{s})$ in the following way:

$$T(s) = \frac{1}{\mathcal{K}(s)^{-1} - i\rho(s)} \tag{3.41}$$

Which is an analogous to Eq.(3.37) if we take $\mathcal{K}(s)^{-1} = \mathcal{T}(s)^{-1} + \mathrm{Re}\, g(s)$.

Another interesting method of unitarization is the so-called Inverse Amplitude Method (IAM) [93] which also relies in unitarity and the analyticity properties of the scattering amplitude. In fact, from an analogous to Eq.(3.41) with $\mathcal{K}(s) = \mathrm{Re}(1/T)$ and expanding up to $\mathcal{O}(q^3)$ in the chiral series, the authors of Ref.[94] obtained up to $\mathcal{O}(q^3)$ within the IAM:

$$T(s) \simeq \frac{(T^{(1)})^2}{T^{(1)} - T^{(2)} + (T^{(2)})^2/T^{(1)} - \mathrm{Re}\, T^{(3)} - i\frac{|\mathbf{p}|}{8\pi\sqrt{s}}(T^{(1)})^2} \tag{3.42}$$

Which can be obtained solely from the chiral amplitudes $T^{(1)}$, $T^{(2)}$ and $T^{(3)}$ if we use $T^{(3)} = \mathrm{Re}\, T^{(3)} + i\frac{\mathbf{p}}{8\pi\sqrt{s}}(T^{(1)})^2$:

$$T(s) \simeq \frac{1}{1/T^{(1)} - T^{(2)}/(T^{(1)})^2 + (T^{(2)})^2/(T^{(1)})^3 - T^{(3)}/(T^{(1)})^2} \tag{3.43}$$

It is interesting that this technique allow us to obtain the $\Delta(1232)$ pole position and Breit-Wigner parameters, since Eq.(3.42) (or (3.43)) resums the tree level contributions which, according to Resonance Saturation [95] (RS), contains the contribution of the resonances that are integrated out. This was achieved in Ref.[96] by analyzing the $\Delta(1232)$ phase shifts with Heavy Baryon Chiral Perturbation Theory.

Chapter 4

Infrared Regularization

As explained before, covariant BChPT does not respect the power counting, Eq.(2.123), if we apply dimensional regularization, breaking, therefore, the hierarchy that allows us to apply perturbation theory (see Sec. 2.8). This chapter is dedicated to explain a regularization method that allow us to recover the power counting keeping manifestly the Lorentz invariance: the Infrared Regularization scheme (IR). In Sec. 4.1 it is explained how IR recovers the power counting. Later, in Sec. 4.2, this scheme is applied for the calculation of the πN scattering amplitude up to $\mathcal{O}(q^3)$, which involves one-loop amplitudes. The explicit expressions for the amplitudes are shown in Appendices C and D. In Sec. 4.3 this amplitude is fitted to the data of two different partial wave analyses already commented in the Chapter 3, the one of the Karlsruhe group [16] (KA85) and the current solution of the George Washington University group [17] (WI08), to fix the value of the $\mathcal{O}(q^2)$ and $\mathcal{O}(q^3)$ low energy constants and extract from them relevant physical information. In Sec. 4.5, the results obtained in Sec. 4.3 are applied to extract the value of the Goldberger-Treiman relation deviation from PWAs data. The convergence of the chiral series in IR-ChPT is studied in Sec. 4.4 and, finally, the amplitude is unitarized to extend the range of validity of the perturbative description. These results were presented in our paper [21].

4.1 Recovering the Power Counting

In this section we explain how Infrared Regularization (IR) recovers the standard power counting preserving the covariant formulation of the theory. This method relies on dimensional regularization and, following [97], we will use a simple example to explain its essence: the self-energy diagram of Fig.3.5.

The corresponding scalar loop integral reads:

$$\mathcal{H}_{11} = \frac{1}{i}\int \frac{d^dk}{(2\pi)^d}\frac{1}{(M^2-k^2-i\epsilon)(m^2-(P-k)^2-i\epsilon)} \tag{4.1}$$

This integral converges for $d<4$ and we need to analyze it for momenta close to the mass shell which means that $P^2-m^2=\mathcal{O}(q)$. In the limit $M\to 0$, the integral develops an infrared singularity generated by small values of the variable of integration ($k\sim q$). In that region, the first denominator is of $\mathcal{O}(q^2)$ and the second is of $\mathcal{O}(q)$. According to this, the chiral expansion of $\mathcal{H}_{11}$ contains contributions of $\mathcal{O}(q^{d-3})$ that can be enhanced by considering small dimensions. For $d<3$, the leading term in the chiral expansion of $\mathcal{H}_{11}$ comes from the $k=\mathcal{O}(q)$ region, which generates a singular contribution of $\mathcal{O}(q^{d-3})$, as well as nonleading terms of $\mathcal{O}(q^{d-2})$, $\mathcal{O}(q^{d-1})$, ... The rest of the integration region does not contain infrared singularities and gives a contribution that can be expanded in an ordinary power series. For sufficiently large negative values of d the infrared region dominates the chiral expansion to any desired order. In IR we split the original integral $\mathcal{H}_{11}$ in two integrals: one containing the infrared singular part ($\mathcal{I}_{11}$), that comes form the $k=\mathcal{O}(q)$ region and respect the chiral power counting and another containing the infrared regular part ($\mathcal{R}_{11}$), that comes from the rest of the integration region and can be expanded in an ordinary power series. To illustrate this, we will continue with the self-energy example and use the Feynman parameterization:

$$\frac{1}{ab}=\int_0^1 \frac{dz}{\{(1-z)a+zb\}^2} \tag{4.2}$$

Integrating over k, one obtains:

$$\mathcal{H}_{11} = \kappa\int_0^1 dz\, C^{\frac{d}{2}-2},\quad \kappa=(4\pi)^{-\frac{d}{2}}\mu^{d-4}\Gamma\left(2-\frac{d}{2}\right) \tag{4.3}$$

$$C = z^2-2\alpha\Omega z(1-z)+\alpha^2(1-z)^2-i\epsilon \tag{4.4}$$

$$\alpha = \frac{M}{m},\quad \Omega=\frac{P^2-m^2-M^2}{2mM} \tag{4.5}$$

In this representation, the infrared singularity arises from the small values of z, which make that C vanishes if $\alpha\to 0$. One can isolate the divergent part by scaling the variable of integration, $z=\alpha u$, and the upper limit in the u variable becomes large. Extending the integration to infinity, we define the infrared singular part:

$$\mathcal{I}_{11} = \kappa \int_0^\infty dz\, C^{\frac{d}{2}-2} = \kappa\alpha^{d-3} \int_0^\infty du\, D^{\frac{d}{2}-2} \tag{4.6}$$

$$D = 1 - 2\Omega u + u^2 + 2\alpha u(\Omega u - 1) + \alpha^2 u^2 - i\epsilon \tag{4.7}$$

And the remainder part of $\mathcal{H}_{11}$, $\mathcal{R}_{11}$, is given by:

$$\mathcal{R}_{11} = -\kappa \int_1^\infty dz\, C^{\frac{d}{2}-2} \tag{4.8}$$

With the decomposition:

$$\mathcal{H}_{11} = \mathcal{I}_{11} + \mathcal{R}_{11} \tag{4.9}$$

We split the infrared singular part form the regular one. The $\mathcal{I}_{11}$ expansion reads:

$$\mathcal{I}_{11} = \mathcal{O}(q^{d-3}) + \mathcal{O}(q^{d-2}) + \mathcal{O}(q^{d-1}) + \ldots \tag{4.10}$$

While for $\mathcal{R}_{11}$ reads:

$$\mathcal{R}_{11} = \mathcal{O}(q^0) + \mathcal{O}(q^1) + \mathcal{O}(q^2) + \ldots \tag{4.11}$$

In Appendix B we explain how this method can be extended to an arbitrary number of mesonic and baryonic propagators.

This decomposition has the following advantages:

- The chiral expansion of the *infrared regular part* of a one loop integral is a *polynomial* in the *quark masses* and the *external momenta* to any given order.
- The *infrared regular part* of the one loop amplitudes is *chirally symmetric*.
- The *infrared singular part* of the one loop amplitudes *respects the standard power counting of ChPT*.

This implies that, in a one loop calculation, one only needs to calculate the infrared singular part ($\mathcal{I}_{11}$) because the contribution of the infrared regular part ($\mathcal{R}_{11}$) can be absorbed in the coupling constants of the effective Lagrangian. We proceed now to apply this regularization procedure to an $\mathcal{O}(q^3)$ calculation.

4.2 Calculation of the Chiral Amplitude

Now we calculate the set of diagrams in Fig. 3.2 regularizing the loop diagrams within IR. The result is shown in Appendices C and D. As explained in the previous section, the IR regularized loops diagrams result from taking only the infrared singular part ($\mathcal{I}_{mn}$) and dropping the infrared regular part ($\mathcal{R}_{mn}$), with m and n the number of mesonic and baryonic propagators, respectively. This is done by taking the following substitutions in the scalar integrals of Appendix D:[♯1]

$$\begin{array}{llll} \mathcal{H}_{10} \to \mathcal{I}_{10}, & \mathcal{H}_{01} \to 0, & \mathcal{H}_{20} \to \mathcal{I}_{20}, & \mathcal{H}_{11} \to \mathcal{I}_{11} \\ \mathcal{H}_{02} \to 0, & \mathcal{H}_{21} \to \mathcal{I}_{21}, & \mathcal{H}_{A} \to \mathcal{I}_{A}, & \mathcal{H}_{B} \to \mathcal{I}_{B} \\ \mathcal{H}_{21} \to \mathcal{I}_{21}, & \mathcal{H}_{03} \to 0, & \mathcal{H}_{13} \to \mathcal{I}_{13} & \end{array}$$

Where the definition for the infrared singular part is the same as in the full covariant case (Appendix D), except that the integration is performed over the infrared singular region taking $z \in [0, +\infty)$, as explained in the previous section. Comparing our IR-ChPT calculation [21] with the result of Ref.[19], one sees that we agree with all the one-loop integrals given there except for the integrals that contain any contribution of the so-called integral $I_B^{(2)}$, which is the infrared singular part of the integral $\mathcal{H}_B^{(2)}$ defined in Appendix D. We find that the contributions of $I_B^{(2)}$ in Ref.[19], which appear in diagrams (c)+(d), (g)+(h) and (i), should be reversed in sign to match our result. To solve this discrepancy we performed the calculations of the Feynman loop amplitudes using *FeynCalc*, and checked that we obtained the same result. Moreover, we checked that the expressions given in Ref.[19] violate perturbative unitarity,[♯2] while our results satisfies it. Perturbative unitarity results because unitarity, Eq.(3.10), is a nonlinear relation that mixes up orders in a power expansion. Denoting with a superscript the chiral order so that $T_{IJ\ell} = T_{IJ\ell}^{(1)} + T_{IJ\ell}^{(2)} + T_{IJ\ell}^{(3)} + \mathcal{O}(q^4)$ the unitarity relation Eq.(3.10) up to $\mathcal{O}(q^3)$ implies:

$$\mathrm{Im}T_{IJ\ell}^{(3)} = \frac{|\mathbf{p}|}{8\pi\sqrt{s}} \left(T_{IJ\ell}^{(1)}\right)^2 \tag{4.12}$$

[♯1] The integrals $\mathcal{H}_{01}$, $\mathcal{H}_{02}$ and $\mathcal{H}_{03}$ are dropped in this scheme because they do not contain mesonic propagators and, therefore, have not infrared singular parts.

[♯2] The authors of Ref.[19] state in page 30 that the scattering amplitude calculated obeys perturbative unitarity. It seems then that the difference in the sign referred above corresponds to a typo in [19].

4.3 Fits

Now we proceed to compare our perturbative calculation with the experimental phase shifts for the low-energy data on the πN S- and P-waves (which are the relevant partial waves for such energies). Since our solution is perturbative we have to use Eq.(3.14), as explained in Sec. 3.2 of Chapter 3, to calculate the resulting phase shifts:

$$\delta_{IJ\ell} = \frac{|\mathbf{p}|}{8\pi\sqrt{s}} \mathrm{Re} T_{IJ\ell} \tag{4.13}$$

With $T_{IJ\ell}$ evaluated in the IR-ChPT series (in our present case up to $\mathcal{O}(q^3)$).

We now consider the reproduction of the πN phase shifts of the partial wave analyses (PWAs) of the Karlsruhe (KA85) group [16] and the current one of the GWU (WI08) group [17]. In order to fit the data, we consider two strategies that will be explained in the following sections.

4.3.1 Strategy-1

The fits are done with the full IR-ChPT calculation to $\mathcal{O}(q^3)$. Due to the absence of error in these analyses [16, 17] there is some ambiguity in the definition of the χ^2. Here we follow a similar strategy to that of Ref.[98] and define an error assigned to every point as the sum in quadrature of a systematic plus a statistical error:

$$\mathrm{err}(\delta) = \sqrt{e_s^2 + e_r^2 \delta^2} \tag{4.14}$$

Where e_s is the systematic error and e_r the relative one. In Ref.[63] a relative error of 3% was taken while in Ref.[98] a 5% error was considered. In the following we take for e_s just 0.1 degrees and $e_r = 2\%$. Regarding these values for the errors notice that, as commented in the previous chapter, isospin breaking corrections in πN scattering are estimated to be rather small (see Sec. 3.3 of Chapter 3). We then consider a 2% value as a safe estimate for isospin breaking effects not taken into account in our isospin symmetric study. Notice also that the $\mathcal{O}(q^4)$ contributions are expected to be suppressed compared with the leading term by a relative factor $\sim (M_\pi/\Lambda_{\chi SB})^3 \sim (0.14/0.7)^3 \sim 0.01$. On the other hand, a finite value for e_s helps to stabilize fits. Otherwise, with $e_s = 0$, extra weight is given to the small energy region close to threshold, where PWAs have not experimental

data to compare with. Tiny differences between the calculation and points in the input become then exceedingly relevant. We take $e_s = 0.1$ degrees since it is much smaller than typical values of the phase shifts and is also the typical size for the difference between the phase shifts of Refs.[16, 17] in the low-energy region for the P_{11} partial wave. We have also convinced ourselves that changes in these values for e_s and e_r do not affect our conclusions.

Within this strategy, the χ^2 function to be minimized is defined in a standard way as:

$$\chi^2 = \sum_i \frac{(\delta - \delta_{th})^2}{\mathrm{err}(\delta)^2} \tag{4.15}$$

With δ_{th} the phase shift calculated theoretically. A data point is included every 4 MeV in $\sqrt{s}$. We fit directly these data from threshold up to an upper value denoted by $\sqrt{s}_{max}$, and consider several values for $\sqrt{s}_{max}$, employing the program MINUIT [99].

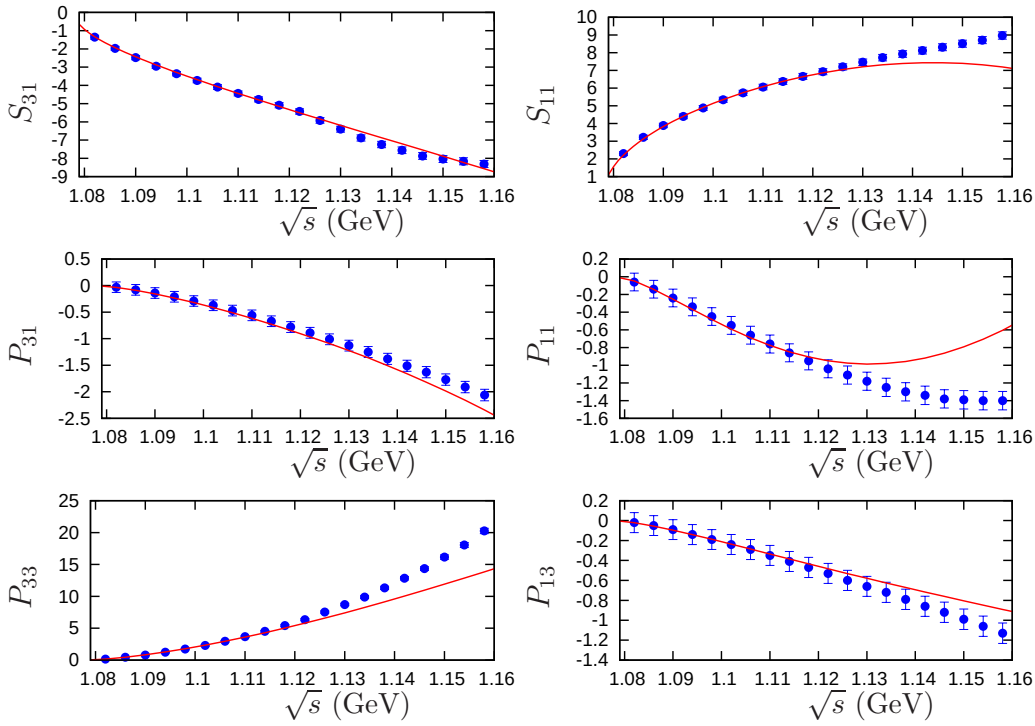

Figure 4.1: Fits to KA85 [16] data with errors calculated by using Eq.(4.14). The result (solid line) corresponds to KA85-1 of Table 4.1.

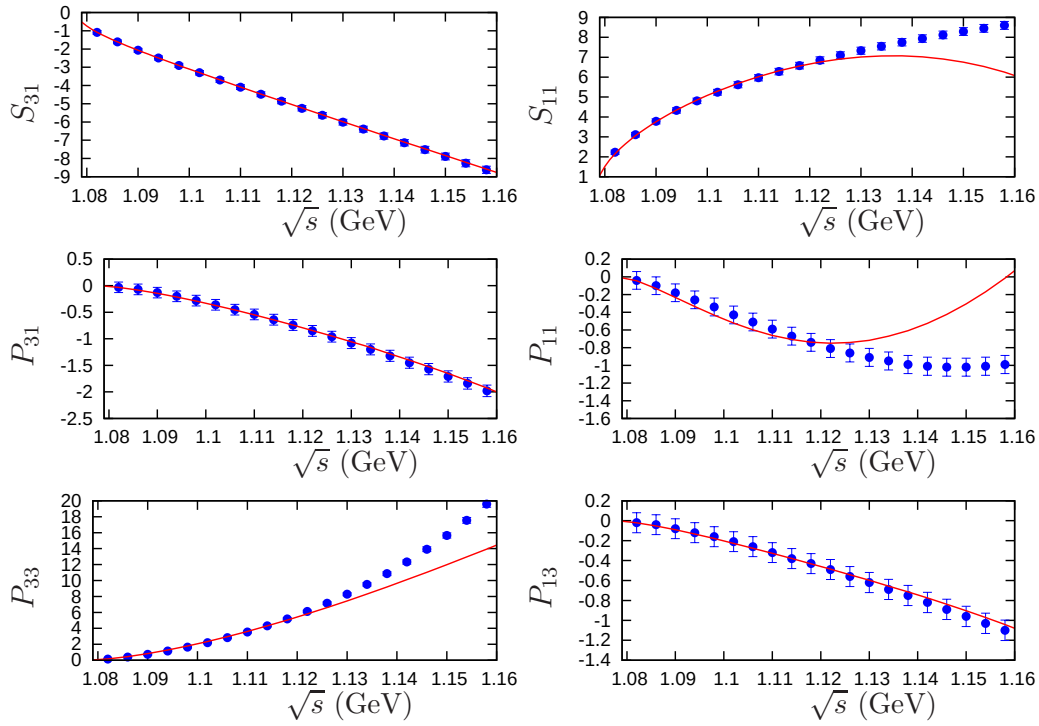

Figure 4.2: Fits to WI08 [17] data with errors calculated by using Eq.(4.14). The result (solid line) corresponds to WI08-1 of Table 4.1.

One observes that the χ^2 per degree of freedom ($\chi^2_{d.o.f.}$) is below 1 for $\sqrt{s}_{max} \lesssim 1.13$ GeV, and then rises fast with energy so that for $\sqrt{s}_{max} = 1.14$ GeV the $\chi^2_{d.o.f.}$ is 2.1 and for $\sqrt{s}_{max} = 1.15$ GeV it becomes 3.6. In Figs. 4.1 and 4.2 we show by the solid line the result of the fit for $\sqrt{s}_{max} = 1.13$ GeV. At the level of the resulting curves the differences are small when varying $\sqrt{s}_{max}$ within the range indicated above. A good reproduction of the data is achieved up to around $\sqrt{s} \lesssim 1.14$ GeV, a similar range of energies to that obtained in the $\mathcal{O}(q^3)$ HBChPT fits of Fettes and Meißner [63]. From Figs. 4.1 and 4.2 one can readily see the origin of the rise in the χ^2 with increasing $\sqrt{s}_{max}$. It stems from the last points of the partial waves P_{33}, P_{31} and P_{11} for which the resulting curves depart from them, getting worse as the energy increases. The fast rising of the P_{33} phase shifts is due to the $\Delta(1232)$ resonance. Though the tail of this resonance is mimicked in ChPT by the LECs, its energy dependence is too steepy to be completely accounted for at $\mathcal{O}(q^3)$ due to the closeness of the $\Delta(1232)$ to the πN threshold. Indeed, this deficiency already occurred in the $\mathcal{O}(q^3)$ HBChPT calculation of Ref.[63]. However, at $\mathcal{O}(q^4)$ the fit to data improves because of the appearance of new

higher order LECs [64]. It is also worth emphasizing that our fits to the phase shifts of the KA85 analysis, as shown in Fig. 4.1, offer a good reproduction of the data and the worsening for higher energies shows up in a smooth way as in $\mathcal{O}(q^3)$ HBChPT [63]. This is certainly an improvement compared with the previous πN study in IR-ChPT to $\mathcal{O}(q^3)$ of Ref.[43]. In this latter reference, data could only be fitted up to around $\sqrt{s} \approx 1.12$ GeV and large discrepancies above that energy, rapidly increasing with energy, emerged in the S_{31}, P_{13} and P_{11} partial waves. For the fits to the WI08 phase shifts, the same situation occurs except for the P_{11}, where IR-ChPT seems not to be able to fit this partial wave even for very low energies. Whether this is due to the IR scheme or to the PW data will be answered in the next chapter.

Low Energy Constants

LEC	KA85-1	WI08-1
c_1	$-0.71(49)$	$-0.27(51)$
c_2	$4.32(27)$	$4.28(27)$
c_3	$-6.53(33)$	$-6.76(27)$
c_4	$3.87(15)$	$4.08(13)$
$d_1 + d_2$	$2.48(59)$	$2.53(60)$
d_3	$-2.68(1.02)$	$-3.65(1.01)$
d_5	$2.69(2.20)$	$5.38(2.40)$
$d_{14} - d_{15}$	$-1.71(73)$	$-1.17(1.00)$
d_{18}	$-0.26(40)$	$-0.86(43)$
$\chi^2_{d.o.f.}$	0.9	$\lesssim 1$

Table 4.1: Values of the low-energy constants for the KA85-1 (column 2) and WI08-1 (column 3) fits. The c_i are given in GeV^{-1} and the d_i (or their combinations) in GeV^{-2}. The renormalization scale for $d_i(\mu)$ is $\mu = 1$ GeV.

The resulting values for the strategy-1 LECs are shown in the second and third column of Table 4.1, denoted by KA85-1 and WI08-1, respectively, in units of GeV^{-1} and GeV^{-2} for the c_i and d_i, respectively. Note that at $\mathcal{O}(q^3)$ only the combinations of counterterms $d_1 + d_2$, d_3, d_5, $d_{14} - d_{15}$ and d_{18} appear in πN scattering. The first four combinations were already explicitly shown in the expression for $\mathcal{L}^{(3)}_{\pi N}$, Eq.(3.21). The counterterm d_{16} does not appear because it is re-absorbed in the physical value of the pion-nucleon axial-vector coupling g_A, once the lowest order g constant is fixed in terms of the former [19]. Under variations of $\sqrt{s}_{max}$ most of the counterterms present a rather stable behavior, with the $\mathcal{O}(q^3)$ ones being the most sensitive. The

LEC	HBChPT $\mathcal{O}(q^3)$ [63]	HBChPT Disp. [100]	HBChPT $\mathcal{O}(q^3)$ [101]	RS [101]
c_1	$(-1.71, -1.07)$	$-0.81(12)$	$-1.02(6)$	
c_2	$(3.0, 3.5)$	$8.43(56.9)$	$3.32(3)$	3.9
c_3	$(-6.3, -5.8)$	$-4.70(1.16)$	$-5.57(5)$	-5.3
c_4	$(3.4, 3.6)$	$3.40(0.04)$		3.7
$d_1 + d_2$	$(3.2, 4.1)$			
d_3	$(-4.3, -2.6)$			
d_5	$(-1.1, 0.4)$			
$d_{14} - d_{15}$	$(-5.1, -4.3)$			
d_{18}	$(-1.6, -0.5)$			
$\chi^2_{d.o.f.}$	$(0.83 - 1.34)$			

Table 4.2: In the second column we give the interval of values obtained in [63] by fitting low-energy πN scattering data with HBChPT at $\mathcal{O}(q^3)$. Other determinations are given in columns third [100] and fourth [101]. Resonance saturation estimates are collected in the last column [101]. The c_i are given in GeV^{-1} and the d_i (or their combinations) in GeV^{-2}. The renormalization scale for $d_i(\mu)$ is $\mu = 1$ GeV.

change in the LECs when varying $\sqrt{s}_{max}$ between 1.12 to 1.15 GeV is a source of uncertainty that is added in quadrature with the statistical error from the fit with $\sqrt{s}_{max} = 1.13$ GeV, which has a $\chi^2_{d.o.f.}$ of 0.9. The central values shown correspond to the same fit too. We also give in Table 4.2 the values obtained from other approaches at $\mathcal{O}(q^3)$ [63, 100, 101, 102], including the $\mathcal{O}(q^3)$ HBChPT fit to πN data [63], the dispersive analysis within the Mandelstam triangle of Ref.[100] and the results at $\mathcal{O}(q^3)$ from Ref.[101], that also includes an estimation of the $\mathcal{O}(q^2)$ LECs from resonance saturation (RS). Within uncertainties, our values for c_1, c_3 and c_4 are compatible with these other determinations. Instead, c_2 is somewhat larger, which is one of the main motivations for considering other fits to πN scattering following the so-called strategy-2, as explained below. Our values are also compatible with those determined from the πN parameters up to $\mathcal{O}(q^4)$ in Ref.[103] that gives the intervals $c_1 = (-1.2, -0.9)$, $c_2 = (2.6, 4.0)$ and $c_3 = (-6.1, -4.4)$. Regarding the $\mathcal{O}(q^3)$ counterterms the comparison with HBChPT is not so clear due to the large uncertainties both from our side as well as from [63]. As discussed in more detail below, the $\mathcal{O}(q^3)$ contribution is typically the smallest between the different orders studied so that it is harder to pin down precise values for these counterterms. Indeed, we observe from the second column in Table 4.1 that d_3, d_5 and $d_{14} - d_{15}$ have large errors, much larger

than those of the $\mathcal{O}(q^2)$ counterterms. Our values for the LECs d_i, again within the large uncertainties, are compatible with those of Ref.[63]. Only $d_{14} - d_{15}$ is larger in our case, out of the range given in [63] by around a factor 2.

Threshold Parameters

To extract the value of the threshold parameters we fit the effective range expansion in Eq.(4.16) to our ChPT results in the threshold region ($\sqrt{s} \lesssim 1.084$ GeV):

$$|\mathbf{p}|^{2\ell+1}\cot\delta_{IJ\ell} = \frac{1}{a_{IJ\ell}} + \frac{1}{2} r_{IJ\ell}|\mathbf{p}|^2 \tag{4.16}$$

Where $a_{IJ\ell}$ is the scattering length/volume and $r_{IJ\ell}$ the effective radius.

Partial Wave	KA85-1	KA85 [16]	WI08-1	WI08 [17]
$a_{S_{31}}$	$-10.0(1)$	$-10.0(4)$	$-8.1(1)$	-8.4
$a_{S_{11}}$	17.1(1)	17.5(3)	16.5(2)	17.1
a^+_{0+}	$-1.0(1)$	-0.8^a	0.1(1)	$-0.10(12)$
a^-_{0+}	9.0(1)	9.2^a	8.2(1)	8.83(5)
$a_{P_{31}}$	$-5.2(1)$	$-4.4(2)$	$-4.8(1)$	-3.8
$a_{P_{11}}$	$-7.8(1)$	$-7.8(2)$	$-7.3(1)$	-5.8
$a_{P_{33}}$	25.1(2)	21.4(2)	25.2(2)	19.4
$a_{P_{13}}$	$-3.4(1)$	$-3.0(2)$	$-3.2(1)$	-2.3

Table 4.3: S-wave scattering lengths and P-wave scattering volumes in units of $10^{-2}M_\pi^{-1}$ and $10^{-2}M_\pi^{-3}$, respectively. Our results for the fits following strategy-1 to the KA85 and WI08 data are given in the second and fourth columns, respectively. The third and fifth columns correspond to the values of the KA85 [16] and WI08 [17], respectively. The errors given in the fifth column, are extracted from Ref.[104].
[a] These numbers are given without errors because no errors are provided in Ref.[16]. They are deduced from the KA85 ones for $a_{S_{31}}$ and $a_{S_{11}}$.

The threshold parameters for the fits KA85-1 and WI08-1 are collected in the second and fourth columns of Table 4.3, respectively. The error given to our threshold parameters is just statistical. It is so small because the values of the scattering lengths and volumes are rather stable under changes of $\sqrt{s}_{max}$

and LECs within their uncertainties (taking into account the correlation among them). If treated in an uncorrelated way the error would be much larger. In the third and fifth columns of Table 4.3, we give the values from the partial wave analyses of Refs.[16, 17]. Notice that the differences between the central values from the latter two references are larger than one standard deviation, except for the P_{33} case. The differences between the S_{31} scattering lengths and P_{13} scattering volumes are specially large. Given this situation we consider that our calculated scattering lengths and volumes are consistent with the values obtained in the KA85 and WI08 partial wave analyses, except for the P_{33} one for which our result is significantly larger. It is also too large compared with the values obtained in the $\mathcal{O}(q^3)$ HBChPT fits to phase-shifts of Ref.[63].

4.3.2 Strategy-2

The large values for c_2 and $a_{P_{33}}$ obtained within strategy-1 lead us to consider a second strategy (strategy-2). As it was commented above, the rapid increase in the phase shifts due to the tail of the $\Delta(1232)$ is not well reproduced at $\mathcal{O}(q^3)$. As a result, instead of fitting the P_{33} phase shifts as a function of energy we fit now the function $\tan\delta_{P_{33}}/|\mathbf{p}|^3$ for three points with energy less than 1.09 GeV, where $\delta_{P_{33}}$ is the phase shifts for the P_{33} partial wave. The form of this function is, of course, dictated by the ERE and at threshold it directly gives the corresponding scattering volume. Within the second strategy, we take a 2% of relative error and a systematic error of 0.1 degrees for all the partial waves except for P_{33}. For the latter, in which we fit the scattering volume, we also take a relative error of 2% since, within errors, this is the range of values spanned in Table 4.3 by the KA85 and WI08 results for $a_{P_{33}}$.

Low Energy Constants

The resulting values for the LECs within the strategy-2 are given in the second and third columns of Table 4.4 and their corresponding curves for $\sqrt{s}_{max} = 1.13$ GeV are shown in Figs. 4.3 and 4.4 by the solid lines, that have a $\chi^2_{d.o.f.} = 0.86$. We observe that these curves are quite similar to the ones previously obtained in the strategy-1 (KA85-1 and WI08-1). Nevertheless, for the P_{11} partial wave the description is slightly worse above 1.12 GeV and it is the main contribution to the final χ^2.

For the P_{33} phase shifts one also observes a clear difference between the two strategies as the lines corresponding to the strategy-2 run lower than the lines corresponding to the strategy-1 (displayed in Figs. 4.1 and 4.2).

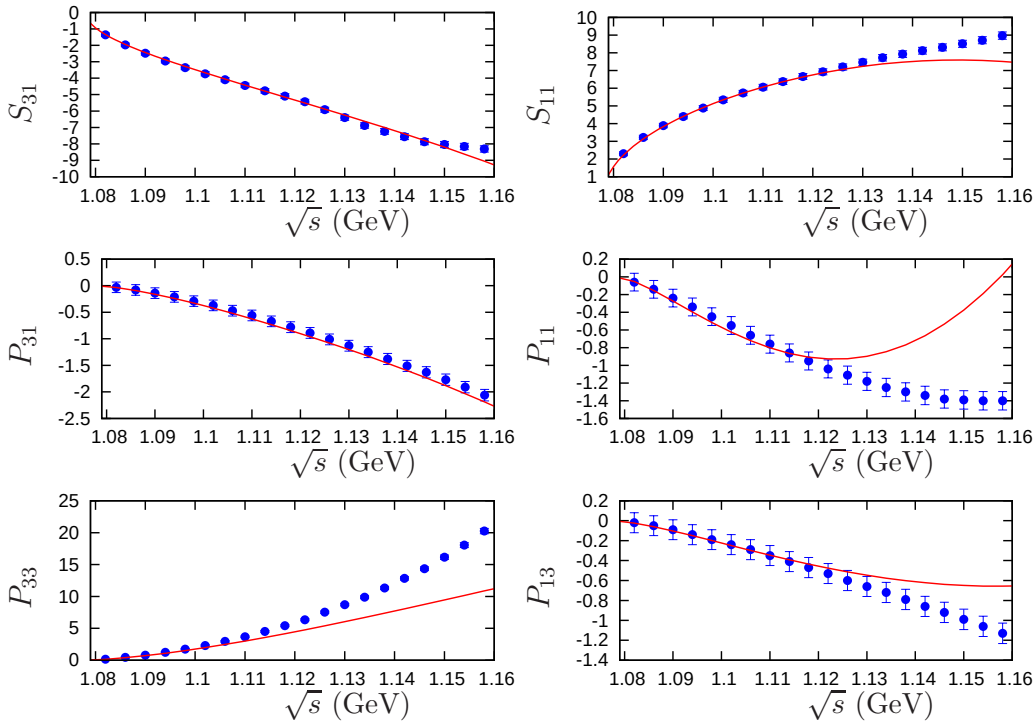

Figure 4.3: Fits to KA85 [16] data with errors calculated by using Eq.(4.14) following strategy-2. The result (solid line) corresponds to KA85-2 of Table 4.4.

LEC	KA85-2	WI08-2
c_1	$-0.79(51)$	$-0.30(48)$
c_2	$3.49(25)$	$3.55(30)$
c_3	$-5.40(13)$	$-5.77(29)$
c_4	$3.32(13)$	$3.60(16)$
$d_1 + d_2$	$0.94(56)$	$1.16(65)$
d_3	$-1.10(1.16)$	$-2.32(1.04)$
d_5	$1.86(2.28)$	$4.83(2.18)$
$d_{14} - d_{15}$	$1.03(71)$	$1.27(1.11)$
d_{18}	$-0.07(44)$	$-0.72(40)$
$\chi^2_{d.o.f.}$	0.86	0.86

Table 4.4: Values of the low-energy constants for the KA85-2 (column 2) and WI08-2 (column 3) fits. The c_i are given in GeV^{-1} and the d_i (or their combinations) in GeV^{-2}. The renormalization scale for $d_i(\mu)$ is $\mu = 1$ GeV.

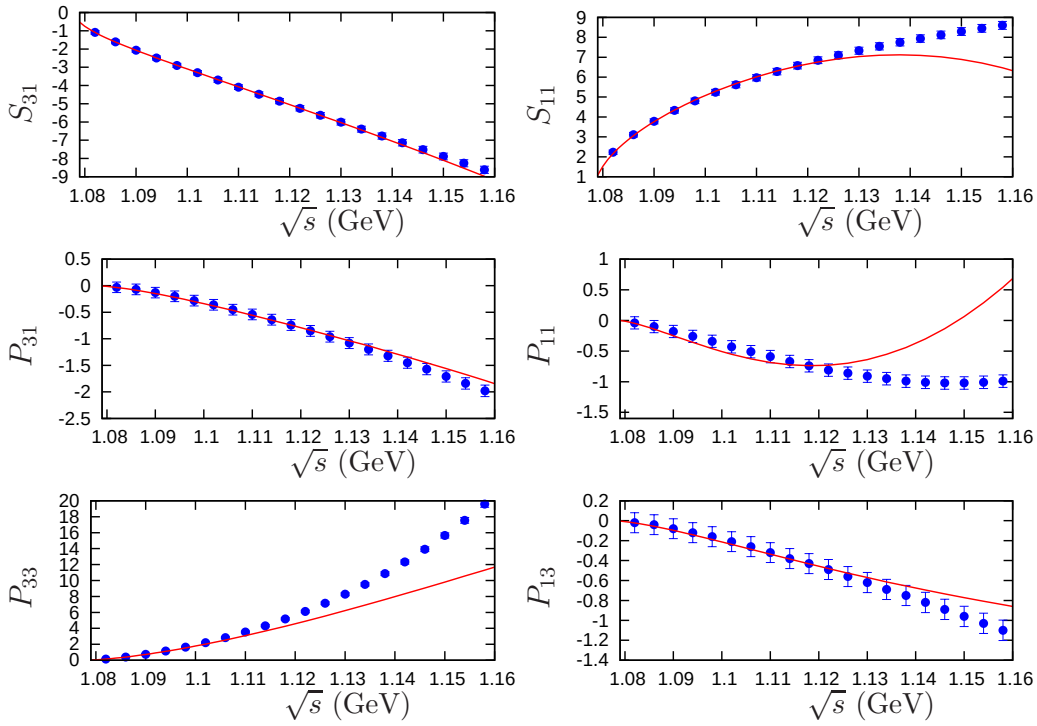

Figure 4.4: Fits to WI08 [17] data with errors calculated by using Eq.(4.14) following strategy-2. The result (solid line) corresponds to WI08-2 of Table 4.4.

The former reproduces the standard values for the P_{33} scattering volume, see column three of Table 4.6, while for the latter it is larger. This is another confirmation that the description of the rapid rise of the P_{33} phase shifts at $\mathcal{O}(q^3)$ enforces the fit to enlarge the value of the resulting scattering volume. It is remarkable that now the value of the $\mathcal{O}(q^2)$ LEC c_2 is smaller and perfectly compatible with the interval of values of [63] (Table 4.2). It is also interesting to note that c_3 is also smaller, which is a welcome feature especially for two- and few-nucleon systems that are rather sensitive to large sub-leading two-pion exchange NN potential that is generated by the inclusion of the LECs c_1, c_3 and c_4 [105]. See refs. [106, 107, 108] for a thorough discussion on this issue for two- and few-nucleon systems. Related to this point, one has determinations of c_3 and c_4 by a partial wave analysis of the pp and np scattering data from Ref.[109] with the results:

$$\begin{aligned} c_3 &= -4.78 \pm 0.10 \text{ GeV}^{-1} \\ c_4 &= +3.96 \pm 0.22 \text{ GeV}^{-1} \end{aligned} \tag{4.17}$$

The systematic errors are not properly accounted for yet in these determinations due to the dependence on the matching point that distinguishes between the long-range part of the NN potential (parameterized from ChPT) and the short-range one (with a purely phenomenological parameterization). Namely, the same authors in Ref.[110] considered this issue and when varying the matching point from 1.8 fm to 1.4 fm the LECs changed significantly: $c_3 = -5.08(28) \to -4.99(21)$ and $c_4 = 4.70(70) \to 5.62(69)$ GeV^{-1}. With respect to the $\mathcal{O}(q^3)$ counterterms we see that the central values have shifted considerably compared with KA85-1 and WI08-1. Within uncertainties d_3, d_5 and d_{18} overlap at the level of one sigma. The LECs $d_1 + d_2$ and $d_{14} - d_{15}$ require to take into account a variation of 2 sigmas. In view of this situation we consider that one should be conservative and give ranges of values for these latter combination of LECs in order to make them compatible:

$$\begin{aligned} d_1 + d_2 &= +0.4 \ldots + 3 \text{ GeV}^{-2} , \\ d_{14} - d_{15} &= -2.4 \ldots + 1.75 \text{ GeV}^{-2} . \end{aligned} \tag{4.18}$$

These values correspond to the minimum and maximum of those shown in the second and third columns of Table 4.4 allowing a variation of one standard deviation. One observes that the resulting LECs at $\mathcal{O}(q^2)$ are quite similar between KA85-1 and WI08-1, on the one hand, and KA85-2 and WI08-2, on the other, so that within uncertainties they are compatible in either of the two strategies. In the second column of Table 4.5 we present the average of the LECs from our fits in Tables 4.1 and 4.4. The error given for every LEC is the sum in quadrature of the largest of the statistical errors shown in the previous tables and the one resulting from the dispersion in the central values. This is a conservative procedure which recognizes that both strategies are acceptable for studying low-energy πN scattering and that takes into account the dispersion in the LECs that results from changes in the data set. Within errors, the averaged values of the LECs are compatible with those from HBChPT at $\mathcal{O}(q^3)$, except for $d_{14} - d_{15}$, which is the only counterterm that differs by more than one standard deviation from the interval of values of Ref.[63].

LEC	Average	HBChPT $\mathcal{O}(q^3)$ [63]	HBChPT Disp. [100]	HBChPT $\mathcal{O}(q^3)$ [101]	RS [101]
c_1	$-0.52(60)$	$(-1.71, -1.07)$	$-0.81(12)$	$-1.02(6)$	
c_2	$3.91(54)$	$(3.0, 3.5)$	$8.43(56.9)$	$3.32(3)$	3.9
c_3	$-6.12(72)$	$(-6.3, -5.8)$	$-4.70(1.16)$	$-5.57(5)$	-5.3
c_4	$3.72(37)$	$(3.4, 3.6)$	$3.40(4)$		3.7
$d_1 + d_2$	$1.78(1.10)$	$(3.2, 4.1)$			
d_3	$-2.44(1.60)$	$(-4.3, -2.6)$			
d_5	$3.69(2.93)$	$(-1.1, 0.4)$			
$d_{14} - d_{15}$	$-0.145(1.88)$	$(-5.1, -4.3)$			
d_{18}	$-0.48(58)$	$(-1.6, -0.5)$			

Table 4.5: Averaged values from Tables 4.1 and 4.4 for the LECs. Columns 3–6 are that same as in Tables 4.1 and 4.4.

Threshold Parameters

Partial Wave	KA85-2	KA85	WI08-2	WI08
$a_{S_{31}}$	$-10.3(1)$	$-10.0(4)$	$-8.2(1)$	-8.4
$a_{S_{11}}$	$17.2(2)$	$17.5(3)$	$16.7(2)$	17.1
a^+_{0+}	$-1.1(1)$	-0.8^a	$0, 1(1)$	$-0.10(12)$
a^-_{0+}	$9.2(1)$	9.2^a	$8.3(1)$	$8.83(5)$
$a_{P_{31}}$	$-5.1(1)$	$-4.4(2)$	$-5.1(1)$	-3.8
$a_{P_{11}}$	$-8.8(1)$	$-7.8(2)$	$-8.0(1)$	-5.8
$a_{P_{33}}$	$21.4(2)$	$21.4(2)$	$22.2(2)$	19.4
$a_{P_{13}}$	$-3.5(1)$	$-3.0(2)$	$-3.5(1)$	-2.3

Table 4.6: S-wave scattering lengths and P-wave scattering volumes in units of $10^{-2}M_\pi^{-1}$ and $10^{-2}M_\pi^{-3}$, respectively. Our results for the fits to the KA85-2 and WI08-2 are given in the second and fourth columns, respectively. The third column corresponds to the values of the KA85 analysis [16]. The values for WI08 (column 5) are extracted from Ref.[17] and the errors, when given, from Ref.[104].
[a] These numbers are given without errors because no errors are provided in Ref.[16]. They are deduced from the KA85 ones for $a_{S_{31}}$ and $a_{S_{11}}$.

The scattering lengths and volumes for KA85-2 and WI08-2 are collected in the second and fourth columns of Table 4.6. They are calculated from our results similarly as explained above for the KA85-1 and WI08-1 fits. In gen-

eral, we see a good agreement between our $\mathcal{O}(q^3)$ IR-ChPT results and the scattering lengths/volumes for KA85 and WI08. Only the P_{11} scattering volume is slightly different, though the difference between the KA85 and WI08 results is significantly larger for this case too. One also observes differences beyond the error estimated in KA85 for the P_{13} scattering volume between the KA85 and WI08 values. IR-ChPT result is closer to the KA85 one.

Partial Wave	Average	KA85	WI08
$a_{S_{31}}$	$-9.2(12)$	$-10.0(4)$	-8.4
$a_{S_{11}}$	16.9(4)	17.5(3)	17.1
a^+_{0+}	$-0.5(7)$	-0.8^a	$-0.10(12)$
a^-_{0+}	8.7(5)	9.2^a	8.83(5)
$a_{P_{31}}$	$-5.1(2)$	$-4.4(2)$	-3.8
$a_{P_{11}}$	$-8.0(6)$	$-7.8(2)$	-5.8
$a_{P_{33}}$	23.2(17)	21.4(2)	19.4
$a_{P_{13}}$	$-3.4(2)$	$-3.0(2)$	-2.3

Table 4.7: S-wave scattering lengths and P-wave scattering volumes in units of $10^{-2}M_\pi^{-1}$ and $10^{-2}M_\pi^{-3}$, respectively. Our averaged result is given in the second column. The third column corresponds to the values of the KA85 analysis [16]. The values for WI08 (column 4) are extracted from Ref.[17] and the errors, when given, from Ref.[104].
[a] These numbers are given without errors because no errors are provided in Ref.[16]. They are deduced from the KA85 ones for $a_{S_{31}}$ and $a_{S_{11}}$.

4.4 Convergence of the Chiral Series

Finally, we show in Fig. 4.5 the different chiral order contributions to the total phase shifts (depicted by the solid lines) for the fit KA85-1[♯3] (shown in Fig. 4.1). The dotted lines correspond to the leading result, the dashed ones to NLO and the dash-dotted ones to N^{2}LO. A general trend observed is the partial cancellation between the $\mathcal{O}(q^2)$ and $\mathcal{O}(q^3)$ contributions. For the P-waves, the cancellation is almost exact at low energies while at higher energies the $\mathcal{O}(q^2)$ contribution is larger in modulus than the $\mathcal{O}(q^3)$ one (except for the P_{31} partial wave where the cancellation is almost exact all over the energy range shown, so that the first order describes well this partial

[♯3]The same conclusions are obtained for the fit WI08-1.

wave). For the S-waves at low energies ($\sqrt{s} \lesssim 1.11$ GeV) the first order contribution dominates, though the second order one tends to increase rapidly with energy. For these partial waves the second order contribution is much larger than the third order one and the partial cancellation between these orders is weak (even both orders add with the same sign for S_{31} at the highest energies shown). The smallness of the third order contribution for the S-waves together with the fact that it is also clearly smaller than the second order one for most of the P-waves explain the difficulties to pin down precise values for the $\mathcal{O}(q^3)$ LECs (the d_i's), as already indicated above.

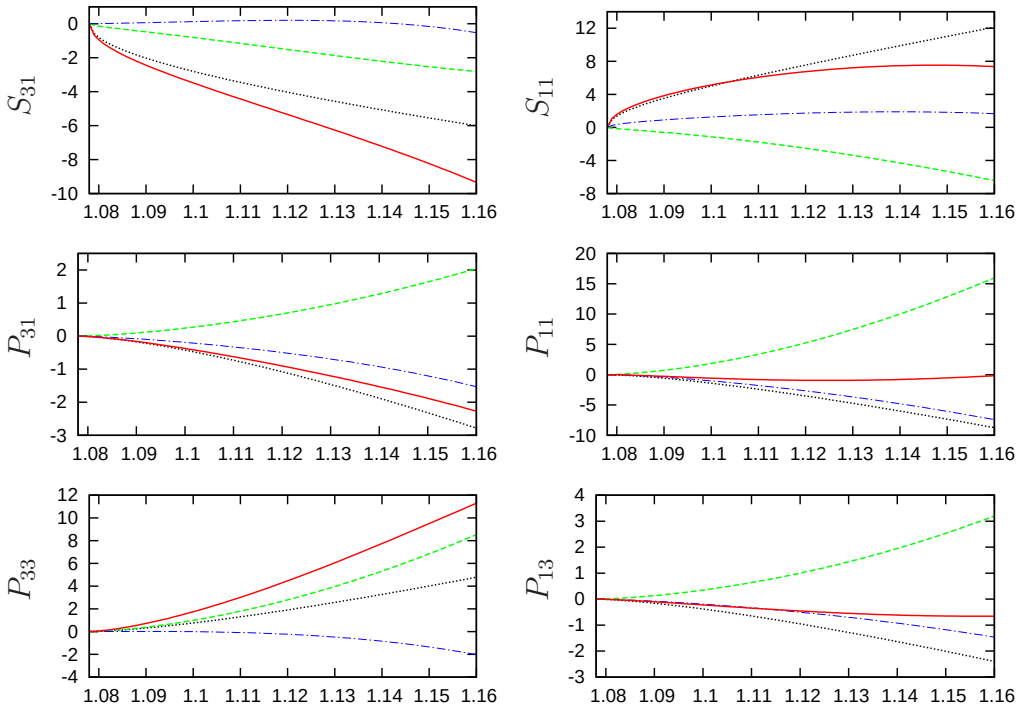

Figure 4.5: (Color online.) Different chiral orders contributing to the phase shifts for the KA85-1 fit. The (black) dotted, (green) dashed and (blue) dash-dotted are the first, second and third order, respectively. The (red) solid line is the sum of all of them.

4.5 The Goldberger-Treiman Relation

The Goldberger-Treiman relation is a pre-PCAC relation that relies on the conservation of the spontaneously broken chiral symmetry. The non-exact conservation of this symmetry due to the quark masses leads to a deviation from this relation (Δ_{GT}) that can be extracted from experimental information. This deviation is usually defined as:

$$g_{\pi N} = \frac{g_A m_N}{f_\pi}(1 + \Delta_{GT}) \tag{4.19}$$

Studies based on πN and NN PWA leads to $\Delta_{GT} = 2{-}3\%$ [111, 112, 113]. In ChPT, Δ_{GT} is directly related to the LEC d_{18} through the relation [19]:

$$\Delta_{GT} = -\frac{2M_\pi^2 d_{18}}{g_A} + \Delta_{loops} \tag{4.20}$$

With Δ_{loops} a contribution due to the loop diagrams which is subdominant in the standard chiral power counting. Actually, this contribution is $\mathcal{O}(M_\pi^4)$ because the $\mathcal{O}(M_\pi^3)$ loop contribution cancels [64, 19].

Inserting our averaged value of d_{18} in the third column of Table 4.5 into Eq.(4.19), we then find:

$$\Delta_{GT} = 0.015 \pm 0.018 \tag{4.21}$$

Which is compatible with the values around 2–3% that are nowadays preferred from πN and NN partial wave analyses [111, 112, 113]. In terms of the πN coupling constant, from Eq.(4.20) our value for d_{18} translates in:

$$g_{\pi N} = 13.07(23) \quad \text{or} \quad f^2 = \left(g_{\pi N} M_\pi / 4m_N\right)^2 / \pi = 0.077(2) \tag{4.22}$$

Within uncertainties our result at strict $\mathcal{O}(M_\pi^3)$ is compatible at the level of one sigma with the determinations of Refs.[111, 112, 113].

However, IR-ChPT at $\mathcal{O}(q^3)$ gives rise to a caveat concerning the GT relation. The point is that the full calculation at this order (IR-ChPT contains higher orders due to the $1/m_N$ relativistic resummation) contributes to the GT relation violation with $\Delta_{loops} \approx 20\%$, similarly as in Ref.[43]. For the evaluation of the GT relation discrepancy in our present calculations we study the $\pi^- p \to \pi^- p$ scattering. We select this particular process in the charge basis of states because the crossed u-channel process, $\pi^+ p \to \pi^+ p$,

is purely $I = 3/2$ and thus there is no u-channel nucleon pole, which requires the same quantum numbers as for the nucleon, in the isospin limit. Otherwise the s- and u-channel nucleon poles overlap for some values of the scattering angle. When projecting the u-channel nucleon pole in a partial wave it produces a cut for $m_N^2 - 2M_\pi^2 + M_\pi^4/m_N^2 < s < m_N^2 + 2M_\pi^2$, with the branch points very close to the nucleon pole at $s = m_N^2$. As a result, there is not soft way to calculate the residue at the s-channel nucleon pole unless the u-channel nucleon pole is removed, as done by considering the $\pi^- p \to \pi^- p$ scattering. The latter is finally projected in the partial wave P_{11}, with the same quantum numbers as the nucleon. The ratio of the residues at the nucleon pole of the full $\mathcal{O}(q^3)$ IR-ChPT partial wave and the direct (s-channel) Born term calculated with g_A, M_π and m_N at their physical values, gives us directly the ratio between the squares of the full pion-nucleon coupling and the one from the GT relation.[♯4]

$$\lim_{s\to m_N^2} \frac{T^{\mathcal{O}(q^3)}_{\pi^- p\to\pi^- p}}{T^{\mathcal{O}(q)}_{\pi^- p\to\pi^- p}} = \left(\frac{g_{\pi N}}{g_A m_N/f_\pi}\right)^2 = (1+\Delta_{GT})^2 \tag{4.23}$$

Numerically we find that the full calculation gives rise to a violation of the GT relation of around $\Delta_{GT} = 20 - 25\%$, while its strict $\mathcal{O}(M_\pi^3)$ restriction is much smaller, Eq.(4.21). Related to this one has a significant renormalization scale dependence on the GT violation.[♯5] In this way, for the fit KA85-1 (second column of Table 4.1) at $\mu = 1$ GeV one has a $\Delta_{GT} \approx 22\%$ while for $\mu = 0.5$ GeV a $\Delta_{GT} \approx 15\%$ stems. On the other hand, Ref.[13] performed a relativistic calculation of Δ_{GT} directly in dimensional regularization within the $\overline{MS} - 1$ renormalization scheme and obtained a natural (much smaller) and renormalization scale independent loop contribution to Δ_{GT}. It seems then that the problem that we find for the calculation of Δ_{GT} with IR, obtained earlier in Ref.[43], is related to the peculiar way the chiral counting is restored in the IR approach [67, 114]. We tentatively conclude that a neat advance in the field would occur once a relativistic regularization method were available that conserved the chiral counting in the evaluation of loops while, at least, avoided any residual renormalization scale dependence. As we will see in the next chapter, this can be achieved by using the so-called Extended-On-Mass-Shell renormalization scheme.

[♯4] Note that there is no crossed Born term for $\pi^- p \to \pi^- p$ and that the LO Born term expressed in terms of physical parameters satisfies exactly the GT relation.

[♯5] Eq.(4.21) is renormalization scale independent because the beta function for d_{18} is zero [63].

4.6 Unitarized amplitudes and higher energies

In order to resum the right-hand cut or unitarity cut we consider the unitarization method of Refs.[90, 92, 98], already explained in Sec. 3.4 of Chapter 3. In Ref.[98] this approach was used for unitarizing the $\mathcal{O}(q^3)$ HBChPT πN partial waves from Ref.[63]. However, no explicit Lorentz-invariant one-loop calculation for πN scattering has been unitarized in the literature until [21]. This is an interesting point since by taking explicitly into account the presence of the unitarity cut the rest of the amplitude is expected to have a softer chiral expansion. Recalling Eq.(3.37), we express the unitary amplitude $T_{IJ\ell}$ as:

$$T_{IJ\ell} = \frac{1}{\mathcal{T}^{-1}_{IJ\ell} + g(s)} \tag{4.24}$$

Where the unitarity pion-nucleon loop function $g(s)$ was given in Sec. 3.4 of Chapter 3. The subtraction constant a_1, contained in the loop function $g(s)$, see Eq.(3.38), is determined by requiring that this function vanishes at the nucleon mass $s = m_N^2$. In this way the P_{11} partial-wave has the nucleon pole at its right position, otherwise it would disappear. This is due to the fact that for the partial wave $\mathcal{T}^{-1}_{\frac{1}{2}\frac{1}{2}1}$ vanishes at $s = m_N^2$ so it is required that $g(m_N^2) = 0$. Otherwise $T_{\frac{1}{2}\frac{1}{2}1}$, Eq.(4.24), would be finite at $s = m_N^2$.

Due to the closeness of the $\Delta(1232)$ resonance to the πN threshold it is expedient to implement a method to take into account its presence in order to provide a higher energy description of πN phase-shifts beyond the purely perturbative results discussed in Secs. 4.2 and 4.3. As commented in Ref.[90] we can add a CDD pole [115], in this case in the P_{33} channel, so as to reach the region of the $\Delta(1232)$ resonance. The addition of the CDD pole conserves the discontinuities of the partial wave amplitude across the cuts, and every CDD corresponds to a zero of the partial wave-amplitude along the real axis and hence to a pole in the inverse of the amplitude. We then modify Eq.(4.24) by including such a pole in $T^{-1}_{\frac{3}{2}\frac{3}{2}1}$,

$$T_{\frac{3}{2}\frac{3}{2}1} = \left(\mathcal{T}^{-1}_{\frac{3}{2}\frac{3}{2}1} + \frac{\gamma}{s - s_P} + g(s) \right)^{-1} \tag{4.25}$$

Where γ and s_P are the residue and pole position of the CDD pole, in order, so that two new free parameters enter. The amplitude $\mathcal{T}_{IJ\ell}$ is

determined by matching to our $\mathcal{O}(q^3)$ IR-ChPT calculation, as commented before. We also distinguish here between the fits to the KA85 [16] and WI08 [17] phase-shifts. The fits are done up to $\sqrt{s}_{max} = 1.25$ GeV for all the partial waves. One cannot afford to go to higher energies because of an intrinsic limitation of IR-ChPT. Additional unphysical cuts and poles are generated by the infinite order resummation of the sub-leading $1/m_N$ kinetic energy terms accomplished in IR [67, 114, 116]. In our case the limiting circumstance is the appearance of a pole when the Mandelstam variable $u = 0$.[♯6] When projecting in the different partial waves this singularity gives rise to a strong branch point at $s = 2(m_N^2 + M_\pi^2) \simeq 1.34^2$ GeV^2, which indicates the onset of a non-physical right-hand cut that extends to infinity and that produces strong violation of unitarity. This translates into strong rises of the phase-shifts calculated employing Eqs.(4.24) and (4.25) for energies $\sqrt{s} \gtrsim 1.26$ GeV. This is why we have taken $\sqrt{s}_{max} = 1.25$ GeV, because for higher energies these effects are clearly visible in the calculated phase-shifts. The χ^2 to be minimized is the same as already used for the pure perturbative study (strategy-1), Eq.(4.15), employing also the same definition for err(δ). The resulting fits are shown in Figs. 4.6 and 4.7, which correspond to the fits to KA85 and WI08 data, respectively. One can see a rather good agreement with data in the whole energy range from threshold up to 1.25 GeV, including the reproduction of the raise in the P_{33} phase shifts associated with the $\Delta(1232)$ resonance. The improvement is manifest in the P_{11} partial wave although some discrepancy with the WI08 data in the lower energy region remains, being better the agreement with KA85 phase-shifts. Compared with the perturbative treatment of Secs. 4.3.1 and 4.3.2 one observes a drastic increase in the range of energies for which a globally acceptable description of the data is achieved.

The values of the resulting LECs are collected in Table 4.8. We consider that the pure perturbative study of Secs. 4.3.1 and 4.3.2 is the proper way to determine the chiral LECs. The new values in Table 4.8 do not constitute an alternative determination to those offered in Tables 4.1 and 4.4 and should be employed within UChPT studies. Nonetheless, it is remarkable that the values for the LECs obtained are compatible with the average of values given in Table 4.5, in particular, for the $\mathcal{O}(q^2)$ LECs the central values are also rather close to the fitted values in Table 4.8. Since we have a procedure to generate the $\Delta(1232)$ resonance through the CDD pole in Eq.(4.25), such agreement is surprising since the contribution of this resonance to the LECs

[♯6] Many of the tensor integrals involved in the one-loop calculations of πN scattering develop such a pole. In particular, it arises in the simplest scalar two-point loop function $\mathcal{I}_{11}(u)$.

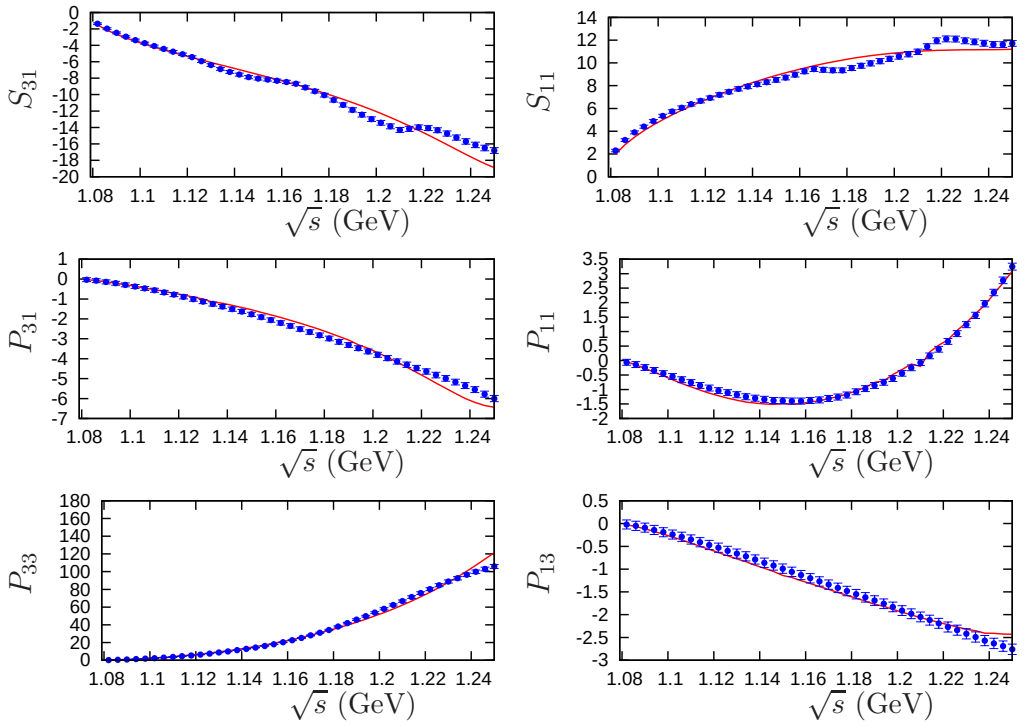

Figure 4.6: Fits to KA85 [16] data (blue points) with errors calculated by using Eq.(4.14). The result (solid line) corresponds to the unitarized amplitude, Eq.(4.24), fitting the points of KA85.

is very important [101]. The point is that the typical value of $\gamma/(s-s_P)$ in the low-energy region studied in Secs. 4.3.1 and 4.3.2 is only around a factor 2 larger in modulus than the subtraction constant $a_1/(4\pi)^2$ in Eq.(3.38), being the latter a quantity of first chiral order. As a result, at low energies, the CDD pole gives a contribution that can be computed as $\mathcal{O}(q^3)$, since the lowest order ones comes from $-(T^{(1)}_{IJL})^2\gamma/(s-s_P)$. This explains why the values of the second order LECs are preserved, despite having included the CDD pole.

The values of the resulting threshold parameters with the present unitarized amplitudes are collected in the last two columns of Table 4.8. We observe that all of them are compatible with the averaged values given in the second column of Table 4.7. The P_{33} scattering volume turns out to be too high in the lines of the values obtained with the perturbative fits following strategy-1, despite the reproduction of the $\Delta(1232)$ resonance. Finally, we also mention that similarly huge values for the GT violation are also obtained from the unitarized amplitudes as in the pure perturbative treatment. In-

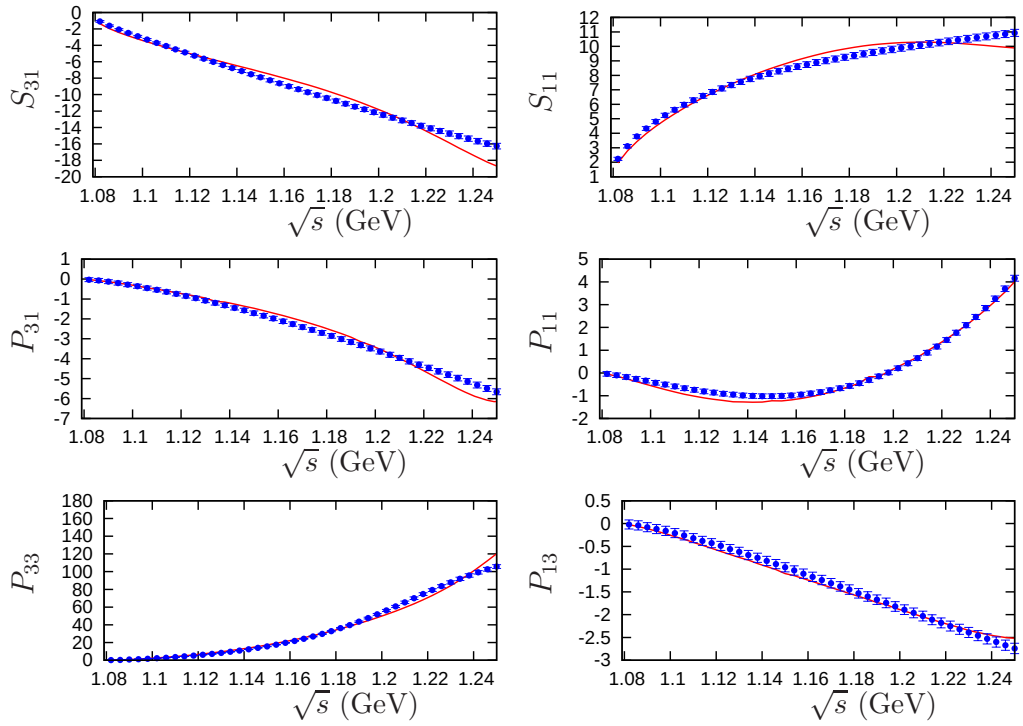

Figure 4.7: Fits to WI08 [17] data (blue points) with errors calculated by using Eq.(4.14). The result (solid line) corresponds to the unitarized amplitude, Eq.(4.24), fitting the points of WI08.

LEC	Fit KA85	Fit WI08	Partial Wave	Fit KA85	Fit WI08
c_1	-0.48 ± 0.51	-0.53 ± 0.48	$a_{S_{31}}$	-11.5	-10.4
c_2	4.62 ± 0.27	4.73 ± 0.30	$a_{S_{11}}$	15.2	15.0
c_3	-6.16 ± 0.27	-6.41 ± 0.29	a^+_{0+}	-2.6	-2.0
c_4	3.68 ± 0.13	3.81 ± 0.16	a^-_{0+}	8.9	8.5
$d_1 + d_2$	2.55 ± 0.60	2.70 ± 0.65	$a_{P_{31}}$	-5.0	-4.8
d_3	-1.61 ± 1.01	-1.73 ± 1.04	$a_{P_{11}}$	-8.0	-7.5
d_5	0.93 ± 2.40	1.13 ± 2.18	$a_{P_{33}}$	24.5	25.0
$d_{14} - d_{15}$	-0.46 ± 1.00	-0.61 ± 1.11	$a_{P_{13}}$	-4.1	-3.9
d_{18}	0.01 ± 0.21	-0.03 ± 0.20			

Table 4.8: Fitted LECs in units GeV^{-1} (c_i) and GeV^{-2} (d_i) for the fits KA85 and WI08 employing the unitarized partial waves. We also give the scattering lengths and volumes in units of $10^{-2}M_\pi$ and $10^{-2}M_\pi^{-3}$, respectively.

deed, the same value for Δ_{GT} is obtained in the unitarized case for the same values of the LECs because $g(m_N^2) = 0$ (there is no CDD pole in the P_{11} partial wave).

4.7 Summary and Conclusions

In this chapter we have studied the elastic pion-nucleon scattering employing covariant CHPT up-to-and-including $\mathcal{O}(q^3)$ in Infrared Regularization [97]. We followed two strategies for fitting the phase shifts provided the partial wave analyses of Refs.[16, 17]. In one of them, instead of fitting the P_{33} phase-shifts, we considered the reproduction of the function $|\mathbf{p}|^3/\tan\delta_{P_{33}}$ around the threshold region (for $\sqrt{s} \leq 1.09$ GeV). The rational behind this is to reduce the impact of the $\Delta(1232)$ when performing fits to data, avoiding the rapid rise of phase-shifts with energy that tends to increase the value of the resulting scattering volume. An accurate reproduction of pion-nucleon phase-shifts up to around 1.14 GeV results. The main difference between both strategies has to do with the values of the $\mathcal{O}(q^2)$ LECs c_2 and c_3, that are smaller in absolute value for strategy-2 fits. As expected, the P_{33} scattering volume is also smaller for these fits and compatible with previous determinations. On the other hand, we obtain a much better reproduction of the P_{11} phase shifts for the KA85 partial wave analysis, while IR-ChPT at $\mathcal{O}(q^3)$ is not able to reproduce the P_{11} phase shifts of the current solution of the GWU group even at very low energies. This could be due to the WI08 PWA or to the IR method.[♯7] The averaged values for the LECs and threshold parameters resulting from the two strategies and all data sets are given in the second column of Tables 4.5 and 4.7, respectively, and are in good agreement with other previous determinations. The reproduction of experimental phase-shifts is similar in quality to that obtained previously with $\mathcal{O}(q^3)$ HBChPT [63], showing also a smooth onset of the departure from experimental data for higher energies. This is an improvement compared with previous work [43]. In addition, we obtain a small violation of the Goldberger-Treiman relation at strict $\mathcal{O}(M_\pi^3)$, compatible with present determinations. However, the deviation from the Goldberger-Treiman relation is still a caveat because when all the terms in the full IR CHPT calculation at $\mathcal{O}(q^3)$ are kept the resulting discrepancy is much higher, around 20-30%. We have also employed the non-perturbative methods of Unitary CHPT [92, 98] to resum the right-hand cut of the pion-nucleon partial waves. The $\Delta(1232)$ resonance is incorporated in the approach as a Castillejo-Dalitz-Dyson pole in the inverse of the amplitude. A good reproduction of the phase shifts is

[♯7] This question will be answered in the next chapter.

reached for $\sqrt{s}$ up to around 1.25 GeV. There is an intrinsic limitation in IR-ChPT for reaching higher energies due to the presence of a branch cut at $s = 2(m^2 + M_\pi^2) \simeq 1.34^2$ GeV^2. Above that energy strong violations of unitarity occurs due to the onset of an unphysical cut associated with the infinite resummation of relativistic corrections accomplished in IR. This also originates a strong rise of phase-shifts noticeable already for $\sqrt{s} \gtrsim 1.25$ GeV. The values of the LECs at $\mathcal{O}(q^2)$ is compatible to those obtained with the pure perturbative study.

Chapter 5

Extended-On-Mass-Shell

The results obtained in Chapter 4 are unsatisfactory in the sense that the IR scheme does not provide a covariant amplitude with its full potential. Namely, the IR-BChPT has some analytical problems in the physical region (unphysical cuts) and is not able to predict a reliable value for a quantity so fundamental as the Goldberger-Treiman deviation (Δ_{GT}). Some authors point to the bad analytical behavior as the reason for the unsatisfactory results in IR, such as the bad prediction for the magnetic moments [67], appearance of unphysical cuts [21] or unphysically large (Δ_{GT}) [43, 21]. Fortunately, there is another relativistic approach to BChPT in the literature, the so-called Extended-On-Mass-Shell (EOMS) renormalization scheme [72, 73]. This approach relies on the realization that the power counting breaking terms (PCBT) are analytical in the quark masses and external momenta [72] which means that they can be absorbed in the set of low-energy constants (LECs) and bare couplings of the original Lagrangian. Contrary to IR, EOMS only subtracts a finite polynomial so it does not modify the analytical properties of the full covariant amplitude. Thus, inevitably comes out the question whether a calculation within the EOMS scheme could overcome the difficulties that appear in IR, improving both the HB and IR approaches. We show in this chapter that the answer is *yes*.

5.1 The Extended-On-Mass-Shell renormalization

The calculation of the scattering amplitude is performed in a full covariant manner so, according to what we explained in Chapter 3, we will have pieces that break the power counting. However, as shown in Refs.[72, 73], these

pieces are *analytical* in the quark masses and momenta. To see this explicitly, we consider the integral $\mathcal{H}_{11}$, defined in Appendix D, and introduce the quantity $\Delta = (P^2 - m^2)/m^2 = \mathcal{O}(q)$. The standard power counting is respected if $\mathcal{H}_{11}$ is of order p^{d-3}. As Refs.[72, 73, 117] show, the result of the integration is of the form:

$$\mathcal{H}_{11} \propto F(d, \Delta) + \Delta^{d-3} G(d, \Delta) \tag{5.1}$$

Where F and G are hypergeometric functions which are analytic in Δ for any d. So, as we see, we have a non-analytical contribution that respects the power counting (the part with Δ^{d-3}) and an analytical contribution which can be absorbed by analytical pieces in the Lagrangian.

This property of the PCBT was also exploited by IR to recover the power counting, since the so-called infrared regular part of the covariant integral,[♯1] that is the contribution which is absorbed in the LECs, is analytical in the quark masses and momenta. But, whereas IR tries to absorb an infinite series which contains PCBT (and non-PCBT) and has a finite radius of convergence, EOMS only removes a finite polynomial in the quark masses and momenta that consists entirely in PCBT. This means that in the EOMS scheme we do not have the analyticity (unphysical cuts) and causality problems (see Ref.[71]) that IR introduces in the process of recovering the power counting. On the other hand, in a full covariant calculation the contribution of the PCBT is directly absorbed in the LECs of the chiral Lagrangians, since they accompany invariant monomials that generate analytical contributions. However, if one wants to relate those LECs to physical quantities is necessary to renormalize them in order to remove the spurious contribution that comes from such pieces. This is an analogous situation to the $\overline{MS}$ renormalization, in which one removes the divergent parts to connect the parameters of the original Lagrangian to physical quantities. To apply the EOMS scheme is then necessary, a way to calculate analytically the terms coming from the loop integrals that can generate PCBT in the full amplitude. The method that we used to do so is explained in detail in Appendix E, and the renormalization of the LECs is shown in Appendix F. There, we show how the LECs must be renormalized in order to cancel the divergent terms along with the PCBT. In the following, we explain in detail three simple calculations where the EOMS renormalization is used: the chiral expansion of the nucleon mass, the axial coupling of the nucleon and the scalar form factor of the nucleon. They illustrate well the EOMS renormalization procedure and

[♯1] See Ref.[97] for the definitions.

allow us to explain easily how we can recover the standard power counting while keeping our amplitudes scale-independent.

5.1.1 Chiral corrections to the nucleon mass

The study of the chiral corrections to the nucleon mass is necessary to write the unknown nucleon mass in the chiral limit (m) in terms of its physical value (m_N). It is also interesting because allow us to calculate the nucleon sigma term from the quark masses dependence of the nucleon mass, via the Hellmann-Feynman theorem [118]. On the other hand, to study the chiral corrections to the nucleon mass up to $\mathcal{O}(q^3)$ we need to consider the modifications of the nucleon propagator due to the term $c_1\langle\chi_+\rangle\bar{\psi}\psi$ in $\mathcal{L}^{(2)}_{\pi N}$ and the self-energy diagram shown in Fig. 5.1.

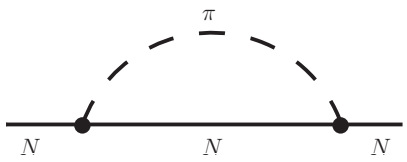

Figure 5.1: One-loop self-energy of the nucleon.

The monomial $c_1\langle\chi_+\rangle\bar{\psi}\psi$ contributes with $-4c_1M^2$, while an explicit calculation of the self-energy diagram $i\Sigma_{S.E.}$ gives:

$$\Sigma_{S.E.}(P) = \frac{3g^2}{4f^2}\left[(P^2-m^2)\not{P}\mathcal{H}^{(1)}_{11}(P^2) - (\not{P}+m)(M^2\mathcal{H}_{11}(P^2)-\mathcal{H}_{01})\right] \quad (5.2)$$

Where the loop functions $\mathcal{H}_{11}$, $\mathcal{H}^{(1)}_{11}$ and $\mathcal{H}_{01}$ are given in Appendix D. For the calculation of the chiral corrections to the nucleon mass, $\Sigma_{S.E.}$ is evaluated at $\not{P} = m_N$. According to the standard power counting, the self-energy diagram has terms of $\mathcal{O}(q^3)$ or higher, but if one introduces the expressions of Eqs.(D.1), (D.2) and (D.4) one obtains (minding that the difference between m_N and m is of higher order):

$$\Sigma_{S.E.}(P=m_N)=\frac{3g^2}{4f^2}\Big\{2\bar{\lambda}m_N(2M^2+2m_N^2)\underbrace{-\frac{m_N}{8\pi^2}(M^2(1-\log\left(\frac{m_N^2}{\mu^2}\right))}_{PCBT}$$
$$\underbrace{-m_N^2\log\left(\frac{m_N^2}{\mu^2}\right))}_{PCBT}+\frac{1}{16\pi^2}\left[\frac{M^4}{m_N}\log\left(\frac{M^2}{m_N^2}\right)-4M^3\sqrt{1-\frac{M^2}{4m_N^2}}\arccos\left(\frac{M}{2m_N}\right)\right]\Big\} \tag{5.3}$$

Where the PCBT are umbraced.

As pointed out before, the spirit of EOMS lies in realizing that these PCBT are analytical in the quark masses and external momenta so that they can be reabsorbed via a redefinition of the LECs and bare parameters of the chiral Lagrangians. For the case of m_N:

$$\begin{aligned} m_N &= m-4c_1M^2-\frac{3g^2m_N}{2f^2}(2\bar{\lambda}(m_N^2+M^2)) \\ &+\underbrace{\frac{3g^2m_NM^2}{32\pi^2f^2}(1-\log\left(\frac{m_N^2}{\mu^2}\right))-\frac{3g^2m_N^3}{32\pi^2f^2}\log\left(\frac{m_N^2}{\mu^2}\right)}_{PCBT} \\ &-\frac{3g^2M^3}{64\pi^2f^2}\Big[\frac{M}{m_N}\log\left(\frac{M^2}{m_N^2}\right)-4\sqrt{1-\frac{M^2}{4m_N^2}}\arccos\left(\frac{M}{2m_N}\right)\Big] \end{aligned} \tag{5.4}$$

Here the PCBT can be cancelled, along with the divergences, if we redefine m and c_1 in the following as:

$$m\to m'+\frac{3g^2m_N^3}{2f^2}(2\bar{\lambda})+\frac{3g^2m_N^3}{32\pi^2f^2}\log\left(\frac{m_N^2}{\mu^2}\right) \tag{5.5}$$
$$c_1\to c_1'-\frac{3g^2m_N}{8f^2}(2\bar{\lambda})+\frac{3g^2m_N}{128\pi^2f^2}(1-\log\left(\frac{m_N^2}{\mu^2}\right)) \tag{5.6}$$

In this way we recover de standard power counting, and the final expression for the chiral expansion of the nucleon mass becomes:

$$m_N=m'-4c_1'M^2-\frac{3g^2M^3}{64\pi^2f^2}\Big[\frac{M}{m_N}\log\left(\frac{M^2}{m_N^2}\right)-4\sqrt{1-\frac{M^2}{4m_N^2}}\arccos\left(\frac{M}{2m_N}\right)\Big] \tag{5.7}$$

Another quantity needed in this $\mathcal{O}(q^3)$ calculation is the nucleon wave function renormalization (Z_N). It can be easily determined from the calculation of the nucleon self energy, Eq.(5.2), by evaluating the derivative with respect to the momentum at the nucleon pole:

$$Z_N = \left[1 + \left.\frac{\partial \Sigma_{S.E.}}{\partial \not{P}}\right|_{\not{P}=m_N}\right]^{-1} \approx 1 - \left.\frac{\partial \Sigma_{S.E.}}{\partial \not{P}}\right|_{\not{P}=m_N}$$
$$= 1 + \frac{3g^2}{4f^2}\left[2m_N M^2 \left.\frac{\partial \mathcal{H}_{11}(P^2)}{\partial \not{P}}\right|_{\not{P}=m_N} - \mathcal{H}_{10}\right] \qquad (5.8)$$

Where we have expanded Z_N up to $\mathcal{O}(q^2)$ in order to guarantee the explicit cancellation of the divergences. The derivatives can be performed directly from Eqs.(D.1), (D.2) and (D.4), and the result does not contain PCBT because the ones coming from $\mathcal{H}_{11}(P^2)$ are independent of P^μ and disappear in the derivation procedure, while $\mathcal{H}_{10}$ has not.

5.1.2 The Axial Coupling of the Nucleon

Another calculation needed in our covariant study of πN scattering is the nucleon axial coupling, where the set of diagrams of Fig. 5.2 has to be considered.

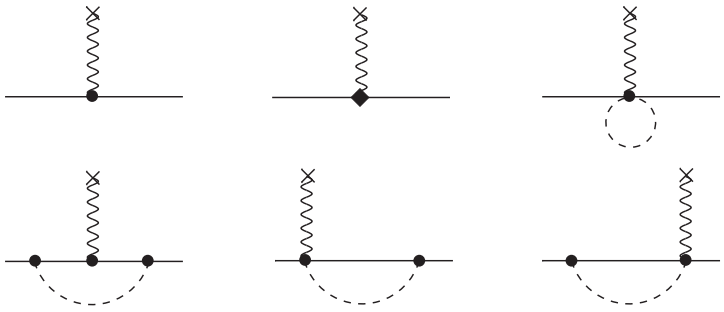

Figure 5.2: Diagrams that contribute to the nucleon axial form factor up to $\mathcal{O}(q^3)$. The notation of the vertices is the same as in Fig. 3.2. The wavy line with the cross at the free end corresponds to an external axial-vector source.

Proceeding with the calculation in a covariant manner, we obtain the following result:

$$g_A = g\Big\{1 + \frac{4d_{16}M^2}{g} - 2\bar{\lambda}\frac{(g^2-2)m^2+(g^2-1)M^2}{f^2} - \frac{(g^2-1)M^2}{16\pi^2 f^2}\log\left(\frac{m^2}{\mu^2}\right)$$
$$+ \underbrace{-\frac{(g^2-2)m^2}{16\pi^2 f^2}\log\left(\frac{m^2}{\mu^2}\right) - \frac{g^2m^2}{16\pi^2 f^2}}_{PCBT} - \frac{(2+3g^2)M^2}{16\pi^2 f^2}$$
$$+ \frac{((2+3g^2)M^2 - 2(1+2g^2)m^2)M^2}{32\pi^2 m^2 f^2}\log\left(\frac{M^2}{m^2}\right)$$
$$+ \frac{(8(1+g^2)m^2 - (2+3g^2)M^2)M^3}{16\pi^2 m^2 f^2\sqrt{4m^2-M^2}}\arccos\left(\frac{M}{2m}\right)\Big\} \tag{5.9}$$

As in Sec. 5.1.1, we have to cancel both the divergences and the PCBT. From Eq.(5.9) it is easy to see that this is achieved through the following redefinitions:

$$g \to g' + 2\bar{\lambda}\frac{g(g^2-2)m^2}{f^2} + \frac{g(g^2-2)m^2}{16\pi^2 f^2}\log\left(\frac{m^2}{\mu^2}\right) + \frac{g^3m^2}{16\pi^2 f^2} \tag{5.10}$$

$$d_{16} \to d_{16}' + 2\bar{\lambda}\frac{g(g^2-1)}{4f^2} + \frac{g(g^2-1)}{64\pi^2 f^2}\log\left(\frac{m^2}{\mu^2}\right) \tag{5.11}$$

5.1.3 The Scalar Form Factor of the Nucleon

The last but not less important example is the calculation of the scalar form factor of the nucleon, $\sigma(t)$. In fact, this magnitude is of great interest because $\sigma(t=0) = \sigma_{\pi N}$, which importance was stressed before. The diagrams contributing to $\sigma(t)$ up to $\mathcal{O}(q^3)$ are displayed in Fig. 5.3.

Figure 5.3: Diagrams that contribute to the nucleon scalar form factor up to $\mathcal{O}(q^3)$. The vertex with the cross represents the external scalar source and it counts as $\mathcal{O}(q^2)$ in the chiral counting.

Since we are only interested in $\sigma_{\pi N}$ and not in the t dependence of the form factor, we consider the special case $\sigma(t=0)$, where the loop integrals can be solved analytically. One obtains then the following result:

$$\sigma(0) = -4c_1 M^2 + \frac{3g^2 m M^2}{2f^2}(2\bar{\lambda}) \underbrace{+\frac{3g^2 m M^2}{32\pi^2 f^2}\log\left(\frac{m_N^2}{\mu^2}\right) - \frac{3g^2 m M^2}{32\pi^2 f^2}}_{PCBT}$$
$$- \frac{3g^2 M^3}{16\pi^2 f^2 m}\left(\frac{3m^2 - M^2}{\sqrt{4m^2 - M^2}}\arccos\frac{M}{2m} + M\log\frac{M}{m}\right) \tag{5.12}$$

We see from Eq.(5.12) that the divergences (along with their scale dependence) and PCBT are absorbed by taking the same redefinition of the c_1, Eq.(5.6), as in Sec. 5.1.1. Taking a look to Appendix F, where we show the $\mathcal{O}(q^2)$ and $\mathcal{O}(q^3)$ LECs renormalization for πN scattering, one can check that the LECs redefinition is the same for all these calculations (chiral corrections to the nucleon mass, scalar form factor of the nucleon and πN scattering). This proves explicitly that *EOMS is consistent*, at least, up to the order considered here.

5.1.4 Scale Independence

It is well known that in the covariant framework of IR, the renormalized amplitudes depend on the scale μ used in the regularization procedure. This is because the divergences, and therefore the scale-dependent logarithms, were not included completely in the infrared regular part of the loop integrals as it would be desirable, since they can be formally considered as power counting breaking terms. Instead, their contributions were splitted into the infrared singular and regular part. In a practical calculation, one only calculates the infrared singular part and drops the divergent term (assuming that it can be absorbed in the LECs) but, in what concerns to the scale-dependent logarithms, their contributions are entangled with the full (divergent-free) infrared singular contribution. Within IR, one typically fixes the renormalization scale μ to the nucleon mass $\mu = m_N$ to cancel the scale-dependent terms, since they always appear as $\log(m_N^2/\mu^2)$ (see Appendix F). This fact means that IR has a spurious and unphysical dependence on the scale in the physical quantities calculated within this scheme. This is dramatically manifested in the calculation of the Goldberger-Treiman deviation (Δ_{GT}) where, as showed in [21], the huge value obtained with IR depends strongly on the value of renormalization scale employed.

On the contrary, the EOMS scheme handles the scale dependence in the same way as the $\overline{MS}$ does. This means that the scale dependent logarithms can be absorbed in the same way as the divergent parts, giving rise to amplitudes that do not depend on the renormalization scale. In order to prove this

explicitly, we performed various fits with different values of μ (by orders of magnitude) leaving the scale-dependent pieces along with the PCBT. What we observed is that the χ^2 was exactly the same for all the fits and that the LECs that do not absorb divergences (d_3 and d_{18}) kept exactly the same value.[♯2] Once the scale-independence is explicitly checked, one can redefine scale-independent LECs by introducing the μ-dependent logarithms in their redefinition, as we show in Appendix F.

5.2 Calculation of the Scattering Amplitude

According to the power counting [49], for the calculation of the chiral amplitude up to $\mathcal{O}(q^3)$ one has to consider the diagrams of Fig. 3.2 plus their crossed versions. For the calculation of the scattering amplitude, we decide to write the loop amplitudes by means of the 1-, 2-, 3- and 4-points scalar loop integrals using the Passarino-Veltman decomposition. This decomposition has the advantage of leaving all the loop diagrams written in terms of a few scalar integrals which are the only possible source of power counting breaking terms. So, if one can identify the terms contained in the different scalar loop integrals that can give rise to PCBT in the full covariant amplitude, those PCBT can be explicitly cancelled via a redefinition of the relevant LECs. The method used for the identification of those problematic terms is shown in Appendix E. In the numerical evaluation of the scattering amplitudes used in the fitting procedure presented below, we employed the the subroutine LoopTools [119]. On the other hand, up to this order we have chiral corrections to the axial coupling (g_A), pion weak decay constant (f_π), nucleon mass (m_N) as well as the wave function renormalization constants of the nucleon (Z_N) and pion (Z_π) fields, whereas the pion mass (M_π) does not receive chiral corrections yet. We work with the physical value of these constants, so we write their values in the chiral limit as their physical ones minus the chiral corrections. These corrections only enter in the expression for the $\mathcal{O}(q)$ πN scattering amplitude and give rise to $\mathcal{O}(q^3)$ contributions. In the practical way, we pass from an $\mathcal{O}(q)$ amplitude written as a function of these bare constants to an $\mathcal{O}(q)$ plus a correction of $\mathcal{O}(q^3)$, all written in terms of these constants at their physical value. On the other hand, the physical values can be directly used for the $\mathcal{O}(q^2)$ and $\mathcal{O}(q^3)$ scattering amplitude

[♯2]It is important to point out that, in order to keep exactly the same χ^2 in this $\mathcal{O}(q^3)$ calculation, it was necessary to introduce in the calculations the monomials accompanying the LECs e_8, e_9 and e_{11} of Ref.[19], because some divergences (and hence scale-dependent pieces) were accompanied by terms of $\mathcal{O}(q^4)$. Otherwise a small variation in the χ^2 was observed.

because chiral corrections are of higher order. The explicit calculations of the chiral expansion of the nucleon mass and Z_N are presented in Sec. 5.1.1. We also calculate the chiral corrections to the nucleon axial coupling, which is shown in Sec. 5.1.2, whereas chiral corrections to f_π and Z_π (which come both from the pionic sector) are taken from [19]:

$$f_\pi = f\left\{1 - 2\bar{\lambda}\frac{M^2}{f^2} + \frac{M^2}{f^2}\left[\ell_4 - \frac{1}{16\pi^2}\log\left(\frac{M^2}{\mu^2}\right)\right]\right\} + \mathcal{O}(M^4) \tag{5.13}$$

$$Z_\pi = 1 - 2\bar{\lambda}\frac{M^2}{f^2} - \frac{M^2}{f^2}\left(2\ell_4 + \frac{1}{16\pi^2}\log\left(\frac{M^2}{\mu^2}\right)\right) + \mathcal{O}(M^3) \tag{5.14}$$

Both constants appear in the combination Z_π/f_π^2 multiplying the $\mathcal{O}(q)$ amplitude. This factor is independent of ℓ_4 up to the order considered here, so ℓ_4 does not appear as a free parameter in our chiral amplitude. Explicit expressions for the tree level up to $\mathcal{O}(q^3)$ and the one-loop amplitudes are given in Appendices C and D, respectively.

5.3 Fits

In order to fix the LECs that appear in the Lagrangian and extract the physical information, we consider the πN phase shifts provided by three different partial wave analyses (PWAs): The PWA of the Karlsruhe-Helsinki group [16] (KA85), the current solution of the George Washington University group [17] (WI08), and the low energy phase shift analysis of the Matsinos' group [18] (EM06). As explained in Chapter 3, both KA85 and WI08 assume fixed-t analyticity, but whereas KA85 uses the data set [54], WI08 employs [53], which contains more points and more recent high quality data. A very different systematics is followed by EM06 which consists in a low-energy ($\sqrt{s} \lesssim 1.16$ GeV) phase shift analysis employing hadronic potentials corrected electromagnetically. In contrast with the methodology followed in [16] and [17], the authors analyze the elastic scattering data (listed in [18]) separately. However, both EM06 and WI08 have in common the inclusion of new data of high quality collected along the last 20 years in meson factories. After this brief comment about the PWAs, that will be our input, we proceed to the explanation of the methodology of our fitting procedure.

Our fits will follow two strategies using, in both cases, Eq.(3.14) for the calculation of the phase shifts, since our calculation is perturbative. We also use, for the two strategies, the χ^2 defined in Eq.(4.15), with the same assignment of errors to the data points, if needed.

5.3.1 Strategy-I

The strategy-I corresponds to the strategy-1 of Sec. 4.3.1, and is used so as to compare fairly both covariant methods: EOMS and IR. This strategy consists of fitting phase shifts up to energies of $\sqrt{s}_{max} = 1.13$ GeV taking only the pion and the nucleon as the relevant degrees of freedom. In this case we can also compare with the results of HBChPT obtained in [63], where the $\Delta(1232)$ was not included. Figs. 5.4, 5.5 and 5.6 show the results of the fits to KA85, WI08 and EM06, respectively, within this strategy.

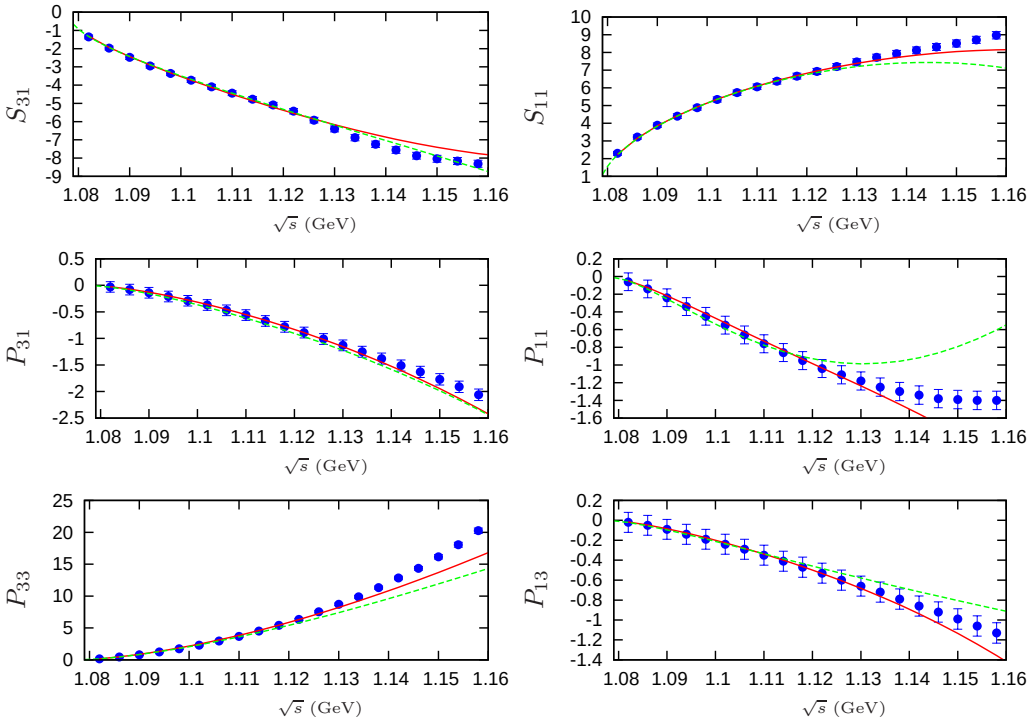

Figure 5.4: Fits to KA85 [16] with strategy-I. The solid lines correspond to the EOMS result and the dashed ones to IR. Both fits are performed up to $\sqrt{s}_{max} = 1.13$ GeV.

LECs

In Table 5.1 we show the results obtained using the EOMS scheme, columns 2–4. We see that the LECs obtained using the different PWAs for the EOMS calculation are compatible between each other, with the largest variation taking place in the value of d_5 and d_{18}. We also show in Table 5.2 (columns 2–3) the previous results that we obtained in Chapter 4 with the IR prescription

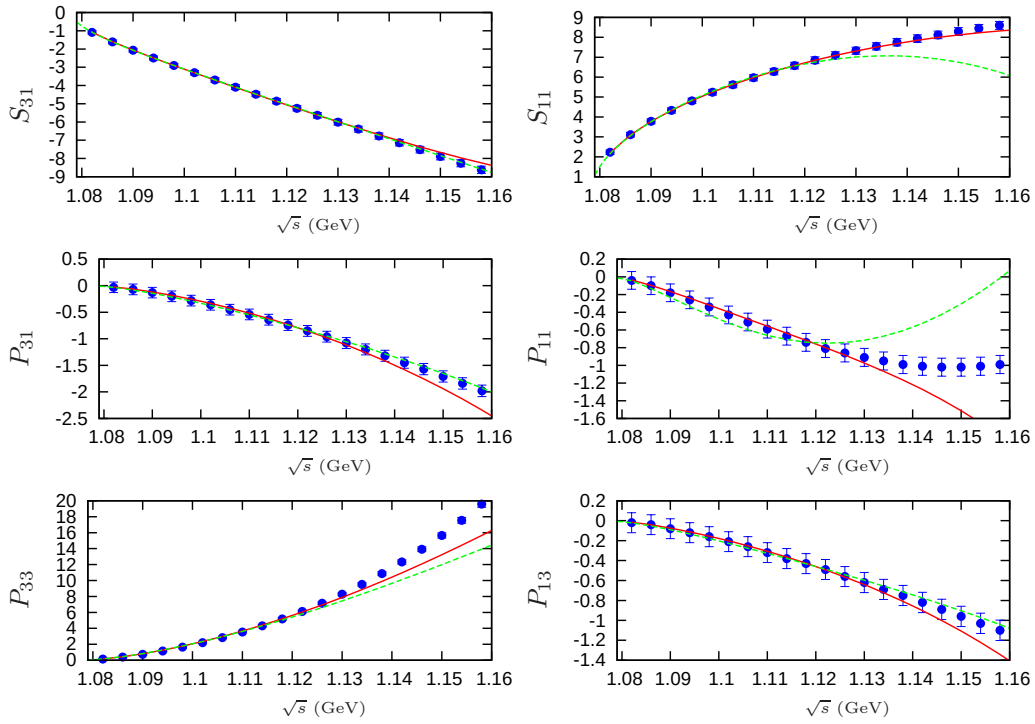

Figure 5.5: Fits to WI08 [17] with strategy-I. The solid line correspond to the EOMS result and the dashed ones to IR. Both fits are performed up to $\sqrt{s}_{max} = 1.13$ GeV.

[21], and the result of Fettes *et al.* [63] within the HBChPT formalism, last column. In Figs. 5.4 and 5.5 we see that the bigger difference respect to IR comes out in the P_{11} partial wave for the solution WI08. In this case, we see that EOMS is able to reproduce satisfactorily the data up to the fitted energy, in contrast to IR, which fails even at very low energies (see Sec. 4.3.2 of Chapter 4, or Ref.[21] for details). Respect to the quality of the fits ($\chi^2_{d.o.f.}$), it is important to stress that the EOMS and IR can be compared fairly because both results are obtained using the same strategy with the same assignment of errors, whereas the HBChPT number is taken from Ref.[63] with different error assignment. With this in mind, we see that for both KA85 and WI08 PWAs the EOMS representation gives a much lower $\chi^2_{d.o.f.}$ result than the IR ones. It is however striking the huge $\chi^2_{d.o.f.}$ obtained for the EM06 solution. This huge value can be traced back to the saturation of the $\Delta(1232)$-resonance to the $\mathcal{O}(q^2)$ LECs needed to reproduce the P_{33} partial wave (see Sec. 5.3.3). This affects considerably the theoretical prediction of the rest of the partial waves, in particular the P_{11}. Together to the

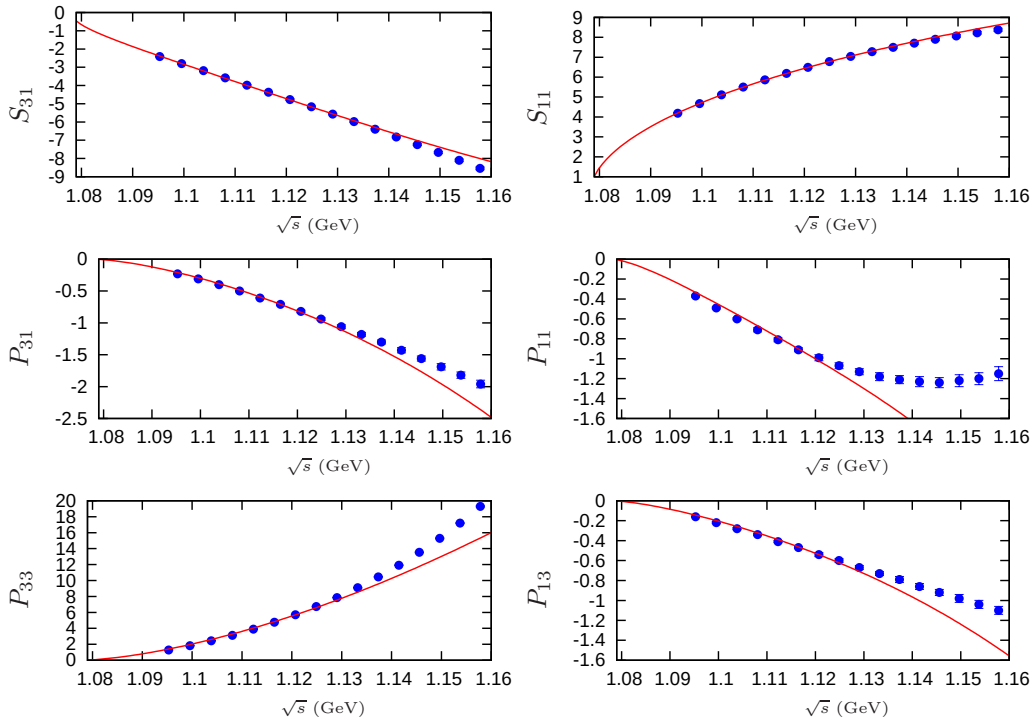

Figure 5.6: Fits to EM06 [18] with strategy-I. Fits are performed up to $\sqrt{s}_{max} = 1.13$ GeV.

small errors given in EM06, this is the reason for such a big value of $\chi^2_{d.o.f.}$. This will be seen more clearly in Sec. 5.3.2, where we study the effects of including the $\Delta(1232)$ as an explicit degree of freedom in our calculations.

Threshold parameters

We consider two methods to extract the values of the threshold parameters. The first one consist in fitting the effective range expansion, Eq.(4.16), to our ChPT prediction in the threshold region ($\sqrt{s} \lesssim 1.084$ GeV), just as we did in Chapter 4. The second method consist of using the Eq.(3.14) in Eq.(4.16) to obtain, in the limit $s \to (m_N + M_\pi)^2$ ($|\mathbf{p}| \to 0$):

$$a_{IJ\ell} = \frac{\mathrm{Re}[T_{IJ\ell}(s = (m_N + M_\pi)^2)]}{8\pi(m_N + M_\pi)} \tag{5.15}$$

Since $T_{IJ\ell}$ cannot be evaluated numerically just on the threshold, we had to take the values very near this point, where the numerical evaluation of

LEC	KA85-I	WI08-I	EM06-I
c_1	$-1.26(7)$	$-1.50(6)$	$-1.47(2)$
c_2	$4.08(9)$	$3.74(9)$	$3.63(2)$
c_3	$-6.74(8)$	$-6.63(8)$	$-6.42(1)$
c_4	$3.74(5)$	$3.68(5)$	$3.56(1)$
d_1+d_2	$3.25(55)$	$3.67(54)$	$3.64(8)$
d_3	$-2.72(51)$	$-2.63(51)$	$-2.21(8)$
d_5	$0.50(13)$	$-0.07(13)$	$-0.56(4)$
$d_{14}-d_{15}$	$-6.10(1.08)$	$-6.80(1.07)$	$-6.49(2)$
d_{18}	$-2.96(1.44)$	$-0.50(1.43)$	$-1.07(22)$
$\chi^2_{d.o.f.}$	0.38	0.23	25.08

Table 5.1: Results for the scale independent LECs obtained from different PWAs. The $\mathcal{O}(q^2)$ and $\mathcal{O}(q^3)$ are given in units of GeV^{-1} and GeV^{-2}, respectively.

LEC	KA85-IR [21]	WI08-IR [21]	HBChPT [63]
c_1	$-0.71(49)$	$-0.27(51)$	$(-1.71,-1.07)$
c_2	$4.32(27)$	$4.28(27)$	$(3.0,3.5)$
c_3	$-6.53(33)$	$-6.76(27)$	$(-6.3,-5.8)$
c_4	$3.87(15)$	$4.08(13)$	$(3.4,3.6)$
d_1+d_2	$2.48(59)$	$2.53(60)$	$(3.2,4.1)$
d_3	$-2.68(1.02)$	$-3.65(1.01)$	$(-4.3,-2.6)$
d_5	$2.69(2.20)$	$5.38(2.40)$	$(-1.1,0.4)$
$d_{14}-d_{15}$	$-1.71(73)$	$-1.17(1.00)$	$(-5.1,-4.3)$
d_{18}	$-0.26(40)$	$-0.86(43)$	$(-1.6,-0.5)$
$\chi^2_{d.o.f.}$	$\lesssim 1$	$\lesssim 1$	$(0.83-1.34)$

Table 5.2: For comparison, we show in this table (columns 2 and 3) the averaged values for the $\mathcal{O}(q^2)$ (in units of GeV^{-1}) and $\mathcal{O}(q^3)$ (in units of GeV^{-2}) LECs obtained in Chapter 4 using the IR method [21]. The results obtained by HBChPT [63] is shown in column 4.

the loop diagrams converges well. We checked that both methods gives the same value for the threshold parameters presented here.

The scattering lengths and volumes for the different partial waves, together with the scalar-isoscalar and scalar-isovector scattering lengths, are shown in Table 5.3. There, one can see a good agreement between the values

extracted from the fits and their corresponding PWA. The only exception is the P_{33} scattering volume because of the influence of the $\Delta(1232)$ in this partial wave, as discussed in Chapter 4 as well as in Ref.[21]. When this resonance is not included as an explicit degree of freedom in the calculation, the $\mathcal{O}(q^2)$ LECs absorb its contribution raising their values considerably. This makes that, in the extrapolation of the amplitudes to threshold, one has a large contribution of the $\Delta(1232)$ in a region where this resonance is kinematically suppressed, which gives rise to a larger value of the scattering volume than the experiment. This is explicitly illustrated in Sec. 5.3.2, where the $\Delta(1232)$ is included as a degree of freedom in our theoretical calculation.

Partial Wave	KA85-I	KA85 [16]	WI08-I [17]	WI08	EM06-I	EM06 [18]
$a_{S_{31}}$	$-9.9(13)$	$-10.0(4)$	$-8.0(12)$	-8.4	$-7.1(6)$	$-7.52(16)$
$a_{S_{11}}$	17.5(21)	17.5(3)	17.2(21)	17.1	15.9(10)	15.71(13)
a^+_{0+}	$-0.8(8)$	-0.8	0.4(8)	$-0.10(12)$	0.6(4)	0.22(12)
a^-_{0+}	9.2(10)	9.2	8.4(10)	8.83(5)	7.7(4)	7.742(61)[♯3]
$a_{P_{31}}$	$-4.0(7)$	$-4.4(2)$	$-3.5(7)$	-3.8	$-3.7(2)$	$-4.176(80)$
$a_{P_{11}}$	$-7.7(18)$	$-7.8(2)$	$-6.0(18)$	-5.8	$-7.2(3)$	$-7.99(16)$
$a_{P_{33}}$	25.1(9)	21.4(2)	23.7(9)	19.4	23.6(2)	21.00(20)
$a_{P_{13}}$	$-2.7(7)$	$-3.0(2)$	$-2.3(6)$	-2.3	$-2.7(3)$	$-3.159(67)$

Table 5.3: Comparison between the extracted threshold parameters and their corresponding PWA values. The scattering lengths and volumes are shown in units of $10^{-2}M_\pi^{-1}$ and $10^{-2}M_\pi^{-3}$ respectively.

[♯3] A later work performed by the same authors [87] obtain $a^-_{0+} = 8.78(11)10^{-2}M_\pi^{-1}$, which reconciles their value for this scattering length with the values obtained by KA85 and WI08. They also obtain in [87] $a^+_{0+} = -0.20(11)10^{-2}M_\pi^{-1}$.

5.3.2 Strategy-II

The strategy-II consists of fitting phase shifts up to energies of $\sqrt{s} = 1.20$ GeV including *explicitly* the $\Delta(1232)$ resonance, besides the pion and the nucleon field. The main motivation is to extract more precise and reliable values for the LECs, free from the important contribution of the $\Delta(1232)$. As shown below, this will allow us to obtain a very good description of the phase shifts up to $\sqrt{s} = 1.20$ GeV for all the PWAs. Moreover, we also show that with the extracted LECs one can reproduce independent phenomenology, as well as connect the physical region with the subthreshold region and extract, from the PWAs, an accurate and reliable value of the pion-nucleon sigma term ($\sigma_{\pi N}$). We show the results of the fits to KA85, WI08 and EM06 in Figs. 5.7, 5.8 and 5.9, respectively, employing this strategy.

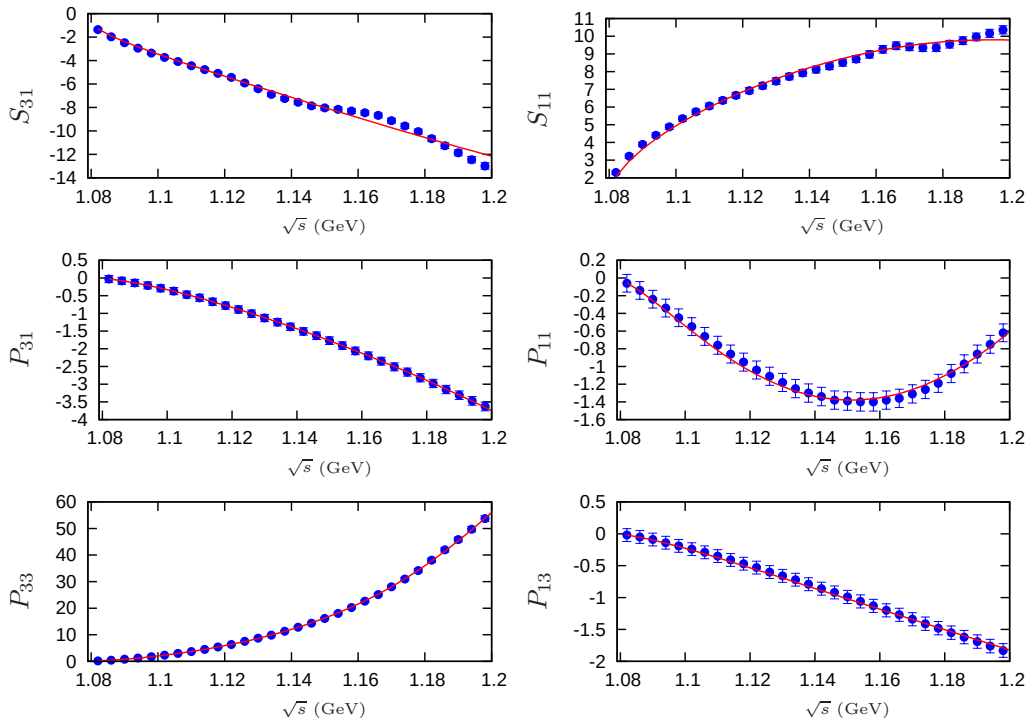

Figure 5.7: Fits to the KA85 data [16] with strategy-II. The fits are performed up to $\sqrt{s}_{max} = 1.20$ GeV.

LECs

Within this strategy, we are able to reproduce the S- and P-wave phase shifts up to energies of $\sqrt{s} = 1.20$ GeV with good accuracy keeping $\chi^2_{d.o.f.} < 1$.

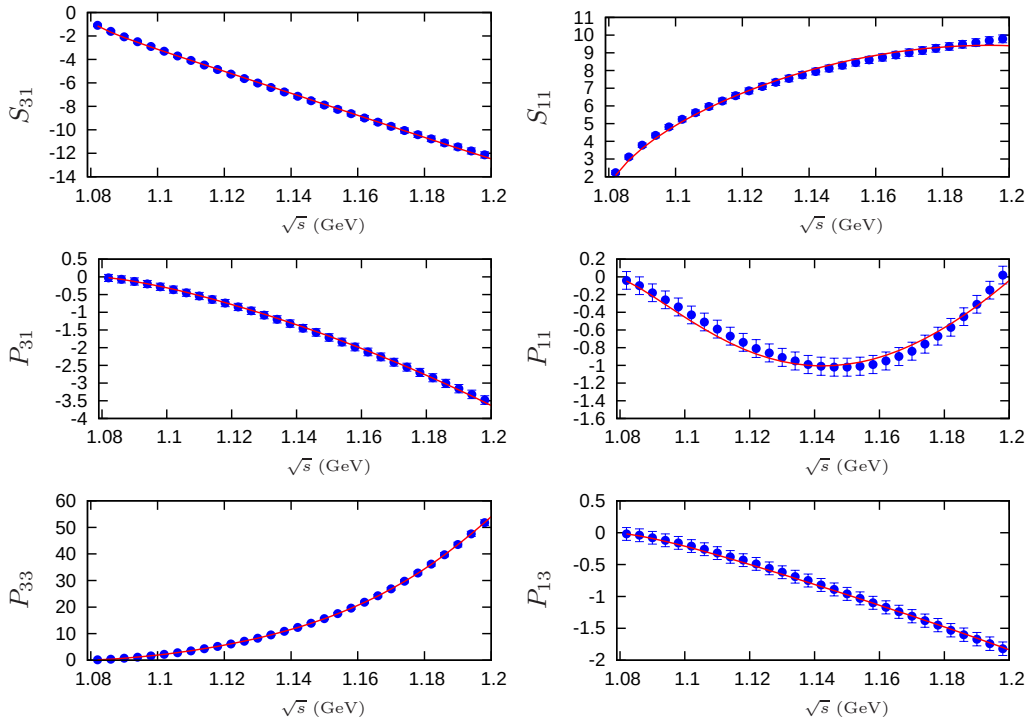

Figure 5.8: Fits to the WI08 data [17] with strategy-II. The fits are performed up to $\sqrt{s}_{max} = 1.20$ GeV.

These fits up to higher energy also allow us to extract more reliable values for the LECs. As shown in Table 5.4, with this strategy the $\mathcal{O}(q^2)$ and $\mathcal{O}(q^3)$ LECs relax their values, and that is because now the $\Delta(1232)$ is included as an explicit degree of freedom. Comparing the results for the three PWAs used, we see that the LECs are compatible between them, with the largest spread in the values for c_1, that is directly connected to $\sigma_{\pi N}$. It is remarkable that the inclusion of the $\Delta(1232)$ reduces drastically the $\chi^2_{d.o.f.}$ for EM06 from ≈ 25 (strategy-I) to ≈ 0.1 (strategy-II). This shows that the $\Delta(1232)$ resonance is a key ingredient in πN scattering, even in the low energy region.[♯4] For KA85 the $\chi^2_{d.o.f.}$ increases considerably but this is understandable if we consider that we increase the range of our fit from $\sqrt{s}_{max} = 1.13$ GeV to $\sqrt{s}_{max} = 1.20$ GeV. It is more remarkable that for WI08 the $\chi^2_{d.o.f.}$ remains practically the same, which means that EOMS-BChPT with the $\Delta(1232)$ describes better the WI08 solution than the KA85 one. On the other hand,

[♯4] In this latter cases, the large reduction in magnitude of the $c_i s$ greatly improves the convergence in the calculation of the NN potential [120]. Moreover, the $\Delta(1232)$ is important even below the πN threshold, as we show in Sec. 5.5.

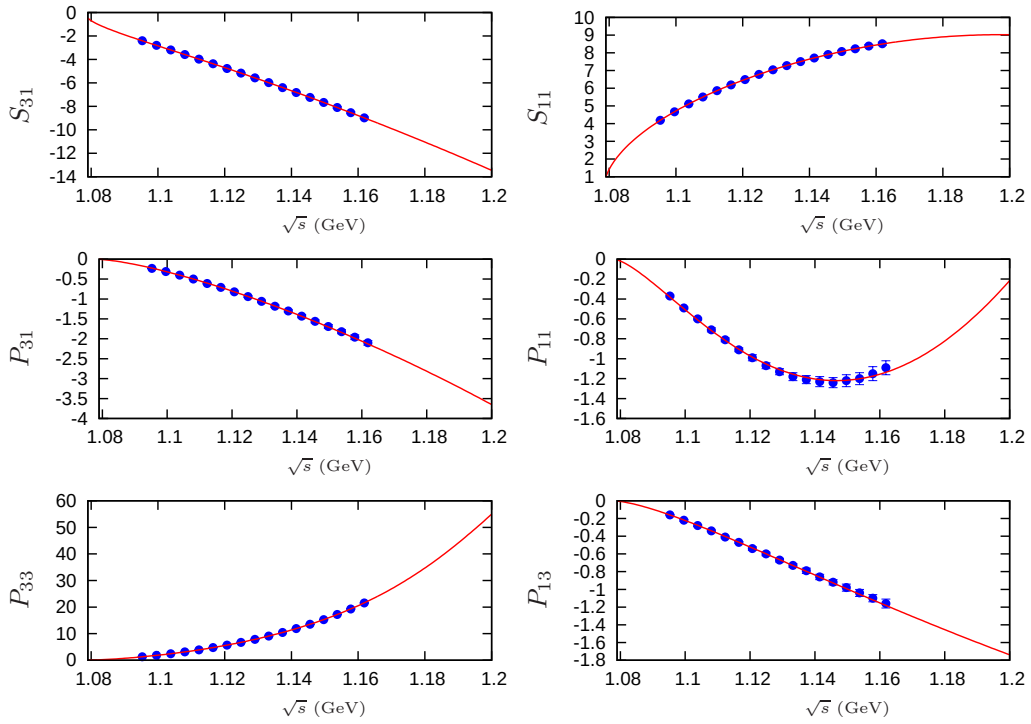

Figure 5.9: Fits to the EM06 data [18] with strategy-II. The fits are performed up to $\sqrt{s}_{max} = 1.16$ GeV.

the WI08 solution provides a value for h_A that is perfectly compatible with the value extracted directly from the $\Delta(1232)$ Breit-Wigner width ($\Gamma_\Delta = 118(2)$ MeV [83]), $h_A = 2.90(2)$ [121, 76], while for KA85, EOMS-BChPT obtains a value of h_A that is compatible with the overestimation for the width that this solution provides [16]. The EM06 solution, on the other hand, is a low energy phase shift analysis performed below the $\Delta(1232)$ region and has no estimation for its width. As one can see in Table 5.4, with our analysis we have found that the EM06 solution leads to a h_A higher than the one extracted form the $\Delta(1232)$ width. However this value is slightly lower that the one extracted from the KA85 solution. Thus, we conclude that the WI08 solution is the only one that gives a $\Delta(1232)$ width compatible with the value listed in the PDG.

By taking the difference between the values of the $c_i s$ in Tables 5.1 and 5.4 one can estimate the influence of the $\Delta(1232)$ in the $\mathcal{O}(q^2)$ and $\mathcal{O}(q^3)$ LECs. This is given in Table 5.5 where we also compare with the estimation of Ref.[101] from resonance saturation (RS) [95]. A good agreement between our results and the estimates from RS [101] results. On the other hand, we

LEC	KA85-II	WI08-II	EM06-II
c_1	-0.75 ± 0.03	-0.94 ± 0.03	-1.00 ± 0.01
c_2	0.97 ± 0.10	1.08 ± 0.09	0.58 ± 0.03
c_3	-2.72 ± 0.13	-3.03 ± 0.12	-2.51 ± 0.04
c_4	1.90 ± 0.06	2.04 ± 0.06	1.77 ± 0.02
$d_1 + d_2$	-0.27 ± 0.10	0.06 ± 0.09	-0.36 ± 0.06
d_3	-0.05 ± 0.06	-0.15 ± 0.05	0.30 ± 0.04
d_5	0.72 ± 0.04	0.43 ± 0.04	0.20 ± 0.02
$d_{14} - d_{15}$	0.14 ± 0.15	-0.32 ± 0.15	0.40 ± 0.10
d_{18}	-1.62 ± 0.27	-0.69 ± 0.26	-0.61 ± 0.12
h_A	3.02 ± 0.04	2.87 ± 0.04	2.99 ± 0.02
$\chi^2_{d.o.f.}$	0.77	0.24	0.11

Table 5.4: Results for the LECs within the strategy-II. In columns 2–4 we show the results for the fits to the KA85, WI08 and EOM06 PWAs, respectively.

observe a shift in c_1 by an amount of $\approx$ 0.5–0.6 GeV^{-1}, while RS gives a negligible result for the contribution of the $\Delta(1232)$ to this LEC. This can be interpreted as a clear indication that the LECs are stabilized once the tree-level $\Delta(1232)$ exchange contributions are taken into account [122, 120] (see also Sec. 5.3.3).

	c_2^Δ	c_3^Δ	c_4^Δ
KA85	3.11	-4.02	1.82
WI08	2.66	-3.60	1.64
EM06	3.05	-3.91	1.79
RS[101]	$1.9 \ldots 3.8$	$-3.8 \ldots -3.0$	$1.4 \ldots 2.0$

Table 5.5: Estimation of the $\Delta(1232)$ contribution to c_2, c_3 and c_4 in units of GeV^{-1} , from the difference between the results obtained with (Table 5.4) and without (Table 5.1) the inclusion of this resonance as an explicit degree of freedom. In the last row we show the results of Ref.[101] employing RS.

Threshold parameters

For this second strategy we consider the same methods to extract the values of the scattering lengths and volumes, Eqs.(4.16) and (5.15). In the present case, where the $\Delta(1232)$ is explicitly included in our calculations, we observe

an improvement in the P_{33} partial wave. It is also remarkable that such higher energy fits can describe the threshold region in a way that leads to such a good agreement as we observe in Table 5.6.

Partial Wave	KA85-II	KA85 [16]	WI08-II	WI08 [17]	EM06-II	EM06 [18]
$a_{S_{31}}$	−9.9(8)	−10.0(4)	−8.6(7)	−8.4	−7.5(3)	−7.52(16)
$a_{S_{11}}$	16.0(8)	17.5(3)	16.1(8)	17.1	15.6(3)	15.71(13)
a^{+}_{0+}	−1.2(8)	−0.8	−0.3(7)	−0.10(12)	0.2(3)	0.22(12)
a^{-}_{0+}	8.7(2)	9.2	8.2(2)	8.83(5)	7.7(1)	7.742(61)[♯5]
$a_{P_{31}}$	−4.3(2)	−4.4(2)	−4.0(2)	−3.8	−4.1(1)	−4.176(80)
$a_{P_{11}}$	−9.0(4)	−7.8(2)	−7.9(4)	−5.8	−8.5(2)	−7.99(16)
$a_{P_{33}}$	22.2(3)	21.4(2)	21.6(2)	19.4	20.8(1)	21.00(20)
$a_{P_{13}}$	−3.2(2)	−3.0(2)	−3.0(2)	−2.3	−3.1(1)	−3.159(67)

Table 5.6: Comparison between the extracted threshold parameters and their corresponding PWA values for the strategy-II fits. The scattering lengths and volumes are shown in units of $10^{-2}M_\pi^{-1}$ and $10^{-2}M_\pi^{-3}$, respectively.

5.3.3 Convergence of the Chiral series

It is interesting to study the convergence pattern of the chiral series in this novel calculation that uses the EOMS scheme both with and without the $\Delta(1232)$ resonance. In Figs. 5.10 and 5.11 the contributions of the different orders to the total result (solid red line) are shown for the fits WI08-I and WI08-II, respectively.[♯6] The comparison of Fig. 5.10 with Fig. 7 of Ref.[63] and Fig. 4.5 of Chapter 4 shows the same hierarchy for the three orders.

Once we include the $\Delta(1232)$ as an explicit degree of freedom, the $\mathcal{O}(q^2)$ LECs reduce in absolute values and the fits of Fig. 5.8 result. With the $\mathcal{O}(q^2)$ free from the $\Delta(1232)$ contribution, now it can absorb the contribution of the rest of the partial waves up to higher energies. This improves the the convergence of the series (as shown in Sec. 5.3.2) which results in a more natural value for c_2, c_3 and c_4 and in a shift in c_1 of ≈ 0.5 GeV. As one could expect, the $\Delta(1232)$ is the main responsible of the raise in the P_{33} phase shifts, though it gives also a small contribution to the rest of the P-waves. For the S-waves its contribution is even much smaller, as it is evident by comparing the dashed (green) lines in Figs. 5.10 and 5.11. Moreover, the

[♯5] See footnote ♯3.

[♯6] The conclusions of this study are the same for the KA85 and EM06 solutions.

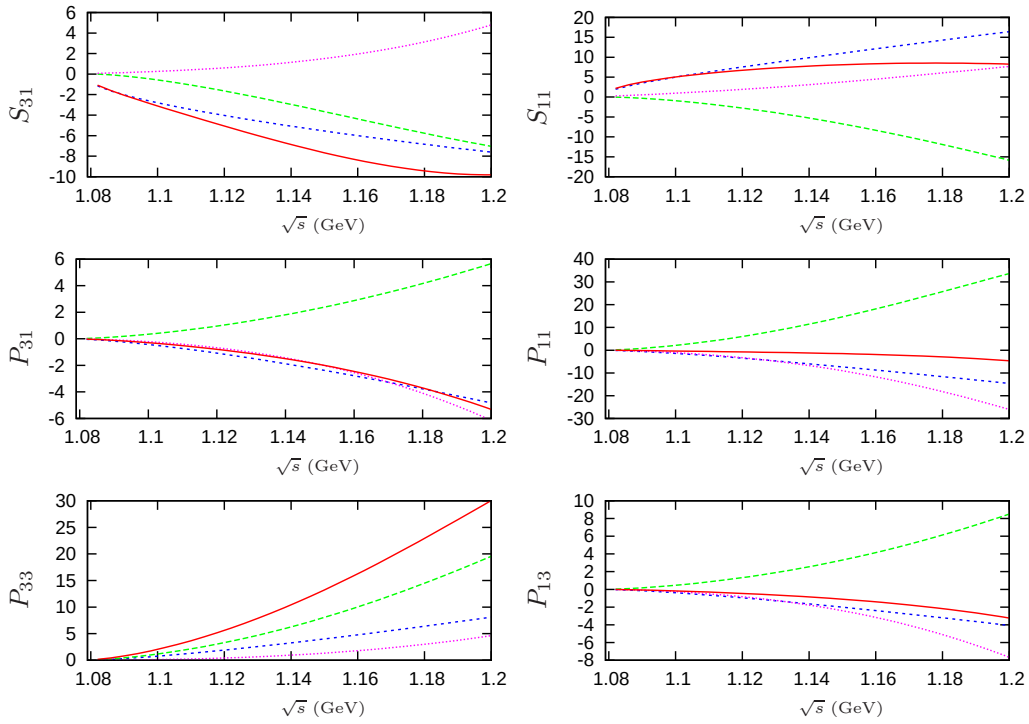

Figure 5.10: Convergence of the chiral series for the fit WI08-I. The short dashed (blue), dashed (green), dashed (pink) and solid (red) lines correspond to the contributions of the $\mathcal{O}(q)$, $\mathcal{O}(q^2)$, $\mathcal{O}(q^3)$ and the total sum, respectively.

inclusion of the $\Delta(1232)$ does not affect the hierarchy of the different orders contributing to the S-wave whereas for the P_{31}, P_{11} and P_{13} partial waves one observes a smaller contribution of the $\mathcal{O}(q^3)$ compared with the case without that resonance. This was reflected in the values of the $\mathcal{O}(q^3)$ LECs of Table 5.4, which show a more natural value. This, together with the better fits of Figs. 5.7–5.9, lead us to conclude that the inclusion of the $\Delta(1232)$ improves significatively the convergence of the chiral series. And, as we will show below, this conclusion can be also extended to the subthreshold region.

5.4 The Goldberger-Treiman relation

One of the most striking results obtained in Chapter 4, where we used IR, is the unphysically large value obtained for the Goldberger-Treiman deviation ($\Delta_{GT} \approx 20 - 30\%$), with the main contribution coming from the IR regularized loop diagrams. This result, that is in clear contradiction with both

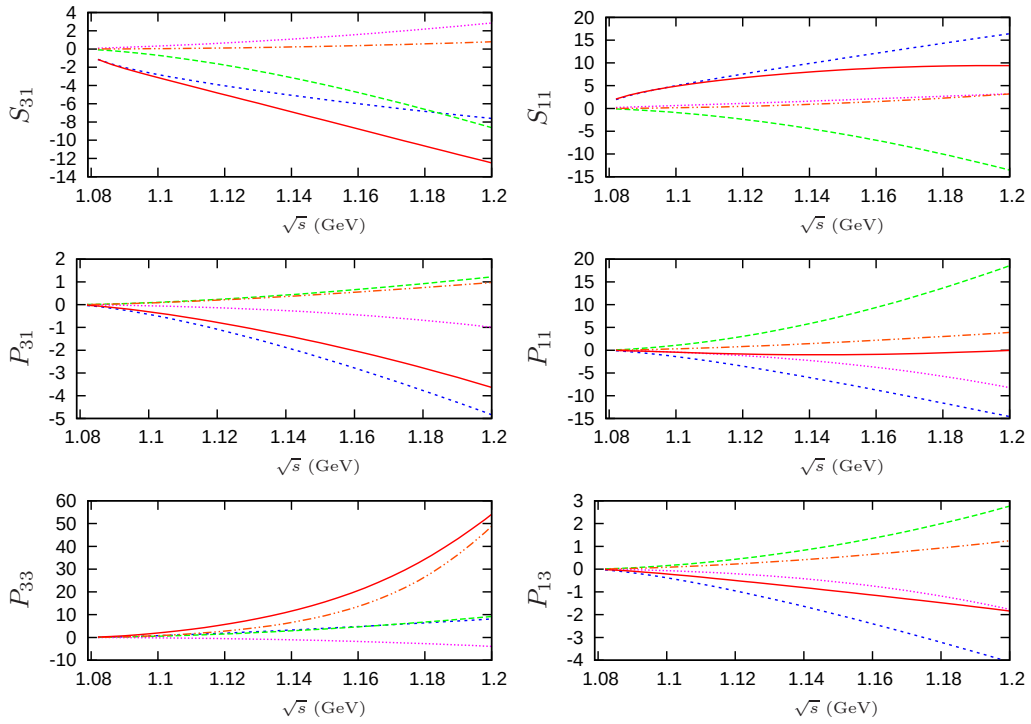

Figure 5.11: Convergence of the chiral series for the fit WI08-II. The short dashed (blue), dashed (green), dotted (pink), dash-double-dotted (orange) and solid (red) lines correspond to the contributions of the $\mathcal{O}(q)$, $\mathcal{O}(q^2)$, $\mathcal{O}(q^3)$, $\Delta(1232)$ and the total sum, respectively.

PWAs and chiral power counting, jeopardized the applicability of covariant BChPT to the πN system. It also raised the question whether this problem is due just to the IR prescription or, more generally, to the covariant formulation of BChPT once the chiral power counting is restored. Therefore, one of the main interests of this novel calculation is to show whether one can extract from experimental data or PWAs a Δ_{GT} value within experimental bounds.

To extract the value of Δ_{GT} we follow three different methods. The first one is the same one used in Sec. 4.5 of Chapter 4. The second method is more direct, and consists of comparing the pseudoscalar and axial couplings, both given above. Finally, the third method consists of writing the amplitude by means of $D^{\pm}$ and $B^{\pm}$ (see Eq.(3.3)) to write the pole term in the pseudovector form as (see Ref.[97] for definitions):

$$D^+(\nu,t) = \frac{g_{\pi N}^2}{m_N}\frac{\nu_B^2}{\nu_B^2-\nu^2} + \bar{D}^+(\nu,t) \tag{5.16}$$

Where $\nu_B = (t-2M_\pi^2)/4m_N$ and $\bar{D}^+$ is the Born-subtracted part of D^+, which is analytical in ν and t. Taking profit of the analyticity of $\bar{D}^+$ we approach to the point ($\nu=0$, $t=2M_\pi^2$) in two different ways:

$$\lim_{t\to 2M_\pi^2}\lim_{\nu\to 0} D^+(\nu,t) = \frac{g_{\pi N}^2}{m_N} + \bar{D}^+(\nu=0,t=2M_\pi^2) \tag{5.17}$$

$$\lim_{\nu\to 0}\lim_{t\to 2M_\pi^2} D^+(\nu,t) = \bar{D}^+(\nu=0,t=2M_\pi^2) \tag{5.18}$$

The difference of Eq.(5.17) and Eq.(5.18) gives directly $g_{\pi N}^2/m_N$, from where we can extract the value of $g_{\pi N}$ and, therefore, Δ_{GT}. From the three methods we obtain values of $g_{\pi N}$ and Δ_{GT} compatible with their corresponding PWA determinations (see Tables 5.7 and 5.8), although larger errors attached to Δ_{GT} of strategy-I are due to the bigger uncertainties in d_{18} for that case.

	KA85-I	WI08-I	EM06-I	KA85-II	WI08-II	EM06-II
Δ_{GT}	9(4)%	2(4)%	3.6(7)%	4.9(8)%	2.1(8)%	1.9(4)%
$g_{\pi N}$	14.03(52)	13.13(52)	13.34(10)	13.51(10)	13.15(10)	13.12(5)

Table 5.7: Second and third rows show the values for Δ_{GT} and $g_{\pi N}$ for the strategies I and II, respectively.

	KA85 [16]	WI08 [17]	EM06 [18]	NN scattering [113]	Pionic atoms [25]
Δ_{GT}	4.5(7)%	2.1(1)%	0.2(10)%	1%	1.9(7)%
$g_{\pi N}$	13.46(9)	13.15(1)	12.90(12)	$\simeq 13.0$	13.12(9)

Table 5.8: Values for Δ_{GT} and $g_{\pi N}$ obtained by different analyses.

From the three methods referred above we also conclude that EOMS-BChPT gives the loop contribution to the GT deviation $\Delta_{loops} \approx 0.002$. This result has the expected size of an $\mathcal{O}(q^4)$ correction due to explicit chiral symmetry breaking and is compatible with the relativistic calculation of Gasser *et al.* [13]. As a result, EOMS-BChPT solves the long-standing problem concerning the Goldberger-Treiman deviation and tell us that this problem was an artifact of IR, not due to a convergence problem of BChPT.

5.5 Subthreshold region

The subthreshold region, despite not having experimental information, is of great interest in ChPT because within this region lie special points that are connected with important low energies theorems; these are: the soft point, the Adler point [8] and the Cheng-Dashen point [20]. The latter is the subject of a intense study, since the Born-subtracted isospin even πN scattering amplitude at this point is directly related to the pion-nucleon sigma term ($\sigma_{\pi N}$). In fact, the IR scheme was proposed in order to achieve a good convergence in the subthreshold region [97], where HBChPT fails in part of it [60]. Unfortunately, despite the apparent good convergence of IR in this region, it fails to connect the physical region (where one has experimental data) with the subthreshold one [19]. For all these reasons it is interesting to check the convergence of our novel calculation within EOMS in the subthreshold region. In order to do so, we calculate the values of different interesting subthreshold quantities that have been studied both in dispersive and BChPT approaches. The first two quantities are d_{00} and d_{01} which are two coefficients of a power expansion of the Born-subtracted isospin even πN scattering amplitude $\bar{D}^+(\nu, t)$ around the point $\nu = 0$ and $t = 0$.[♯7]

$$\bar{D}^+(\nu, t) = d_{00} + d_{01}t + d_{10}\nu^2 + \dots \tag{5.19}$$

The third important quantity is the so-called Σ-term:

$$\Sigma = f_\pi^2 \bar{D}^+(\nu = 0, t = 2M_\pi^2), \tag{5.20}$$

Which is given by $\bar{D}^+$ at the Cheng-Dashen point ($\nu = 0, t = 2M_\pi^2$).

In order to see the length of this extrapolation, we show in Fig. 5.12 the physical region studied in this chapter in the Mandelstam plane (blue vertical lines) and the location, in the same plane, of the Cheng-Dashed point (blue cross).

Table 5.9 gathers the results of these three quantities for the different fits obtained in Secs. 5.3.1 and 5.3.2. As a general trend, one observes an overestimation of these three quantities when the $\Delta(1232)$ resonance is not included in the formalism. This is easy to understand because, according to Secs. 5.3.2 and 5.3.3 the LECs suffer a tension in their values when the

[♯7] Due to its crossing symmetry, the pion nucleon-scattering amplitude is usually defined as a function of the variables $\nu = \frac{s-u}{4m_N}$ and t, where s, t and u are the usual Mandelstam variables.

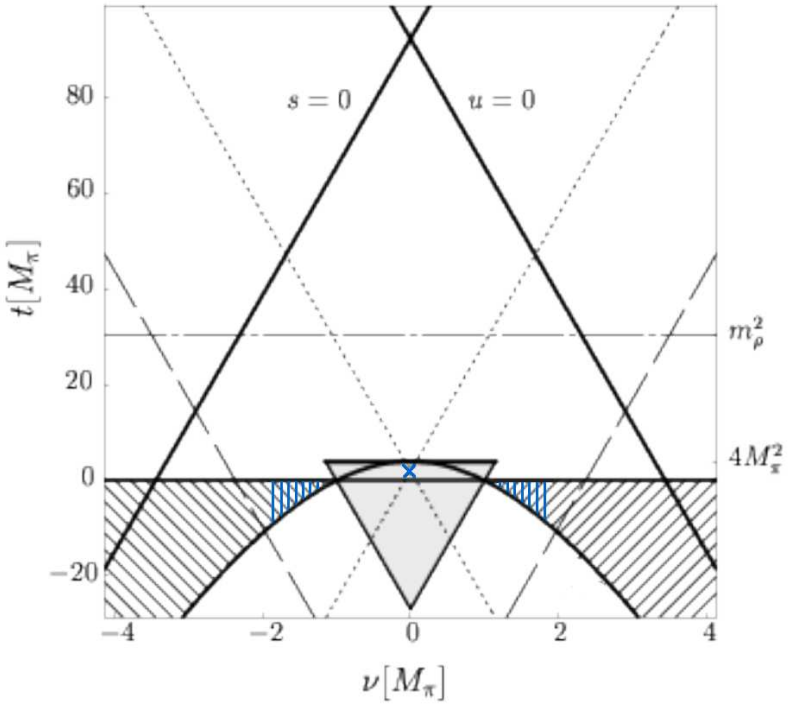

Figure 5.12: The Mandelstam plane. The physical region of πN scattering corresponds to the hatched zone. The vertical lines (blue) shows the region from threshold to $\sqrt{s} \approx 1.20$ GeV. On the other hand, the shaded region correspond to the values $s < (m_N + M_\pi)^2$, $u < (m_N + M_\pi)^2$ and $t < (m_N + M_\pi)^2$, where the amplitude is analytical (and real) once the nucleon poles in the s and u channels are removed. Inside there lies the Cheng-Dashen point ($\nu = 0$, $t = 2M_\pi^2$) (blue cross). The dotted, dashed and dot-dashed lines correspond to the nucleon poles, Δ-resonance and ρ-resonance, respectively.

$\Delta(1232)$ is not incorporated that raises artificially the value of these subthreshold quantities. By comparing the results in Table 5.9 for strategy-II with their values from the corresponding PWA, we deduce that once the contribution of the $\Delta(1232)$ is included explicitly, the EOMS-BChPT amplitude achieves an excellent convergence also in the subthreshold region. This result answer a long standing question opened in Ref.[19], which questioned the converge of the chiral series once the threshold is crossed. As we proved here, the convergence is achieved once the $\Delta(1232)$ is considered as an explicit degree of freedom in a theory with the right analytical properties as EOMS-BChPT.

	KA85-I	WI08-I	EM06-I	KA85-II	WI08-II	EM06-II
d_{00} (M_π^{-1})	$-2.02(4)$	$-1.65(3)$	$-1.56(3)$	$-1.44(5)$	$-1.27(5)$	$-0.97(2)$
d_{01} (M_π^{-3})	1.73(3)	1.70(3)	1.64(3)	1.16(4)	1.19(4)	1.08(2)
Σ (MeV)[♯8]	84(5)	103(5)	103(2)	45(2)	60(2)	64(1)

Table 5.9: Results for d_{00}, d_{01} and Σ for the fits following the strategies I and II.

	KA85 [16]	WI08 [17]
d_{00} (M_π^{-1})	-1.46	-1.30
d_{01} (M_π^{-3})	1.14	1.19
Σ (MeV)	64(8)	79(7)

Table 5.10: Results for d_{00}, d_{01} and Σ obtained by KA85 [16] and WI08 [17].

Another important subject is to check the Adler condition of our EOMS-BChPT amplitudes. According to Adler [8], the isospin even amplitude satisfies:

$$D^+(\nu = 0, t = M_\pi^2) \simeq \frac{g_{\pi N}^2}{m_N} \tag{5.21}$$

Or, equivalently, $\bar{D}^+(\nu = 0, t = M_\pi^2) \simeq 0$. Table 5.11 shows the result for the different fits performed in this work, which can be compared (Table 5.12) with values obtained by the George-Washington group [124] and by Ref.[100] for the Karlsruhe-Helsinki analysis. As shown, there is no much difference between strategy-I and strategy-II. On the other hand, Ref.[100] show a deviation of only 1%, what is in perfect agreement with the value obtained here within the EOMS scheme. Nonetheless, the fits to the more modern PWAs of WI08 and EM06 fulfill much better the Adler condition, although all these fits are within the theoretical bounds established by Adler [8]. It is important to point out that with the inclusion of the $\Delta(1232)$ we are able to reproduce the value provided by their corresponding PWA,as happened with the subthreshold coefficients, the Σ-term and the Goldberger-Treiman relation.

[♯8]It is important to point out that the values of Σ obtained a ChPT $\mathcal{O}(q^3)$ calculation differs from the exact result in an amount of ≈ 10 MeV [123].

	KA85-I	WI08-I	EM06-I	KA85-II	WI08-II	EM06-II
$f_\pi^2 \bar{D}^+(0, M_\pi^2)$	-16 MeV	4 MeV	6 MeV	-17 MeV	-4 MeV	7 MeV
%	1	0.3	0.4	1	0.3	0.5

Table 5.11: Check of the Adler condition to our results following strategies I and II. The second and third row show the deviation from this condition and the relative value for this deviation, respectively.

	KA85 [100]	WI08 [124]
$f_\pi^2 \bar{D}^+(0, M_\pi^2)$	–	-4 MeV
%	1	0.3

Table 5.12: Check of the Adler condition to the KA85 [16] and WI08 [17] performed in Refs.[100] and [124]. As in Table 5.12, the second and third row show the deviation from this condition and the relative value for this deviation, respectively.

5.6 The pion-nucleon sigma term

The pion-nucleon sigma term ($\sigma_{\pi N}$) is an observable of fundamental importance that embodies the internal scalar structure of the nucleon, becoming an essential piece to understand the origin of the mass of ordinary matter. It has been studied for more than 30 years using dispersion relations, partial wave analyses, ChPT or, more recently LQCD [24]. It is also a key ingredient in investigations of the QCD phase diagram and neutronic systems [125, 126], and appears as a necessary hadronic matrix element of the neutralino-nucleon elastic scattering cross section [22, 23, 127]. The usual method to extract this quantity from PWAs was extrapolating the Born-subtracted isospin even amplitude $\bar{D}^+$ to the Cheng-Dashen point and relate the Σ-term to $\sigma_{\pi N}$ by means of the relation [128]:

$$\Sigma = \sigma(2M_\pi^2) + \Delta_R = \sigma_{\pi N} + \Delta_\sigma + \Delta_R \tag{5.22}$$

Where Δ_R is a remainder due to non-vanishing quark masses with an estimated upper limit of $\simeq 2$ MeV [129], and the quantity $\Delta_\sigma \approx \sigma(2M_\pi^2) - \sigma_{\pi N} = 15.2$ MeV was calculated by Gasser *et al.* by means of dispersion relations [123]. The main difficulty of this method relies in the assignment of errors that propagate in the extrapolation to the Cheng-Dashen point form the systematic uncertainties associated to a particular parameterization of the data. This becomes more dramatic once we compare the values for $\sigma_{\pi N}$ from the different PWAs. On one hand, Gasser *et. al.* obtained $\sigma_{\pi N} \simeq 45$ MeV [130]

using the old analysis of the Karlsruhe-Helsinki group, whereas the analysis of the George Washington University group, which includes modern meson factory data, leads to $\sigma_{\pi N} = 64(7)$ MeV. On the other hand, the analysis of Matsinos *et al.*, which is based in a partial wave parameterization of the modern data at very low energies without imposing dispersive constraints form the high energy region, gives $\sigma_{\pi N} = 56(9)$ MeV according to the Olsson sum rule [131]. These different results started a longstanding dispute whether this difference [132] was due to the method of extraction or due to the data base used or both.

An advantage of ChPT over dispersive methods is that one can estimate the magnitude of the uncertainties of each quantity calculated, order by order. This advantage associated to the well convergent kernel of EOMS-BChPT can answer this longstanding question and extract a reliable value of $\sigma_{\pi N}$ associated to each PWA. Another interesting point of ChPT is that chiral symmetry allows to relate $\sigma_{\pi N}$ to the LEC c_1, which is obtained from a region where data actually exist (the physical region). This is in contrast with the large extrapolations across the subthreshold region (where there are no data to compare with) that the dispersive methods use.

The definition of the pion-nucleon sigma term is by means of the commutators of the axial charge with the symmetry breaking part of the Hamiltonian [133]:

$$\sigma_{\pi N} = \frac{1}{3}\sum_{a=1}^{3}\langle N(p)|[Q_A^a,[Q_A^a,H_{SB}]]|N(p)\rangle \tag{5.23}$$

With Q_A^a the axial charge and H_{SB} is the symmetry breaking part of the Hamiltonian. The H_{SB} dependence of the sigma term means that this quantity is related to the explicit breaking of the chiral symmetry and, therefore, should be small compared with $\Lambda_{\chi SB}$. From Eq.(5.23) is straightforward to obtain from H_{SB} in QCD:

$$\sigma_{\pi N} = \langle N(p)|\hat{m}(\bar{u}u + \bar{d}d)|N(p)\rangle \tag{5.24}$$

Where $\hat{m} = (m_u + m_d)/2$. So, the sigma term is the nucleon scalar form factor $\sigma(t) = \langle N(p')|\hat{m}(\bar{u}u + \bar{d}d)|N(p)\rangle$ evaluated at $t = 0$. However, there is another possibility for computing $\sigma(t = 0)$ and is based in the Hellmann-Feynman theorem (HF theorem) [118]. By applying this theorem to the chiral expansion of the nucleon mass calculated in Sec. 5.1.1, one can obtain the matrix element $\langle N|\hat{m}(\bar{u}u + \bar{d}d)|N\rangle$ that appears in Eq.(5.24) from the expression:

$$\sigma_{\pi N} = M_\pi^2 \frac{\partial m_N}{\partial M_\pi^2} \tag{5.25}$$

In this work we compute the explicit expression for $\sigma_{\pi N}$ up to $\mathcal{O}(q^3)$ in two ways. First, we calculate the scalar form factor of the nucleon up to $\mathcal{O}(q^3)$, as shown in Sec. 5.1.3 and evaluate it at $t = 0$. And second, we apply the HF theorem, Eq.(5.25), to the chiral expansion of the nucleon mass, Eq.(5.7). One can check that both results give the same expression which, as already shown in [45], is:

$$\sigma_{\pi N} = -4c_1 M_\pi^2 - \frac{3g_A^2 M_\pi^3}{16\pi^2 f_\pi^2 m_N}\left(\frac{3m_N^2 - M_\pi^2}{\sqrt{4m_N^2 - M_\pi^2}} \arccos\frac{M_\pi}{2m_N} + M_\pi \log\frac{M_\pi}{m_N}\right) \tag{5.26}$$

For the values of the LEC c_1 in Tables 5.1 and 5.4 we obtain the numbers for $\sigma_{\pi N}$ in the second and fourth rows of Table 5.13, respectively. In the last row, we give the results from the corresponding dispersive analyses. First, one sees that the strategy-II achieves a quite remarkable agreement within errors with the corresponding PWA result based on dispersion relations. Second, considering the values for Σ in Table 5.9, one recovers the $\mathcal{O}(q^3)$ ChPT result $\Sigma - \sigma_{\pi N} \approx$ 5–6 MeV, whereas the remaining 10 MeV, lost in the underestimation of Σ by an $\mathcal{O}(q^3)$ ChPT calculation, can be recovered in the $\mathcal{O}(q^4)$ calculation [19].

	KA85-I	WI08-I	EM06-I
$\sigma_{\pi N}$ (MeV)	78(5)	97(5)	95(2)
	KA85-II	WI08-II	EM06-II
$\sigma_{\pi N}$ (MeV)	39(2)	54(2)	59(1)
	KA85 [16]	WI08[17]	EM06[18]
$\sigma_{\pi N}$ (MeV)	45(8)	64(7)	56(9)

Table 5.13: Results for $\sigma_{\pi N}$ for the fits following the strategies I and II in Tables 5.1 and 5.4. We also give in the last row the values obtained in the dispersive studies referred.

In order to take into account the spread in c_1 due to the range of values for $\sqrt{s}_{max}$, we perform various fits with the $\Delta(1232)$ included explicitly varying $\sqrt{s}_{max}$ from 1.14 to 1.20 GeV in intervals of 10 MeV. This implies the following spreads in $\sigma_{\pi N}$ for the different PWAs: 39–48 MeV for KA85,

54–65 MeV for WI08 and 58–59 MeV for EM06. From these results we calculate the mean value and the standard deviation corresponding to each PWA fitted. The results are shown in Table 5.14, and confirm form ChPT the discrepancy between the values of $\sigma_{\pi N}$ obtained from dispersion relations employing the KA85 and WI08 solutions.

	Mean value KA85	Mean value WI08	Mean value EM06	KA85 [16]	WI08 [17]	EM06 [18]
c_1 (GeV^{-1})	$-0.80(6)$	$-1.00(4)$	$-1.00(1)$	–	–	–
c_2 (GeV^{-1})	1.12(13)	1.01(4)	0.58(3)	–	–	–
c_3 (GeV^{-1})	$-2.96(15)$	$-3.04(2)$	$-2.51(4)$	–	–	–
c_4 (GeV^{-1})	2.00(7)	2.02(1)	1.77(2)	–	–	–
$\sigma_{\pi N}$ (MeV)	43(5)	59(4)	59(2)	45(8)	64(7)	56(9)

Table 5.14: Mean values for $\sigma_{\pi N}$ for the different PWA taking into account the spread in $\sqrt{s}_{max}$.

Besides the error due to the spread in c_1, Eq.(5.25) carries a theoretical uncertainty coming form higher order contributions. We estimate them by computing the next subleading correction, at $\mathcal{O}(q^{7/2})$ in the δ-counting, which is given by a loop diagram with an insertion of a Δ propagator [134], see Fig. 5.13. This amounts to a contribution of -6 MeV to be compared with the one at $\mathcal{O}(q^3)$ of -19 MeV. It is important to stress that we take this correction as an irreducible uncertainty of our determination. In order to explicitly add this contribution to our present calculation, one should to include the same type of terms, arising from loops with one insertion of a Δ, into the πN scattering amplitude and take into account the changes in the LECs. Furthermore, we have evaluated the $\mathcal{O}(q^4)$ corrections given by the loop diagram of Fig. 5.14 using the result of [19][♯9] with insertion of the mean values for the $\mathcal{O}(q^2)$ LECs given in Table 5.14, and obtained an $\mathcal{O}(q^4)$ contribution which varies from -4 to -2 MeV. The contribution of the $\mathcal{O}(q^4)$ LECs, on the other hand, is estimated to be of approximately 1 MeV.[♯10] These results suggest a clear convergence pattern for the chiral expansion of $\sigma_{\pi N}$, as is shown in Table 5.15. They also confirm the hierarchy at low energies between the nucleon and Δ contributions that is implemented

[♯9] Although in Ref.[19] the IR prescription is used, for the diagram of Fig.5.14 both the IR and EOMS methods must give the same result because this loop does not include nucleonic propagators.

[♯10] Namely, only the LEC e_1 from $\mathcal{L}^{(4)}_{\pi N}$ (see Ref.[19] for definitions) contributes to $\sigma_{\pi N}$, and it is multiplied times a factor $2M_\pi^4$ (see Ref.[97]). Assigning a natural size of ($\sim$ 1 GeV^{-3}), we obtain $2e_1 M_\pi^4 \approx 1$ MeV.

in the δ-counting [134, 135].

	LO	NLO	N^{2}LO	N^{3}LO
$\sigma_{\pi N}$ (MeV)	78–62	-19	-6	$-3(2)$

Table 5.15: Convergence pattern of $\sigma_{\pi N}$. The LO results corresponds to the different values obtained from the c_1s displayed in Table 5.14.

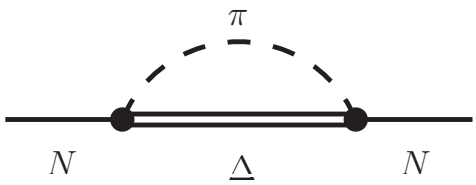

Figure 5.13: Diagram corresponding to the insertion of the Δ propagator (double line) in the nucleon self-energy. The dashed line is the pion propagator.

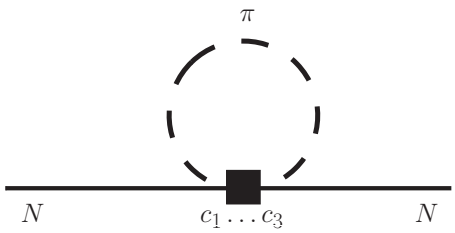

Figure 5.14: Diagram corresponding to the insertion of the $\mathcal{O}(q^2)$ vertices (square) in the nucleon self-energy.

We also want to stress the consistency between the results derived for the WI08 and EM06 PWAs, as shown in Table 5.14. This is very remarkable since, as pointed out before, these are quite different PW parameterizations that have in common the inclusion of the wealth of low-energy data collected along the last 20 years in meson and pion factories [17, 18], with many points not included in KA85 [16]. It is also remarkable that our mean value for $\sigma_{\pi N}$ from WI08 PWA also agrees with $\sigma_{\pi N} = 57(2)$ MeV that can be deduced from the Σ-term obtained in [136]. There, more sophisticated and reliable dispersive techniques were used on the earlier solution GWU06 of the George Washington University.

Another important and independent source of information comes from the pionic-atom data on a_{0+}^+. It has been noted before, in dispersive studies [130, 124, 131], that the sign of this observable is strongly correlated with the value of $\sigma_{\pi N}$. While the KA85 result of Table 5.14 is only compatible with the old negative results, it is not anymore with the recent positive values extracted from modern pionic-atom data and using improved approaches [25]. These are, on the other hand, compatible with the scattering data determinations obtained from the WI08 and the EM06 PWAs. However, one should take into account that the sign of a_{0+}^+ depends critically on the isospin breaking corrections which definitely require a systematic treatment that nowadays can only be given by effective field theory. In this regard, Ref.[25] obtains $a_{0+}^+ = (7.6 \pm 3.1)10^{-3} M_\pi^{-1}$ including isospin breaking corrections. Nevertheless, since the result of the different PWA rely on $\pi^+ p$ and $\pi^- p$ scattering data, it is more more reasonable to compare our a_{0+}^+ extracted from PWA with a scalar isoscalar scattering length computed from $\pi^+ p$ and $\pi^- p$ scattering, that we call $a_{\pi^+ p}^+$ and $a_{\pi^- p}^+$, respectively, including its isospin breaking corrections. Taking the values of $a_{\pi^+ p}^+$ and $a_{\pi^- p}^+$ from Ref.[25], we obtain $a_{0+}^+ = (a_{\pi^- p}^+ + a_{\pi^+ p}^+)/2 = (-1.0 \pm 0.9)10^{-3} M_\pi^{-1}$. Notice that this value is compatible with the modern analyses of WI08 and EM06, while the older solution of KA85 gives a value much smaller for that quantity (see Tables 5.3 and 5.6). The effect that a non-negative value of a_{0+}^+ has on $\sigma_{\pi N}$ was quantitatively studied by the George Washington University group concluding that a value of $a_{0+}^+ \gtrsim 0$ produces a raise on the sigma term of, at least, 7 MeV [124], which explains the correlation we observe between $a_{0+}^+ \gtrsim 0$ and a larger $\sigma_{\pi N}$.

Finally, we want to emphasize that only our results based in the WI08 PWA are perfectly compatible with all the phenomenology that can be extracted from independent experimental sources, while EM06 only fails in the reproduction of the $\Delta(1232)$ BW width. On the other hand we remind here that, besides the isoscalar scattering length just discussed above, the KA85 PWA gives rise to a value for h_A that is not compatible with the value obtained from the Breit-Wigner width (see Table 5.4). In addition, its result for $g_{\pi N}$ leads to a sizable violation of the GT relation, which is nowadays theoretically implausible [19]. Therefore, our results suggest that the modern πN scattering data studied within Lorentz covariant BChPT in the EOMS scheme up to $\mathcal{O}(q^3)$ in the δ-counting leads to:

$$\sigma_{\pi N} = 59(7) \text{ MeV} \tag{5.27}$$

The error includes the higher-order uncertainty estimated above added in quadrature with the one given by the dispersion of the values in the average

of the WI08 and EM06 mean values displayed in Table 5.14. Had we included the KA85 mean value in this estimation, the result would be slightly reduced by 2–3 MeV.

Another source of information on $\sigma_{\pi N}$ comes from $\mathrm{Re}D^+(\nu, t = 0)$, that can be extracted from $\pi^+ p$ and $\pi^- p$ experimental cross sections [137, 138]. We have checked that the inclusion in our fits of the electromagnetically corrected data of [138] provided by [139] tends to lower the value of $\sigma_{\pi N}$ around 5–10 MeV. However, the inclusion of these new data in fits together with the PWA phase shifts already considered, push the values of a^+_{0+} to the negative side, which are then in disagreement with the modern result of pionic-atom $a^+_{0+} \gtrsim 0$ [25]. If one fits only the data of Ref.[139], a value of $a^+_{0+} = (-1.7 \pm 1.9)10^{-2} M_\pi^{-1}$ results. Although this value is compatible with the results of the three PWAs, its large error prevent us to make any conclusion. However, it is clear from both methods (with and without PWA data), that the data of Ref.[139] point towards a negative a^+_{0+}.

It is important to stress the fact that this relatively large value for $\sigma_{\pi N}$ is not necessary in contradiction with some phenomenology related to the strangeness content of the nucleon or chiral approaches to nuclear matter [45]. For the first one, is known that ChPT provides a $SU(3)_F$ breaking of the baryon-octet masses that allows to relate $\sigma_{\pi N}$ to the strangeness content of the nucleon y [140, 141]. If one calculates this relation using HBChPT up to $\mathcal{O}(q^4)$ without the inclusion of the decuplet resonances, a relatively large $\sigma_{\pi N} \simeq 60$ MeV implies a strange quark contribution to the nucleon mass of several hundreds of MeV, which is a scenario very hard to understand. However, it has been observed that the effect of the decuplet resonances largely cancel those of the octet [116, 142], being able to reconcile a relatively large $\sigma_{\pi N}$ with a negligible strangeness in the nucleon.

In what concerns to the chiral approaches of nuclear matter, we remind here that $\rho\, \sigma_{\pi N}$ controls the leading contribution in density (ρ) of the quark in-medium condensate. At this order, a value of $\sigma_{\pi N} \simeq 60$ MeV would imply a vanishing in-medium quark condensate already at $\simeq 2\rho_0$ (with ρ_0 the nuclear saturation density), while this occurs at a density of $\simeq 3\rho_0$ using $\sigma_{\pi N} \simeq 45$ MeV. However, to have a spontaneous breaking of chiral symmetry it is mandatory a non-vanishing temporal component of the pion axial coupling f_t [143]. On the other hand, the leading contribution to f_t is controlled by $c_2 + c_3$, which is a combination not related to $\sigma_{\pi N}$ at this order. Using the results of Table 5.14, we have a difference of only a 10% between the set of KA85 and WI08, which means that the running with density for f_t as obtained in [143] (which also includes NN interactions), differs also on a 10%. This figure is much smaller than the difference of around a 30% in

density dependence of the quark condensate due to the different values of $\sigma_{\pi N}$ [143]. As a result, the vanishing of f_t, as calculated within in-medium ChPT [143], occurs at around $3.5\rho_0$ for both PWAs. A more thorough analysis is necessary to put in agreement the simultaneous vanishing of f_t and the quark condensate with density in order to properly discuss about chiral symmetry restoration in nuclear matter.

5.7 Unitarized amplitudes

Another important comparison between the covariant schemes EOMS and IR comprises their behavior under unitarization techniques. These techniques take care of the analyticity properties associated with the right-hand cut and have proved to be very successful in the description of non-perturbative phenomena with ChPT [88, 89]. It was shown in Ref.[21] that the unphysical cut introduced by IR spoils the description of the phase shifts for energies $\sqrt{s} \gtrsim 1.26$ GeV.

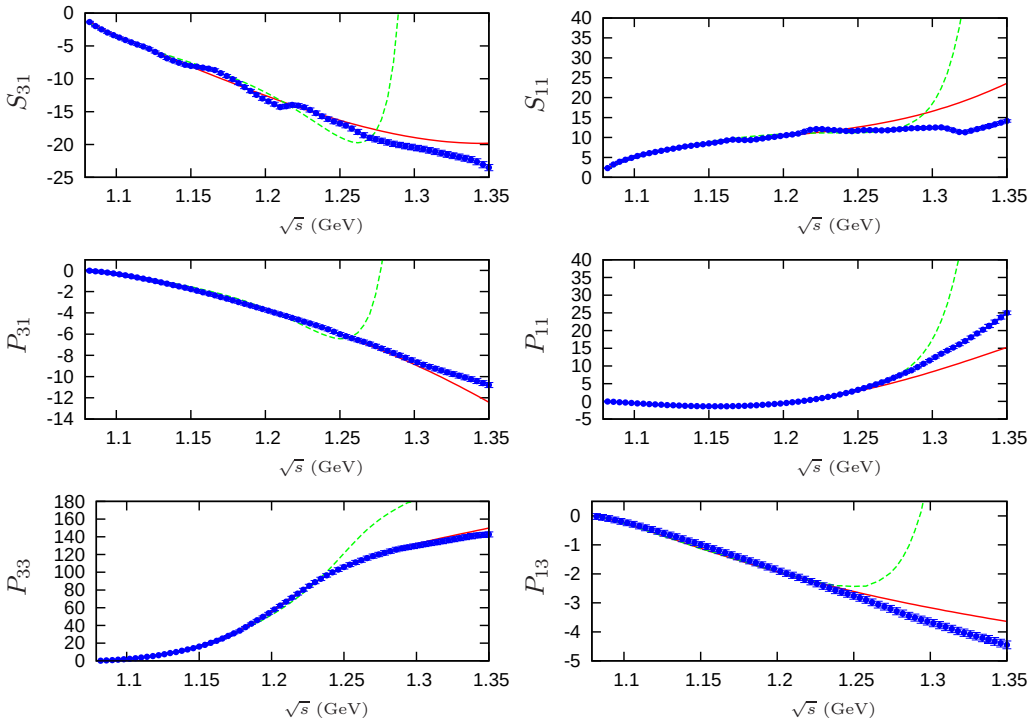

Figure 5.15: Unitarized fits performed up to $\sqrt{s}_{max} = 1.3$ GeV to the KA85 solution. Solid line: EOMS. Dashed line: IR [21] (or Chapter 4).

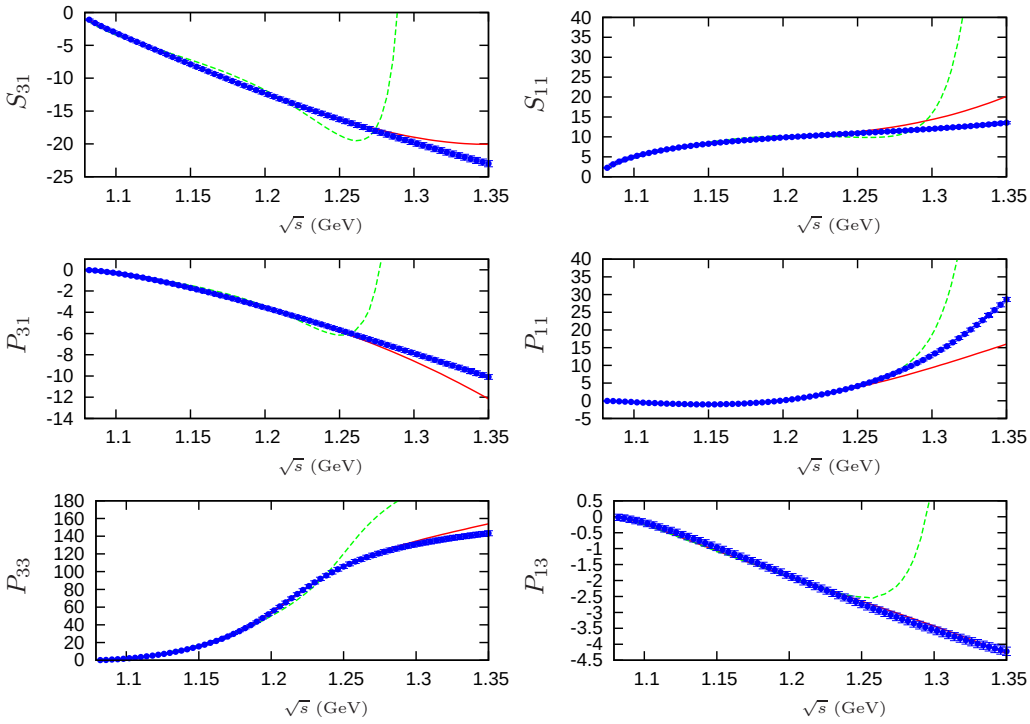

Figure 5.16: Unitarized fits performed up to $\sqrt{s}_{max} = 1.3$ GeV to the WI08 solution. Solid line: EOMS. Dashed line: IR [21] (or Chapter 4).

Since the EOMS scheme has the right analytical properties, it is interesting to see the potential of the unitarization techniques applied on a well behaved kernel. As in [21], and in order to compare with IR, we use the unitarization method of Refs.[90, 98, 92] and introduce a Castillejo-Dalitz-Dyson pole (CDD) to take into account of the contribution of the $\Delta(1232)$ in the P_{33} partial wave. This corresponds to unitarize the amplitude of strategy-I, supplemented by the CDD in the P_{33} channel to take into account the contribution of the $\Delta(1232)$-resonance.

$$T_{IJ\ell}(s) = \frac{1}{\mathcal{T}_{IJ\ell}(s)^{-1} + g(s)} \qquad \text{for } I \neq 3/2 \text{ and } J \neq 3/2$$

$$T_{IJ\ell}(s) = \left(\mathcal{T}_{IJ\ell}(s)^{-1} + \frac{\gamma}{s - s_P} + g(s)\right)^{-1} \qquad \text{for } I = 3/2 \text{ and } J = 3/2$$

Where $T_{IJ\ell}$ is the unitarized amplitude, $\mathcal{T}_{IJ\ell}$ the interaction kernel, $g(s)$ the unitary pion-nucleon loop function and γ and s_P are the residue and pole position of the CDD pole, respectively. We refer the reader to Sec. 4.6 of

Chapter 4 or Ref.[21] for further details on the definitions. We show in Figs. 5.15 and 5.16 the fits of the unitarized amplitudes to KA85 and WI08 PWAs (solid line), and the previous result obtained within the IR scheme (dashed line). We do not consider the points of EM06 because this is a low energy analysis that only reach to $\sqrt{s} \approx 1.16$ GeV.

The EOMS fits are performed up to energies of $\sqrt{s} = 1.3$ GeV and achieve a very good description of data up to energies of $\sqrt{s} = 1.35$ GeV, being better the description of the WI08 phase shifts. Moreover, thanks to the CDD pole, the P_{33} partial wave is described almost perfectly up to 1.35 GeV for both PWAs. From Figs. 5.15 and 5.16 it is also easy to see how the unphysical cut of IR affects the description of the phase shifts giving rise to sharp rises at around $\sqrt{s} \approx 1.26$ GeV. This is clearly absent in the results obtained by the present calculation because the EOMS kernel has the right analytical properties. A much better description of data is then achieved.

5.8 Summary and Conclusions

In this chapter we have performed a novel calculation in Lorentz covariant BChPT within the EOMS scheme up to $\mathcal{O}(q^3)$ in the chiral expansion. Unlike IR, this scheme allow us to work with scale-independent renormalized amplitudes that are free from unphysical cuts and have the right analytical and causality properties [71]. Our calculations are done first without including the $\Delta(1232)$ resonance (this is called strategy-I), and including it as an explicit degree of freedom later (strategy-II). In order to fix the LECs and extract physical information we considered the solutions KA85 [16], WI08 [17] and EM06 [18] coming from different partial wave analyses. We showed that, without the inclusion of the $\Delta(1232)$, EOMS shows a better description of the phase shifts than IR [21] (lower $\chi^2_{d.o.f.}$). The former also gives rise to values of the threshold parameters that are compatible with their corresponding PWAs results. On the other hand, the LECs obtained in this case are compatible with previous determinations of HBChPT [63] and IR [21]. The first remarkable result of this chapter concerns to the Goldberger-Treiman deviation Δ_{GT}. Here we showed that EOMS can extract from data values for this quantity that are compatible with the present experimental information. This solves a long standing problem that appeared in earlier covariant IR renormalized analyses of πN scattering which jeopardized the applicability of ChPT to this system. On the other hand, the convergence of the chiral series is considerably improved once the $\Delta(1232)$ is included as an explicit degree of freedom (strategy-II). In this case we are able to reproduce the S- and P-wave phase shifts up to energies of $\sqrt{s} = 1.20$ GeV

obtaining more natural values for the LECs. With this extracted values we could, for first time in ChPT, extrapolate our chiral amplitudes to the subthreshold region and extract subthreshold quantities that are compatible with their corresponding PWA values. This means that we can connect, within EOMS-BChPT with the $\Delta(1232)$ resonance, the physical information with subthreshold quantities, which answers a long standing question on the convergence of the chiral series above threshold [19]. This good convergence allows us to extract accurately and reliably the value of the pion-nucleon sigma term $\sigma_{\pi N}$ by fitting our amplitude to scattering data from three different PWAs. It is remarkable that our covariant BChPT study gives results for $\sigma_{\pi N}$ which are in agreement with their corresponding PWA, which use dispersive methods. Our analysis, that takes into account independent phenomenology, shows that modern data favor a relatively large value of $\sigma_{\pi N}$. We report the value $\sigma_{\pi N} = 59(7)$ MeV.

All these results show that EOMS-BChPT achieves the best convergence for the πN system in ChPT, and that this convergence can be considerably improved once we include the $\Delta(1232)$ as an explicit degree of freedom. Finally, we tested our EOMS-BChPT $\mathcal{O}(q^3)$ kernel with the same unitarization techniques used in [21] with IR-BChPT at $\mathcal{O}(q^3)$. We show that our EOMS calculation achieves much better description of the phase shifts, being able to reproduce them up to energies of $\sqrt{s} = 1.35$ GeV, which is 100 MeV higher than the IR description [21]. This is thanks to the good analytical properties of this kernel, that follows the standard power counting of ChPT without changing the analytical properties of a covariant calculation.

Chapter 6

$\phi(1020)f_0(980)$ and $\phi(1020)a_0(980)$ S-wave scattering and the $Y(2175)$ resonance

In recent years, the existence of a new resonance, the $Y(2175)$, with quantum numbers $J^{PC} = 1^{--}$ and mass around 2.15 GeV has been revealed by several experiments. The $Y(2175)$ was first observed in the reaction $e^+e^- \to \phi(1020)f_0(980)$ by the BABAR Collaboration [144, 145]. Its mass and width were determined to be $M_Y = 2.175 \pm 0.010 \pm 0.015$ GeV and $\Gamma_Y = 0.058 \pm 0.016 \pm 0.020$ GeV [144]. It was then observed in $e^+e^- \to \phi(1020)\eta$ by the same collaboration [146], though with much less statistical significance, and in $J/\Psi \to \eta\phi(1020)f_0(980)$ by BES [147] with $M_Y = 2.186 \pm 0.010(\text{stat}) \pm 0.006(\text{syst})$ GeV and $\Gamma_Y = 0.065 \pm 0.023(\text{stat}) \pm 0.017(\text{syst})$ GeV. The Belle Collaboration [148] has also identified the $Y(2175)$ in the most precise study so far of the reactions $e^+e^- \to \phi(1020)\pi^+\pi^-$ and $e^+e^- \to \phi(1020)f_0(980)$. The resulting resonance parameters are $M_Y = 2.13^{+0.07}_{-0.12}$ GeV and $\Gamma_Y = 0.17^{+0.11}_{-0.09}$ GeV. The large errors reflect, among other sources of systematic error, the uncertainties in the determination of the non-resonant background and the possible existence of additional resonances in the vicinity of the $Y(2175)$. In Ref.[145] an extensive study of the reaction $e^+e^- \to K^+K^-f_0(980)$, with the $f_0(980)$ reconstructed from the $\pi^+\pi^-$ or $\pi^0\pi^0$ signals, is also given. It shows an even more prominent $Y(2175)$ signal than the $\phi(1020)f_0(980)$ data. The resulting masses then spread in the range 2.12–2.21 GeV and the width between 0.045–0.13 GeV, taking into account both central values and the one sigma deviation from them.

These experimental findings have renewed the theoretical interest in the region of the $Y(2175)$. It has been suggested that this resonance could be a tetraquark state [149, 150, 151]. A QCD sum rule calculation taking into account the correlator $(s\bar{s})(s\bar{s})$ between the meson-meson currents is performed

in Ref.[149] obtaining $M_Y = 2.21 \pm 0.09$ GeV. Both standard and finite energy QCD sum rules are considered in Ref.[150] with meson-meson and diquark-antidiquark $(ss)(\bar{s}\bar{s})$ currents. The mass value obtained is 2.3 ± 0.4 GeV. Quark models have also been used to address the nature and properties of this resonance. Ref.[152] studies the decay modes of the lightest hybrid $s\bar{s}g$ resonance, whose mass was predicted to be in the range 2.1-2.2 GeV [153, 154], consistently with that of the $Y(2175)$. Its width is estimated to be around 100-150 MeV [152]. The identification of the $Y(2175)$ as the quarkonium $(s\bar{s})$ states 2^3D_1 and 3^3S_1[♯1], whose masses have also been predicted to be close to that of the $Y(2175)$ [155], has been considered in Ref.[156]. The 3^3S_1 assignment is disfavored due to its expected large width, $\Gamma \simeq 0.38$ GeV [157], while the width of a 2^3D_1 state is estimated in the range 0.15-0.21 GeV [156]. It is argued that the clearly different decay patterns could be used to distinguish between the 2^3D_1 $\bar{s}s$ and the hybrid $s\bar{s}g$ descriptions [152, 156]. Instead, Ref.[151] concludes that the diquark-antidiquark picture for the $Y(2175)$ would be characterized by a prominent $\Lambda\bar{\Lambda}$ decay mode. A Faddeev-type calculation for the $\phi(1020)K\bar{K}$ system is presented in Ref.[40] where the interactions between pseudoscalar-pseudoscalar and vector-pseudoscalar mesons are taken from unitarized Chiral Perturbation Theory (Refs.[158] and [159], respectively). Remarkably, a peak in the $\phi(1020)K\bar{K}$ strong amplitude is obtained at the mass of the $Y(2175)$, though the width, around 20 MeV, is too small. This study indicates that the $Y(2175)$ might have large components corresponding to a resonant $\phi(1020)K\bar{K}$ state.

In Sec. 6.2 we present our study of the S-wave scattering amplitude of the $\phi(1020)f_0(980)$ system around its threshold [41]. This is feasible because both the $\phi(1020)$ and the $f_0(980)$ are rather narrow resonances. We investigate this process from the theoretical point of view by first deriving the interaction kernel for $\phi(1020)f_0(980)$ and then the scattering amplitude. In this way, by construction, one can distinguish the $\phi(1020)f_0(980)$ 1^{--} dynamically generated bound states or resonances from others pre-existing states or due to genuine three body effects in $\phi(1020)K\bar{K}$ scattering. The needed formalism is elaborated and discussed in Sec. 6.2. We discuss the appearance of a $\phi(1020)f_0(980)$ resonance with mass and width compatible with those reported for the $Y(2175)$ [144, 145, 148] in Sec. 6.2.2. We also reproduce the data on $e^+e^- \to \phi(1020)f_0(980)$ from the same set of references.

Later, in Sec. 6.3, we present our investigations concerning to the possibility of an isovector companion of the isoscalar $Y(2175)$ [46]. Such an investigation will help constraining theoretical models and their parameters,

[♯1]The spectroscopic notation $n^{2S+1}L_J$ corresponds to the n^{th} state with spin S, orbital momentum L and total angular momentum J.

leading to a better understanding of meson properties in the energy region around 2 GeV. In particular, the Faddeev-type calculation of Ref.[40] that obtains the $Y(2175)$ as a dynamically generated state finds no resonance in the isovector $\phi(1020)a_0(980)$ S-wave channel. Experimentally, this isovector resonance could show up in $e^+e^- \to \phi(1020)a_0(980) \to \phi(1020)\pi^0\eta$, as suggested in a recent theoretical study of this process [160]. It could also be observed in the $e^+e^- \to \phi(1020)K^+K^-$ reaction because the $a_0(980)$ couples strongly to K^+K^- [161]. One should stress that the calculations of Refs.[160, 161] do not take into account $\phi(1020)a_0(980)$ final state interactions (FSI) which, resonant or not, could be large and have a sizable impact on the predicted cross sections.

We apply the formalism of Sec. 6.2 to the S-wave $\phi(1020)a_0(980)$ scattering and discuss the possible presence of an isovector $J^{PC} = 1^{--}$ dynamically generated resonance around the $\phi(1020)a_0(980)$ threshold for parameters that satisfactorily describe the isoscalar $\phi(1020)f_0(980)$ channel. FSI corrections to the process $e^+e^- \to \phi(1020)a_0(980) \to \phi(1020)\pi^0\eta$ are also studied. The formalism for $\phi(1020)a_0(980)$ scattering is developed in Sec. 6.3 followed by the derivation of the scattering amplitudes. Sec. 6.3.1 contains the results and discussions thereof. Finally, our concluding remarks are given in Sec. 6.4.

6.1 Formalism

We obtain the different vertices required to determine the $\phi K\bar{K}$ scattering from the lowest order $SU(3)$ chiral Lagrangian [162]:

$$\mathcal{L}_2 = \frac{f^2}{4}\mathrm{Tr}\left(D_\mu U^\dagger D^\mu U + \chi^\dagger U + \chi U^\dagger\right) \tag{6.1}$$

With f the pion weak decay constant in the chiral limit, that we approximate to $f_\pi = 92.4$ MeV. The octet of the lightest pseudoscalar fields are included in U as:

$$\begin{aligned} U &= \exp\left(i\frac{\sqrt{2}\Phi}{f}\right) \\ \Phi &= \frac{1}{\sqrt{2}}\sum_{i=1}^{8}\phi_i\lambda_i = \begin{pmatrix} \frac{\pi^0}{\sqrt{2}} + \frac{1}{\sqrt{6}}\eta_8 & \pi^+ & K^+ \\ \pi^- & -\frac{\pi^0}{\sqrt{2}} + \frac{1}{\sqrt{6}}\eta_8 & K^0 \\ K^- & \overline{K}^0 & -\frac{2}{\sqrt{6}}\eta_8 \end{pmatrix} \end{aligned} \tag{6.2}$$

The covariant derivative with external sources, $D_\mu U$, is given by:

$$D_\mu U = \partial_\mu U - i r_\mu U + i U \ell_\mu \,, \tag{6.3}$$

With r_μ and ℓ_μ external right and left fields related to the vector (v_μ) and axial-vector (a_μ) fields by:

$$\begin{aligned} r_\mu &= v_\mu + a_\mu \,, \\ \ell_\mu &= v_\mu - a_\mu \,, \end{aligned} \tag{6.4}$$

This is a generalization of Eq.(2.105) including couplings to external field which are invariant under *local* chiral transformations. The local invariance is important since the chiral Ward identities originating in the global $SU(N_f)_L \times SU(N_f)_R$ symmetry of QCD are obtained from a generating functional invariant under local transformations of the external fields [30, 33]. It is easy to see that if ℓ_μ and r_μ transform under $SU(3)_L \times SU(3)_R$ as:

$$r_\mu \to R\, r_\mu\, R^\dagger \tag{6.5}$$

$$\ell_\mu \to L\, \ell_\mu\, L^\dagger \tag{6.6}$$

Then, under a local chiral transformation, Eq.(6.3) transforms as:

$$D_\mu U \to R(x)(D_\mu U)L^\dagger(x) \tag{6.7}$$

In the following we identify the external vector fields v_μ with the lightest octet of vector resonances, and the vertices are then determined assuming minimal coupling. This is a generalization of the way in which vector mesons are introduced in vector meson dominance [163, 164, 165]. Here we are only interested in the vector fields:

$$r_\mu = g\, v_\mu \;,\; \ell_\mu = g\, v_\mu \,. \tag{6.8}$$

Where g is a universal coupling constant. We assume ideal mixing, in terms of which $\phi = -\sqrt{\frac{2}{3}}\omega_8 + \frac{1}{\sqrt{3}}\omega_1$ and $\omega = \frac{1}{\sqrt{3}}\omega_8 + \sqrt{\frac{2}{3}}\omega_1$, with ω_8 and ω_1 the $I = 0$ octet and singlet vector states, in that order. Whence:

$$v_\mu = \begin{pmatrix} \frac{\rho^0}{\sqrt{2}} + \frac{1}{\sqrt{2}}\omega & \rho^+ & K^{*+} \\ \rho^- & -\frac{\rho^0}{\sqrt{2}} + \frac{1}{\sqrt{2}}\omega & K^{*0} \\ K^{*-} & \overline{K}^{*0} & \phi \end{pmatrix}_\mu \tag{6.9}$$

As a result, the following couplings involving vector and pseudoscalar mesons arise:

$$\begin{aligned}
\mathcal{L}_{V^2\Phi^2} &= g^2\mathrm{Tr}\left(v_\mu v^\mu\Phi^2 - v_\mu\Phi v^\mu\Phi\right)\\
\mathcal{L}_{V^2\Phi^4} &= -\frac{g^2}{6f^2}\mathrm{Tr}\left(v_\mu v^\mu\Phi^4 - 4v_\mu\Phi^3 v^\mu\Phi + 3v_\mu\Phi^2 v^\mu\Phi^2\right)\\
\mathcal{L}_{V\Phi^2} &= -ig\mathrm{Tr}\left(v_\mu\Phi\partial^\mu\Phi - v_\mu\partial^\mu\Phi\Phi\right)\\
\mathcal{L}_{\Phi^4} &= -\frac{1}{6f^2}\mathrm{Tr}\left(\partial_\mu\Phi\partial^\mu\Phi\Phi^2 - \partial_\mu\Phi\Phi\partial^\mu\Phi\Phi - \frac{1}{2}M\Phi^4\right)
\end{aligned} \tag{6.10}$$

Where $M = diag(m_\pi^2, m_\pi^2, 2m_K^2 - m_\pi^2)$ and m_π and m_K the pion and kaon masses. In addition there are vertices of three and four vectors fields which originate from:

$$\mathcal{L}_{free} = -\frac{1}{4}\mathrm{Tr}\left(F_{\mu\nu}F^{\mu\nu}\right) \tag{6.11}$$

With the strength tensor:

$$F_{\mu\nu} = \partial_\mu v_\nu - \partial_\nu v_\mu - ig[v_\mu, v_\nu] \tag{6.12}$$

The resulting couplings involving three and four vector mesons are:

$$\begin{aligned}
\mathcal{L}_{V^3} &= ig\mathrm{Tr}\left(\partial_\mu v_\nu[v^\mu, v^\nu]\right)\\
\mathcal{L}_{V^4} &= \frac{1}{2}g^2\mathrm{Tr}\left(v_\mu v_\nu[v^\mu, v^\nu]\right)
\end{aligned} \tag{6.13}$$

6.2 $\phi(1020)$ $f_0(980)$ scattering

We first work out the scattering of the $\phi(1020)$ with a $K\bar{K}$ state of isospin (I) zero, denoted as $|K\bar{K}\rangle_0$. Then, we take take advantage of the fact that the $f_0(980)$ scalar meson is successfully described as a $|K\bar{K}\rangle_0$ bound state [158, 166, 167]. Therefore, the $\phi(1020)f_0(980)$ scattering can be determined from the $\phi(1020)K\bar{K}$ one by extracting the residue at the $f_0(980)$ double pole position that arises from the initial and final $|K\bar{K}\rangle_0$ states.

The diagrams that contribute to $\phi K\bar{K} \to \phi K\bar{K}$ from the Lagrangians of Eqs.(6.10) and (6.13) are depicted in Fig. 6.1. Both S- and D-waves

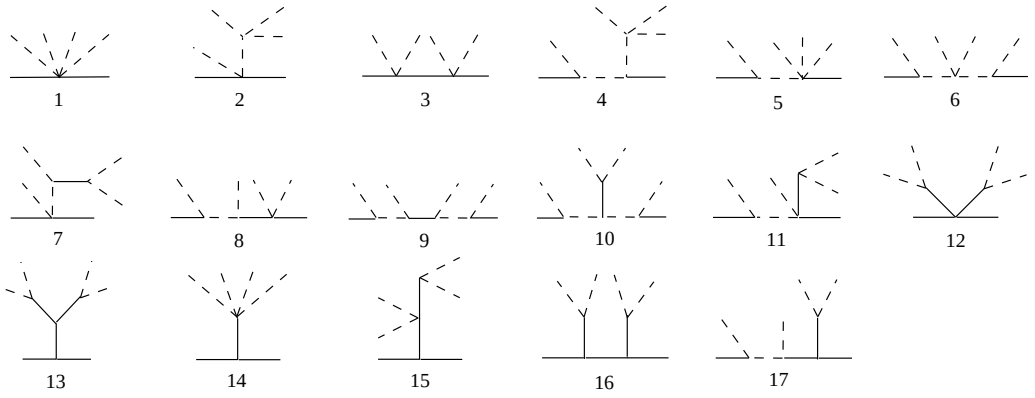

Figure 6.1: Feynman diagrams for $\phi K\bar{K}$ scattering that result from the Lagrangians of Eqs.(6.10) and (6.13). The dashed lines denote kaons and the solid ones vector mesons (ϕ or ρ_0).

contribute to the $\phi(1020)f_0(980)$ scattering in the 1^{--} channel but since we are interested in the threshold region around 2 GeV, the D-wave terms can be neglected. They are suppressed by powers of $|\mathbf{p}|^{2n}$, where $|\mathbf{p}|$ is the three momentum in the center of mass (CM) of the $\phi(1020)f_0(980)$ pair and $n = 1, 2$ is the number of possible D-wave $\phi(1020)f_0(980)$ states in both the initial and final scattering states. It is also worth stressing that since the $f_0(980)$ is so close to the $K\bar{K}$ threshold, the three-momentum $\mathbf{q}$ of the kaons in the rest frame of the $f_0(980)$ is small compared to the kaon masses. In this way, a suppression by powers of $|\mathbf{q}|$ and $|\mathbf{p}|$ can be used to simplify the calculation of the $\phi K\bar{K}$ scattering. On the contrary, the appearance of almost on-shell intermediate mesons enhances some diagrams with respect to the rest. Joining both conditions we find that the set of amplitudes represented by the diagram 2 of Fig. 6.1 are dominant because the contributing vertices do not involve any small three-momentum and the intermediate kaon is almost on-shell. In addition, these diagrams involve an extra large numerical factor because the four-kaon vertex is around $M_{f_0}^2/f^2 \simeq 10^2$, with M_{f_0} the $f_0(980)$ mass. This factor is much larger than the one of a $\phi\phi KK$ vertex, which scales as g^2. Such a vertex appears twice in diagram 3 and once in 2. In spite of the fact that the ϕ propagator in diagram 3 is close to its mass shell when one kaon is going in and the other out in each of the vertices, the resulting amplitude is suppressed by more than one order of magnitude with respect to the one from diagram 2 because, $(M_{f_0}^2/f^2)/g^2$ is large, and also because it involves less enhanced configurations than the diagram 2.[♯2]

[♯2] An explicit calculation shows that the suppression factor is the inverse of $6M_{f_0}^2/g^2f^2 \simeq 30$ for $|g| \simeq 5$.

Following similar steps we show in Appendix H that the rest of diagrams in Fig. 6.1 are suppressed compared with the second one.

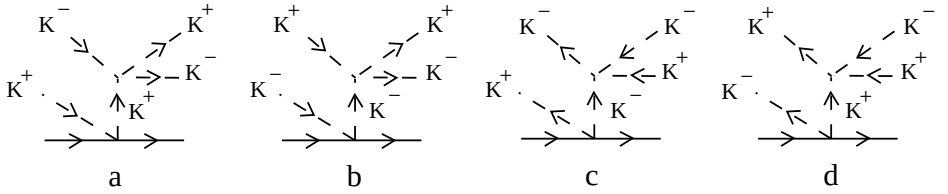

Figure 6.2: All possible arrangements of kaons in the $\phi(p_1)\,K^+(k_1)\,K^-(k_2) \to \phi(p_1')\,K^+(k_1')\,K^-(k_2')$ scattering from the second diagram of Fig. 6.1 are shown.

Let us proceed with the evaluation of the contribution from diagram 2 of Fig. 6.1 to the $\phi(p_1)\,K^+(k_1), K^-(k_2) \to \phi(p_1')\,K^+(k_1')\,K^-(k_2')$ scattering represented by the diagrams in Fig. 6.2. We consider first the $K^+(k)\,K^-(k_2) \to K^+(k_1')\,K^-(k_2')$ amplitude that corresponds to the vertex on the top of Fig. 6.2(a), with k the momentum of the intermediate kaon. Using $\mathcal{L}_{\Phi^4}$ it can be cast as:

$$T^{(a)}_{K^+K^-\to K^+K^-} = -\frac{u_a - 2m_K^2}{f^2} - \frac{m_K^2 - k^2}{3f^2} \tag{6.14}$$

With $u_a = (k_1' - k_2)^2$. Here the off shell part, which is proportional to the inverse of the kaon propagator, has been explicitly separated; it leads to a contact term in the full amplitude of diagram (a). Proceeding analogously with the other three diagrams in Fig. 6.2 and summing all the contributions it results:

$$\begin{aligned} T_{cc} = &-\frac{8g^2\epsilon\cdot\epsilon'}{3f^2} - \frac{2g^2\epsilon\cdot\epsilon'}{f^2}(u_a - 2m_K^2)\Big[D(Q+k_1) + D(Q-k_2')\Big] \\ &- \frac{2g^2\epsilon\cdot\epsilon'}{f^2}(u_b - 2m_K^2)\Big[D(Q+k_2) + D(Q-k_1')\Big] \end{aligned} \tag{6.15}$$

Where ϵ (ϵ') is the polarization four-vector of the initial (final) ϕ meson, $u_b = (k_2' - k_1)^2$ and $Q = p - p'$. The kaon propagator is given by:

$$D(k) = \frac{1}{m_K^2 - k^2 - i\varepsilon} \tag{6.16}$$

With $\varepsilon \to 0^+$. The subscript cc in T_{cc} indicates that all the kaons are charged. The amplitudes for the $\phi(p_1)\,K^0(k_1)\,\bar{K}^0(k_2) \to \phi(p_1')\,K^+(k_1')\,K^-(k_2')$

and $\phi(p_1)\,K^0(k_1)\,\bar{K}^0(k_2) \to \phi(p_1')\,K^0(k_1')\,\bar{K}^0(k_2')$ reaction channels correspond to diagrams analogous to those in Fig. 6.2. Denoting them as T_{nc} and T_{nn}, respectively, they read:

$$T_{nc} = \frac{1}{2}T_{cc}, \qquad\qquad T_{nn} = T_{cc} \tag{6.17}$$

Here we have assumed an exact isospin symmetry and used the same values for the masses of charged and neutral kaons. Note then that the scattering amplitude for $\phi(p_1)\,K^+(k_1)\,K^-(k_2) \to \phi(p_1')\,K^0(k_1')\,\bar{K}^0(k_2')$, T_{cn}, can be obtained from T_{nc} by crossing symmetry and indeed $T_{cn} = T_{nc}$ since the u variables are not altered in the transformation.

To construct the $I = 0$ amplitude we take into account that $|K\bar{K}\rangle_0$ is:

$$|K(\mathbf{q}_1)\bar{K}(\mathbf{q}_2)\rangle_0 = -\frac{1}{\sqrt{2}}|K^+(\mathbf{q}_1)K^-(\mathbf{q}_2) + K^0(\mathbf{q}_1)\bar{K}^0(\mathbf{q}_2)\rangle \tag{6.18}$$

The minus sign appears because we identify $|K^-\rangle = -|I = 1/2, I_3 = -1/2\rangle$ to be consistent with the convention adopted in the chiral Lagrangians, Eq.(6.2). Therefore, the resulting $\phi(1020)|K\bar{K}\rangle_0 \to \phi(1020)|K\bar{K}\rangle_0$ scattering amplitude from diagram 2 of Fig. 6.1, $T^{(2)}_{I=0}$, is:

$$T^{(2)}_{I=0} = \frac{1}{2}\left\{T_{cc} + T_{nn} + T_{cn} + T_{nc}\right\} = \frac{3}{2}T_{cc} \tag{6.19}$$

The contact term in Eq.(6.15) cannot be separated from the one arising from diagram 1 of Fig. 6.1 in a model independent way so we consider this smaller contribution as well. From $\mathcal{L}_{2V\Phi^4}$ in Eq.(6.10) one has:

$$\mathcal{L}_{\phi^2(K\bar{K})^2} = -\frac{2g^2}{3f^2}\phi_\mu\phi^\mu(K^+K^- + K^0\bar{K}^0)^2 \tag{6.20}$$

The resulting contact term, when projected into the $I = 0$ channel taking into account Eq.(6.19) gives:

$$T^{(1)}_{I=0} = -\frac{8g^2}{f^2}\epsilon\cdot\epsilon' \tag{6.21}$$

Therefore, the resulting $\phi|K\bar{K}\rangle_0 \to \phi|K\bar{K}\rangle_0$ scattering amplitude from the first two diagrams in Fig. 6.1 is:

$$\begin{aligned} T_{I=0} = \frac{6g^2}{f^2}\epsilon\cdot\epsilon'\Big\{&-2 + k_2\cdot k_1'\big[D(Q+k_1) + D(Q-k_2')\big] \\ &+ k_1\cdot k_2'\big[D(Q+k_2) + D(Q-k_1')\big]\Big\} \end{aligned} \tag{6.22}$$

6.2.1 Extracting the $f_0(980)$ poles

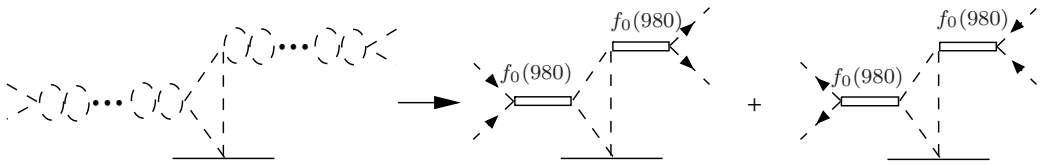

Figure 6.3: The two $f_0(980)$ poles originate because of the $K\bar{K}$ interactions. The kaons and anti-kaons are indicated by the dashed lines.

The $K\bar{K}$ pairs re-scatter giving rise to the diagram shown on the left hand side of Fig. 6.3. The resulting infinite chain of diagrams contains the poles of the initial and final $f_0(980)$ resonances, as depicted on the right side of the figure. The residue at the $f_0(980)$ double pole is the $f_0(980)\phi(1020)$ potential $V_{\phi f_0}$. Close to threshold, the two kaons, initial or final, interact predominantly in S-wave. The $K\bar{K}$ $I = 0$ S-wave amplitude from $\mathcal{L}_{\Phi^4}$, Eq.(6.10), is [158]:

$$V_{K\bar{K}}^{\text{full}}(s_{K\bar{K}}) = \frac{3s_{K\bar{K}}}{4f^2} - \frac{1}{4f^2}\sum_i \left(r_i^2 - m_K^2\right) \tag{6.23}$$

Where $s_{K\bar{K}}$ stands for the invariant mass of the two kaons. The sum runs over all the four kaon states involved in the vertex whose four-momenta are denoted by r_i. The last term is the off-shell part of the amplitude. We use Eq.(6.23) in the four-pseudoscalar vertices of the diagrams in Fig. 6.4, where $k = k_1 + k_2$ and $k' = k_1' + k_2'$ are the total four-momenta of the initial and final $|K\bar{K}\rangle_0$ states, respectively. At the $f_0(980)$ double pole $k^2 = k'^2 = M_{f_0}^2$. A K^+ or K^0 runs in the loop of the diagrams in Fig. 6.4. Taking into account that the $K^+K^- \to |K\bar{K}\rangle_0$ and $K^0\bar{K}^0 \to |K\bar{K}\rangle_0$ vertices are equal to $-\sqrt{1/2}\,V_{K\bar{K}}^{full}$ one gets the same result for the four amplitudes represented in Fig. 6.4.

The off-shell parts comprised in the last term of Eq.(6.23), are equal to the inverse of kaon propagators. In the loops of Fig. 6.4 they cancel with the kaon propagators giving rise to amplitudes that do not correspond anymore to the dominant triangular kaon-loop but to other topologies so that we disregard them. Therefore, we obtain for the sum of the diagrams in Fig. 6.4:

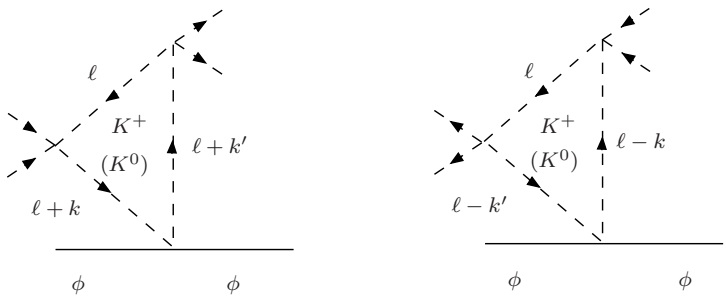

Figure 6.4: Triangular kaon-loop graphs with a K^+ or a K^0 running in the loop. All the diagrams give the same result.

$$\begin{aligned}\mathcal{M} &= 4\epsilon\cdot\epsilon' g^2 V_{K\bar{K}}(k^2)V_{K\bar{K}}(k'^2)\\ &\times i\int\frac{d^4\ell}{(2\pi)^4}\frac{1}{[\ell^2-m_K^2+i\varepsilon]\,[(\ell+k)^2-m_K^2+i\varepsilon]\,[(\ell+k')^2-m_K^2+i\varepsilon]}\\ &= -\frac{\epsilon\cdot\epsilon' g^2}{4\pi^2}V_{K\bar{K}}(k^2)V_{K\bar{K}}(k'^2)\\ &\times\int_0^1\int_0^1 dz_1dz_2\frac{\theta(1-z_1-z_2)}{k^2z_1(1-z_1)+k'^2z_2(1-z_2)-2k\cdot k'z_1z_2-m_K^2+i\varepsilon}\end{aligned} \tag{6.24}$$

Where $V_{K\bar{K}}$ is the on-shell part of Eq.(6.23) given by its first term. Next, we perform the following change of integration variables:

$$\begin{aligned}x =&\frac{1}{2}(z_1+z_2)\\ y =&z_1-z_2\end{aligned} \tag{6.25}$$

After performing the integration on y we have:

$$\mathcal{M} =\epsilon\cdot\epsilon' g^2 V_{K\bar{K}}(k^2)V_{K\bar{K}}(k'^2)\frac{1}{\pi^2Q^2}\int_0^{1/2}dx\frac{\log(1-2x/c)-\log(1+2x/c)}{c} \tag{6.26}$$

With:

$$\begin{aligned} c =& \sqrt{-\frac{16k^2}{Q^2}\left(1-\frac{Q^2}{4k^2}\right)\left[(x-x_0)^2+a^2\right]} \\ x_0 =& \frac{1}{4\left(1-\frac{Q^2}{4k^2}\right)} \\ a^2 =& \frac{1}{16\left(1-\frac{Q^2}{4k^2}\right)^2}\left[\frac{4m_K^2}{k^2}\left(1-\frac{Q^2}{4k^2}\right)-1\right] \end{aligned} \tag{6.27}$$

Inside the integral we take $k^2 = k'^2$, which is correct at the $f_0(980)$ double pole. Next, we have to project into the S-wave state of the $\phi(1020)f_0(980)$ system, which amounts to integrating over $\cos\rho \in [-1,1]$, with ρ the relative angle between $\mathbf{p}$ and $\mathbf{p}'$ in the CM frame. In terms of it $Q^2 = -2\mathbf{p}^2(1-\cos\rho)$. The leading non-relativistic contribution for $\epsilon(\mathbf{p},s)\cdot\epsilon'(-\mathbf{p},s') = -\delta_{ss'} + \mathcal{O}(\mathbf{v}^2)$, with $\mathbf{v} = \mathbf{p}/W$ and W denotes the total CM energy of the $\phi(1020)f_0(980)$ pair. Since $\mathbf{v}$ is small we just keep the first term and replace $\epsilon\cdot\epsilon' \to -1$ in Eq.(6.26) and in the tree-level contact term of Eq.(6.22) that we add to the former, obtaining the S-wave amplitude:

$$\begin{aligned} \mathcal{M}^S_{I=0} = \frac{12g^2}{f^2} - V_{K\bar{K}}(s_1)V_{K\bar{K}}(s_1')\frac{g^2}{2\pi^2}\int_{-1}^{+1}\frac{d\cos\rho}{Q^2} \\ \times\int_0^{1/2} dx \frac{\log(1-2x/c)-\log(1+2x/c)}{c} \end{aligned} \tag{6.28}$$

One should bear in mind that some of the discarded contributions to the triangle loops from the off-shell parts of (6.23) lead to contact terms that would just renormalize the first term of the previous equation.

The next step is to resum the re-scattering chain for each of the $(K\bar{K})_0$ pairs, as represented in the left diagram of Fig. 6.3. This can be done by multiplying $\mathcal{M}^S$ by the factor [168]:

$$\frac{1}{D(k^2)D(k'^2)} \tag{6.29}$$

With:

$$D(k^2) = 1 + V_{K\bar{K}}(k^2)G_2(k^2) \tag{6.30}$$

The function G_2 represents the unitary loop of two kaons. In Ref.[158] it was established that the $f_0(980)$ is predominantly a $|K\bar{K}\rangle_0$ S-wave bound state that slightly modifies its mass and acquires a narrow width due to the coupling to pions. Then, in order to reproduce the $f_0(980)$ pole properties due to its coupling to kaons, one can consider single channel kaon scattering and write [158]:

$$T_{K\bar{K}}(k^2) = \frac{V_{K\bar{K}}(k^2)}{1 + V_{K\bar{K}}(k^2)G_2(k^2)} = \frac{V_{K\bar{K}}(k^2)}{D(k^2)} \tag{6.31}$$

This equation can be interpreted as the evolution of a $|K\bar{K}\rangle_0$ pair produced by the potential $V_{K\bar{K}}$ that undergoes re-scattering as determined by the factor $[(1 + V_{K\bar{K}}(k^2)G_2(k^2)]^{-1} = 1 - V_{K\bar{K}}G_2 + V_{K\bar{K}}G_2V_{K\bar{K}}G_2 + \ldots$. For our present problem on the $\phi(1020)f_0(980)$ scattering two $|K\bar{K}\rangle_0$ pairs re-scatter by initial and final state interactions. Analogously, from Eq.(6.28) one has:

$$M^S = \frac{\mathcal{M}^S}{D(k^2)D(k'^2)} = \left[\frac{12g^2/f^2}{V_{K\bar{K}}(k^2)V_{K\bar{K}}(k'^2)} - \frac{g^2}{2\pi^2}\int_{-1}^{+1}\frac{d\cos\rho}{Q^2} \times \int_0^{1/2} dx \frac{\log(1-2x/c) - \log(1+2x/c)}{c}\right] T_{K\bar{K}}(k^2)T_{K\bar{K}}(k'^2) \tag{6.32}$$

It is worth stressing here that this equation can be interpreted as a purely phenomenological one corresponding to the topology of the diagrams 1 and 2 of Fig. 6.1. It is parameterized in terms of the $K\bar{K}$ $I = 0$ S-wave amplitude $T_{K\bar{K}}$. The first term corresponds to a general contact interaction at threshold.[♯3]

The scattering amplitude $T_{K\bar{K}}(k^2)$ has a pole below the $K\bar{K}$ threshold due to the $f_0(980)$ bound state, which implies that:

$$\lim_{k^2 \to M_{f_0}^2} (M_{f_0}^2 - k^2)T_{K\bar{K}}(k^2) = \gamma_{K\bar{K}}^2 \tag{6.33}$$

[♯3] In our fits to data (see next subsection) we have allowed two different values of g^2, one for the contact term and another for the kaon pole terms in Eq.(6.32). However, we have not found any significant difference in our conclusions so that we skip any further comment on this issue.

Then, at k^2, $k'^2 \to M_{f_0}^2$:

$$V_{\phi f_0} = \frac{1}{\gamma_{K\bar{K}}^2} \lim_{k^2, k'^2 \to M_{f_0}^2} (k^2 - M_{f_0}^2)(k'^2 - M_{f_0}^2) M^S = \left[\frac{12 g^2}{f^2 V_{K\bar{K}}(M_{f_0}^2)^2} - \frac{g^2}{2\pi^2} \int_{-1}^{+1} \frac{d\cos\rho}{Q^2} \int_0^{1/2} dx \frac{\log(1 - 2x/c) - \log(1 + 2x/c)}{c} \right] \gamma_{K\bar{K}}^2 \tag{6.34}$$

The coupling of the $f_0(980)$ to $|K\bar{K}\rangle_0$, $\gamma_{K\bar{K}}$, has the value $\gamma_{K\bar{K}} \simeq 4$ GeV [90, 169]. The $1/\gamma_{K\bar{K}}^2$ factor appears because M^S contains two extra couplings $f_0(980) \to |K\bar{K}\rangle_0$ that should be removed when isolating the $f_0(980)$ resonances. In Ref.[170] extra terms contributing to $V_{\phi f_0}$ are pointed out employing the fixed center approximation.

Finally, the $\phi(1020) f_0(980)$ S-wave scattering amplitude is obtained by an expression analogous to Eq. (6.31):

$$T_{\phi f_0} = \frac{V_{\phi f_0}}{1 + V_{\phi f_0} G_{\phi f_0}} \tag{6.35}$$

Here, $G_{\phi f_0}$ is the unitary loop function of a $\phi(1020)$ and a $f_0(980)$ resonances and is given by [88, 90]:

$$G_{\phi f_0}(s) = \frac{1}{(4\pi)^2} \left\{ a_1 + \log \frac{M_{f_0}^2}{\mu^2} - \frac{M_\phi^2 - M_{f_0}^2 + s}{2s} \log \frac{M_{f_0}^2}{M_\phi^2} + \frac{|\mathbf{p}|}{\sqrt{s}} \left[\log(s - \Delta + 2\sqrt{s}|\mathbf{p}|) + \log(s + \Delta + 2\sqrt{s}|\mathbf{p}|) - \log(-s + \Delta + 2\sqrt{s}|\mathbf{p}|) - \log(-s - \Delta + 2\sqrt{s}|\mathbf{p}|) \right] \right\} \tag{6.36}$$

With $\Delta = M_\phi^2 - M_{f_0}^2$. While the renormalization scale μ is fixed to value of the ρ meson mass, $\mu = 770$ MeV, the subtraction constant a_1 has to be fitted to data [90].

6.2.2 $\boldsymbol{\phi(1020)\, f_0(980)}$ resonant states

The potential $V_{\phi f_0}$, Eq.(6.34), depends on g^2 mainly through the vertex at the bottom of the diagrams of Fig. 6.2 that corresponds to $\phi(1020)K$ scattering. In the present problem on the $\phi(1020) f_0(980)$ scattering around its

threshold we are also close to the $\phi(1020)K$ threshold itself. On the other hand, the $K_1(1400)$ resonance is only 100 MeV below it. Therefore, it is quite reasonable to expect that the $\phi(1020)K$ scattering is dominated by this resonance which implies that $g^2 < 0$ because, for a bare pole:

$$g^2 \sim \frac{\gamma^2_{K_1\phi K}}{M^2_{K_1} - (M_\phi + m_K)^2} < 0 \tag{6.37}$$

In this way, g^2 is interpreted as a parameter that mimics the $\phi(1020)K$ scattering amplitude in the energy region of the $\phi(1020)f_0(980)$ scattering close to threshold. On the other hand, we restrict g^2 to be real so that $V_{\phi f_0}$ is also real above the $\phi(1020)f_0(980)$ threshold and the resulting S-wave $T_{\phi f_0}$ amplitude, Eq.(6.35), fulfils unitarity.[♯4] With $g^2 < 0$, $V_{\phi f_0}$ is positive (attractive) around the $\phi(1020)f_0(980)$ threshold. In this situation $|T_{\phi f_0}|^2$ has resonant peaks with mass and width compatible with those measured for the $Y(2175)$ [145, 147, 148]. The $Y(2175)$ mass and width values extracted by BABAR [145] and BES [147] are compatible between each other. In the following we take, as reference values, their average:

$$\begin{aligned} M_Y &= 2.180 \pm 0.008 \text{ GeV} \\ \Gamma_Y &= 0.060 \pm 0.014 \text{ GeV} \end{aligned} \tag{6.38}$$

In Fig. 6.5 we show $|T_{\phi f_0}|^2$ for $(\sqrt{-g^2}, a_1) = (5, -7.1)$, $(6, -5.2)$ and $(7, -4.1)$ with $M_{f_0} = 0.98$ GeV in all the curves. The peak is located at 2.18 GeV as in Eq.(6.38) and the width increases with $\sqrt{-g^2}$, taking the values of 48, 72 and 100 MeV for $\sqrt{-g^2} = 5$, 6 and 7, in that order. Although the width increases, the size at the peak remains constant because the former is proportional to g^2 so that the ratio g^2/Γ_Y, which fixes the amplitude at the maximum, is roughly independent of the value of g^2 used for a fixed peak position. On the other hand, there have been some criticisms about the value of $|T_{\phi f_0}|^2$ [170], since at the resonance position ($\sqrt{s} = 2.175$ GeV) the value of this modulus is two orders of magnitude bigger than the one that is obtained if one uses the ϕK amplitude provided by the Chiral Unitary approach of Ref.[159].

To sharpen our conclusions we now compare directly with the $e^+e^- \to \phi(1020)f_0(980)$ data [144, 145, 148]. The $\phi(1020)f_0(980)$ strong scattering amplitude, Eq.(6.35), is employed to correct by final state interactions (FSI)

[♯4] We have checked that our fits to data are stable if we allow g^2 to become complex.

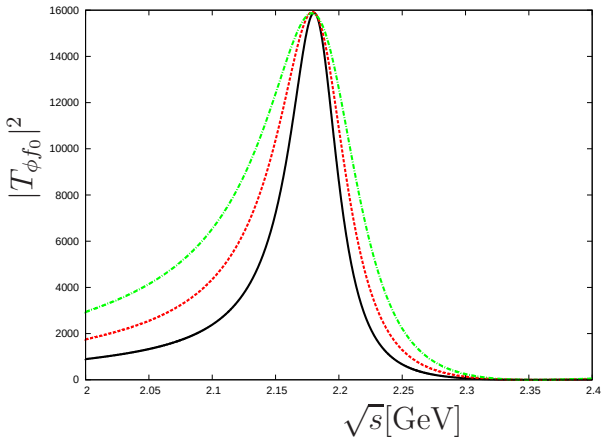

Figure 6.5: $|T_{\phi f_0}|^2$ with the peak at 2.18 GeV as a function of the ϕf_0 invariant mass. The solid, dashed and dot-dashed lines are for $\sqrt{-g^2} = 5$, 6, 7 and $a_1 = -7.1$,-5.2, -4.1 respectively.

a given production process for $e^+e^- \to \phi(1020)f_0(980)$. This is achieved [168] by multiplying the production amplitude by:

$$\frac{1}{1 + G_{\phi f_0} V_{\phi f_0}} \tag{6.39}$$

In the same manner as already done in Eq.(6.29) for the $K\bar{K}$ re-scattering. We take as the non-resonant production cross section $\sigma_{NR}(s)$ the one fitted in Fig. 6(b) of Ref.[148]. Therefore, after FSI:

$$\sigma_{NR}(s) \to \sigma_R(s) = \frac{\sigma_{NR}(s)}{|1 + V_{\phi f_0} G_{\phi f_0}|^2} \tag{6.40}$$

In order to take into account the mass distribution of the $f_0(980)$ resonance, the previous result is convoluted with the $f_0(980)$ mass distribution $P(W_{f0})$:

$$\langle \sigma_R(s) \rangle = \mathcal{N} \sigma_{NR}(s) \int dW_{f_0} \frac{P(W_{f_0})}{|1 + V_{\phi f_0} G_{\phi f_0}(s, W_{f_0})|^2} \tag{6.41}$$

For practical purposes we take $P(M_{f_0})$ as a Lorentzian distribution centered at $M_{f_0} = 0.98$ or 0.99 GeV with a width Γ_{f_0} =50 MeV [171]:

$$P(W_{f_0}) = \frac{1}{2\pi} \frac{\Gamma_{f_0}}{(W_{f_0} - M_{f_0})^2 + \frac{\Gamma_{f_0}^2}{4}} \tag{6.42}$$

The normalization constant $\mathcal{N}$ is included in Eq. (6.41) to account for the fact that the $\sigma_{NR}(s)$ of Ref.[148] is extracted assuming an specific shape and strength for the resonant signal.

$\sqrt{-g^2}$	a_1	$\mathcal{N}$	$\chi^2_{d.o.f.}$	M_{f_0}
7.33 ± 0.30	-2.41 ± 0.14	0.79 ± 0.06	$88/(46-3)$	0.98 GeV (fixed)
3.94 ± 0.18	-2.84 ± 0.18	0.52 ± 0.05	$108/(46-3)$	0.99 GeV (fixed)

Table 6.1: Fits to the data from BABAR [145] and Belle [148] on $e^+e^- \to \phi(1020)f_0(980)$. The first fit uses $M_{f_0} = 0.98$ GeV and the second one $M_{f_0} = 0.99$ GeV.

We have performed fits using the data points around the $Y(2175)$ peak, for $\sqrt{s} \in [2, 2.6]$ GeV, taking into account the bin size. The best-fit parameters for $M_{f_0} = 0.98$ and 0.99 GeV are given in Table 6.1. The results of these fits are the solid and dot-dashed lines in Fig. 6.6, where the points used to draw the curves are separated in energy according to the bin size of the experimental points of Refs.[148, 145] for the data set from the $\phi(1020)\pi^+\pi^-$ final state. The rest of the points (diamonds) are obtained from the $\phi(1020)\pi^0\pi^0$ final state [145]. Notice that the data from Ref.[148] are slightly more precise than those from Ref.[144, 145]. The fitted parameters do not depend on the precise value of the upper energy limit. We have used $\sqrt{s} = 2.6$ GeV as a large enough value to cover the energy region where our approach is valid, namely, near the $\phi(1020)f_0(980)$ threshold.

The suppression of our results for $\sqrt{s} \lesssim 2$ GeV in Fig. 6.6 is not due to a negative interference of $T_{\phi f_0}$ with the non-resonant contribution. Instead, it is due to fact that at the $\phi(1020)f_0(980)$ threshold, the $V_{\phi f_0}$ potential of Eq.(6.34) is large because of the $1/Q^2$ factor. This threshold effect is very sensitive to the procedure to disentangle the $f_0(980)$ resonant signal. Here, we have taken for it a precise mass value given by the $f_0(980)$ pole position. However, experimentally it is obtained from the $e^+e^- \to \phi(1020)\pi\pi$ data by integrating the two pion invariant mass distribution within an energy region around the $f_0(980)$ signal, typically for 0.85 GeV$\leq \sqrt{s_{\pi\pi}} \leq 1.1$ GeV [144], with $\sqrt{s_{\pi\pi}}$ the two pion invariant mass.

In Fig. 6.7, $|V_{\phi f_0}|$ is shown for the two sets of parameters given in Table 6.1. The solid line is for $M_{f_0} = 0.98$ GeV and the dot-dashed one for $M_{f_0} = 0.99$ GeV. Both have a similar peak value, though to accomplish this $|g^2|$ is smaller by around a factor 3 for the first fit in Table 6.1 compared to the second. The reason is again related to the factor $1/Q^2$ in $V_{\phi f_0}$, Eq.(6.34). Indeed, the integration in x is logarithmically divergent for those $Q^2 > 0$

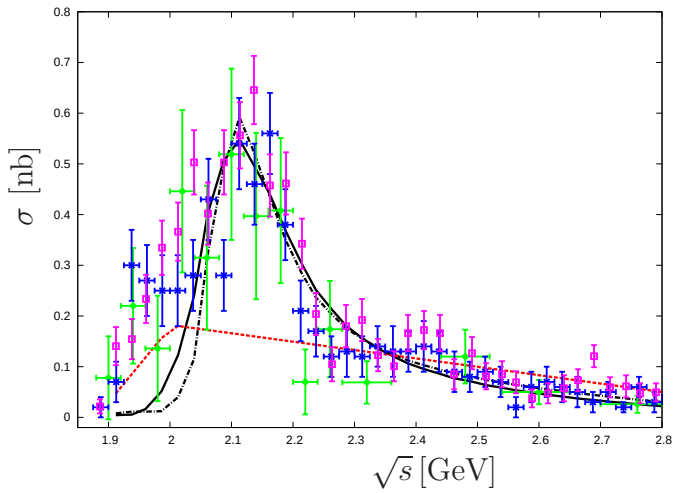

Figure 6.6: Cross-section for $e^+e^- \to \phi(1020) f_0(980)$. The experimental data are from Ref.[145] (diamonds and crosses) and Ref.[148] (empty boxes). The solid and dash-dotted lines correspond to the first and second fits of Table 6.1. The dashed line shows $\mathcal{N}\sigma_{NR}(s)$ for the first fit.

values (below the $\phi(1020) f_0(980)$ threshold) which are large enough [around $M_{f_0}^2(4 - M_{f_0}^2/m_K^2)$] to make a^2 in Eq.(6.27) vanish. However, the logarithmic divergence in x disappears after the integration in $\cos\theta$ is performed. The onset of this behavior gives rise to the maximum of $V_{\phi f_0}$ below threshold, as can be seen in Fig. 6.7. There is an exception for which the logarithmic divergence in x remains; this occurs exactly at the $\phi(1020) f_0(980)$ threshold and only for $M_{f_0} = 2m_K$. In this case $a^2 = 0$ for all $\cos\theta$ and the final result after the two integrations is logarithmically divergent at threshold. This is the reason why, for a fixed value of g^2, as M_{f_0} approaches $2m_K$ the potential becomes larger with a narrower peak structure. This is the limit that corresponds exactly to the suppression mechanisms used to establish that the diagram 2 of Fig. 6.1 is the dominant one. The appearance of the $Y(2175)$ peak within our approach is driven by the large value of $V_{\phi f_0}$ at threshold and its rather fast decrease in energy for $\sqrt{s}$ somewhat above the $\phi(1020) f_0(980)$ threshold.

It is interesting to mention that while $\sqrt{-g^2}$ in Table 6.1 is in the range of values used in Fig. 6.5, the a_1 values in the table are smaller in modulus by around a factor 2–3 compared to those used in Fig. 6.5, to obtain $M_Y =$ 2.18 GeV as in Eq.(6.38). This implies that $|T_{\phi f_0}|^2$ from the fits to data has a peak at smaller energies (around 2.09 GeV) and wider, with a width of around 150 MeV. This is in line with the findings of the Belle Collaboration [148] discussed in the introduction. In all cases a_1 is negative, as it should

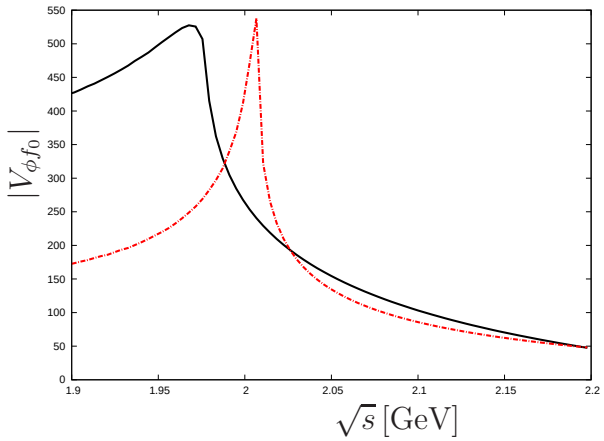

Figure 6.7: $|V_{\phi f_0}|$ for the two sets in Table 6.1. The solid and dot-dashed lines correspond to the first and second fits, respectively.

be for a dynamically generated resonance. In this situation the potential should be attractive so that $1/V_{\phi f_0}$ can cancel with a_1 in Eq.(6.35). On the other hand, for the a_1 values in Table 6.1, the resulting unitary ChPT scale, $\Lambda = (4\pi f)/\sqrt{|a_1|} \simeq 0.75$ GeV, preserves a natural size around M_ρ. However, since the $|a_1|$ values in Fig. 6.5 are significantly larger, the interpretation of these peaks as fully dynamically generated states is more arguable because in this case the unitarity scale is just around 0.5 GeV. Nonetheless, even in these cases one can still conclude that these peaks have a large $\phi(1020)f_0(980)$ re-scattering component. On the other hand, for a resonance mass $M_Y = 2.09$ GeV one has $1/p = 0.65$ fm and for $M_Y = 2.18$ GeV, $1/p = 0.45$ fm. This indicates that although the $Y(2175)$ had large a $\phi(1020)f_0(980)$ meson-meson components, as our results point out, it is a rather compact object.

6.3 Derivation of the $\phi(1020)a_0(980)$ scattering amplitude

In order to obtain the $\phi(1020)a_0(980)$ amplitude we follow the methodology of the previous section with the isovector $a_0(980)$ instead of the isoscalar $f_0(980)$. First, the scattering of the $\phi(1020)$ resonance with an S-wave neutral pair of the lightest pseudoscalar mesons in $I = 1$ is investigated. Two types of meson pair are then possible, namely, $|1\rangle \equiv |K\bar{K}\rangle_{I=1}$ and $|2\rangle \equiv |\pi^0\eta_8\rangle$ (already a pure isospin (I) 1 state). The following channels result:

$$\begin{aligned}
&(1 \to 1): \quad \phi(1020)\,|K\bar{K}\rangle_{I=1} \to \phi(1020)\,|K\bar{K}\rangle_{I=1}\\
&(1 \to 2): \quad \phi(1020)\,|K\bar{K}\rangle_{I=1} \to \phi(1020)\,|\pi^0\eta_8\rangle\\
&(2 \to 1): \quad \phi(1020)\,|\pi^0\eta_8\rangle \to \phi(1020)\,|K\bar{K}\rangle_{I=1}\\
&(2 \to 2): \quad \phi(1020)\,|\pi^0\eta_8\rangle \to \phi(1020)\,|\pi^0\eta_8\rangle
\end{aligned} \tag{6.43}$$

Both $\phi(1020)a_0(980)$ S- and D-waves contribute to the 1^{--} channel but since we are interested in the threshold region around 2 GeV, D-wave terms can be neglected, as we did in Sec. 6.2. Again, as both $\phi(1020)$ and $a_0(980)$ are very close to the $K\bar{K}$ threshold, the amplitude at tree level is dominated by diagram Fig. 6.8a. The main reason is that the propagator of the kaon intermediate state is almost on-shell.[♯5] As we did before, we also include the local term of Fig. 6.8b because the off-shell part of the four-pseudoscalar-meson vertex can cancel the kaon propagator generating local terms. Therefore one has to consider simultaneously the sum of amplitudes from both diagrams as any splitting would depend on field parameterization.

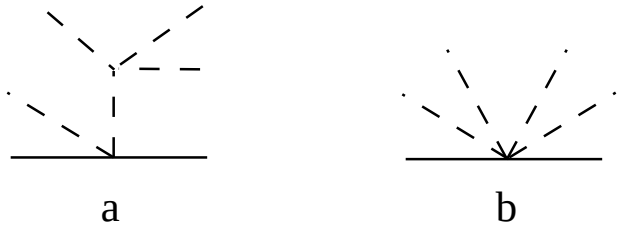

Figure 6.8: Dominant tree-level contributions to the scattering of a $\phi(1020)$ with a neutral pair of pseudoscalar mesons close to threshold. The dashed lines denote the pseudoscalar mesons and the solid line stands for the $\phi(1020)$.

[♯5] In this case, the possible intermediate states are kaon or anti-kaon because of the absence of $\phi^2\pi^0\pi^0$, $\phi^2\pi^0\eta_8$ and $\phi^2\eta_8\eta_8$ vertices in the $V^2\Phi^2$ Lagrangian of Eq.(6.10).

To construct the $(1 \to 1)$ amplitude we cast $|K\bar{K}\rangle_{I=1}$ as:

$$|K(k_1)\bar{K}(k_2)\rangle_{I=1} = -\frac{1}{\sqrt{2}}|K^+(k_1)K^-(k_2) - K^0(k_1)\bar{K}^0(k_2)\rangle\,, \tag{6.44}$$

With k_1 and k_2 the kaon four-momenta. We denote as T_{cc}, T_{nc}, T_{cn} and T_{nn} (in order from top to bottom), the amplitudes for the reaction channels:

$$\begin{aligned}
\phi(p)\,K^+(k_1)\,K^-(k_2) &\to \phi(p')\,K^+(k_1')\,K^-(k_2') \\
\phi(p)\,K^0(k_1)\,\bar{K}^0(k_2) &\to \phi(p')\,K^+(k_1')\,K^-(k_2') \\
\phi(p)\,K^+(k_1)\,K^-(k_2) &\to \phi(p')\,K^0(k_1')\,\bar{K}^0(k_2') \\
\phi(p)\,K^0(k_1)\,\bar{K}^0(k_2) &\to \phi(p')\,K^0(k_1')\,\bar{K}^0(k_2')
\end{aligned} \tag{6.45}$$

The result for diagram Fig. 6.8a is:

$$T_{cc}^{(a)} = -\frac{2g^2}{3f^2}\epsilon\cdot\epsilon'\left\{4 + 6(u_a - 2m_K^2)\Big[D(Q+k_1) + D(Q-k_2')\Big]\right. \tag{6.46}$$

$$\left. +6(u_b - 2m_K^2)\Big[D(Q+k_2) + D(Q-k_1')\Big]\right\} \tag{6.47}$$

$$T_{nn}^{(a)} = T_{cc}^{(a)} \tag{6.48}$$

$$T_{nc}^{(a)} = \frac{1}{2}T_{cc}^{(a)} \tag{6.49}$$

$$T_{cn}^{(a)} = T_{nc}^{(a)} = \frac{1}{2}T_{cc}^{(a)} \tag{6.50}$$

Where ϵ (ϵ') is the polarization four-vector of the initial (final) $\phi(1020)$ meson, $u_a = (k_1' - k_2)^2$, $u_b = (k_2' - k_1)^2$ and $Q = p - p'$. The kaon propagator $D(q)$ is given by:

$$D(q) = \frac{1}{m_K^2 - q^2 - i\varepsilon} \tag{6.51}$$

With $\varepsilon \to 0^+$. For the contact term (diagram of Fig. 6.8b) the result is:

$$\begin{aligned}
T_{cc}^{(b)} &= -\frac{16g^2}{3f^2}\epsilon\cdot\epsilon' \\
T_{nn}^{(b)} &= T_{cc}^{(b)} \\
T_{nc}^{(b)} &= T_{cn}^{(b)} = \frac{1}{2}T_{cc}^{(b)}
\end{aligned} \tag{6.52}$$

Taking into account Eq. (6.44) one finds for the $(1 \to 1)$ channel of Eq.(6.43):

$$T_{11}^{I=1} = \frac{1}{2}\left\{T_{cc} + T_{nn} - T_{cn} - T_{nc}\right\} = \frac{1}{2}T_{cc} \tag{6.53}$$

Where $T_{cc} = T_{cc}^{(a)} + T_{cc}^{(b)}$ (and analogously for T_{nn}, T_{cn} and T_{nc}). Therefore:

$$\begin{aligned} T_{11}^{I=1} = \frac{2g^2}{f^2}\epsilon\cdot\epsilon'\Big\{ & -2 + k_2\cdot k_1'\big[D(Q+k_1) + D(Q-k_2')\big] \\ & + k_1\cdot k_2'\big[D(Q+k_2) + D(Q-k_1')\big]\Big\} \end{aligned} \tag{6.54}$$

Proceeding in the same way, the $(1 \to 2)$ and $(2 \to 1)$ amplitudes are found to be:

$$\begin{aligned} T_{12}^{I=1} &= -\frac{2g^2}{\sqrt{6}f^2}\epsilon\cdot\epsilon'\left[3k_1'\cdot k_2' + m_\pi^2\right]\left[D(Q+k_1) + D(Q+k_2)\right] \\ T_{21}^{I=1} &= -\frac{2g^2}{\sqrt{6}f^2}\epsilon\cdot\epsilon'\left[3k_1\cdot k_2 + m_\pi^2\right]\left[D(Q-k_1') + D(Q-k_2')\right] \end{aligned} \tag{6.55}$$

Where k_1, k_2 (k_1', k_2') are the four-momenta of the initial (final) pseudoscalars. Notice that there is no local term due to a cancellation between the contact term from Fig. 6.8b and the local part from Fig. 6.8a. In Eq. (6.55) we have made use of the Gell-Mann-Okubo mass relation $m_\eta^2 = 4m_K^2/3 - m_\pi^2/3$ so as to simplify the final expressions. Finally, the transition $(2 \to 2)$ is absent at tree level because there are no $\phi^2\Phi^2$ or $\phi^2\Phi^4$ vertexes with only π^0 and η mesons. Because of the absence of the contact terms for $(1 \to 2)$, $(2 \to 1)$ and $(2 \to 2)$ there is no need to further consider these processes in order to obtain the interaction kernel for $\phi(1020)a_0(980)$ scattering. It can be obtained directly from $(1 \to 1)$, as it is explicitly worked out below.

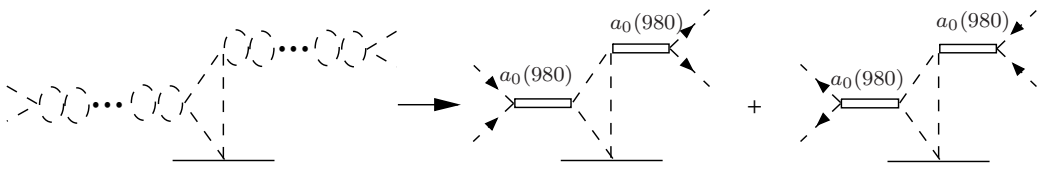

Figure 6.9: The two $a_0(980)$ poles that arise from meson-meson interactions in $I = 1$ and S-wave.

Next, we consider initial- and final-state re-scattering of the pseudoscalar mesons in $I = 1$ and S-wave from the diagrams in Fig. 6.8, as we show in

Fig. 6.9 for the nonlocal part of the interaction. The re-scattering chains, made of $K\bar{K}$ and $\pi^0\eta$ pairs, contain the poles of the initial and final $a_0(980)$ resonances [90, 158, 166, 167, 169]. Below, the residue at the $a_0(980)$ double pole will be identified as the $\phi(1020)a_0(980)$ interaction kernel $\mathcal{K}_{\phi a_0}$. We follow Refs.[90, 158, 169] where the $I = 1$ S-wave meson-meson scattering was studied in terms of the $K\bar{K}$ and $\pi^0\eta$ coupled channels and the $a_0(980)$ resonance was dynamically generated from the meson-meson self-interactions. This is also the case for other approaches like Refs.[166, 167]. The $I = 1$ S-wave meson-meson amplitudes T_{ij} fulfill the Bethe-Salpeter equation in coupled channels:

$$T_{ij} = \sum_m \mathcal{K}_{im} \left(\delta_{mj} - G_m T_{mj}\right) \tag{6.56}$$

Where the indices $i, j, k, m = 1, 2$ denote the $K\bar{K}$ and $\pi^0\eta$ channels, respectively. The T-matrix is given in terms of the on-shell part of the $I = 1$ S-wave meson-meson amplitudes at tree level and the $K\bar{K}$ and $\pi^0\eta$ unitary scalar loop functions, G_1 and G_2 in this order.[♯6] Notice that the $\mathcal{K}_{ij}$ factorize in Eq. (6.56) [158]. The latter were calculated in the same reference from $\mathcal{L}_{\Phi^4}$, Eq.(6.10), with the resulting expressions:

$$\begin{aligned}
\mathcal{K}_{11} \equiv \mathcal{K}_{K\bar{K}\to K\bar{K}} &= \frac{k^2}{4f^2} \\
\mathcal{K}_{12} = \mathcal{K}_{21} \equiv \mathcal{K}_{\pi^0\eta\to K\bar{K}} &= -\frac{\sqrt{3/2}}{6f^2}(3k^2 - 4m_K^2) \\
\mathcal{K}_{22} \equiv \mathcal{K}_{\pi^0\eta\to\pi^0\eta} &= \frac{m_\pi^2}{3f^2}
\end{aligned} \tag{6.57}$$

With k^2 being the invariant mass squared of the meson pair.

The V_{mn} part, which contains the $\phi(1020)$ interaction with the pseudoscalar pair projected into S-wave, consist of two terms, $V_{mn} = V_{mn}^{(c)} + V_{mn}^{(t)}$. The first is a local term, present only in the $(1 \to 1)$ channel as shown above. From Eq.(6.54):

$$V_{mn}^{(c)} = \frac{4g^2}{f^2}\delta_{m1}\delta_{n1} \tag{6.58}$$

[♯6]The expressions given in Eqs.(6.36) and (6.68), obtained from a dispersion relation and with cut-off regularization, respectively, are also applicable here after the appropriate replacement of masses.

Where only the leading non relativistic contribution to $\epsilon(\mathbf{p},s)\cdot\epsilon'(\mathbf{p}',s') \approx -\delta_{ss'}$ has been kept; this approximation is justified for small $\phi(1020)$ (and $a_0(980)$) velocities in the $\phi(1020)a_0(980)$ CM frame.

The second term is given by the triangular loop diagrams depicted in Fig. 6.4 with only kaons in the internal lines. For the Φ^4 vertices we take only the on-shell amplitudes of Eq.(6.57). The off-shell parts are proportional to the inverse of kaon propagators and cancel with them in the calculation of the loop, giving rise to amplitudes that do not correspond anymore to the dominant triangular kaon-loop but to other topologies. Nonetheless, one should bare in mind that some of these sub-leading contributions may alter the contact term fixed above from the tree level amplitudes.

We obtain:

$$V_{mn}^{(t)} = -4g^2\mathcal{K}_{m1}(k^2)\mathcal{K}_{1n}(k'^2)L_S \tag{6.59}$$

Where:

$$L_S = \frac{1}{8\pi^2}\int_{-1}^{+1}\frac{d\cos\rho}{Q^2}\int_0^{1/2}dx\frac{1}{c}\left[\log\left(1-2x/c\right)-\log\left(1+2x/c\right)\right] \tag{6.60}$$

$$c^2 = \frac{4}{Q^2}\left[x^2Q^2+2k^2x(1-2x)-m_K^2+i\epsilon\right] \tag{6.61}$$

With k^2 (k'^2) the invariant mass squared of the initial (final) pseudoscalar-meson pair. Inside the integral we take $k^2 = k'^2$, which holds at the $a_0(980)$ double pole. We account for the S-wave projection by averaging over $\cos\rho$ with ρ the relative angle between $\phi(1020)$ incoming ($\mathbf{p}$) and outgoing ($\mathbf{p}'$) momenta in the CM frame. In terms of this angle $Q^2 = -2\mathbf{p}^2(1-\cos\rho)$. As for the contact term we approximate $\epsilon(\mathbf{p},s)\cdot\epsilon'(\mathbf{p}',s') \approx -\delta_{ss'}$.

Altogether:

$$V_{mn} = 4g^2\left(\frac{\delta_{m1}\delta_{1n}}{f^2}-\mathcal{K}_{m1}(k^2)\mathcal{K}_{1n}(k'^2)L_S\right) \tag{6.62}$$

In presence of re-scattering of the initial and final two-body hadronic states the V_{ij} amplitudes are corrected giving rise to the final $\mathcal{M}_{ij}$ dressed amplitudes:

$$\mathcal{M}_{ij} = \sum_{mn}(\delta_{im}-T_{im}G_m)V_{mn}(\delta_{nj}-G_nT_{nj}) \tag{6.63}$$

In this equation the first term between brackets accounts for the initial state interactions and the second one does so for the final state interactions

between the pseudoscalars in $I = 1$ S-wave pairs. For its derivation and other applications see Refs.[168, 172]. Substituting in Eq.(6.63) and using Eq.(6.56) one finds that:

$$\mathcal{M}_{ij} = 4g^2 \left\{ \frac{1}{f^2}[\delta_{i1} - T_{i1}(k^2)G_1(k^2)][\delta_{1j} - G_1(k'^2)T_{1j}(k'^2)] - T_{i1}(k^2)T_{1j}(k'^2)L_S \right\} \tag{6.64}$$

Now we proceed to extract the $\phi(1020)a_0(980)$ interaction kernel as we did in the previous section. For this purpose we notice that the scattering amplitude $T_{11}(k^2)$ contains the $a_0(980)$ resonance pole with residue:

$$\lim_{k^2 \to M_{a_0}^2} (M_{a_0}^2 - k^2) T_{11}(k^2) = \gamma_{K\bar{K}}^2 \tag{6.65}$$

Where $M_{a_0}^2$ denotes the $a_0(980)$ pole position. Therefore:

$$\begin{aligned} \mathcal{K}_{\phi a_0} &= \frac{1}{\gamma_{K\bar{K}}^2} \lim_{k^2, k'^2 \to M_{a_0}^2} (k^2 - M_{a_0}^2)(k'^2 - M_{a_0}^2)\mathcal{M}_{11} \\ &= 4g^2\gamma_{K\bar{K}}^2 \left[\frac{1}{f^2} G_1(M_{a_0}^2)^2 - L_S \right] \end{aligned} \tag{6.66}$$

The $1/\gamma_{K\bar{K}}^2$ factor appears because $\mathcal{M}_{11}$ contains two extra $a_0(980) \to |K\bar{K}\rangle_{I=1}$ couplings that should be removed in order to isolate the $a_0(980)$ resonances.

As in the case with the $f_0(980)$, the $\phi(1020)a_0(980)$ S-wave scattering amplitude is:

$$T_{\phi a_0} = \frac{\mathcal{K}_{\phi a_0}}{1 + \mathcal{K}_{\phi a_0} G_{a_0 f_0}} \tag{6.67}$$

With $G_{\phi a_0}(s)$ the unitary loop function, Eq.(6.36), for $a_0(980)$ as intermediate state instead of $f_0(980)$. With the renormalization scale μ fixed to value of the ρ meson mass, $\mu = 770$ MeV. On the other hand, the subtraction constant a_1 has to be fitted to data [90]. The loop-function can also be regularized with a three-momentum cut-off q_{max} [158]:

$$G_{\phi a_0}(s) = \int_0^{q_{max}} \frac{|\mathbf{k}|^2 d|\mathbf{k}|}{(2\pi)^2} \frac{w_\phi + w_{a_0}}{w_\phi w_{a_0}(s - (w_\phi + w_{a_0})^2 + i\epsilon)} \tag{6.68}$$

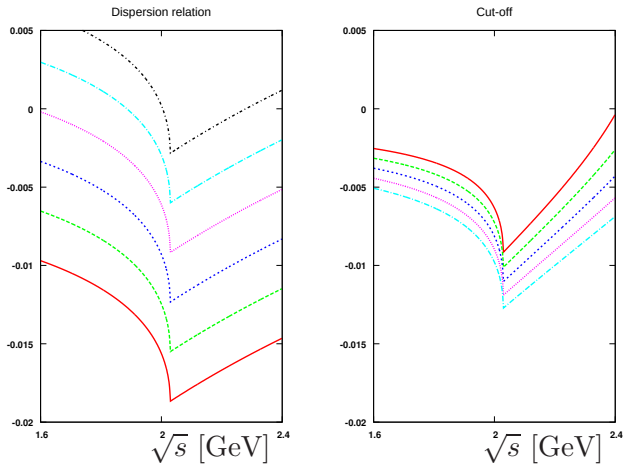

Figure 6.10: (Color online). The $G_{\phi a_0}$ function calculated from a dispersion relation, Eq. (6.36), left panel, and with a three-momentum cut-off, Eq. (6.68), right panel. From top to bottom, the subtraction constant a_1 is varied from -1.0 to to -3.5 in steps of -0.5 while the three-momentum cut-off, q_{max}, goes from 0.8 to 1.2 GeV in steps of 0.1 GeV.

With $w_i = \sqrt{m_i^2 + |\mathbf{k}|^2}$. It is instructive to compare the real part of the $G_{\phi a_0}$ functions that result from the two methods. For this we fix $M_{a_0} = 1.009$ GeV, corresponding to the pole mass obtained in Ref.[158]. The comparison is presented in Fig. 6.10. On the left panel, Eq.(6.36) is evaluated varying the subtraction constant a_1 from -1.0 to -3.5 in steps of -0.5 starting from the top while on the right one, Eq.(6.68) is plotted for q_{max} between 0.8 and 1.2 GeV (around the typical hadronic scale $\sim 4\pi f_\pi$) in steps of 0.1 GeV, from top to bottom. We observe a significant coincidence between both functions in the threshold region (~ 2 GeV) for values of a_1 between -3 and -2. This interval contains indeed the a_1 values obtained in the previous section by fitting the $e^+e^- \to \phi(1020)f_0(980)$ cross section. This coincidence is interpreted as an indication that the $Y(2175)$ resonance is to a large extent dynamically generated. Now, we investigate this possibility for the $I = 1$ S-wave $\phi(1020)a_0(980)$ scattering.

6.3.1 Results and discussion

- **Possible $\phi(1020)\,a_0(980)$ resonances**

In this investigation, we consider two possibilities for the $a_0(980)$ properties (pole position and residue), as they depend on the framework followed.

In the first one, the Bethe-Salpeter (BS) equation for meson-meson scattering was solved using cut-off regularization for the loop function [158]. In the second case, the N/D method was used with the meson-meson loop function obtained with a dispersion relation [90]. In both studies the $K\bar{K}$ and $\pi^0\eta$ coupled channels were included. The $a_0(980)$ properties extracted in these references are listed in Table. 6.2.

	M_{a_0} [GeV]	$\gamma^2_{K\bar{K}}$ [GeV^2]
BS [158]	$1.009 + i\,0.056$	$24.73 - i\,10.82$
N/D [90]	$1.055 + i\,0.025$	$17.37 - i\,24.77$

Table 6.2: $a_0(980)$ properties, pole position M_{a_0} and residue $\gamma^2_{K\bar{K}}$, used as input.

Furthermore, we employ two sets of values for the coupling g and the ϕa_0 subtraction constant a_1 corresponding to the values we obtained in Sec. 6.2 fitting BABAR [145] and Belle [148] data on $e^+e^- \to \phi(1020)\, f_0(980)$. The first of the fits corresponds to the fit on the top of Table 6.1, with mass and couplings for the $f_0(980)$ resonance from Ref.[171], while the second one is similar to that in the last line of Table 6.1 but obtained with slightly different values of the $f_0(980)$ mass and $K\bar{K}$ residue ($\gamma^2_{f_0K\bar{K}}$), corresponding to those values of Ref.[90]. The values for the $f_0(980)$ properties from refs. [90, 171] and the resulting fit parameters are collected in Table 6.3 from top to bottom, respectively. Notice that $g^2 < 0$. As remarked before, g^2 should be understood as a parameter characterizing the $\phi(1020)K$ scattering around its threshold, with presumably large influence from the $I(J^P) = \frac{1}{2}(1^+)$ $K_1(1400)$ resonance [173], which would determine the negative sign for g^2.

	M_{f_0} [GeV] (fixed)	$\gamma^2_{f_0K\bar{K}}$ [GeV^2] (fixed)	$\sqrt{-g^2}$	a_1
Fit 1	0.980	16	7.33(30)	$-2.41(14)$
Fit 2	0.988	13.2	5.21(12)	$-2.61(14)$

Table 6.3: Fits to BABAR [145] and Belle [148] $e^+e^- \to \phi(1020)\, f_0(980)$ data for two different choices of the $f_0(980)$ properties.

We calculate $|T_{\phi a_0}|^2$ for the four possible combinations of the parameter values in Tables 6.2 and 6.3 for M_{a_0}, $\gamma^2_{\bar{K}K}$, $\sqrt{-g^2}$ and a_1. As mentioned above, some of the discarded contributions to the triangle loop could modify the local term in Eq.(6.66). For this reason, we first exclude the local contribution and concentrate on the more robust triangular topology. The $|T_{\phi a_0}|^2$ dependence

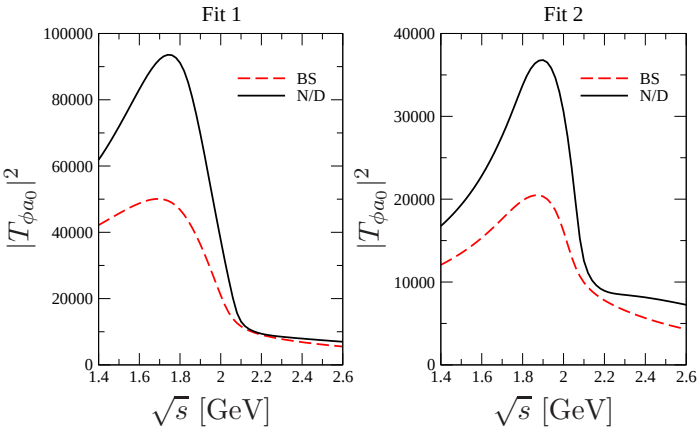

Figure 6.11: (Color online). $|T_{\phi a_0}|^2$ without local term in the kernel $\mathcal{K}_{\phi a_0}$ as a function of the ϕa_0 invariant mass for the possible combinations of parameters in Tables 6.2 and 6.3.

on the $\phi(1020)a_0(980)$ invariant mass is shown in Fig. 6.11. All the curves show a prominent enhancement below the $\phi K\bar{K}$ threshold, at 2.01 GeV, that hints at the presence of a dynamically generated resonance located quite close but above the $\pi^0\eta$ threshold (1.7 GeV). For Fit 2, the peak is narrower and has a maximum at a higher $\sqrt{s}$ but it is 2.5 times stronger for Fit 1 (notice the different scales in the plots).

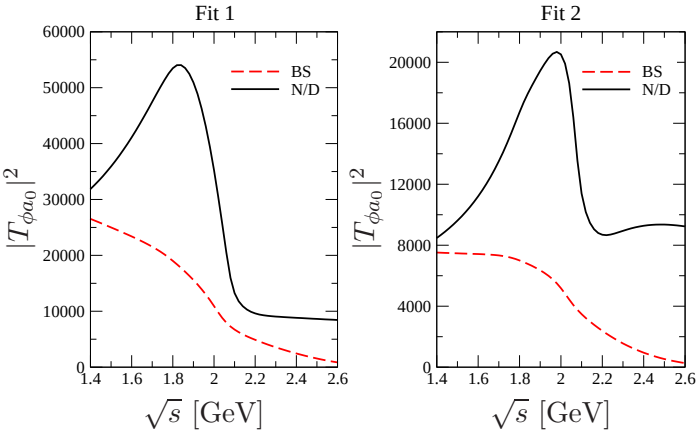

Figure 6.12: (Color online). Same as Fig. 6.11 but with the local term in the kernel as in Eq. (6.66).

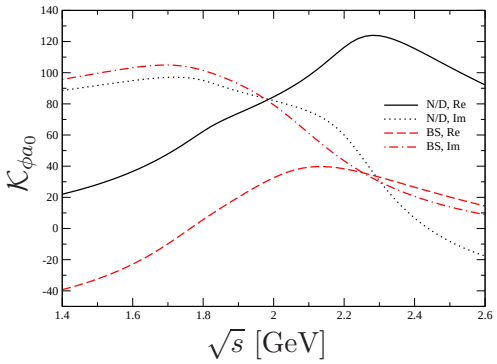

Figure 6.13: (Color online). $\mathcal{K}_{\phi a_0}$ for Fit 2 and both BS and N/D sets.

Let us now take into account the local term in the kernel as given in Eq.(6.66). For the sake of consistency the $K\bar{K}$ unitarity scalar loop function, $G_1(k^2)$, is evaluated making use of the same regularization procedure as that employed in generating the $a_0(980)$ resonance from Refs.[158, 90]. Hence, when the BS set is used, $G_1(M_{a_0}^2)$ is computed using a cut off regularization with $q_{max} = 1$ GeV [158] while, when the N/D parameters are considered, $G_1(M_{a_0}^2)$ is obtained from a dispersion relation with the renormalization scale fixed at the ρ mass, $\mu_{K\bar{K}} = 0.77$ GeV, and a subtraction constant of $a_{KK} = -0.81$ [90]. The new results are shown in Fig 6.12. In the BS case, for both fits 1, 2, the enhancements observed before in Fig. 6.11 are flatten away by the presence of the local term. This fact agrees with the results of Ref.[40] where no isovector 1^{--} resonance was generated. Remarkably, when the N/D set is employed the resonance peak is still clearly seen, and at a higher invariant mass with respect to Fig. 6.12, but with a $|T_{\phi a_0}|^2$ smaller by almost a factor two. Considerable differences between BS and N/D results are also observed above $\sqrt{s} > 2.2$ GeV: while the BS curve goes fast to zero, the N/D one remains nearly flat at least up to $\sqrt{s} = 2.6$ GeV. The main difference between the two choices has to do with the actual value of the coupling squared $\gamma_{K\bar{K}}^2$, particularly for its imaginary part. In this way, if the BS [158] $a_0(980)$ pole position in Table 6.2 were used with the couplings of the N/D [90] pole one would obtain also $\phi(1020)a_0(980)$ broad peaks similar to those shown by the dashed lines in Fig. 6.11. In the previous section, it was found that the fits to BABAR [145] and Belle [148] data in the region of the $Y(2175)$ resonance were stable against variation of the contact term in the $\phi(1020)f_0(980)$ kernel. Now there is more sensitivity because the $a_0(980)$ pole positions taken, collected in Table 6.2, are not so close to the $K\bar{K}$ threshold, given in Table 6.3. In this way the three loop point function L_S,

Eq.(6.60), is smaller than in the $f_0(980)$ case so that there is more sensitive to interferences with smaller contributions. For the N/D [90] $a_0(980)$ pole position the local term contributions amounts at around a 20% of the leading L_S contribution. However, for the B/S [158] pole the corrections from the local terms increase significantly with energy above typically 2 GeV. One should notice that $G_1(M_{a_0}^2)^2$ in Eq.(6.66) is larger by around a factor 4 for the B/S pole than for the N/D one. Due to the uncertainties in the pole position and couplings of the $a_0(980)$ resonance and in the local term in $\mathcal{K}_{\phi a_0}$, Eq.(6.66), we cannot arrive to a definite conclusion on the existence of an isovector companion to the $Y(2175)$ in the $\phi(1020)a_0(980)$ system. Nevertheless, we can state that if the $a_0(980)$ properties are close to those predicted by the N/D study of Ref.[90] the present model predicts a resonance behavior of dynamical origin in the $\phi(1020)a_0(980)$ scattering around 1.8-2 GeV.[♯7]

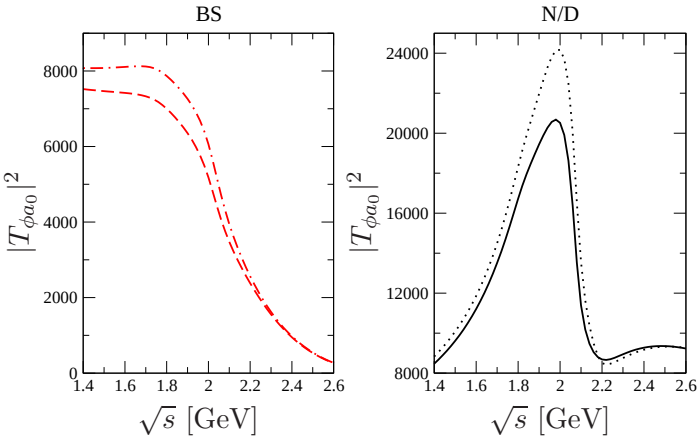

Figure 6.14: (Color online). $|T_{\phi a_0}|^2$ as a function of the ϕa_0 invariant mass evaluated at a fixed $a_0(980)$ pole position (dashed and solid lines) or with a convolution according to Eq. (6.69) (dash-dotted and dotted lines). All curves were obtained with fit 2.

In Fig. 6.13 we show real and imaginary parts of the interaction potential $\mathcal{K}_{\phi a_0}$ for fit 2 and both BS and N/D sets. In the region of $\sqrt{s} = 1.6-2.2$ GeV, where $|T_{\phi a_0}|^2$ has a peak in the N/D case, the imaginary parts corresponding to BS and N/D are quite similar. Instead, the real part for the N/D choice is positive (attractive) in the hole energy range of interest and larger than the BS real part, which even turns negative (repulsive) at $\sqrt{s} < 1.77$ GeV.

[♯7]The N/D study of Ref.[90] is a more elaborated model than that of Ref.[158].

This explains the large differences observed in $|T_{\phi a_0}|^2$. One should stress that $\mathcal{K}_{\phi a_0}$ has an imaginary part due to a number of reasons: the finite $a_0(980)$ width, responsible for the imaginary part of the $a_0(980)$ pole position, the fact that $\gamma^2_{K\bar{K}}$ is complex, and also the imaginary part of $G_1(M^2_{a_0})$. Actually, $\mathcal{K}_{\phi a_0}$ should be interpreted as an optical potential.[♯8]

The $a_0(980)$ pole position has been used as a complex value for the M_{a_0} mass. It is instructive to calculate the amplitude squared taking instead a convolution over the $a_0(980)$ mass distribution according to its width, so that a real mass for the $a_0(980)$ is always used in $G_{\phi a_0}$, which then has its cut along the real axis above threshold as required for two-body unitarity with real masses. Namely, we calculate:

$$|T_{\phi a_0}|^2_{\rm conv}(s) = \frac{1}{N}\int_{{\rm Re}\,(M_{a_0})-\delta}^{{\rm Re}\,(M_{a_0})+\delta} dW \frac{{\rm Im}\,(M_{a_0})}{\{W-{\rm Re}\,(M_{a_0})\}^2+{\rm Im}\,(M_{a_0})^2}|T_{\phi a_0}(s,M_{a_0},W)|^2 \tag{6.69}$$

With $T_{\phi a_0}(s,M_{a_0},W)$ defined as:

$$T_{\phi a_0}(s,M_{a_0},W) = \frac{\mathcal{K}_{\phi a_0}(s,M_{a_0})}{1+\mathcal{K}_{\phi a_0}(s,M_{a_0})G_{a_0 f_0}(s,W)} \tag{6.70}$$

And the normalization:

$$N = \int_{{\rm Re}\,[M_{a_0}]-\delta}^{{\rm Re}\,[M_{a_0}]+\delta} dW \frac{{\rm Im}\,[M_{a_0}]}{(W-{\rm Re}\,[M_{a_0}])^2+{\rm Im}\,[M_{a_0}]^2} \tag{6.71}$$

In the previous equations ${\rm Re}\,(M_{a0})$ and ${\rm Im}\,(M_{a_0})$ are the real and imaginary part taken always positive of the $a_0(980)$ pole position. The integration interval around the maximum of the distribution, characterized by δ, should be enough to cover the region where the $a_0(980)$ strength is concentrated. In Fig. 6.14 we compare the results obtained in this way with those obtained from Eq.(6.67) at a fixed complex M_{a_0}. This is done for fit 2, both BS and N/D parameters and using $\delta = 5{\rm Im}\,(M_{a_0})$. Only small differences arise in the high of the peak so that one can conclude that the two approaches produce the same qualitative features as one would expect on physical reasons.

[♯8] To ensure a continuous limit to zero $a_0(980)$ width, one has to evaluate $\mathcal{K}_{\phi a_0}$ at the $a_0(980)$ pole position with positive imaginary part so that $k^2 \to {\rm Re}\,[M_{a_0}]^2 + i\epsilon$, in agreement with Eq.(6.61). Instead, in $G_{\phi a_0}$ M_{a_0} should appear with a negative imaginary part to guarantee that, in the zero-width limit, the sign of the imaginary part is the same dictated by the $i\epsilon$ prescription of Eq.(6.68). Such analytical extrapolations in the masses of external particles are discussed in Refs.[174, 175, 176].

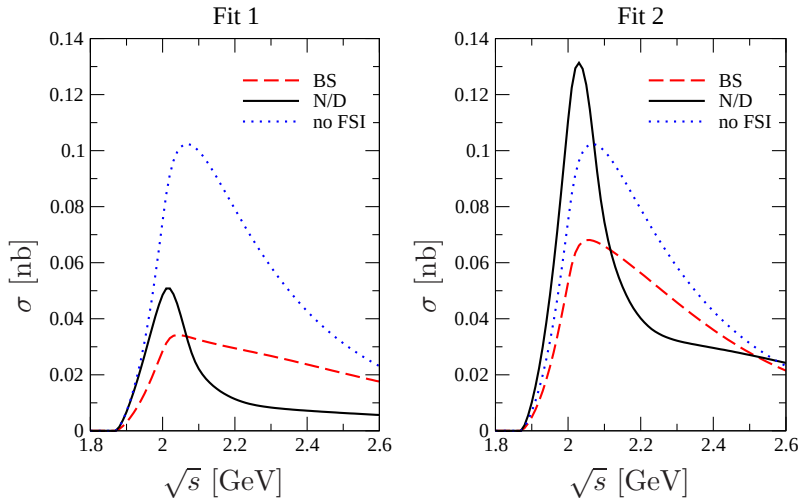

Figure 6.15: (Color online). $e^+e^- \to \phi(1020)\pi^0\eta$ cross section in the $a_0(980)$ region ($M_{\pi\eta} \in [0.85, 1.10]$ GeV). The dotted line in both plots is the result of Ref.[160] where final state $\phi(1020)a_0(980)$ re-scattering was not considered. The rest of the lines include FSI according to Eq. (6.72) for the sets of parameters given in Tables 6.2, 6.3.

- $\phi(1020)\,a_0(980)$ **scattering corrections to** $e^+e^- \to \phi(1020)\pi^0\eta$

The findings described above have direct implications for the $e^+e^- \to \phi(1020)\pi^0\eta$ reaction with the $\pi^0\eta$ invariant mass in the $a_0(980)$ mass region.[♯9] This process has been investigated in Ref.[160] where the presence of the $a_0(980)$ is properly taken into account by replacing the lowest order $K\bar{K} \to \pi\eta$ tree level vertex from $\mathcal{L}_2$, Eq.(6.1), by the unitarized amplitude of Ref.[158]. However, the corrections due $\phi(1020)a_0(980)$ re-scattering (FSI) were not included. Here we consider the impact of these FSI on the total $e^+e^- \to \phi(1020)\pi^0\eta$ cross section using the previously derived $\phi(1020)a_0(980)$ amplitude. Under the assumption that the $e^+e^- \to \phi(1020)\pi^0\eta$ reaction is dominated by the $\phi(1020)a_0(980)$ channel, the cross section after FSI can be cast as [41, 168, 172]:

$$\sigma_{FSI} = \sigma_0 \left| \frac{1}{1 + \mathcal{K}_{\phi a_0}(s) G_{\phi a_0}(s)} \right|^2 \tag{6.72}$$

[♯9]Here, for simplicity, we identify the η_8 state with the physical η particle, neglecting $\eta_8 - \eta_1$ mixing as done in Refs.[158, 90] which have been employed to obtain the meson-meson scattering amplitudes in the $a_0(980)$ channel.

We take σ_0 from Ref.[160] (Fig. 5), which was obtained by integrating the $\pi\eta$ invariant mass $M_{\pi\eta}$ in the $a_0(980)$ region (850-1100 MeV) so that our assumption of ϕa_0 dominance is justified. The results are shown in Fig. 6.15 for the different parameter sets. We find considerable FSI corrections. In particular, for Fit 1 the reduction of the cross section is large, even a factor five at some energies. With the BS choice, the cross section does not exhibit any structure, it just decreases faster after the maximum compared to the one without FSI. Instead, for the N/D set a peak (quite prominent for fit 2) is observed at $\sqrt{s} \sim 2.03$ GeV. These results clearly show the interest of measuring experimentally the $\pi\eta$ invariant mass distribution so as to confirm the existence of this new isovector $J^{PC} = 1^{--}$ resonance that would be observed as a clear peak in data. The existence of this resonance is favored by our results since it appears when the N/D [90] $a_0(980)$ properties are used.

6.4 Summary and conclusions

In this chapter we have studied the $\phi(1020)f_0(980)$ and $\phi(1020)a_0(980)$ S-wave dynamics in the threshold region.

First, the $\phi K\bar{K}$ scattering amplitude at tree level has been determined from the chiral Lagrangians using minimal coupling. The re-scattering of the two kaons in an $I = 0$, S-wave state gives rise to the $f_0(980)$ as a bound state. The residue at the $f_0(980)$ double pole in the initial and final states is used to determine the interaction potential between the resonances $\phi(1020)$ and $f_0(980)$ without introducing new extra free parameters. Afterwards, the $\phi(1020)f_0(980)$ S-wave scattering amplitude is determined by resuming the unitarity loops or right hand cut. Resonant peaks with mass and width in agreement with those of the $Y(2175)$ are obtained within the approach. In addition, we are able to describe the $e^+e^- \to \phi(1020)f_0(980)$ experimental data [144, 145, 148] in terms of the resulting $\phi(1020)f_0(980)$ S-wave amplitude using natural values of the coupling g^2 and the subtraction constant a_1. The negative value of g^2 is reasonable, viewed as a parameter that accounts for the ϕK scattering above the $K_1(1400)$ resonance. The negative values of a_1 is characteristic of dynamically generated resonances. Nonetheless, the a_1 values required to obtain the $Y(2175)$ resonance at the nominal mass of 2.18 GeV [145, 147] are larger in modulus than those obtained in our direct fits to $e^+e^- \to \phi(1020)f_0(980)$ data. The latter values fit better for interpreting the $Y(2175)$ as mainly a $\phi(1020)f_0(980)$ dynamically generated resonance while the former ones tend to indicate some extra (preexisting) contribution. Taking into account both possibilities, our results suggest that the $Y(2185)$ is a resonant with at least a large $\phi(1020)f_0(980)$ component.

Later, we studied the $I = 1$ S-wave $\phi(1020)a_0(980)$ dynamics around threshold paying special attention to the possible dynamical generation of an isovector $J^{PC} = 1^{--}$ scalar resonance. Following the approach of Sec. 6.2, where the related isoscalar S-wave $\phi(1020)f_0(980)$ scattering was investigated, we first considered the scattering of a $\phi(1020)$ resonance with a pair of light pseudoscalar mesons at tree level using chiral Lagrangians coupled to vector mesons by minimal coupling. The re-scattering of the two pseudoscalars in $I = 1$ and S-wave generates dynamically the $a_0(980)$. We have used the information about this state (pole position and residue in the $K\bar{K}$ channel) from two different studies of meson-meson scattering in coupled channels for determining the $\phi(1020)a_0(980)$ scattering potential without introducing new extra free parameters. Afterwards the full amplitude is obtained by resummation of the $\phi(1020)a_0(980)$ loops. The parameter g^2, characterizing $\phi(1020)K$ scattering at threshold, and the ϕa_0 subtraction constant a_1 are obtained from two different fits to $e^+e^- \to \phi(1020)f_0(980)$ BABAR [145] and Belle [148] data. We find that if the physical $a_0(1980)$ properties correspond to those extracted with the N/D method in Ref.[90] (see Table 6.2), the present model predicts a resonance of dynamical origin around 1.8-2 GeV. A broader resonance is also generated when the $a_0(980)$ pole position and couplings are taken from Ref.[158] if the strength of the local term in the $\phi(1020)a_0(980)$ interaction kernel is reduced.

Furthermore, we have determined the $\phi(1020)a_0(980)$ final state interactions that strongly modify the cross section for the reaction $e^+e^- \to \phi(1020)\pi^0\eta$ when the $\pi^0\eta$ invariant mass is in the $a_0(980)$ region. If the $a_0(980)$ properties from the N/D method are taken, a strong clearly visible peak around 2.03 GeV is observed, signaling the presence of the dynamically generated isovector 1^{--} resonance. For the other $a_0(980)$ pole taken from Ref.[158] no peak is generated but a strong reduction of the cross-section takes place. These results further support the idea that a study of the $e^+e^- \to \phi(1020)a_0(980)$, which should be accessible at present e^+e^- factories [144, 147, 148], may provide novel relevant information about hadronic structure and interaction in the 2 GeV region.

Chapter 7

Summary and Outlook

In this thesis we deal first with the problem of describing the πN scattering process in the low-energy domain. This is a fundamental problem which gives access to many open questions in physics since, at low energies, allows to test the chiral dynamics of QCD in the one nucleon sector, and is essential for *ab initio* calculations of the nuclear structure. Moreover, it also allows to study the effects of isospin violation in nuclear phenomena. On the other hand, at higher energies πN provides a way to explore the baryonic spectrum of QCD and nucleon resonances. However, from the theoretical point of view, there are open questions not satisfactorily answered yet, as the exact value of the pion-nucleon coupling constant ($g_{\pi N}$) or the value of the pion-nucleon sigma term ($\sigma_{\pi N}$). The latter is specially important for the understanding of the internal scalar structure of the ordinary matter and has direct applications in the calculations of QCD phase diagrams, nuclear matter approaches and direct detection of dark matter.

At low energies, πN scattering can be studied within Chiral Perturbation Theory, which takes into account the spontaneously broken chiral symmetry that rules the low energy interaction of the Goldstone boson (identified with the pions in the $SU(2)$ sector) with the nucleon, including the symmetry breaking terms due to the non-vanishing mass of the light quarks. But, despite the numerous efforts made in this direction, we had not a satisfactory chiral representation of the πN scattering amplitude valid in the low-energy domain that allow us to extract reliably the relevant information mentioned above.

In Chapter 4 we present the results of Ref.[21], where we studied the πN scattering within the IR scheme. In this research we found that, although IR described the physical region better than a previous work showed [43], this method gives rise to an unphysically large value for the Goldberger-Treiman

relation [21], confirming the result of [43] for this quantity. This could have been a serious problem for ChPT with baryons since a so large deviation from the exact Goldberger-Treiman relation could indicate a breaking in the convergence pattern. Another important question not studied before in ChPT is the behavior of the $SU(2)$ kernel of under unitarization techniques. Such techniques can be of special interest in the $SU(3)$ strangeness -1 sector, where the existence of the $\Lambda(1405)$ under the $\bar{K}N$ threshold needs the application of nonperturbative techniques. Our result show that unitarized ChPT allows to extend the range of validity of the IR-BChPT amplitude but, due to the unphysical cuts introduced by the IR method, the high energy description of the phase shifts is very limited. From these results we conclude that the IR method is not appropriate to study the $SU(3)$ sector.

However, in Chapter 5 we overcome the previous difficulties found within the IR method by applying the EOMS scheme. As explained in this chapter, this scheme allows us to solve the power counting problem of BChPT without altering the analytical properties of a covariant calculation. First, it is observed that EOMS reproduce the phase shifts better than IR. More importantly, within this scheme we obtain a value for the GT deviation compatible with theoretical and experimental bounds, solving the problem that IR has with this quantity and leaving clear that it was an intrinsic problem of IR, not a convergence problem of BChPT. We also included the contribution of the resonance up to $\mathcal{O}(q^3)$ in the δ counting and achieved an excellent description of the phase shifts up to energies of $\sqrt{s} = 1.20$ GeV (just below the resonance region). By extrapolating our amplitudes to the subthreshold region we checked that the EOMS-BChPT fitted in the physical low-energy region including the $\Delta(1232)$-resonance also achieves a good convergence in the subthreshold region, being able to reproduce subthreshold quantities obtained previously by dispersive approaches. This is a remarkable result since after the IR analysis of Ref.[19] it was though that BChPT could not connect both regions. The good convergence also allowed us to extract a reliable and accurate value of the pion-nucleon sigma term. Based in modern pion-factory data we obtain $\sigma_{\pi N} = 59(7)$ MeV. We also discuss the impact of this result on the estimation of the strangeness content of the nucleon and nuclear matter approaches, showing that relatively large value of $\sigma_{\pi N}$ is not at odds with the established phenomenology. On the other hand, we studied the application of unitarization techniques on the EOMS kernel and observed a remarkable improvement compared with the IR results. This is due to the good analytical properties of a covariant calculation that are preserved by the EOMS scheme.

The main conclusion of these researches is that only EOMS provides a

representation of the chiral amplitude consistent with the standard power counting of ChPT that preserves the good analytical properties of a relativistic calculation. In addition, with the inclusion of the $\Delta(1232)$ as an explicit degree of freedom, it achieves the best convergence in the low-energy region (below the $\Delta(1232)$ region, including the subthreshold one). This representation allowed us to extract a reliable value of $\sigma_{\pi N}$ from PWAs.

However, since our result relies on the PWAs, the next step for this $SU(2)$ calculation will be the extraction of these information directly from cross section data. For this task, it will be necessary to include consistently the isospin breaking effects due to electromagnetism and the quark mass differences. This would allow us to check our extracted value for $\sigma_{\pi N}$ and provide the community with an independent PWA based on a effective field theory analysis. On the other hand, it will be of special interest the application of the methodology described in Chapter 5 to the study of pion photoproduction experiments, currently running at MAMI, JLab and ELSA.

The immediate extension of this work will be to the $SU(3)$ sector, where the convergence of the chiral series is expected to be worse. First, we will use the result obtained for $\sigma_{\pi N}$ to obtain an estimation of the strangeness content of the nucleon σ_s including the effects of the decuplet resonances. Second, we will calculate the $SU(3)$ meson-baryon scattering in EOMS-BChPT. There, the good analytical properties of this scheme could make a difference respect to previous ChPT works. Surely this will manifest in the strangeness -1 sector, where unitarization methods become indispensable due to the presence of bound states below the threshold. The $SU(3)$ kernel obtained could be directly applied to the study of strangeness photoproduction experiments running at MAMI, JLab and ELSA, by means of the chiral unitary approach.

On the other hand, the phenomenological approach followed in Chapter 6 allowed us to study the nature of the $Y(2175)$. We showed that the properties of this resonance can be well described by a $\phi(1020)f_0(980)$ resonant state. In fact, the values obtained for our free parameters indicates that the $Y(2175)$-resonance has, at least, a large $\phi(1020)f_0(980)$ component. These values allowed us to investigate the possibility of an isovector companion of the $Y(2175)$. This was done by studying the $\phi(1020)a_0(980)$ final state interaction that modify the $e^+e^- \to \phi(1020)\pi^0\eta$ when the $\pi^0\eta$ invariant mass is in the $a_0(980)$ region. We concluded that, for some values of the free parameters, the presence of an isovector companion for the $Y(2175)$ is revealed. The next step of this research will be the study of the reaction $e^+e^- \to \phi(1020)K^+K^-$ within unitary chiral perturbation theory.

Appendix A

The Goldstone Theorem*

In this section we will show the Goldstone theorem for the relativistic, infinite degrees of freedom case. The Goldstone theorem states that when a continuous global symmetry is *spontaneously broken*[♯1] then appear new massless[♯2] scalar particles in the spectrum that have the same quantum numbers than the generators associated to the charges that do not preserve the ground state. Those particles are called *Goldstone bosons*.

Consider a Lagrangian which is invariant under the transformation of the group G and let A an observable not invariant under the broken symmetry generators. We consider the commutator evaluated in the ground state $|0\rangle$:

$$\begin{aligned}\langle 0|\left[J^\mu(y),A(x)\right]|0\rangle &= \sum_N(\langle 0|J^\mu(y)|N\rangle\langle N|A(x)|0\rangle - \langle 0|A(x)|N\rangle\langle N|J^\mu(y)|0\rangle) = \\ &= \sum_N(\langle 0|J^\mu(0)|N\rangle\langle N|A(0)|0\rangle e^{-ip_N(y-x)} - \langle 0|A(0)|N\rangle\langle N|J^\mu(0)|0\rangle e^{-ip_N(x-y)}) = \\ &= \frac{i}{(2\pi)^3}\int d^4p\left[\rho_N^\mu(p)e^{-ip(y-x)} - \tilde{\rho}_N^\mu(p)e^{-ip(x-y)}\right] \qquad \text{(A.1)}\end{aligned}$$

Where an spectral resolution of the identity was inserted in the first line and the fact that the four-momentum operator is the generator of the space-time translations was used in the second line. The spectral functions ρ and $\tilde{\rho}$ are defined as follows:

*We follow here the proof provided by Weinberg in [48].

♯1Spontaneously broken means that the Noether currents of the symmetry are conserved but the ground state is not invariant under the action of all the charges associated to that currents.

♯2If the symmetry is exact. If not, they acquire a mass.

$$\rho_N^\mu(p) = -i(2\pi)^3 \sum_N \langle 0|J^\mu(0)|N\rangle\langle N|A(0)|0\rangle \delta^{(4)}(p-p_N) \quad (A.2)$$

$$\tilde{\rho}_N^\mu(p) = -i(2\pi)^3 \sum_N \langle 0|A(0)|N\rangle\langle N|J^\mu(0)|0\rangle \delta^{(4)}(p-p_N) \quad (A.3)$$

Due to Lorentz covariance and that $p_N^0 \geq 0$ (because p_N represent the four-momentum of the physical state N), we can state that:

$$\rho_N^\mu(p) = p^\mu \rho_N(p^2)\theta(p^0) \quad (A.4)$$

$$\tilde{\rho}_N^\mu(p) = p^\mu \tilde{\rho}_N(p^2)\theta(p^0) \quad (A.5)$$

So, we have:

$$\begin{aligned}
&\langle 0|\left[J^\mu(y), A(x)\right]|0\rangle = \\
&\frac{i}{(2\pi)^3}\int d^4p \left[p^\mu \rho_N(p^2)\theta(p^0)e^{-ip(y-x)} - p^\mu \tilde{\rho}_N(p^2)\theta(p^0)e^{-ip(x-y)}\right] = \\
&\frac{1}{(2\pi)^3}\frac{\partial}{\partial y_\mu}\int d^4p \left[\rho_N(p^2)\theta(p^0)e^{-ip(y-x)} + \tilde{\rho}_N(p^2)\theta(p^0)e^{-ip(x-y)}\right]
\end{aligned} \quad (A.6)$$

Writing $\rho_N(p^2) = \int d\mu^2 \delta(p^2-\mu^2)\rho_N(\mu^2)$ and $\tilde{\rho}_N(p^2) = \int d\mu^2 \delta(p^2-\mu^2)\tilde{\rho}_N(\mu^2)$, and introducing it into (A.6):

$$\begin{aligned}
\langle 0|\left[J^\mu(y), A(x)\right]|0\rangle = \frac{1}{(2\pi)^3}\frac{\partial}{\partial y_\mu}\int d\mu^2 \Big[\rho_N(\mu^2) \underbrace{\int d^4p\ \theta(p^0)e^{-ip(y-x)}\delta(p^2-\mu^2)}_{(2\pi)^3\Delta_+(y-x;\mu^2)} + \\
+ \tilde{\rho}_N(\mu^2) \underbrace{\int d^4p\ \theta(p^0)e^{-ip(x-y)}\delta(p^2-\mu^2)}_{(2\pi)^3\Delta_+(x-y;\mu^2)}\Big]
\end{aligned} \quad (A.7)$$

Lorentz invariance only allow $\Delta_+(z;\mu^2)$ to depend on z^2, μ^2 and $\theta(z^0)$ for z timelike and, for z spacelike, only depends on z^2 and μ^2. So, for a spacelike dependence $\Delta_+(y-x;\mu^2) = \Delta_+(x-y;\mu^2)$. Microcausality involves that the commutator of two operators spacelike separated vanishes, so for $(y-x)$ spacelike, we have:

$$0 = \langle 0|\left[J^\mu(y), A(x)\right]|0\rangle = \frac{\partial}{\partial y_\mu}\int d\mu^2 \Big[\rho_N(\mu^2) + \tilde{\rho}_N(\mu^2)\Big]\Delta_+(y-x;\mu^2) \quad (A.8)$$

And we can conclude that $\rho_N(\mu^2) = -\tilde{\rho}_N(\mu^2)$ (note that this relation does not depend on the spacetime separation $x - y$). So we can write, without loss of generality:

$$\langle 0| \left[J^\mu(y), A(x)\right] |0\rangle = \frac{\partial}{\partial y_\mu} \int d\mu^2 \rho_N(\mu^2) \Big[\Delta_+(y-x;\mu^2) - \Delta_+(x-y;\mu^2)\Big] \tag{A.9}$$

Because J^μ is a conserved current, $\partial_\mu J^\mu(y) = 0$, and applying this to the commutator:

$$\begin{aligned} 0 = \langle 0| \left[\frac{\partial J^\mu(y)}{\partial y^\mu}, A(x)\right] |0\rangle &= \Box_y \int d\mu^2 \rho_N(\mu^2) \Big[\Delta_+(y-x;\mu^2) - \Delta_+(x-y;\mu^2)\Big] \\ &= -\int d\mu^2 \mu^2 \rho_N(\mu^2) \Big[\Delta_+(y-x;\mu^2) - \Delta_+(x-y;\mu^2)\Big] \end{aligned} \tag{A.10}$$

Where in the last line we have made use that $\Delta_+(y;\mu^2)$ satisfies the equation $(\Box_y + \mu^2)\Delta_+(y-x;\mu^2) = 0$.

For a timelike separation $\Delta_+(z;\mu^2)$ is *not* even and we have in this case, from (A.10):

$$\mu^2 \rho_N(\mu^2) = 0 \tag{A.11}$$

We could conclude prematurely that $\rho_N(\mu^2)$ vanishes for all μ^2, but for a broken symmetry this is *not* possible. To illustrate that, we can consider (A.9) and take the temporal component. After taking the derivative, it results at equal times:

$$\begin{aligned} &\langle 0| \left[J^0(\vec{y},t), A(\vec{x},t)\right] |0\rangle = \\ &\frac{-2i}{(2\pi)^3} \int d\mu^2 \rho_N(\mu^2) \Big[\int d^4p \sqrt{\vec{p}^{\,2} + \mu^2} \delta(p^2 - \mu^2) e^{i\vec{p}\cdot(\vec{y}-\vec{x})} \theta(p^0) \Big] \end{aligned} \tag{A.12}$$

Performing the integral in p:

$$\langle 0| \left[J^0(\vec{y},t), A(\vec{x},t)\right] |0\rangle = -i\delta(\vec{y}-\vec{x}) \int d\mu^2 \rho_N(\mu^2) \tag{A.13}$$

Integrating in the $\vec{y}$ variable, we obtain the charge in the commutator, and from the previous equation we obtain:

$$\langle 0| \left[Q(t), A(\vec{x}, t)\right] |0\rangle = -i \int d\mu^2 \rho_N(\mu^2) \neq 0 \tag{A.14}$$

The previous equation cannot vanish because the symmetry is broken. Equations (A.11) and (A.14) can only be reconciled if:

$$\rho_N(\mu^2) = i\delta(\mu^2)\langle 0| \left[Q(t), A(\vec{x}, t)\right] |0\rangle^{\sharp 3} \tag{A.15}$$

And pointing out that $\langle N|A(0)|0\rangle$ is rotationally invariant and must vanish for any state N which has non-zero helicity, and that $\langle 0|J^0(0)|N\rangle$ vanishes for any state N that has different intrinsic parity or internal quantum numbers from J^0, we can conclude that *for every generator that does not leave invariant the ground state, we have in the spectrum a massless particle with spin zero and the same parity and quantum numbers than the corresponding generator*. These particles are called *Goldstone bosons*.[♯4]

[♯3]The term proportional to $\delta(\mu^2)$ only arises in a theory that has massless particles because otherwise the spectrum of center-of-mass squared energies p_N^2 would not extend down to zero.

[♯4]The above argument breaks down when the spontaneously broken symmetry is a local rather than a global symmetry.

Appendix B

Generalization of IR

The procedure explained in Chapter 4 can be extended to scalar integrals with more mesonic and baryonic propagators by combining all of each type into one unique propagator. This can be done by using the next trick [97]:

$$\frac{1}{a_1 \dots a_m} = \left(-\frac{\partial}{\partial M^2}\right)^{(m-1)} \int_0^1 dx_1 \dots \int_0^1 dx_{m-1} \frac{X}{A}$$

Where the a_i $(i = 1, \dots, m)$ correspond to m mesonic propagators of mass M^2 and internal momenta $k - P_i$. On the other hand, the numerator is given by:

$$\text{If } m = 2: \qquad X = 1 \tag{B.1}$$

$$\text{If } m > 2: \qquad X = x_2 (x_3)^2 \dots (x_{m-1})^{m-2} \tag{B.2}$$

And the denominator is obtained recursively for:

$$A_{p+1} = x_p A_p + (1 - x_p) a_{p+1} \quad (p = 1, \dots, m-1) \tag{B.3}$$

$$A_1 = a_1, \qquad A = A_m \tag{B.4}$$

Where the result for A is always quadratic in k, obtaining an expression with the next shape:

$$A = \bar{A} - (k - \bar{q})^2 - i\epsilon \tag{B.5}$$

Here the $\bar{A}$ term is of $\mathcal{O}(q^2)$, while $\bar{q}$ represents a linear combination of external momenta and is of $\mathcal{O}(q)$.

For several baryonic propagators we can use the same strategy, obtaining a denominator of the form:

$$B = \bar{B} - (\bar{P} - k)^2 - i\epsilon \tag{B.6}$$

With $\bar{P}^2 = m^2 + \mathcal{O}(q)$, $\bar{B} = m^2 + \mathcal{O}(q)$.

Appendix C

Tree Level Calculations

In this Appendix we show the results concerning the tree level calculation of πN scattering. The Born-terms, which are expressed in terms of the Mandelstam variables s and u, include also their crossed version.

C.1 $\mathcal{O}(q)$

- Born-term:

$$A^+(s,t,u) = \frac{g^2(m_2+m_N)}{4f^2}\left[\frac{s-m_N^2}{s-m_2^2}+\frac{u-m_N^2}{u-m_2^2}\right]$$
$$B^+(s,t,u) = -\frac{g^2}{4f^2}\left[\frac{(s+2m_2m_N+m_N^2)}{(s-m_2^2)}-\frac{(u+2m_2m_N+m_N^2)}{(u-m_2^2)}\right]$$
$$A^-(s,t,u) = \frac{g^2(m_2+m_N)}{4f^2}\left[\frac{s-m_N^2}{s-m_2^2}-\frac{u-m_N^2}{u-m_2^2}\right]$$
$$B^-(s,t,u) = -\frac{g^2}{4f^2}\left[\frac{(s+2m_2m_N+m_N^2)}{(s-m_2^2)}+\frac{(u+2m_2m_N+m_N^2)}{(u-m_2^2)}\right]$$

Where $m_2 \equiv m - 4c_1M^2$ includes the $\mathcal{O}(q^2)$ correction to the nucleon mass.

- Contact term:

$$A^+(s,t,u) = B^+(s,t,u) = A^-(s,t,u) = 0$$
$$B^-(s,t,u) = \frac{1}{2f^2}$$

C.2 $\mathcal{O}(q^2)$

- Contact term:

$$A^+(s,t,u) = \frac{1}{f_\pi^2}\left[-4c_1M_\pi^2 + \frac{c_2(s-u)^2}{8m_N^2} + c_3(2M_\pi^2 - t)\right] + \mathcal{O}(q^4)$$
$$B^+(s,t,u) = 0$$
$$A^-(s,t,u) = -\frac{c_4(s-u)}{2f_\pi^2}$$
$$B^-(s,t,u) = \frac{2c_4m_N}{f_\pi^2}$$

C.3 $\mathcal{O}(q^3)$

- Born-term:

$$A^+(s,t,u) = \frac{4g(2d_{16}-d_{18})m_NM_\pi^2}{f_\pi^2}$$
$$B^+(s,t,u) = \frac{4g(2d_{16}-d_{18})m_N^2M_\pi^2(s-u)}{f_\pi^2(s-m_N^2)(u-m_N^2)}$$
$$A^-(s,t,u) = 0$$
$$B^-(s,t,u) = \frac{2g(2d_{16}-d_{18})M_\pi^2(3m_N^4 - su - m_N^2(s+u))}{f_\pi^2(s-m_N^2)(u-m_N^2)}$$

- Contact term:

$$A^+(s,t,u) = -\frac{(d_{14}-d_{15})(s-u)^2}{4m_Nf_\pi^2} + \mathcal{O}(q^4)$$
$$B^+(s,t,u) = \frac{(d_{14}-d_{15})(s-u)}{f_\pi^2} + \mathcal{O}(q^3)$$
$$A^-(s,t,u) = \frac{s-u}{2m_Nf_\pi^2}\left[2(d_1+d_2+2d_5)M_\pi^2 - (d_1+d_2)t + 2d_3(s-u)^2\right] + \mathcal{O}(q^5)$$
$$B^-(s,t,u) = 0$$

C.4 The $\Delta(1232)$ contribution

The Born-term with the exchange of a $\Delta(1232)$-resonance $\Delta(1232)$is the only contribution to the πN scattering amplitude that we need to include up to $\mathcal{O}(q^3)$. In Fig. C.1 we show the $\mathcal{O}(q^{3/2})$ contribution of the $\Delta(1232)$ to the πN amplitude:

Figure C.1: Diagram corresponding to the insertion of the Δ propagator (double line) in the πN Born-term. The filled circles correspond to vertices of $\mathcal{L}^{(1)}_{\Delta N\pi}$.

For the s-channel exchange we have:

$$
\begin{aligned}
A^{\pm}(s,t) &= -\frac{h_A^2}{4f_\pi^2 m_\Delta^2} C_I^{\pm} \frac{1}{s-m_\Delta^2} \left(m_N^5 - 2\left(M_\pi^2+2s\right) m_N^3 - 2m_\Delta \left(M_\pi^2+s\right) m_N^2 \right. \\
&\left. + \left(M_\pi^4 - 4sM_\pi^2 + 3s(s+t)\right) m_N + 2m_\Delta \left(m_\pi^2 - s\right)^2 + 3m_\Delta st \right) \\
B^{\pm}(s,t) &= -\frac{h_A^2}{4f_\pi^2 m_\Delta^2} C_I^{\pm} \frac{1}{s-m_\Delta^2} \left(m_N^4 - 2\left(M_\pi^2+3s\right) m_N^2 \right. \\
&\left. -2m_\Delta \left(m_N^2 - M_\pi^2 + s\right) m_N + \left(M_\pi^2 - s\right)^2 + 3st \right)
\end{aligned}
\tag{C.1}
$$

With $C_I^+ = 1/9$ and $C_I^- = -1/18$. For the full result one should also add the $\Delta(1232)$ u-channel exchange that can be easily obtained from the previous equation by crossing. The general rule is given in Appendix D.3.

At $\mathcal{O}(q^{5/2})$, we have the following corrections to the Born-term contribution in the s-channel (Fig. C.2):

$$
\begin{aligned}
A_2^{\pm}(s,t) &= \frac{h_A}{2f_\pi^2 m_\Delta^2} C_I^{\pm} \frac{F_A(s,t)}{s-m_\Delta^2} \\
B_2^{\pm}(s,t) &= \frac{h_A}{2f_\pi^2 m_\Delta^2} C_I^{\pm} \frac{F_B(s,t)}{s-m_\Delta^2}
\end{aligned}
\tag{C.2}
$$

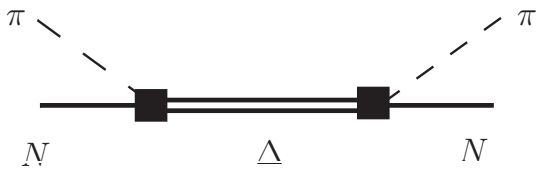

Figure C.2: Diagram corresponding to the insertion of the Δ propagator (double line) in the πN Born-term. The filled squares correspond to vertices of $\mathcal{L}^{(2)}_{\Delta N\pi}$.

With:

$$
\begin{aligned}
F_A(s,t) = \frac{1}{6m_\Delta}\Big(&d_4^\Delta\left(m_N^2 - M_\pi^2 - s\right)\left(m_N^5 - 2\left(M_\pi^2 + 2s\right)m_N^3\right.\\
&-2m_\Delta\left(M_\pi^2 + s\right)m_N^2 + \left(M_\pi^4 - 4sM_\pi^2 + 3s(s+t)\right)m_N + 2m_\Delta\left(M_\pi^2 - s\right)^2\\
&+3stm_\Delta) + 2d_3^\Delta m_\Delta\left(-m_N^6 + 2\left(M_\pi^2 + 2s\right)m_N^4 - \left(M_\pi^4 - 2sM_\pi^2\right.\right.\\
&\left.\left.+s(5s+3t)\right)m_N^2 + m_\Delta\left(\left(m_N^2 - s\right)^2 - M_\pi^4\right)m_N + s\left(2\left(M_\pi^2 - s\right)^2 + 3st\right)\right)\Big)
\end{aligned}
$$

$$
\begin{aligned}
F_B(s,t) = \frac{1}{6m_\Delta}\Big(&d_4^\Delta\left(m_N^2 - M_\pi^2 - s\right)\left(m_N^4 - 2\left(M_\pi^2 + 3s\right)m_N^2\right.\\
&-2m_\Delta\left(m_N^2 - m_\pi^2 + s\right)m_N + \left(M_\pi^2 - s\right)^2 + 3st\Big) + 2d_3^\Delta m_\Delta\left(m_\Delta\left(3m_N^4\right.\right.\\
&\left.-4\left(m_\pi^2 + s\right)m_N^2 + \left(M_\pi^2 - s\right)^2 + 3st\right) - m_N\left(m_N^4 - 2\left(M_\pi^2 + 2s\right)m_N^2\right.\\
&\left.\left.+M_\pi^4 - 4m_\pi^2 s + 3s(s+t)\right)\right)\Big)
\end{aligned}
$$

With the new contributions, there are two new constants to fit, d_3^Δ and d_4^Δ. In the HB limit these two constants seem to have the same contribution and what matters is a combination of both. These contributions are subleading, scale as E_π at low-energies and are suppressed by one factor of M_π^2 in the subthreshold region as compared with the leading contribution. However, it could have more important contributions for higher energies. What we observe in our fits up to $\sqrt{s}_{\rm max} = 1.20$ GeV is that these constants gives very small values compatible with zero (within errors) so, in order to reduce the correlations and the number of free parameters we decided to set $d_3^\Delta = d_4^\Delta = 0$.

Appendix D

Loop Level Calculations

In this section we list the scalars and tensor integrals needed for the one-loop calculations performed in this thesis. These integrals, calculated in dimensional regularization, are denoted by $\mathcal{H}_{mn}$, where the subscripts m and n correspond to the number of mesonic and baryonic propagators, in order, that each integral has.

We will use the following variables:

$$\begin{aligned}\Sigma^\mu &= (P+q)^\mu = (P'+q')^\mu \\ \Delta^\mu &= (q'-q)^\mu = (P-P')^\mu \\ Q^\mu &= (P'+P)^\mu\end{aligned}$$

Were P (P') corresponds to the incoming (outgoing) nucleon and q (q') to the incoming (outgoing) pion, so $P^2 = P'^2 = m_N^2$ and $q^2 = q'^2 = M_\pi^2$.

We also give explicit expressions for some scalar integrals that are needed in Chapter 5.

D.1 Definitions

- **1 meson, 0 nucleons:**

$$\begin{aligned}\mathcal{H}_{10} &= \frac{1}{i}\int \frac{d^dk}{(2\pi)^d}\frac{1}{M^2-k^2} \\ \mathcal{H}_{10} &= 2\bar{\lambda}M^2 + \frac{M^2}{16\pi^2}\log\left(\frac{M^2}{\mu^2}\right)\end{aligned} \tag{D.1}$$

- **0 mesons, 1 nucleon:**

$$\begin{aligned}\mathcal{H}_{01} &= \frac{1}{i}\int\frac{d^dk}{(2\pi)^d}\frac{1}{m^2-k^2}\\ \mathcal{H}_{01} &= 2\bar{\lambda}m^2+\frac{m^2}{16\pi^2}\log\left(\frac{m^2}{\mu^2}\right)\end{aligned} \tag{D.2}$$

- **2 mesons, 0 nucleon:**

$$\begin{aligned}\{\mathcal{H}_{20},\mathcal{H}^{\mu}_{20}\} &= \frac{1}{i}\int\frac{d^dk}{(2\pi)^d}\frac{\{1,k^{\mu}\}}{(M^2-k^2)(M^2-(k-\Delta)^2)}\\ \mathcal{H}^{\mu}_{20} &= \frac{\Delta^{\mu}}{2}\mathcal{H}_{20}(t)\\ \mathcal{H}^{\mu\nu}_{20} &= (\Delta^{\mu}\Delta^{\nu}-g^{\mu\nu}\Delta^2)\mathcal{H}^{(1)}_{20}(t)+\Delta^{\mu}\Delta^{\nu}\mathcal{H}^{(2)}_{20}(t)\end{aligned}$$

- **1 meson, 1 nucleon:**

$$\begin{aligned}\{\mathcal{H}_{11},\mathcal{H}^{\mu}_{11}\} &= \frac{1}{i}\int\frac{d^dk}{(2\pi)^d}\frac{\{1,k^{\mu}\}}{(M^2-k^2)(m^2-(P-k)^2)}\\ \mathcal{H}_{11}(P^2) &= -2\bar{\lambda}+\frac{1}{16\pi^2}\left\{1+\log\left(\frac{\mu^2}{m^2}\right)-\frac{P^2-m^2+M^2}{2P^2}\log\left(\frac{M^2}{m^2}\right)\right.\\ &\quad+\frac{\sqrt{4M^2P^2-(P^2-m^2+M^2)^2}}{P^2}\\ &\quad\times\left[\arctan\left(\frac{m^2-M^2-P^2}{\sqrt{4M^2P^2-(P^2-m^2+M^2)^2}}\right)\right.\\ &\quad\left.\left.-\arctan\left(\frac{m^2-M^2+P^2}{\sqrt{4M^2P^2-(P^2-m^2+M^2)^2}}\right)\right]\right\}\\ \mathcal{H}^{\mu}_{11} &= P^{\mu}\mathcal{H}^{(1)}_{11}(P^2)\end{aligned} \tag{D.3}$$

- **0 mesons, 2 nucleons:**

$$\mathcal{H}_{02} = \frac{1}{i}\int\frac{d^dk}{(2\pi)^d}\frac{1}{(m^2-k^2)(m^2-(k-\Delta)^2)}$$

- **2 mesons, 1 nucleon:**

$$\{\mathcal{H}_{21}, \mathcal{H}^{\mu}_{21}, \mathcal{H}^{\mu\nu}_{21}\} = \frac{1}{i}\int \frac{d^dk}{(2\pi)^d} \frac{\{1, k^\mu, k^{\mu\nu}\}}{(M^2-k^2)(M^2-(k-\Delta)^2)(m^2-(P-k)^2)}$$
$$\mathcal{H}^{\mu}_{21} = Q^\mu \mathcal{H}^{(1)}_{21}(t) + \frac{1}{2}\Delta^\mu \mathcal{H}_{21}(t)$$
$$\mathcal{H}^{\mu\nu}_{21} = g^{\mu\nu}\mathcal{H}^{(2)}_{21}(t) + Q^\mu Q^\nu \mathcal{H}^{(3)}_{21}(t) + \Delta^\mu\Delta^\nu \mathcal{H}^{(4)}_{21}(t) + \frac{1}{2}(\Delta^\mu Q^\nu + Q^\mu \Delta^\nu)\mathcal{H}^{(1)}_{21}(t)$$

- **1 meson, 2 nucleon:**

$$\{\mathcal{H}_{12}, \mathcal{H}^{\mu}_{12}, \mathcal{H}^{\mu\nu}_{12}\} = \frac{1}{i}\int \frac{d^dk}{(2\pi)^d} \frac{\{1, k^\mu, k^{\mu\nu}\}}{(M^2-k^2)(m^2-(P_1-k)^2)(m^2-(P_2-k)^2)}$$

For the topologies displayed in Fig. 3.2, one of the momenta is always on-shell. Choosing this momentum to be P_1, we have for the diagram (m): $P_1 = P$ and $P_2 = P'$. This case defines the integral $\mathcal{H}_A(t)$ as follows:

$$\mathcal{H}_A(t) = \mathcal{H}_{12}(m_N^2, t)$$

For this case, the tensor decomposition is defined as:

$$\mathcal{H}^{\mu}_{A}(t) = Q^\mu \mathcal{H}^{(1)}_{A}(t)$$
$$\mathcal{H}^{\mu\nu}_{A}(t) = g^{\mu\nu}\mathcal{H}^{(2)}_{A}(t) + Q^\mu Q^\nu \mathcal{H}^{(3)}_{A}(t) + \Delta^\mu\Delta^\nu \mathcal{H}^{(4)}_{A}(t)$$

For the diagrams (c), (d), (g) and (h) we have instead $P_1 = P$ and $P_2 = P + q$. This case defines the integral $\mathcal{H}_B(s)$ as follows:

$$\mathcal{H}_B(s) = \mathcal{H}_{12}(s, M_\pi^2)$$

For this case, the tensor decomposition is defined as:

$$\mathcal{H}^{\mu}_{B} = Q^\mu \mathcal{H}^{(1)}_{B}(s) + \Delta^\mu \mathcal{H}^{(2)}_{B}(s)$$

- **0 mesons, 3 nucleon:**

$$\mathcal{H}_{03} = \frac{1}{i}\int \frac{d^d k}{(2\pi)^d} \frac{1}{(m^2-k^2)(m^2-(k-P_1)^2)(m^2-(k-P_2)^2}$$

This integral can appear in two different configurations. In the first one $P_1 = q$ and $P_2 = q'$, which is labeled in Secs. D.2 and D.3 as $\mathcal{H}_{03}(t, M^2)$. For this case its dependence on the t variable comes from the combination $(P_1 - P_2)^2$. For the second configuration, however, the t dependence comes from P_2^2, because in this second case $P_1 = q$ and $P_2 = q - q'$. This configuration is labeled in Secs. D.2 and D.3 as $\mathcal{H}_{03}(M^2, t)$.

- **1 meson, 3 nucleon:**

$$\{\mathcal{H}_{13}, \mathcal{H}^{\mu}_{13}\} = \frac{1}{i}\int \frac{d^d k}{(2\pi)^d} \frac{\{1, k^\mu\}}{(M^2-k^2)(m^2-(P-k)^2)(m^2-(\Sigma-k)^2)(m^2-(P'-k)^2)}$$

$$\mathcal{H}^{\mu}_{13}(s,t) = Q^\mu \mathcal{H}^{(1)}_{13}(s,t) + (\Delta + 2q)^\mu \mathcal{H}^{(2)}_{13}(s,t)$$

D.2 Coefficients of the Passarino-Veltman Decomposition

$$\mathcal{H}^{(1)}_{11}(s) = \frac{1}{2s}\left[(s-m^2+M^2)\mathcal{H}_{11}(s) + \mathcal{H}_{10} - \mathcal{H}_{01}\right] \tag{D.4}$$

$$\mathcal{H}^{(1)}_{A}(t) = \frac{\mathcal{H}_{11}(m^2) + M^2\mathcal{H}_A(t) - \mathcal{H}_{02}(t)}{4m^2-t}$$

$$\mathcal{H}^{(2)}_{A}(t) = \frac{2M^2\mathcal{H}_{11}(m^2) + 2M^2(M^2-4m^2+t)\mathcal{H}_A(t) - (2M^2-4m^2+t)\mathcal{H}_{02}(t)}{2(2-d)(4m^2-t)}$$

$$\mathcal{H}^{(3)}_{A}(t) = \frac{M^2((1-d)M^2+4m^2-t)\mathcal{H}_A(t) + (1-d)M^2\mathcal{H}_{11}(m^2)}{(2-d)(4m^2-t)^2}$$
$$- \frac{(2(1-d)M^2+(3-d)(4m^2-t))\mathcal{H}_{02}(t)}{2(2-d)(4m^2-t)^2} + \frac{M^2\mathcal{H}_{11}(m^2)+\mathcal{H}_{10}-\mathcal{H}_{01}}{4m^2(4m^2-t)}$$

$$\mathcal{H}^{(1)}_{B}(s) = \frac{1}{2(M^4+(m^2-s)^2-2M^2(m^2+s))}\Big[(s-m^2+M^2)((s-m^2-2M^2)\mathcal{H}_B(s)$$
$$- \mathcal{H}_{11}(s)) + (s-m^2-M^2)\mathcal{H}_{11}(m^2) + 2M^2\mathcal{H}_{02}(M^2)\Big]$$

$$\mathcal{H}^{(2)}_{B}(s) = \frac{1}{2(M^4+(m^2-s)^2-2M^2(m^2+s))}\Big[(s-m^2)(s+3m^2-3M^2)\mathcal{H}_B(s)$$
$$+ (M^2-m^2-3s)\mathcal{H}_{11}(s) + (s+3m^2-M^2)\mathcal{H}_{11}(m^2)\Big]$$
$$+ \frac{2(s-m^2)\mathcal{H}_{02}(M^2)}{2(M^4+(m^2-s)^2-2M^2(m^2+s))}$$

$$\mathcal{H}^{(1)}_{21}(t) = \frac{(2M^2-t)\mathcal{H}_{21}(t) - 2\mathcal{H}_{11}(m^2) + 2\mathcal{H}_{20}(t)}{2(4m^2-t)}$$

$$\mathcal{H}^{(2)}_{21}(t) = \frac{-2(M^4+m^2(t-4M^2))\mathcal{H}_{21}(t) + 2(M^2-2m^2)\mathcal{H}_{11}(m^2) + (t-2M^2)\mathcal{H}_{20}(t)}{2(d-2)(4m^2-t)}$$

$$\mathcal{H}^{(3)}_{21}(t) = \frac{(4(d-1)M^4 - 4M^2((d-2)t+4m^2) + t((d-2)t+4m^2))\mathcal{H}_{20}(t)}{4(d-2)(t-4m^2)^2}$$
$$+ \frac{1}{4(d-2)m^2(t-4m^2)^2}\Big[((d-2)(M^2+2m^2)t + 4(3-2d)M^2m^2$$
$$+ 8m^4)\mathcal{H}_{11}(m^2) + (d-2)(4m^2-t)(\mathcal{H}_{01}-\mathcal{H}_{10})\Big] - \frac{(d-1)(t-2M^2)\mathcal{H}_{20}(t)}{2(d-2)(t-4m^2)^2}$$

$$\mathcal{H}^{(1)}_{13}(s,t) = \frac{1}{4(M^4-2M^2(s+m^2)+m^2(m^2-2s)+s(s+t))}\Big[(4M^2+2m^2 - 2s-t)\mathcal{H}_{13}(s,t) + 2(m^2-s-M^2)\mathcal{H}_B(s) + (2s+t-2m^2-2M^2)\mathcal{H}_A(t)\Big] + \frac{(4M^2-t)\mathcal{H}_{03}(M^2,t)}{4(M^4-2M^2(s+m^2)+m^2(m^2-2s)+s(s+t))}$$

$$\mathcal{H}^{(2)}_{13}(s,t) = \frac{1}{4(M^4-2M^2(m^2+s)+m^4-2m^2s+s(s+t))}\Big[\big(M^2(2s+t-2m^2) + (m^2-s)(4m^2-t)-2M^4\big)\mathcal{H}_{13}(s,t) + (2s+t-2m^2-2M^2)\mathcal{H}_{03}(M^2,t)\Big] + \frac{2(s+m^2-M^2)\mathcal{H}_B(s)+(t-4m^2)\mathcal{H}_A(t)}{4(M^4-2M^2(m^2+s)+m^4-2m^2s+s(s+t))}$$

D.3 Results for the loop diagrams

We list in this section the results concerning to the loop integrals. For the diagrams $a+b$, $c+d$, e, f, $g+h$, i, $n+o$ and $p+r$ only the direct version is shown. To construct the full contribution of the mentioned diagrams is necessary to add its crossed version according to the following rules [19]:

$$A^{\pm}_{TOTAL}(s,t,u) = A^{\pm}(s,t) \pm A^{\pm}(u,t)$$
$$B^{\pm}_{TOTAL}(s,t,u) = B^{\pm}(s,t) \mp B^{\pm}(u,t)$$

- **Loops a+b**

$$A^{+}_{a+b}(s) = \frac{g^2 m}{2f^4}\left[\mathcal{H}_{01}+\mathcal{H}_{10}+(s-m^2-M^2)\mathcal{H}_{11}(s)-(s+m^2)\mathcal{H}^{(1)}_{11}(s)\right]$$
$$B^{+}_{a+b}(s) = -\frac{g^2}{8f^4}\left[-\frac{4(3m^2+s)(\mathcal{H}_{01}-M^2\mathcal{H}_{11}(s))}{m^2-s}+4(m^2+s)\mathcal{H}_{11}(s)\right]$$
$$A^{-}_{a+b}(s) = A^{+}_{a+b}(s)$$
$$B^{-}_{a+b}(s) = B^{+}_{a+b}(s)$$

- **Loops c+d**

$$
\begin{aligned}
A^+_{c+d}(s) = \frac{g^4 m}{8f^4(s-m^2)} \big[& 4m^2\mathcal{H}_{01} - 2(m^2+s)\mathcal{H}_{10} \\
& + 2(2m^2(s-m^2) + M^2(m^2+s))\mathcal{H}_{11}(m^2) \\
& - 2(s^2 - m^4 + M^2(3m^2+s))\mathcal{H}_{11}(s) - 4m^2(s+m^2)\mathcal{H}^{(1)}_{11}(m^2) \\
& + (m^4 + 10m^2 s + 5s^2)\mathcal{H}^{(1)}_{11}(s) + 4m^2(m^2(m^2-2s)+s^2)\mathcal{H}_B(s) \\
& + 8m^2(m^2-s)(2(s+m^2) - M^2)\big] \\
B^+_{c+d}(s) = \frac{g^4}{8f^4(m^2-s)} \big[& -(s+7m^2)\mathcal{H}_{01} + 4m^2\mathcal{H}_{10} \\
& + 4m^2(3m^2+s)\mathcal{H}_{02}(M^2) + 4m^2M^2\mathcal{H}_{11}(m^2) + (M^2(s+3m^2) \\
& + 4m^2(s-m^2))\mathcal{H}_{11}(s) - 8m^4\mathcal{H}^{(1)}_{11}(m^2) - (s^2 + 6sm^2 + m^4)\mathcal{H}^{(1)}_{11}(s) \\
& - 4m^2M^2(s+3m^2)\mathcal{H}_B(s) + 4m^2(s-m^2)^2\mathcal{H}^{(1)}_B(s) \\
& + 4m^2(m^2-s)(3m^2+s)\mathcal{H}^{(2)}_B(s)\Big] \\
A^-_{c+d}(s) = A^+_{c+d}(s) & \\
B^-_{c+d}(s) = B^+_{c+d}(s) &
\end{aligned}
$$

- **Loop e**

$$
\begin{aligned}
A^+_e(s) = \frac{3g^4 m}{16f^4(m^2-s)} \big[& 2(s+3m^2)\mathcal{H}_{01} + 2(s-m^2)\mathcal{H}_{10} \\
& + 2((s-m^2)^2 - M^2(3m^2+s))\mathcal{H}_{11}(s) - (s-m^2)^2\mathcal{H}^{(1)}_{11}(s)\Big] \\
B^+_e(s) = \frac{3g^2}{16f^4(m^2-s)^2} \big[& (9m^4 + 6m^2 s + s^2)\mathcal{H}_{01} + 4m^2(s-m^2)\mathcal{H}_{10} \\
& + (4m^2(s-m^2)^2 - M^2(3m^2+s)^2)\mathcal{H}_{11}(s) - (m^2-s)^3\mathcal{H}^{(1)}_{11}(s)\Big] \\
A^-_e(s) = A^+_e(s) & \\
B^-_e(s) = B^+_e(s) &
\end{aligned}
$$

- **Loop f**

$$A_f^+(s) = \frac{m(s-m^2)\mathcal{H}_{11}^{(1)}(s)}{2f^4}$$
$$B_f^+(s) = \frac{(4\mathcal{H}_{01} - \mathcal{H}_{10} - 4M^2\mathcal{H}_{11}(s) + 4\mathcal{H}_{11}^{(1)}(s))}{8f^4}$$
$$A_f^-(s) = \frac{A_f^+(s)}{2}$$
$$B_f^-(s) = \frac{B_f^+(s)}{2}$$

- **Loops g+h**

$$A_{g+h}^+(s) = \frac{g^2 m(s-m^2)}{2f^4}\left[-2\mathcal{H}_{11}(s) + \mathcal{H}_{11}^{(1)}(s) + 8m^2\mathcal{H}_B^{(1)}(s)\right]$$
$$B_{g+h}^+(s) = \frac{g^2}{4f^4}\Big[-2\mathcal{H}_{01} + \mathcal{H}_{10} + 8m^2\mathcal{H}_{02}(M^2) + 2M^2\mathcal{H}_{11}(s) - 2m^2\mathcal{H}_{11}^{(1)}(m^2)$$
$$-2(m^2+s)\mathcal{H}_{11}^{(1)}(s) - 8M^2m^2\mathcal{H}_B(s) - 8m^2(m^2-s)(\mathcal{H}_B^{(1)}(s) - \mathcal{H}_B^{(2)}(s))\Big]$$
$$A_{g+h}^-(s) = 0$$
$$B_{g+h}^-(s) = 0$$

- **Loop i**

$$
\begin{aligned}
A_i^+(s,t) = &-\frac{3g^4 m}{16f^4}\Big[8m^2(\mathcal{H}_{02}(M^2)-\mathcal{H}_{02}(t))+2(4m^2-M^2)\mathcal{H}_{11}(m^2)\\
&+(m^2-s)\mathcal{H}_{11}^{(1)}(s)+2(M^2-(s+3m^2))\mathcal{H}_{11}(s)+32m^4(m^2-s)\mathcal{H}_{13}(s,t)\\
&+8m^2M^2\mathcal{H}_A(t)-32m^4\mathcal{H}_A^{(1)}(t)+8m^2(2s+t-2M^2-2m^2)\mathcal{H}_A^{(3)}(t)\\
&-8m^2(M^2+m^2-s)\mathcal{H}_B(s)+8m^2(M^2+3m^2+s)\mathcal{H}_B^{(1)}(s)\\
&+8m^2(M^2+m^2-s)\mathcal{H}_B^{(2)}(s)\Big]\\
B_i^+(s,t) = &-\frac{3g^4}{16f^4}\Big[-\mathcal{H}_{01}+\mathcal{H}_{10}+4m^2(2\mathcal{H}_{02}(M^2)+\mathcal{H}_{02}(t))+16m^4\mathcal{H}_{03}(t,M^2)\\
&+(M^2-4m^2)\mathcal{H}_{11}(s)-4m^2\mathcal{H}_{11}^{(1)}(m^2)+(m^2-s)\mathcal{H}_{11}^{(1)}(s)+16m^4M^2\mathcal{H}_{13}(s,t)\\
&+32m^4(m^2-s)\mathcal{H}_{13}^{(2)}(s,t)-4m^2M^2\mathcal{H}_A(t)+8m^2\mathcal{H}_A^{(2)}(t)-8m^2M^2\mathcal{H}_B(s)\\
&+8m^2(s+3m^2)\mathcal{H}_B^{(1)}(s)+8m^2(m^2-s)\mathcal{H}_B^{(2)}(s)\Big]\\
A_i^-(s,t) = &-\frac{A_i^+(s,t)}{3}\\
B_i^-(s,t) = &-\frac{B_i^+(s,t)}{3}
\end{aligned}
$$

- **Loop k**

$$
\begin{aligned}
A_k^+(t) &= 0\\
B_k^+(t) &= 0\\
A_k^-(t) &= 0\\
B_k^-(t) &= \frac{t\mathcal{H}_{20}(t)}{f^4}
\end{aligned}
$$

- **Loop l**

$$A_l^+(t) = \frac{g^2 m}{2f^4}\left[-2\mathcal{H}_{01} + 2M^2\mathcal{H}_{11}(m^2) + (M^2-2t)(4m^2\mathcal{H}_{21}^{(1)}(t) - \mathcal{H}_{20}(t))\right]$$
$$B_l^+(t) = 0$$
$$A_l^-(t) = -\frac{4g^2m^3}{f^4}(s-u)\mathcal{H}_{21}^{(3)}(t)$$
$$B_l^-(t) = -\frac{g^2}{f^4}\left[4m^2\mathcal{H}_{21}^{(2)}(t) + t\mathcal{H}_{20}^{(1)}(t)\right]$$

- **Loop m**

$$A_m^+(s,t,u) = 0$$
$$B_m^+(s,t,u) = 0$$
$$A_m^-(s,t,u) = -\frac{g^2m^3}{f^4}(s-u)\mathcal{H}_A^{(3)}(t)$$
$$B_m^-(s,t,u) = -\frac{g^2}{8f^4}\left[\mathcal{H}_{10} - 4m^2(\mathcal{H}_{11}^{(1)}(m^2) - \mathcal{H}_{02}(t) + M^2\mathcal{H}_A(t) - 2\mathcal{H}_A^{(2)}(t))\right]$$

- **Loops n+o**

$$A_{n+o}^+(s,t) = \frac{g^2 m}{f^4}\left[\mathcal{H}_{01} - M^2\mathcal{H}_{11}(m^2)\right]$$
$$B_{n+o}^+(s,t) = \frac{g^2}{4f^4}\frac{(7m^2+s)(\mathcal{H}_{01} - M^2\mathcal{H}_{11}(m^2))}{(m^2-s)}$$
$$A_{n+o}^-(s,t) = A_{n+o}^+(s,t)$$
$$B_{n+o}^-(s,t) = B_{n+o}^+(s,t)$$

- **Loops p+r**

$$A_{p+r}^+(s,t) = \frac{g^2 m}{2f^4}\mathcal{H}_{10}$$
$$B_{p+r}^+(s,t) = \frac{g^2}{4f^4}\frac{(s+3m^2)\mathcal{H}_{10}}{m^2-s}$$
$$A_{p+r}^-(s,t) = A_{p+r}^+(s,t)$$
$$B_{p+r}^-(s,t) = B_{p+r}^+(s,t)$$

- **Loops t+u**

$$A^+_{t+u}(s,t) = \frac{g^2 m}{f^4}(\mathcal{H}_{01} - M^2\mathcal{H}_{11}(m^2))$$
$$B^+_{t+u}(s,t) = \frac{g^2}{2f^4}(\mathcal{H}_{01} - M^2\mathcal{H}_{11}(m^2))$$
$$A^-_{t+u}(s,t) = 0$$
$$B^-_{t+u}(s,t) = 0$$

- **Loop v**

$$A^+_v(s,t) = 0$$
$$B^+_v(s,t) = 0$$
$$A^-_v(s,t) = 0$$
$$B^-_v(s,t) = \frac{5}{8f^4}\mathcal{H}_{10}$$

Appendix E

Identifying the power counting breaking terms

In this Appendix we explain the method used to extract analytically the power counting breaking terms from the $\mathcal{O}(q^3)$ loop amplitude (T_{loops}). First, as we did with the full amplitude, we decompose T_{loops} in terms of its scalar integrals using the Passarino-Veltman decomposition.

$$T_{loops} = \sum_{mn} \mathcal{C}_{mn} \mathcal{H}_{mn} \tag{E.1}$$

Where the scalar integrals $\mathcal{H}_{mn}$ are defined in Appendix D and $\mathcal{C}_{mn}$ refers to the coefficients that result in the decomposition process. Second, we calculate the infrared regular part [97] of these scalar integrals ($\mathcal{R}_{mn}$), because the PCBT arise from that part in the final amplitude. Its calculation, for each of the scalar integrals used here, is straightforward because the chiral expansion and the integration in the Feynman parameters commutes [177]. The chiral order of each $\mathcal{C}_{mn}$ tell us up to which order in the chiral expansion we need to retain the regular part of $\mathcal{H}_{mn}$. So, it results:

$$T_{loops}^{(regular)} = \sum_{mn} \mathcal{C}_{mn} \mathcal{R}_{mn} \tag{E.2}$$

Finally, we only have to expand Eq.(E.2) in a chiral series, to end with a string of terms that can be splitted into a part that has chiral order lower than three (these are the PCBT) and an infinite series that respect the power counting. The (finite) terms that break the power counting have the same analytical structure than the monomials in the original Lagrangian and can be cancelled via redefinition of LECs (see the next Appendix).

Appendix F

Low-Energy Constants Renormalization

In this appendix we show how to redefine the $\mathcal{O}(q^2)$ and $\mathcal{O}(q^3)$ LECs in order to cancel the divergences, the scale-dependent pieces and the PCBT. In this way we have full relativistic scale-independent chiral amplitudes free from divergences that respect the chiral power counting.

F.1 $\mathcal{O}(q^2)$ LECs

The $\mathcal{O}(q^2)$ LECs are redefined in order to cancel both divergent parts, as well as PCBT.

$$c_1 \to c_1^{EOMS} - 2\bar{\lambda}\frac{3g^2m}{8f^2} + \frac{3g^2m}{128\pi^2f^2}(1 - \log\left(\frac{m^2}{\mu^2}\right))$$
$$c_2 \to c_2^{EOMS} + 2\bar{\lambda}\frac{(g^2-1)^2m}{2f^2} + \frac{m}{32\pi^2f^2}[(g^2-1)^2\log\left(\frac{m^2}{\mu^2}\right) - (2+g^4)]$$
$$c_3 \to c_3^{EOMS} + 2\bar{\lambda}\frac{(g^4-6g^2+1)m}{4f^2} + \frac{m}{64\pi^2f^2}[(g^4-6g^2+1)\log\left(\frac{m^2}{\mu^2}\right) + 9g^4]$$
$$c_4 \to c_4^{EOMS} + 2\bar{\lambda}\frac{(3g^4-2g^2-1)m}{4f^2} + \frac{m}{64\pi^2f^2}[(3g^4-2g^2-1)\log\left(\frac{m^2}{\mu^2}\right) - g^2(5+g^2)]$$

F.2 $\mathcal{O}(q^3)$ LECs

In contrast to the $\mathcal{O}(q^2)$ LECs, the $\mathcal{O}(q^3)$ ones only cancel divergent parts (along with their scale-dependent logarithms) because at $\mathcal{O}(q^3)$ the analytical terms do not break the power counting in our calculation done up to $\mathcal{O}(q^3)$. The resulting LECs are renormalized within the $\widetilde{MS}$ scheme (also known as $\overline{MS}-1$).

$$
\begin{aligned}
d_1+d_2 &\to (d_1+d_2)^{\widetilde{MS}} + 2\bar{\lambda}\frac{3g^4-4g^2+1}{48f^2} + \frac{3g^4-4g^2+1}{768\pi^2 f^2}\log\left(\frac{m^2}{\mu^2}\right)\\
d_5 &\to d_5^{\widetilde{MS}} - 2\bar{\lambda}\frac{g^2+8}{48f^2} - \frac{g^2+8}{768\pi^2 f^2}\log\left(\frac{m^2}{\mu^2}\right)\\
d_{14}-d_{15} &\to (d_{14}-d_{15})^{\widetilde{MS}} + 2\bar{\lambda}\frac{(g^2-1)^2}{4f^2} + \frac{(g^2-1)^2}{64\pi^2 f^2}\log\left(\frac{m^2}{\mu^2}\right)\\
d_{16} &\to d_{16}^{\widetilde{MS}} + 2\bar{\lambda}\frac{g(g^2-1)}{4f^2} + \frac{g(g^2-1)}{64\pi^2 f^2}\log\left(\frac{m^2}{\mu^2}\right)
\end{aligned}
$$

Appendix G

Partial Wave Projections

We explain now how we computed Eq.(3.8) to extract the explicit expressions for the partial wave projections. We reproduce Eq.(3.8) here again:

$$T_{J\ell}(a',\alpha';a,\alpha) = \frac{1}{\sqrt{4\pi(2\ell+1)}(0\sigma\sigma|\ell\tfrac{1}{2}J)} \tag{G.1}$$
$$\times\sum_{m,\sigma'}\int d\hat{\mathbf{p}}'\,\langle\pi(-\mathbf{p}';a')N(\mathbf{p}',\sigma';\alpha')|T|\pi(-\mathbf{p};a)N(\mathbf{p},\sigma;\alpha)\rangle(m\sigma'\sigma|\ell\frac{1}{2}J)Y_\ell^m(\hat{\mathbf{p}}')^*$$

For the S-waves ($\ell=0$) we have $J=\ell\pm\frac{1}{2}=\frac{1}{2}$. On the other hand, $\sigma=\frac{1}{2}$ and $m=0$[♯1] so, because $\ell=0\Rightarrow m'=0$, we have from the conservation of the total angular momentum $\sigma'=\frac{1}{2}$. That means that Eq.(G.1) reduces to:

$$\begin{aligned}T_{\frac{1}{2}0}(a',\alpha';a,\alpha) &= \frac{1}{\sqrt{4\pi}(0\frac{1}{2}\frac{1}{2}|0\frac{1}{2}\frac{1}{2})}\\ &\times\int d\hat{\mathbf{p}}'\,\langle\pi(-\mathbf{p}';a')N(\mathbf{p}',\frac{1}{2};\alpha')|T|\pi(-\mathbf{p};a)N(\mathbf{p},\frac{1}{2};\alpha)\rangle(0\frac{1}{2}\frac{1}{2}|0\frac{1}{2}\frac{1}{2})Y_0^0(\hat{\mathbf{p}}')^*\\ &= \frac{1}{4\pi}\int d\hat{\mathbf{p}}'\,\langle\pi(-\mathbf{p}';a')N(\mathbf{p}',\frac{1}{2};\alpha')|T|\pi(-\mathbf{p};a)N(\mathbf{p},\frac{1}{2};\alpha)\rangle\end{aligned}$$

Where the last equality comes from the fact that $Y_0^0(\hat{\mathbf{p}}')^*=\frac{1}{\sqrt{4\pi}}$.

For the P-waves ($\ell=1$) we have $J=1\pm\frac{1}{2}=\frac{3}{2},\frac{1}{2}$. On the other hand, we have in this case the possibilities $m'=-1,0,1$ and from the possible values of the final state nucleon spin $\sigma'=\pm\frac{1}{2}$, we obtain from the conservation of the total angular momentum $m'=\sigma-\sigma'=0,1$.

[♯1] As pointed out in Sec.2 of Chapter 3, this is because $Y_\ell^m(\hat{z})\neq 0$ only for $m=0$.

For $J = \frac{1}{2}$:

$$T_{\frac{1}{2}1}(a',\alpha';a,\alpha) = \frac{1}{\sqrt{12\pi}(0\frac{1}{2}\frac{1}{2}|1\frac{1}{2}\frac{1}{2})} \tag{G.2}$$
$$\times\Big\{\int d\hat{\mathbf{p}}'\,\langle\pi(-\mathbf{p}';a')N(\mathbf{p}',\frac{1}{2};\alpha')|T|\pi(-\mathbf{p};a)N(\mathbf{p},\frac{1}{2};\alpha)\rangle(0\frac{1}{2}\frac{1}{2}|1\frac{1}{2}\frac{1}{2})Y_1^0(\hat{\mathbf{p}}')^*$$
$$+\int d\hat{\mathbf{p}}'\,\langle\pi(-\mathbf{p}';a')N(\mathbf{p}',-\frac{1}{2};\alpha')|T|\pi(-\mathbf{p};a)N(\mathbf{p},\frac{1}{2};\alpha)\rangle(1\frac{-1}{2}\frac{1}{2}|1\frac{1}{2}\frac{1}{2})Y_1^1(\hat{\mathbf{p}}')^*\Big\}$$

If we make use of the following spherical harmonics and Clebsch-Gordan coefficients:

$$Y_1^{0\,*}(0,0) = \sqrt{\frac{3}{4\pi}} \qquad Y_1^{0\,*}(\hat{\mathbf{p}}) = \sqrt{\frac{3}{4\pi}}\cos\theta \qquad Y_1^{1\,*}(\hat{\mathbf{p}}) = -\sqrt{\frac{3}{8\pi}}\sin\theta\, e^{-i\phi}$$
$$(0\frac{1}{2}\frac{1}{2}|1\frac{1}{2}\frac{1}{2}) = -\frac{1}{\sqrt{3}} \qquad (1\frac{-1}{2}\frac{1}{2}|1\frac{1}{2}\frac{1}{2}) = \sqrt{\frac{2}{3}}$$

We obtain the following result for Eq.(G.2):

$$T_{\frac{1}{2}1}(a',\alpha';a,\alpha) = \frac{1}{4\pi}\Big\{\int d\hat{\mathbf{p}}'\,\cos\theta\,\langle\pi(-\mathbf{p}';a')N(\mathbf{p}',\frac{1}{2};\alpha')|T|\pi(-\mathbf{p};a)N(\mathbf{p},\frac{1}{2};\alpha)\rangle$$
$$+\int d\hat{\mathbf{p}}'\,\sin\theta\, e^{-i\phi}\,\langle\pi(-\mathbf{p}';a')N(\mathbf{p}',-\frac{1}{2};\alpha')|T|\pi(-\mathbf{p};a)N(\mathbf{p},\frac{1}{2};\alpha)\rangle\Big\}$$

For $J = \frac{3}{2}$:

$$T_{\frac{3}{2}1}(a',\alpha';a,\alpha) = \frac{1}{\sqrt{12\pi}(0\frac{1}{2}\frac{1}{2}|1\frac{1}{2}\frac{3}{2})} \tag{G.3}$$
$$\times\Big\{\int d\hat{\mathbf{p}}'\,\langle\pi(-\mathbf{p}';a')N(\mathbf{p}',\frac{1}{2};\alpha')|T|\pi(-\mathbf{p};a)N(\mathbf{p},\frac{1}{2};\alpha)\rangle(0\frac{1}{2}\frac{1}{2}|1\frac{1}{2}\frac{3}{2})Y_1^0(\hat{\mathbf{p}}')^*$$
$$+\int d\hat{\mathbf{p}}'\,\langle\pi(-\mathbf{p}';a')N(\mathbf{p}',-\frac{1}{2};\alpha')|T|\pi(-\mathbf{p};a)N(\mathbf{p},\frac{1}{2};\alpha)\rangle(1\frac{-1}{2}\frac{1}{2}|1\frac{1}{2}\frac{3}{2})Y_1^1(\hat{\mathbf{p}}')^*\Big\}$$

For this case, we have to use the following spherical harmonics and Clebsch-Gordan coefficients:

$$Y_1^{1\,*}(\hat{\mathbf{p}}) = -\sqrt{\frac{3}{8\pi}}\sin\theta\, e^{-i\phi} \qquad (0\frac{1}{2}\frac{1}{2}|1\frac{1}{2}\frac{3}{2}) = \sqrt{\frac{2}{3}} \qquad (1\frac{-1}{2}\frac{1}{2}|1\frac{1}{2}\frac{3}{2}) = \frac{1}{\sqrt{3}}$$

Obtaining:

$$T_{\frac{3}{2}1}(a',\alpha';a,\alpha) = \frac{1}{4\pi}\Big\{ \int d\hat{\mathbf{p}}' \, \cos\theta \, \langle \pi(-\mathbf{p}';a')N(\mathbf{p}',\frac{1}{2};\alpha')|T|\pi(-\mathbf{p};a)N(\mathbf{p},\frac{1}{2};\alpha)\rangle$$
$$-\frac{1}{2}\int d\hat{\mathbf{p}}' \, \sin\theta \, e^{-i\phi} \, \langle \pi(-\mathbf{p}';a')N(\mathbf{p}',-\frac{1}{2};\alpha')|T|\pi(-\mathbf{p};a)N(\mathbf{p},\frac{1}{2};\alpha)\rangle\Big\}$$

Now we write the amplitudes $\langle \pi(-\mathbf{p}';a')N(\mathbf{p}',\sigma';\alpha')|T|\pi(-\mathbf{p};a)N(\mathbf{p},\sigma;\alpha)\rangle$ in terms of $A^{\pm}(s,t,u)$ and $B^{\pm}(s,t,u)$ shown in Appendices C and D. But first, we need to write an explicit representation for the Dirac bilinears $\bar{u}_{\sigma'}u_{\sigma}$ and $\bar{u}_{\sigma'}(\not{q}+\not{q}')u_{\sigma}$. We take, for the Dirac spinors, the following representation:

$$u_{\sigma}(s,\theta,\phi) = \sqrt{E_p(s)+m_N}\begin{pmatrix} \chi_{\sigma} \\ \frac{\vec{p}\cdot\vec{\sigma}}{E_p(s)+m_N}\chi_{\sigma} \end{pmatrix}, \text{with } \chi_{\uparrow} = \begin{pmatrix} 1 \\ 0 \end{pmatrix}, \chi_{\downarrow} = \begin{pmatrix} 0 \\ 1 \end{pmatrix}$$

With the following definitions for the angles θ and ϕ:

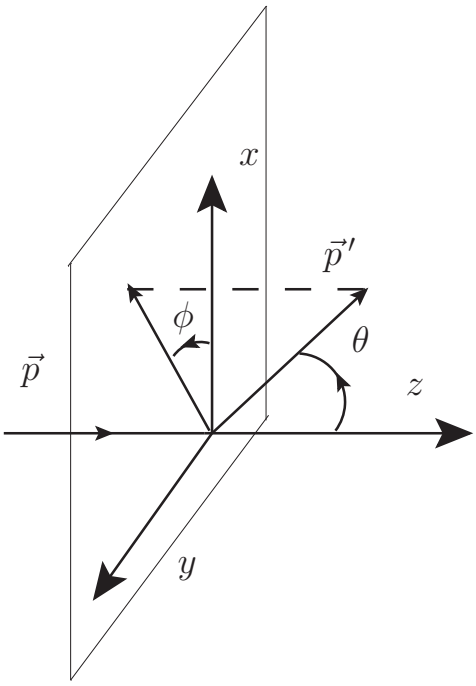

$\vec{p} = (0,0,p)$

$\vec{p}' = (p\cos\phi\sin\theta, p\sin\phi\sin\theta, p\cos\theta)$

From these definitions we obtain the following results:

$$\bar{u}_\uparrow u_\uparrow(s,\theta,\phi) = (E_p(s)+m_N)\left[1-\frac{p^2(s)\cos\theta}{(E_p(s)+m_N)^2}\right]$$
$$\bar{u}_\downarrow u_\uparrow(s,\theta,\phi) = (E_p(s)+m_N)\left[-\frac{p^2(s)\sin\theta}{(E_p(s)+m_N)^2}e^{i\phi}\right]$$
$$\bar{u}_\uparrow(\not{q}+\not{q}')u_\uparrow(s,\theta,\phi) = 2(E_p(s)+m_N)\left[\sqrt{s}-m_N+\frac{\sqrt{s}+m_N}{(E_p(s)+m_N)^2}p^2(s)\cos\theta\right]$$
$$\bar{u}_\downarrow(\not{q}+\not{q}')u_\uparrow(s,\theta,\phi) = 2(E_p(s)+m_N)\left[\frac{\sqrt{s}+m_N}{(E_p(s)+m_N)^2}p^2(s)\sin\theta e^{i\phi}\right]$$

Recalling that our amplitudes are written in terms of $A^\pm(s,t)$ and $B^\pm(s,t)$, Eq.(3.2), we obtain the following representation for the S- and P-waves projections $T_{\ell J}$:

$$T^\pm_{S\frac{1}{2}}(s) = \frac{1}{4\pi}\int_0^{2\pi}d\phi\int_{-1}^{1}d\cos\theta\Big[A^\pm(s,t(s,\cos\theta))\bar{u}_\uparrow u_\uparrow(s,\cos\theta,\phi) + \frac{1}{2}B^\pm(s,t(s,\cos\theta))\bar{u}_\uparrow(\not{q}+\not{q}')u_\uparrow(s,\cos\theta,\phi)\Big] \tag{G.4}$$

$$\begin{aligned}T^\pm_{P\frac{1}{2}}(s) = {}& \frac{1}{4\pi}\int_0^{2\pi}d\phi\int_{-1}^{1}d\cos\theta\Big[A^\pm(s,t(s,\cos\theta))\bar{u}_\uparrow u_\uparrow(s,\cos\theta,\phi) + \frac{1}{2}B^\pm(s,t(s,\cos\theta))\bar{u}_\uparrow(\not{q}+\not{q}')u_\uparrow(s,\cos\theta,\phi)\Big]x \\ & + \frac{1}{4\pi}\int_0^{2\pi}d\phi\int_{-1}^{1}d\cos\theta\Big[A^\pm(s,t(s,\cos\theta))\bar{u}_\downarrow u_\uparrow(s,\cos\theta,\phi) + \frac{1}{2}B^\pm(s,t(s,\cos\theta))\bar{u}_\downarrow(\not{q}+\not{q}')u_\uparrow(s,\cos\theta,\phi)\Big]\sqrt{1-x^2}\,e^{-i\phi}\end{aligned} \tag{G.5}$$

$$\begin{aligned}T^\pm_{P\frac{3}{2}}(s) = {}& \frac{1}{4\pi}\int_0^{2\pi}d\phi\int_{-1}^{1}d\cos\theta\Big[A^\pm(s,t(s,\cos\theta))\bar{u}_\uparrow u_\uparrow(s,\cos\theta,\phi) + \frac{1}{2}B^\pm(s,t(s,\cos\theta))\bar{u}_\uparrow(\not{q}+\not{q}')u_\uparrow(s,\cos\theta,\phi)\Big]x \\ & - \frac{1}{8\pi}\int_0^{2\pi}d\phi\int_{-1}^{1}d\cos\theta\Big[A^\pm(s,t(s,\cos\theta))\bar{u}_\downarrow u_\uparrow(s,\cos\theta,\phi) + \frac{1}{2}B^\pm(s,t(s,\cos\theta))\bar{u}_\downarrow(\not{q}+\not{q}')u_\uparrow(s,\cos\theta,\phi)\Big]\sqrt{1-x^2}\,e^{-i\phi}\end{aligned} \tag{G.6}$$

Appendix H

Suppression of diagrams in Fig. 6.1

Let us now consider the relative size of diagrams 4–17 in Fig. 6.1 of Chapter 6 compared to diagram 2. We show here this figure to make the monitoring easier. On the other hand, diagram 3 is not considered here because it was already discussed at the end of section 6.2.

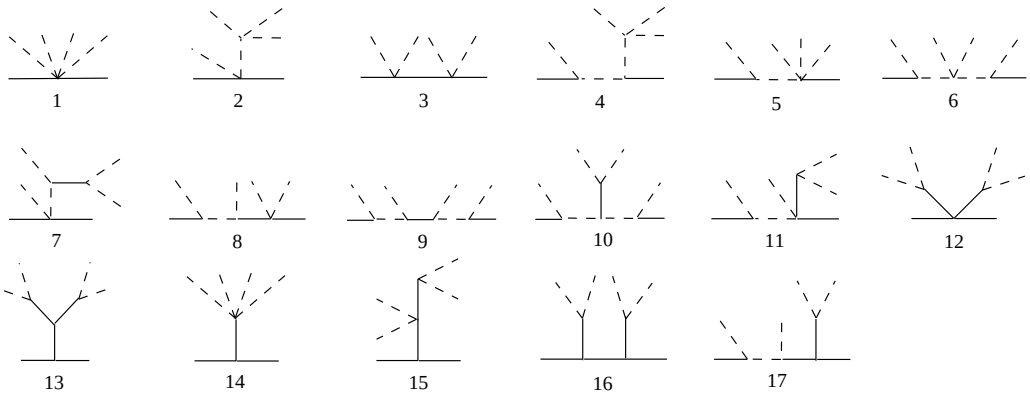

- **Diagram 4**

The enhanced configurations are those in which the kaon line on the left correspond to an outgoing particle. In this way the leftmost intermediate kaon propagator is almost on-shell, taking the value:

$$\frac{1}{(p-k'_{1,2})^2 - m_K^2} \tag{H.1}$$

At threshold it is given by $1/a$ with:

$$a = 2m_K(M_\phi - 2m_K) \equiv 2m_K\delta \tag{H.2}$$

Numerically, $\sqrt{a} \simeq 170$ MeV. Like in diagram 2, the vertical kaon propagator is nearly on-shell and of value $1/a'$ with:

$$a' = (k_1 + k_2 - k'_{2,1})^2 - m_K^2 = (p' - p + k'_{1,2})^2 - m_K^2 \tag{H.3}$$

While a is not large because of the proximity of the ϕ mass to the $K\bar{K}$ threshold, a' is proportional to the small kaon three-momenta. The initial and final $|K\bar{K}\rangle_0$ states are not in their CM. The velocities of the boosts that take these states to their CM frames are $\mathbf{v} = -\mathbf{p}/\sqrt{s}$ and $\mathbf{v}' = -\mathbf{p}'/\sqrt{s}$, respectively. These velocities are small because we are close to threshold so that it is a good approximation to write:

$$\mathbf{k}_{1,2} = \pm\mathbf{q} + m_K\mathbf{v} + \mathcal{O}(|\mathbf{v}|^3) = \pm\mathbf{q} - \frac{2m_K\sqrt{s}}{s + M_{f_0}^2 - M_\phi^2}\mathbf{p} + \mathcal{O}(|\mathbf{v}|^3) \simeq \pm\mathbf{q} - \frac{1}{2}\mathbf{p} \tag{H.4}$$

Similarly:

$$\mathbf{k}'_{1,2} = \pm\mathbf{q}' + m_K\mathbf{v}' + \mathcal{O}(|\mathbf{v}|^3) = \pm\mathbf{q}' - \frac{2m_K\sqrt{s}}{s + M_{f_0}^2 - M_\phi^2}\mathbf{p}' + \mathcal{O}(|\mathbf{v}|^3) \simeq \pm\mathbf{q}' - \frac{1}{2}\mathbf{p}' \tag{H.5}$$

In the last two equations $\mathbf{q}$ and $\mathbf{q}'$ are the CM three-momentum of a kaon in the initial and final $|K\bar{K}\rangle_0$ states, respectively. The last equality in these equations follows because $2m_K\sqrt{s}/(s + M_{f_0}^2 - M_\phi^2) \simeq 1/2$. In this way we can rewrite Eq.(H.3) as:

$$a' = (p' - p + k'_{1,2})^2 - m_K^2 = Q^2 - 2Qk'_{1,2} \simeq -\mathbf{p}^2(1 - \cos\rho) \pm 2\mathbf{Q}\mathbf{q}' \tag{H.6}$$

Which is zero at threshold. On the other hand, the vertices involving the coupling of the external vector resonances to two-kaons are proportional to small three-momenta. As a result, this diagram is of order:

$$\frac{g^2}{f^2}\frac{m_K^2}{a'}\frac{|\mathbf{k}|^2}{a} \tag{H.7}$$

With $|\mathbf{k}|$ representing the modulus of any small external three-momentum. Since $|\mathbf{k}|^2/a = \mathcal{O}(1)$, this diagram seems to be of the same order as diagram 2. However, there is an extra suppression coming from the angular projection into S-wave. The angular dependence is dominated by the ratio $|\mathbf{k}|^2/a'$, since a has a finite angular independent part [Eq.(H.2)]. From the vertices with one vector resonance one gets the factor:

$$[\epsilon(p)\cdot k_1'][\epsilon(p')\cdot(k_1'-p)] \tag{H.8}$$

If the spin direction is given by the unitary vector $\hat{\mathbf{n}}$, such that $\hat{\mathbf{n}}\cdot\mathbf{p}=0$ we can write:

$$\begin{aligned}\epsilon(p) &= (0,\hat{\mathbf{n}})\\ \epsilon(p') &= (\mathbf{p}'\cdot\hat{\mathbf{n}}/p_0',\hat{\mathbf{n}})+\mathcal{O}(\mathbf{v}^2)\end{aligned} \tag{H.9}$$

The following angular structures result from Eq.(H.8):

$$(\mathbf{p}'\cdot\hat{\mathbf{n}})^2, \qquad (\mathbf{p}'\cdot\hat{\mathbf{n}}), \qquad (\hat{\mathbf{n}}\cdot\mathbf{q}'), \qquad (\hat{\mathbf{n}}\cdot\mathbf{q}')^2 \tag{H.10}$$

In the energy region where $|\mathbf{p}| \lesssim \sqrt{a}$, diagram 4 is suppressed compared to diagram 2 because of the ratio $|\mathbf{k}|^2/a$. On the other hand, for $|\mathbf{p}| \gtrsim \sqrt{a}$, a' is dominated by $\mathbf{p}^2(1-\cos\rho)$ because $\mathbf{p}^2 \gg \mathbf{q}^2 \approx M_{f_0}^2/4 - m_K^2$ for typical energies just slightly above threshold. Thus, we can neglect its angular dependence on $\hat{\mathbf{q}}'$ in good approximation. In this case, the second angular structure in the previous equation vanishes because of the integration in $\hat{\mathbf{q}}'$. The last structure is suppressed by a factor κ^2, with $\kappa = |\mathbf{q}|/|\mathbf{p}|$. Regarding the dominant structure in the first line, when divided by a', one has:

$$\int_{-1}^{+1} d\cos\rho \frac{\mathbf{p}^2\sin^2\rho\cos^2\phi}{\mathbf{p}^2(1-\cos\rho)} \tag{H.11}$$

Where we have written $(\mathbf{p}'\cdot\hat{\mathbf{n}})^2 = \mathbf{p}^2\sin^2\rho\cos^2\phi$, since $\hat{\mathbf{n}}$ is perpendicular to $\mathbf{p}$. Eq.(H.11) is finite and equal to $2\cos^2\phi$. For diagram 2 the angular integration on $\hat{\mathbf{p}}'$ is dominated by $1/a'$:

$$\int_{-1}^{+1} d\cos\rho \frac{1}{\mathbf{p}^2(1-\cos\rho)} \tag{H.12}$$

Which is divergent. Keeping also the subleading terms on the right hand side of Eq. (H.6), the angular integration for diagram 2 is not infinite but still large, of order $1/\kappa$. Therefore, we conclude that diagram 4 is suppressed by a factor κ with respect to diagram 2 for $|\mathbf{p}| \gtrsim \sqrt{a}$ and by a factor $|\mathbf{k}|^2/a$ for $|\mathbf{p}| \lesssim \sqrt{a}$.

- **Diagram 5**

For the amplitudes represented globally by diagram 5 in Fig. 6.1 there are no enhanced vertices like those discussed above for diagram 2 or 4. For some kaon arrangements, it is possible that the intermediate kaon is nearly on-shell but each of the vertices in these amplitudes require one power of small three-momentum. Then, the ratio between the enhanced propagator and the suppressed vertices is $\mathcal{O}(1)$. As a result, these diagrams are at most of $\mathcal{O}(g^2/f^2)$.

- **Diagram 6**

The enhanced configurations have an outgoing kaon on the leftmost vertex and an incoming one on the vertex at the far right. In between the kaon propagators are each of them of size $1/a$. On the other hand, the coupling of the external vector resonances with the kaons is suppressed by small powers of three-momentum. Then, the size of the amplitudes is estimated to be:

$$\frac{g^2}{f^2}\frac{m_K^2}{a}\frac{|\mathbf{k}|^2}{a} \tag{H.13}$$

The suppression compared to the diagram 2 happens in the same way as for diagram 4. For $|\mathbf{p}| \lesssim \sqrt{a}$ the last factor in the previous equation is small, and for $|\mathbf{p}| \gtrsim \sqrt{a}$ there is a suppression due to the angular projection. Indeed, from the vertices involving the vector states one gets the product:

$$[\epsilon(p) \cdot k'_{1,2}][\epsilon(p') \cdot k_{1,2}] \tag{H.14}$$

Which implies that the following angular structures [see Eq. (H.9)] are present:

$$(\hat{\mathbf{n}} \cdot \mathbf{p}')^2 \ , \qquad (\hat{\mathbf{n}} \cdot \mathbf{p}')(\hat{\mathbf{n}} \cdot \mathbf{q}), \qquad (\hat{\mathbf{n}} \cdot \mathbf{q}')(\hat{\mathbf{n}} \cdot \mathbf{q}) \tag{H.15}$$

These terms are multiplied by $1/a^2$ which has a lessened angular dependence since a is $2m_K\delta$ close to threshold. The integrals over $\hat{\mathbf{q}}$ and $\hat{\mathbf{q}}'$ in the

second and third lines of Eq.(H.15) are zero. The first line instead is finite and gives a contribution that compared with diagram 2 is suppressed by a factor $\kappa \mathbf{p}^2/a$.

- **Diagram 7**

A $K\bar{K}$ pair must couple to the vector propagator. In addition, the kaon and anti-kaon in the pair cannot belong both to the same $|K\bar{K}\rangle_0$ state because the latter is in S-wave. As a result, the four-momentum running through the vector propagator nearly vanishes due to the vicinity to the $K\bar{K}$ threshold. Notice that from $\mathcal{L}_{V\Phi^2}$ in Eq.(6.10) the vertex for a vector resonance coupled to a $K\bar{K}$ is proportional to the difference of the four-momenta of the kaon and the anti-kaon.

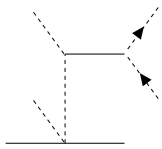

Figure H.1: Configurations left for the coupling of a $K\bar{K}$ to an intermediate vector resonance.

The diagram shown in Fig. H.1 is obtained by modifying the local lowest order meson-meson chiral vertex in the diagram 2 by the exchange of a vector resonance between the kaons with vanishing four-momentum transfer. It is well known that for these modifications to be meaningful [178], they must be calculated together with the exchange of the octet of axial-vector resonances a_μ in Eq.(6.4). After adding them, the result at the lowest chiral order is not modified, i.e., the corrections are of higher order, suppressed by powers of $m_P^2/M_{V,A}^2$ where m_P is the mass of a pseudoscalar meson and $M_{V,A}$, those of the first octet of vector and axial-vector resonances. Let us stress that in Ref.[158] a very good description of the $I = 0{,}1$ meson-meson scattering data was achieved by taking the lowest order Chiral Perturbation Theory amplitudes as the interacting kernels. At the two kaon threshold the $I = 0, 1$, S-waves are dominated by the presence of the $f_0(980)$ and $a_0(980)$ resonances, in that order. Both resonances are well reproduced in Ref.[158], with the same approach followed here. Therefore, since we take diagram 2 into account, we can neglect the contribution of diagram 7 when summed with others not drawn in Fig. 6.1 and that also include the exchange of axial-vector resonances, expressing the result in terms of the full S-wave $K\bar{K}$ strong amplitude derived in Ref.[158].

- **Diagram 8**

The enhanced configurations in diagram 8 have an outgoing kaon coupled to the vertex at the far left and an incoming one on the next vertex to the right. In this way the intermediate kaon propagator $\sim 1/a$ while the vector resonance propagator is $\sim 1/a'$. The two vertices with two pseudoscalars and one vector resonance involve small external three-momenta. Altogether, this diagram is of order:

$$\frac{g^2}{f^2}\frac{g^2 f^2 |\mathbf{k}|^2}{aa'} \tag{H.16}$$

Numerically, $g^2 f^2 \simeq 0.4^2$ GeV$^2 = 0.64\, m_K^2$ which implies already some suppression. In addition there is an additional reduction due to the angular integration, similarly to the situation explained above for diagram 4, so that the additional suppression factor κ with respect to diagram 2 applies also here.

- **Diagram 9**

Here, the enhanced configurations have, from left to right, a kaon going out, the next one coming in, another leaving and the last one entering the vertex. This means that the kaon propagators are of size $1/a$ and the intermediate vector resonance propagator is of size $1/a'$. In addition, one has now four vertices involving one vector resonance and two pseudoscalars. Each of them proportional to the difference between two slow kaon four-momenta. Then, the corresponding amplitudes go as:

$$\frac{g^2}{f^2}\frac{|\mathbf{k}|^4 g^2 f^2}{a^2 a'} \tag{H.17}$$

The ratio $|\mathbf{k}|^4/a^2$ is $\mathcal{O}(1)$ but for $|\mathbf{p}| \lesssim \sqrt{a}$ is suppressed. Calculating explicitly the intermediate vertices, attached to the vector meson propagator, a factor δ^2 appears, so that δ^2/a is suppressed by a factor δ/m_K. Besides, the angular projection suppression due to the vertices involving the external resonances also operates here for their ratio with a'. As a result there is an extra factor κ compared with diagram 2.

- **Diagram 10**

The enhanced configurations arise when there are, from left to right, a kaon leaving the diagram and another entering it on the vertices that couple two pseudoscalars with an external vector resonance. In this case the intermediate kaon propagators are $\sim 1/a$. These contributions are of order:

$$\frac{g^2}{f^2}\frac{m_K^2}{a}\frac{g^2 f^2}{M_\phi^2}\frac{|\mathbf{k}|^2}{a} \tag{H.18}$$

The last factor is due to the vertices with the external resonances and involve small external kaon three-momenta. The angular projection suppression operates here similarly as for diagram 6.

In analogy to diagram 7, the diagrams 9 and 10 are vector resonance contributions to the meson-meson scattering vertex. They must be accompanied by other diagrams involving also the exchange of axial-vector resonances so that the final modification of the lowest order chiral amplitude is further suppressed as indicated in the discussion for the diagram 7.

- **Diagram 11**

This diagram is similar to diagram 5 but including an extra vector resonance exchange that modifies the four-pseudoscalar one-vector vertex to the right of the diagram 5. As for the latter there is a suppression of the enhanced intermediate propagator, when the external kaon to the left of the diagram is leaving, because it is quadratic in the external small three-momentum. Therefore, it is just $\mathcal{O}(g^2/f^2)$.

- **Diagram 12–17**

As in Fig. H.1, one must have a leaving and entering $K\bar{K}$ pair attached to every intermediate vector meson line. As a result, from Eq.(6.13) one can conclude that all these diagrams are zero. Diagram 12 vanishes because there are no four-vector meson vertices coupling $\phi\phi\rho^0\rho^0$, $\phi\phi\rho^+\rho^-$, $\phi\phi\omega\omega$ and in general $\phi\phi VW$, with V and W any vector state. Diagram 13 is also zero because there are no three-vector resonance vertices coupling $\phi\phi V$, with V any vector resonance. For the same reason diagrams 14 and 15 are also zero. Finally, diagrams 16 and 17 vanish because there are no vertices with three vector resonances that couple $\phi\omega\omega$, $\phi\rho^0\rho^0$ and $\phi\rho^+\rho^-$.

Appendix I

Resumen en español

El proceso de dispersión pión-nucleón es un proceso hadrónico básico que ha sido estudiado en profundidad durante los últimos 50 años. Esto es debido a que nos permite probar la dinámica quiral de las interacciones fuertes basada en su teoría fundamental: la cromodinámica cuántica. Una de las principales ventajas de dicho proceso es la enorme cantidad de datos experimentales de gran calidad que hoy en día hay disponibles. Dichos datos, aparte, contienen información experimental sobre los estados excitados del nucleón, cuya determinación es uno de problemas fundamentales de la teoría de las interacciones fuertes. Por otro lado, el cálculo de la amplitud pión-nucleón es de gran interés para el estudio de las interacciones pión-núcleo llevadas a cabo en las factorías de mesones. Históricamente, el cálculo de las amplitudes pión-nucleón ha sido llevado a cabo mediante lo que se denomina *análisis en ondas parciales*. Dichos análisis determinan la amplitud de dispersión a partir de los datos correspondientes a los procesos $\pi^+ p \to \pi^+ p$ y $\pi^- p \to \pi^- p$ haciendo uso de la unitariedad y analiticidad de la amplitud asumiendo además simetría de isospín y analiticidad a t (variable de Mandelstam) fija[♯1] [16, 17], o bien usando modelos de potenciales hadrónicos con la ecuación de Schrödinger relativista [18]. Sin embargo, existe un modo más simple de estudiar esta complicada interacción haciendo uso de la simetría quiral.

La simetría quiral es una simetría que, aunque tiene una explicación directa si asumimos que la cromodinámica cuántica es la teoría fundamental de las interacciones fuertes, puede ser propuesta a partir de estudiar el espectro hadrónico. En dicho espectro se puede observar que parece haber, por cada hadrón con una paridad dada, un "compañero quiral" con los mis-

[♯1] La analiticidad a t fija no es una característica común a todos los análisis en ondas parciales que usan métodos dispersivos, pero sí lo es a todos los que se usan en esta tesis.

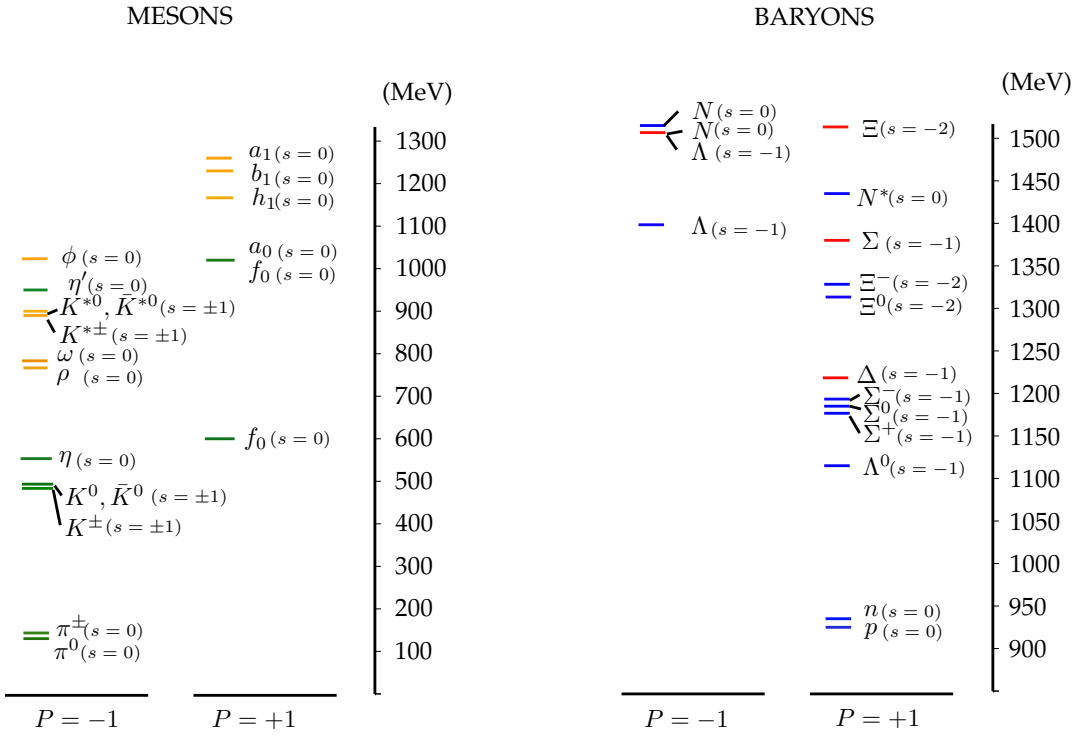

Figure I.1: Espectro hadrónico hasta masas de 1.3 y 1.5 GeV para mesones y bariones, respectivamente, distinguiendo entre hadrones con paridad positiva ($P = +1$) y negativa ($P = -1$). Las lineas azules (rojas) se refieren a bariones con $J = 1/2$ ($J = 3/2$), las verdes (amarillas) se refieren a mesones con $J = 0$ ($J = 1$) y s se refiere a su contenido de extrañeza.

mos números cuánticos pero con paridad opuesta. Sin embargo, si esta simetría quiral fuera exacta, ambos compañeros deberían tener la misma masa, cosa que no se observa en el espectro hadrónico. Así que, si asumimos simetría quiral en las interacciones fuertes, debemos asumir que esta simetria está *espontáneamente rota*, que quiere decir que aunque la interacción tenga dicha simetría, ésta no está realizada sobre los estados físicos (espacio de Fock). El hecho de que el espectro hadrónico esté dominado por una simetría espontáneamente rota (al menos a bajas energías) nos proporciona una potente herramienta de cálculo basada en dos pilares:

- El teorema de Goldstone [6, 7], el cual nos dice que si tenemos una simetría global espontáneamente rota aparecen en nuestro espectro de partículas unos bosones de espín cero y sin masa asociados a los generadores del grupo roto (un bosón por cada generador) que tienen

los mismos números cuánticos que su correspondiente generador. Estas propiedades son justamente las de los mesones pseudoescalares másligeros (π, K, η), y por lo tanto *éstos se identifican con los bosones de Goldstone de la simetría quiral espontáneamente rota*. Una de las consecuencias del teorema de Goldstone es que la intensidad de la interacción de los bosones de Goldstone es más pequeña a medida que su energía va decreciendo, de forma que cuando el momento de dichos bosones tiende a cero su interacción también tiende a cero. Por otro lado, también hay que tener en cuenta que los mesones tienen masa debido a que los quarks tiene masa no nula, lo cual da lugar a una ruptura explícita de la simetría quiral. Sin embargo, esto no plantea grandes problemas en la teoría ya que dichas masas son pequeñas (al menos la de los quarks ligeros) y la desviación con respecto al caso de masa nula puede ser tratada de forma perturbativa.

- La realización no lineal de la simetría quiral, la cual nos permite construir la teoría efectiva en la que la interacción de los mesones (bosones de Goldstone) aparece con acoplos derivativos. La realización no lineal de los Lagrangianos efectivos quirales, los cuales tienen en cuenta la interacción de los mesones con otros hadrones (incluyendo mesones), es crucial para la aplicación de teoría de perturbaciones en procesos hadrónicos ya que, como comentamos anteriormente, dicha interacción decrece con el cuadrimomento del meson y, por lo tanto, podemos establecer una jerarquia entre los infinitos diagramas de Feynman que en principio habría que calcular.

La teoría efectiva que incorpora ambas piezas y nos permite calcular perturbativamente procesos que involucran a los bosones de Goldstone de la simetría quiral es conocida como *Teoría Quiral de Perturbaciones* (ChPT en inglés) y es, por las razones mencionadas anteriormente, una herramienta apropiada para estudiar la interacción pión-nucleón. El primer intento de aplicar ChPT a dicha interacción es debido a Gasser, Sainio y Svarc [30] los cuales encontraron que, trabajando con bariones en ChPT, el contaje estandard de ChPT (que es lo que nos permite aplicar teoría de perturbaciones) está roto en el sentido de que, a un orden dado en el desarrollo quiral, podemos tener contribuciones de todos los órdenes superiores. Este problema surge debido a que la masa del nucleón no es una cantidad pequeña comparada con la escala de energías de las interacciones hadrónicas y, por lo tanto, los cálculos que invoucran bariones generan términos cuya magnitud no decrece en el desarrollo perturbativo. A fin de solucionar este problema, se han llegado a proponer hasta tres soluciones diferentes. La primera solución

consiste en tratar de eliminar la componente pesada del espinor del nucleón de forma que en el Lagrangiano sólo aparezca el remanente asociado a la energía cinética del mismo. Este remanente respeta el contaje quiral en el sentido de que la magnitud del trimomento del nucleón está directamente relacionada con la energía de pión, la cual es pequeña en procesos de baja energía (que son los que nos interesan). Esta reformulación de ChPT con bariones se conoce como *Teoria Quiral de Perturbaciones con Bariones Pesados* (o HBChPT, en inglés) y ha dado resultados bastante buenos a la hora de describir los desfasajes de las interacciones pión-nucleón [63, 64, 85]. Sin embargo, este método rompe la estructura Lorentz de la teoría original, lo que da lugar a problemas de convergencia en regiones cinemáticas de baja energía dentro del triángulo de Mandelstam. Esto se manifiesta claramente cuando se extrapola la amplitud obtenida con HBChPT a la region no física del plano de Mandelstam, en cuyo caso algunas integrales de lazo no convergen. Dichas extrapolaciones son interesantes ya que nos permiten estudiar las predicciones para cromodinámica cuántica basadas en la simetría quiral. Debido al interés de obtener una amplitud quiral que se pueda extrapolar fiablemente a la región no física, Becher y Leutwyler propusieron otra solución al problema del contaje quiral con bariones, preservando la estructura Lorentz [97]. Dicho método es conocido como *Regularización Infrarroja* (IR, en inglés), y está basado en separar la contribución de toda integral de lazo escalar (que es la que genera los términos que rompen el contaje quiral) en dos partes: la parte infrarroja y la parte regular. Dicha división es útil ya que la parte infrarroja tiene la peculiaridad de que respeta el contaje quiral, mientras que la parte regular (que es la que contiene los términos que rompen dicho contaje) es analítica en masas de quarks y momentos de las partículas, lo que hace que su contribución pueda ser absorbida en los parámetros libres del Lagrangiano original (conocidos como constantes de baja energía). Así pues, el método de IR está basado en tomar tan solo la parte infrarroja de las integrales de lazo escalares para dejar que las constantes de baja energía absorban la contribución analítica de los loops. Sin embargo, esta división tiene sus limitaciones ya que posee un radio de convergencia limitado [19] y, como se vio en [21] y en el capítulo 4 de ésta tesis , para energías que pueden hacer que la variable de Mandelstam u se anule, la amplitud calculada en IR desarrolla un corte no físico que da lugar a fuertes violaciones de unitariedad y limita la descripción de los desfasajes πN a la región de bajas energías. Además, como recientemente señaló Pascalutsa en [71], la forma en la que el método de IR recupera el contaje quiral hace que el propagador bariónico cambie de forma que viola conjugación de carga y, por lo tanto, causalidad. Otro posible método que nos permite recuperar el contaje quiral manteniendo

la formulación relativista de la teoría, denominado *Extended-On-Mass-Shell* (EOMS), fue propuesto en [73] a partir de los resultados de [72] en el que se demostraba que los términos que rompen el contaje quiral en el formalismo covariante son analíticos en masas de quarks y momentos, lo que hace que su contribución pueda ser absorbida sin ningún problema por las constantes de baja energía. Esto es muy diferente a lo que proponía IR, ya que este método dividía la integral covariante original en dos integrales con un radio de convergencia finito, y la parte regular, que es la que contiene los términos que rompen el contaje quiral, contenía también términos analíticos que no rompían dicho contaje. Esto significa que, mientras que IR elimina una serie infinita de términos analíticos, EOMS sólo substrae un polinomio finito de la amplitud covariante original, lo cual no altera sus propiedades analíticas, al contrario que IR. En esta tesis se presentan nuestros trabajos realizados con los formalismos de IR y EOMS aplicados al estudio de la dispersión pión-nucleón a bajas energías en el limite de isospín.

En el capítulo 4 presentamos los resultados obtenidos con IR. Allí utilizamos los desfasajes proporcionados por los grupos de Karlsruhe [16] y la Universidad George Washington [17] para comprobar qué tal se comportaba este método a la hora de describir los desfasajes por un lado y, por otro lado, estudiar el comportamiento de la amplitud obtenida en IR bajo métodos de unitarización. Esto último es especialmente interesante ya que en el sector de $SU(3)$ con extrañeza -1 los métodos de unitarización se hacen imprescindibles a la hora de estudiar la región próxima al umbral debido a la presencia de resonancias. Por este motivo el sector de $SU(2)$ es un excelente campo de pruebas para las técnicas que se aplicarán posteriormente a $SU(3)$. Dichas técnicas de unitarización no habían sido aplicadas nunca antes a un cálculo covariante de ChPT [21]. Pero no sólo esto hace interesante el cálculo de IR, ya que un trabajo anterior al nuestro [43] arrojaba unos resultados muy negativos para dicho formalismo, puesto que se obtenían unas descripciones de los desfasajes que eran mucho peores que los resultados no relativistas de HBChPT (en contra de lo que se esperaba) y, por otro lado, encontraban una gran violación de la relación de Goldberger-Treiman, $\Delta_{GT} \approx 20$–30%, que estaba muy alejada de los límites tanto teóricos como experimentales actuales. Nuestro trabajo arrojó luz sobre estas cuestiones y se probó que, en primer lugar, IR es capaz de describir los desfasajes de pión-nucleón con una calidad muy parecida a la que proporciona HBChPT y, en segundo lugar, confirmamos que el cálculo covariante en IR da lugar a una violación de la relación de Goldberger-Treiman de aproximadamente 20–30%. Este último resultado automáticamente da lugar a cuestionarse si esa enorme discrepancia en una relación tan fundamental como la relación

de Goldberger-Treiman era debida al modo en que IR recupera el contaje quiral, alterando las propiedades analíticas del cálculo, o si bien era debida a un problema de convergencia de ChPT covariante con bariones, lo cual podría poner en peligro la aplicabilidad de dicha teoría. Esta pregunta tiene su respuesta en el capítulo 5, donde se procede a realizar el mismo cálculo en EOMS [44], en el que el formalismo relativista conserva sus propiedades analíticas. Aquí se consideran los mismos desfasajes que en el trabajo de IR añadidendo además aquellos proporcionados por el grupo de Matsinos [18]. Se observa primeramente que EOMS reproduce los desfasajes mejor que IR. Es muy importante resaltar que EOMS *sí* que da un resultado para Δ_{GT} compatible con las expectativas teóricas y con diferentes determinaciones a partir de datos experimentales (ver Tablas 5.7 y 5.8). Esto es debido a que la contribución de los diagramas de lazo, que son los que dan una contribución de alrededor de 20% en IR, dan en EOMS una contribución mucho menor ($\approx 0.2\%$), que es perfectamente compatible con lo que se espera de acuerdo al desarrollo quiral. La conclusión a la que nos lleva este resultado es que el enorme valor que IR obtiene para Δ_{GT} no es un problema intrínseco a ChPT covariante con bariones, sino al particular modo que IR tiene para recuperar el contaje quiral manteniendo el carácter covariante de la formulación. Dicho método es el responsable de que se alteren las propiedades analíticas de las amplitudes. El capítulo 5 (Ref.[44]) tiene además una segunda parte todavía másinteresante en la que se incluye la resonancia $\Delta(1232)$ explícitamente en el cálculo. Lo primero que se observa es un incremento notable en la convergencia de la serie quiral. Concretamente, en este caso somos capaces de describir casi perfectamente los desfasajes hasta energías cercanas a la zona de la resonancia ($\sqrt{s} \lesssim 1.20$ GeV). Esto nos da confianza a la hora de utilizar las constantes de baja energía obtenidas para deducir información relevante relacionada con el proceso de dispersión pión-nucleón. En primer lugar, en el la sección 5.4 del capítulo 5 usamos estos valores para calcular Δ_{GT} de forma másfiable y precisa. Lo que observamos es que en los casos en los que incluimos la $\Delta(1232)$, las predicciones de EOMS-BChPT para la desviación de la relación de Goldberger-Treiman son perfectamente compatibles con las estimaciones de sus correspondientes análisis en ondas parciales (ver Tablas 5.7 y 5.7). Esto confirma, por primera vez desde BChPT los resultados obtenidos por los análisis en ondas parciales para Δ_{GT}.[♯2] En este caso en el que incluimos la $\Delta(1232)$, también hemos realizado un estudio pormenorizado del valor del término sigma de pión-nucleón ($\sigma_{\pi N}$) basándonos en los resultados de diferentes análisis en ondas parciales. En primer lugar

[♯2]Esto es porque IR obtiene un valor inaceptablemente alto y HBChPT no da predicciones para Δ_{GT} ya que se suele usar para fijar la constante de baja energía d_{18}.

confirmamos, desde ChPT, la discrepancia existente entre las estimaciones de $\sigma_{\pi N}$ por parte de los diferentes análisis en ondas parciales. Esto es importante ya que no se tenía claro si el origen de esa discrepancia era debido a la forma en la que los diferentes análisis estimaban $\sigma_{\pi N}$ o a la base de datos que cada grupo utilizaba (o ambas cosas). Nosotros vimos con nuestro análisis que esa discrepancia está relacionada con la base de datos utilizada, no con el método. Es más, tomando como entrada los análisis en ondas parciales basados en datos modernos de alta calidad, observamos que para análisis que usan metodologías muy diferentes (como WI08 [17] y EM06 [18]) obteníamos valores para $\sigma_{\pi N}$ idénticos. También realizamos un estudio de los errores teóricos debidos a las correcciones quirales de orden superior. Allí encontramos una notable convergencia del desarrollo quiral de $\sigma_{\pi N}$ confirmando la jerarquía establecida para la $\Delta(1232)$ respecto a los nucleones. Esto nos lleva a concluir que los análisis en ondas parciales basados en datos modernos de alta calidad apuntan a un valor de $\sigma_{\pi N} = 59(7)$ MeV. Además, estudiamos las diferentes implicaciones fenomenológicas derivadas de los resultados obtenidos con los análisis modernos y vimos que éstos reproducían valores compatibles con determinaciones independientes. Concretamente, a partir de los análisis WI08 y EM06 obtenemos valores para Δ_{GT} compatibles con determinaciones provenientes de átomos piónicos y dispersión nucleón-nucleón. Por otro lado, usando como entrada WI08, también somos capaces de determinar una anchura de la $\Delta(1232)$ perfectamente compatible con el valor dado en el PDG. Sin embargo, la comprobación fenomenológica más interesante para $\sigma_{\pi N}$ es la que proviene de la estimación de la longitud de dispersión escalar-isoescalar a_{0+}^{+}, ya que ésta está estrechamente relacionada con el valor de término sigma pión-nucleón. Lo que encontramos es que de los análisis modernos WI08 y EM06 extraemos con ChPT un valor para la a_{0+}^{+} perfectamente compatible con los valores positivos obtenidos hoy en día a partir de análisis modernos de átomos piónicos incluyendo correcciones de isospín. Por otro lado, observamos que usando como entrada el análisis KA85 no somos capaces de obtener ni un Δ_{GT} compatible con determinaciones independientes, ni una anchura para la $\Delta(1232)$ compatible con los valores del PDG. Y, en lo que respecta a la a_{0+}^{+}, los valores extraídos de los datos proporcionada por KA85 son compatibles únicamente con una longitud de dispersión negativa, lo cual está en concordancia con los resultados de Gasser *et al.* [123] que asocian el valor $\sigma_{\pi N} \simeq 45$ MeV con a_{0+}^{+} negativo mientras que $a_{0+}^{+} > 0$ (que es lo que obtienen los análisis modernos de átomos piónicos) está asociado a valores de $\sigma_{\pi N}$ aproximadamente 10 MeV superiores. Estos resultados respecto a $\sigma_{\pi N}$ obtenidos en nuestras investigaciones están siendo sin duda de mucha utilidad para los estudios de detección directa de materia

oscura, aunque también ha causado un cierto impacto en la comunidad de QCD en el retículo.

A nivel global el principal resultado de nuestros estudios de la dispersión πN con ChPT relativista es que una formulación covariante de ChPT que resuelva el problema del contaje quiral sin modificar las propiedades analíticas de la amplitud, con la $\Delta(1232)$ incluida consistentemente como grado de libertad, es capaz de proveer, a $\mathcal{O}(q^3)$ al menos, una representación para la amplitud de dispersión que conecta satisfactoriamente la región física de baja energía (bajo la $\Delta(1232)$) con la región bajo el umbral. Probando, además, que con esta representación se pueden obtener resultados precisos y fiables para importantes magnitudes, siendo éstos perfectamente compatibles con estudios independientes que usan una metodología diferente. Esto es ciertamente un hito en el campo de ChPT con bariones en el que se pensaba que la convergencia de la serie quiral estaba mucho más limitada, siendo incapaz de obtener valores fiables para magnitudes fundamentales como $\sigma_{\pi N}$ o bien de extrapolar con precisión la amplitud a la zona no física.

Por otro lado, en el capítulo 6 se procedió a hacer un estudio fenomenológico de la amplitud de dispersión $\phi(1020)f_0(980)$ en el umbral y la naturaleza de la resonancia $Y(2175)$, que ha sido observada recientemente por la colaboración BABAR en la reacción $e^+e^- \to \phi(1020)f_0(980)$. Allí se aprovechó el hecho de que la $f_0(980)$ está bien descrita como un estado ligado $K\bar{K}$ de isospín cero ($I = 0$) en onda S para construir el potencial de interacción $\phi(1020)f_0(980)$ sin introducir parámetros libres adicionales al acoplo ϕK. Dicho potencial se usó para estudiar los efectos de la interacción en estados finales de $\phi(1020)f_0(980)$ y su relación con la aparición de picos resonantes en la sección eficaz. Nuestros resultados apuntan a que la resonancia $Y(2175)$ tiene una componente molecular $\phi(1020)f_0(980)$ importante. Más adelante, se utilizan estos resultados obtenidos en el canal $I = 0$ para extrapolarlos al canal $I = 1$ e investigar la posible existencia de una compañera isovectorial de la resonancia $Y(2175)$ debido a la interacción $\phi(1020)a_0(980)$ en onda S. Lo que observamos es que, para ciertos valores de los parámetros (dentro del rango de valores obtenidos en el caso $I = 0$), se observa un pico resonante en $\sqrt{s} \approx 2.03$ GeV en la reacción $e^+e^- \to \phi(1020)\pi^0\eta$ debido precisamente a la interacción en estados finales de $\phi(1020)a_0(980)$. El siguiente paso en esta línea de investigación será estudiar el proceso completo $e^+e^- \to \phi(1020)K^+K^-$, que ha sido ya medido, y que involucra simultáneamente las amplitudes con $I = 0$ e $I = 1$.

Bibliography

[1] M. Gell-Mann, CTSL-20,TID-12608.

[2] Y. Ne'eman, Nucl. Phys. **26**, 222 (1961).

[3] Antonio Ferrer Soria. *Física nuclear y de partículas*. Universitat de Valencia. Servei de publicacions, 2007 ISBN 9788437065687

[4] W. Heisenberg. Z. Phys. **77**, 1 (1932).

[5] C. Vafa and E. Witten, Phys. Rev. Lett. **53**, 535 (1984); Nucl. Phys. B **234**, 173 (1984).

[6] J. Goldstone, Nuovo Cim. **19**,154 (1961).

[7] J. Goldstone, A. Salam and S. Weinberg, Phys. Rev. **127**, 965 (1962).

[8] S. L. Adler, Phys. Rev. **137**, B1022 (1965); *ibid* **139**, B1638 (1965).

[9] M. L. Goldberger and S. B. Treiman, Phys. Rev. **110**, 1178 (1958); M. L. Goldberger and S. B. Treiman, Phys. Rev. **111**, 354 (1958).

[10] Y. Nambu and G. Jona-Lasinio, Phys. Rev. **122**, 345 (1961).

[11] S. L. Adler, Phys. Rev. Lett. **14**, 1051 (1965). Phys. Rev. **140**, B736 (1965); [Erratum-ibid. **149**, 1294 (1966)]; [Erratum-ibid. **175**, 2224 (1968)]. W. I. Weisberger, Phys. Rev. Lett. **14**, 1047 (1965); Phys. Rev. **143**, 1302 (1966).

[12] G. Höler, *Pion-nucleon scattering*. Edited by H. Schopper, Landolt-Börnstein, New Series, Group I, Vol. 9, Pt. B2. Springer-Verlag, Berlin, 1983.

[13] J. Gasser, M. E. Sainio and A. Svarc, Nucl. Phys. B **307**, 779 (1988).

[14] E. Epelbaum and U.-G. Meißner, arXiv:1201.2136 [nucl-th].

[15] M. Hoferichter, B. Kubis and U.-G. Meißner, Phys. Lett. B **678**, 65 (2009); M. Hoferichter, B. Kubis and U.-G. Meißner, Nucl. Phys. A **833**, 18 (2010).

[16] R. Koch, Nucl. Phys. A **448**, 707 (1986); R. Koch and E. Pietarinen, Nucl. Phys. A **336**, 331 (1980).

[17] Computer code SAID, online program at http://gwdac.phys.gwu.edu/ , solution WI08; R. A. Arndt *et al.*, Phys. Rev. C **74**, 045205 (2006). Solution SM01.

[18] E. Matsinos, W. S. Woolcock, G. C. Oades, G. Rasche and A. Gashi, Nucl. Phys. A **778**, 95 (2006).

[19] T. Becher and H. Leutwyler, JHEP **0106**, 017 (2001).

[20] T. P. Cheng and R. F. Dashen, Phys. Rev. Lett. **26**, 594 (1971).

[21] J. M. Alarcón, J. M. Camalich, J. A. Oller and L. Alvarez-Ruso, Phys. Rev. C **83**, 055205 (2011).

[22] A. Bottino, F. Donato, N. Fornengo and S. Scopel, Astropart. Phys. **18**, 205 (2002); A. Bottino, F. Donato, N. Fornengo and S. Scopel, Phys. Rev. D **78**, 083520 (2008).

[23] J. R. Ellis, K. A. Olive and C. Savage, Phys. Rev. D **77**, 065026 (2008).

[24] H. Ohki *et al.*, Phys. Rev. D **78**, 054502 (2008); C. Alexandrou *et al.* [European Twisted Mass Collaboration], Phys. Rev. D **78**, 014509 (2008); A. Walker-Loud *et al.*, Phys. Rev. D **79**, 054502 (2009); S. Durr *et al.*, arXiv:1109.4265 [hep-lat]; R. Horsley *et al.*, arXiv:1110.4971 [hep-lat]; G. S. Bali *et al.* [QCDSF Collaboration], arXiv:1111.1600 [hep-lat]; S. Dinter, V. Drach, R. Frezzotti, G. Herdoiza, K. Jansen and G. Rossi, arXiv:1202.1480 [hep-lat]; R. D. Young and A. W. Thomas, Nucl. Phys. A **844**, 266C (2010).

[25] D. Gotta, F. Amaro, D. F. Anagnostopoulos, S. Biri, D. S. Covita, H. Gorke, A. Gruber and M. Hennebach *et al.*, Lect. Notes Phys. **745**, 165 (2008); V. Baru, C. Hanhart, M. Hoferichter, B. Kubis, A. Nogga and D. R. Phillips, Phys. Lett. B **694**, 473 (2011); V. Baru, C. Hanhart, M. Hoferichter, B. Kubis, A. Nogga and D. R. Phillips, Nucl. Phys. A **872**, 69 (2011).

[26] S. R. Beane, W. Detmold, K. Orginos and M. J. Savage, Prog. Part. Nucl. Phys. **66**, 1 (2011).

[27] M. Fukugita, Y. Kuramashi, M. Okawa, H. Mino and A. Ukawa, Phys. Rev. D **52**, 3003 (1995).

[28] S. R. Beane, W. Detmold, T. C. Luu, K. Orginos, A. Parreno, M. J. Savage, A. Torok and A. Walker-Loud, Phys. Rev. D **79**, 114502 (2009).

[29] S. Weinberg, Physica A **96**, 327 (1979).

[30] J. Gasser and H. Leutwyler, Annals Phys. **158**, 142 (1984) .

[31] H. Leutwyler, Annals Phys. **235**, 165 (1994).

[32] G. Ecker, Prog. Part. Nucl. Phys. **35**, 1 (1995).

[33] S. Scherer, Adv. Nucl. Phys. **27**, 277 (2003).

[34] A. Pich, Rept. Prog. Phys. **58**, 563 (1995); U.-G. Meißner, Rept. Prog. Phys. **56**, 903 (1993).

[35] Dashen R.F. Adler, S.L. *Current Algebras and Applications to Particle Physics*. New York, USA. Benjamin (1968) 394 p.

[36] S. Weinberg, Phys. Rev. Lett. **18**, 188 (1967).

[37] L. L. Foldy and S. A. Wouthuysen, Phys. Rev. **78**, 29 (1950).

[38] B. Aubert *et al.* [BABAR Collaboration], Phys. Rev. D **74**, 091103 (2006).

[39] Z. -G. Wang, Nucl. Phys. A **791**, 106 (2007); H. -X. Chen, X. Liu, A. Hosaka and S. -L. Zhu, Phys. Rev. D **78**, 034012 (2008); N. V. Drenska, R. Faccini and A. D. Polosa, Phys. Lett. B **669**, 160 (2008).

[40] A. Martinez Torres, K. P. Khemchandani, L. S. Geng, M. Napsuciale and E. Oset, Phys. Rev. D **78**, 074031 (2008).

[41] L. Alvarez-Ruso, J. A. Oller and J. M. Alarcón, Phys. Rev. D **80**, 054011 (2009).

[42] S. R. Coleman, J. Wess and B. Zumino, Phys. Rev. **177**, 2239 (1969); C. G. Callan, Jr., S. R. Coleman, J. Wess and B. Zumino, Phys. Rev. **177**, 2247 (1969).

[43] K. Torikoshi and P. J. Ellis, Phys. Rev. C **67**, 015208 (2003).

[44] J. M. Alarcón, J. M. Camalich and J. A. Oller. In preparation.

[45] J. M. Alarcón, J. Martin Camalich and J. A. Oller, Phys. Rev. D **85**, 051503(R) (2012).

[46] L. Alvarez-Ruso, J. A. Oller and J. M. Alarcón, Phys. Rev. D **82**, 094028 (2010).

[47] A. Manohar and H. Georgi, Nucl. Phys. B **234**, 189 (1984).

[48] S. Weinberg, *The quantum theory of fields. Vol. 2: Modern applications*, Cambridge, UK: Univ. Pr. (1996) 489 p.

[49] S. Weinberg, Phys. Lett. B **251**, 288 (1990); Nucl. Phys. B **363**, 3 (1991).

[50] H. Georgi, *Weak Interactions and Modern Particle Theory*, Benjamin/Cummings, Menlo Park, 1984.

[51] Y. Nambu and D. Lurie, Phys. Rev. **125**, 1429 (1962); Y. Nambu and E. Shrauner, Phys. Rev. **128**, 862 (1962).

[52] D. V. Bugg. Private communication.
E. Matsinos. Private communication.

[53] The full data base can be accessed via the website http://gwdac.phys.gwu.edu.

[54] K. H. Augenstein, G. Höhler, E. Pietarinen and H. M. Staudenmaier, Karlsruhe Data Tape, ZAED Physics Data (1977).

[55] Concretely, KA85 uses the $\pi^+ p$ cross sections of Bertin *et al.* [56], that nowadays is believed to be erroneous [85].

[56] P. Y. Bertin, B. Coupat, A. Hivernat, D. B. Isabelle, J. Duclos, A. Gerard, J. Miller and J. Morgenstern *et al.*, Nucl. Phys. B **106**, 341 (1976).

[57] B. Tromborg, S. Waldenstrom and I. Overbo, Phys. Rev. D **15**, 725 (1977).

[58] B. Tromborg, S. Waldenstrom and I. Overbo, Helv. Phys. Acta **51**, 584 (1978).

[59] A. Gashi, E. Matsinos, G. C. Oades, G. Rasche and W. S. Woolcock, Nucl. Phys. A **686**, 447 (2001); Nucl. Phys. A **686**, 463 (2001).

[60] V. Bernard, N. Kaiser and U.-G. Meißner, Int. J. Mod. Phys. E **4**, 193 (1995).

[61] V. Bernard, Prog. Part. Nucl. Phys. **60**, 82 (2008).

[62] E. E. Jenkins and A. V. Manohar, Phys. Lett. B **255**, 558 (1991).

[63] N. Fettes, U.-G. Meißner and S. Steininger, Nucl. Phys. A **640**, 199 (1998).

[64] N. Fettes and U.-G. Meißner, Nucl. Phys. A **676**, 311 (2000).

[65] T. Fuchs, J. Gegelia and S. Scherer, Eur. Phys. J. A **19**, 35 (2004).

[66] B. R. Holstein, V. Pascalutsa and M. Vanderhaeghen, Phys. Rev. D **72**, 094014 (2005).

[67] L. S. Geng, J. Martin Camalich, L. Alvarez-Ruso and M. J. Vicente-Vacas, Phys. Rev. Lett. **101**, 222002 (2008).

[68] J. Martin Camalich, L. S. Geng and M. J. Vicente Vacas, Phys. Rev. D **82**, 074504 (2010).

[69] P. J. Ellis and H. B. Tang, Phys. Rev. C **57**, 3356 (1998).

[70] T. Ledwig, J. Martin-Camalich, V. Pascalutsa and M. Vanderhaeghen, Phys. Rev. D **85**, 034013 (2012);

[71] V. Pascalutsa, arXiv:1110.5792 [nucl-th].

[72] J. Gegelia and G. Japaridze, Phys. Rev. D **60**, 114038 (1999).

[73] T. Fuchs, J. Gegelia, G. Japaridze and S. Scherer, Phys. Rev. D **68**, 056005 (2003).

[74] E. E. Jenkins and A. V. Manohar, Phys. Lett. B **259**, (1991) 353.

[75] T. R. Hemmert, B. R. Holstein and J. Kambor, J. Phys. G G **24**, 1831 (1998).

[76] V. Pascalutsa, M. Vanderhaeghen and S. N. Yang, Phys. Rept. **437**, 125 (2007).

[77] N. Fettes and U.-G. Meißner, Nucl. Phys. A **679**, 629 (2001).

[78] J. A. Oller, M. Verbeni and J. Prades, JHEP **0609**, 079 (2006).

[79] W. Rarita and J. Schwinger, Phys. Rev. **60**, 61 (1941).

[80] K. Johnson and E. C. G. Sudarshan, Annals Phys. **13**, 126 (1961); C. R. Hagen, Phys. Rev. D **4**, 2204 (1971).

[81] G. Velo and D. Zwanziger, Phys. Rev. **186**, 1337 (1969); L. P. S. Singh, Phys. Rev. D **7**, 1256 (1973).

[82] V. Pascalutsa and R. Timmermans, Phys. Rev. C **60**, 042201 (1999).

[83] K. Nakamura *et al.* [Particle Data Group Collaboration], J. Phys. G G **37**, 075021 (2010).

[84] L. S. Geng, J. Martin Camalich, L. Alvarez-Ruso and M. J. Vicente Vacas, Phys. Rev. D **78**, 014011 (2008).

[85] N. Fettes and U.-G. Meißner, Nucl. Phys. A **693**, 693 (2001).

[86] E. Matsinos, Phys. Rev. C **56**, 3014 (1997).

[87] G. C. Oades, G. Rasche, W. S. Woolcock, E. Matsinos and A. Gashi, Nucl. Phys. A **794**, 73 (2007).

[88] J. A. Oller, E. Oset and J. R. Peláez, Phys. Rev. D **59**, 074001 (1999); (E)-*ibid* D **60**, 099906 (1999); (E)-*ibid* D **75**, 099903 (2007).

[89] J. A. Oller, E. Oset and A. Ramos, Prog. Part. Nucl. Phys. **45**, 157 (2000).

[90] J. A. Oller and E. Oset, Phys. Rev. D **60**, 074023 (1999).

[91] G. F. Chew and S. Mandelstam, Phys. Rev. **119**, 467 (1960).

[92] J. A. Oller and U.-G. Meißner, Phys. Lett. B **500**, 263 (2001).

[93] A. Dobado and J. R. Pelaez, Phys. Rev. D **56**, 3057 (1997).

[94] A. Gomez Nicola and J. R. Pelaez, Phys. Rev. D **62**, 017502 (2000).

[95] G. Ecker, J. Gasser, A. Pich and E. de Rafael, Nucl. Phys. B **321**, 311 (1989).

[96] A. Gomez Nicola, J. Nieves, J. R. Pelaez and E. Ruiz Arriola, Phys. Lett. B **486**, 77 (2000).

[97] T. Becher and H. Leutwyler, Eur. Phys. J. C **9**, 643 (1999).

[98] U.-G. Meißner and J. A. Oller, Nucl. Phys. A **673**, 311 (2000).

[99] F. James, Minuit Reference Manual D **506** (1994).

[100] P. Buettiker and U.-G. Meißner, Nucl. Phys. A **668**, 97 (2000).

[101] V. Bernard, N. Kaiser and U.-G. Meißner, Nucl. Phys. A **615**, 483 (1997).

[102] M. Mojzis, Eur. Phys. J. C **2**, 181 (1998).

[103] J. Gasser, V. E. Lyubovitskij and A. Rusetsky, Phys. Rep. **456**, 167 (2008).

[104] R. A. Arndt, W. J. Briscoe, I. I. Strakovsky, R. L. Workman and M. M. Pavan, Phys. Rev. C **69**, 035213 (2004).

[105] N. Kaiser, R. Brockmann and W. Weise, Nucl. Phys. A **625**, 758 (1997).

[106] E. Epelbaum, W. Glöckle and U.-G. Meißner, Eur. Phys. A **19**, 125 (2004).

[107] E. Epelbaum, W. Glöckle and U.-G. Meißner, Eur. Phys. A **19**, 401 (2004).

[108] E. Epelbaum, A. Nogga, W. Glöckle, H. Kamada, U.-G. Meißner and H. Witala, Eur. Phys. J. A **15**, 543 (2002).

[109] M. C. M. Rentmeester, R. G. E. Timmermans and J. J. de Swart, Phys. Rev. C **67**, 044001 (2003).

[110] M. C. M. Rentmeester, R. G. E. Timmermans, J. L. Friar and J. J. de Swart, Phys. Rev. Lett. **82**, 4992 (1999).

[111] R. A. Arndt, R. L. Workman and M. M. Pavan, Phys. Rev. C **49**, 2729 (1994).

[112] H.-Ch. Schröder *et al.*, Eur. Phys. J. C **21**, 473 (2001).

[113] J. J. de Swart, M. C. M. Rentmeester and R. G. E. Timmermans, πN Newsletter **13**, 96 (1997).

[114] B. R. Holstein, V. Pascalutsa and M. Vanderhaeghen, Phys. Rev. D **72**, 094014 (2005).

[115] L. Castillejo, R. H. Dalitz and F. J. Dyson, Phys. Rev. **101**, 453 (1956).

[116] V. Bernard, N. Kaiser and U.-G. Meißner, Z. Phys. C **60**, 111 (1993).

[117] T. Fuchs, J. Gegelia and S. Scherer, Eur. Phys. J. A **19**, 35 (2004).

[118] R. P. Feynman, Phys. Rev. **56** , 340 (1939).

[119] T. Hahn and M. Perez-Victoria, Comput. Phys. Commun. **118**, 153 (1999).

[120] H. Krebs, E. Epelbaum and U.-G. Meißner, Eur. Phys. J. A **32**, 127 (2007).

[121] V. Pascalutsa and D. R. Phillips, Phys. Rev. C **67**, 055202 (2003).

[122] B. Long and V. Lensky, Phys. Rev. C **83**, 045206 (2011).

[123] J. Gasser, H. Leutwyler and M. E. Sainio, Phys. Lett. B **253**, 252 (1991).

[124] M. M. Pavan, I. I. Strakovsky, R. L. Workman and R. A. Arndt, PiN Newslett. **16**, 110 (2002).

[125] P. Finelli, N. Kaiser, D. Vretenar and W. Weise, Nucl. Phys. A **735**, 449 (2004); J. A. Oller, A. Lacour and U.-G. Meißner, J. Phys. G G **37**, 015106 (2010); A. Lacour, J. A. Oller and U.-G. Meißner, J. Phys. G G **37**, 125002 (2010); A. Lacour, J. A. Oller and U.-G. Meißner, Annals Phys. **326**, 241 (2011).

[126] T. D. Cohen, R. J. Furnstahl and D. K. Griegel, Phys. Rev. C **45**, 1881 (1992); N. Kaiser and P. de Homont, W. Weise, Phys. Rev. C **77**, 025204 (2008).

[127] J. Giedt, A. W. Thomas and R. D. Young, Phys. Rev. Lett. **103**, 201802 (2009).

[128] L. S. Brown, W. J. Pardee and R. D. Peccei, Phys. Rev. D **4**, 2801 (1971).

[129] V. Bernard, N. Kaiser and U.-G. Meißner, Phys. Lett. B **389**, 144 (1996).

[130] J. Gasser, H. Leutwyler and M. E. Sainio, Phys. Lett. B **253**, 260 (1991).

[131] M. G. Olsson, Phys. Lett. B **482**, 50 (2000).

[132] C. A. Dominguez and P. Langacker, Phys. Rev. D **24**, 1905 (1981).

[133] I. Jameson, A. W. Thomas and G. Chanfray, J. Phys. G G **18**, L159 (1992).

[134] V. Pascalutsa and M. Vanderhaeghen, Phys. Lett. B **636**, 31 (2006).

[135] H. Krebs, E. Epelbaum and U.-G. Meißner, Phys. Rev. C **80**, 028201 (2009).

[136] M. Hadzimehmedovic, H. Osmanovic and J. Stahov, eConf **C070910**, 234 (2007).

[137] C. Joram, M. Metzler, J. Jaki, W. Kluge, H. Matthaey, R. Wieser, B. M. Barnett, R. Bilger *et al.*, Phys. Rev. C **51**, 2159 (1995).

[138] H. Denz, P. Amaudruz, J. T. Brack, J. Breitschopf, P. Camerini, J. L. Clark, H. Clement, L. Felawka *et al.*, Phys. Lett. B **633**, 209 (2006).

[139] J. Stahov. Private comunication.

[140] J. Gasser and H. Leutwyler, Phys. Rept. **87**, 77 (1982).

[141] B. Borasoy and U.-G. Meißner, Annals Phys. **254**, 192 (1997).

[142] E. E. Jenkins and A. V. Manohar, Phys. Lett. B **281**, 336 (1992).

[143] U.-G. Meißner, J. A. Oller and A. Wirzba, Annals Phys. **297**, 27 (2002).

[144] B. Aubert *et al.* [BABAR Collaboration], Phys. Rev. D **74**, 091103 (2006).

[145] B. Aubert *et al.* [BABAR Collaboration], Phys. Rev. D **76**, 012008 (2007).

[146] B. Aubert *et al.* [BABAR Collaboration], Phys. Rev. D **77**, 092002 (2008).

[147] M. Ablikim, *et al.* [BES Collaboration], Phys. Rev. Lett. **100**, 102003 (2008).

[148] C. P. Shen *et al.* [Belle Collaboration], Phys. Rev. D **80**, 031101 (2009).

[149] Z. G. Wang, Nucl. Phys. A **791**, 106 (2007).

[150] H.-X. Chen, X. Liu, A. Hosaka and S.-L. Zhu, Phys. Rev. D **78**, 034012 (2008).

[151] N. V. Drenska, R. Faccini and A. D. Polosa, Phys. Lett. B **669**, 160 (2008).

[152] G.-J. Ding and M.-L. Yan, Phys. Lett. B **650**, 390 (2007).

[153] N. Isgur and J. E. Paton, Phys. Rev. D **31**, 2910 (1985); N. Isgur, R. Kokoski and J. E. Paton, Phys. Rev. Lett. **54**, 869 (1985).

[154] T. Barnes, F. E. Close and E. S. Swanson, Phys. Rev. D **52**, 5242 (1995).

[155] S. Godfrey, N. Isgur, Phys. Rev. D **32**, 189 (1985).

[156] G.-J. Ding and M.-L. Yan, Phys. Lett. B **657**, 49 (2007).

[157] T. Barnes, N. Black and P. R. Page, Phys. Rev. D **68**, 054014 (2003).

[158] J. A. Oller and E. Oset, Nucl. Phys. A **620**, 438 (1997); (E)-ibid. A **652**, 407 (1999).

[159] L. Roca, E. Oset and J. Singh, Phys. Rev. D **72**, 014002 (2005).

[160] C. A. Vaquera-Araujo and M. Napsuciale, Phys. Lett. B **681**, 434 (2009).

[161] S. Gomez-Avila, M. Napsuciale and E. Oset, Phys. Rev. D **79**, 034018 (2009).

[162] J. Gasser and H. Leutwyler, Nucl. Phys. B **250**, 465 (1985).

[163] J. J. Sakurai, Ann. Phys. **11**, 1 (1960).

[164] A. Bramon, *Lectures on Electromagnetic Interactions of Hadrons*, Universitat Autònoma de Barcelona, B-32642 (1979).

[165] J. Prades, Z. Phys. C **63**, 491 (1994); (E)-*ibid.* C **11**, 571 (1999).

[166] G. Janssen, B. C. Pearce, K. Holinde and J. Speth, Phys. Rev. D **52**, 2690 (1995).

[167] J. D. Weinstein and N. Isgur, Phys. Rev. Lett. **48**, 659 (1982); Phys. Rev. D **41**, 2236 (1990).

[168] J. A. Oller, Phys. Rev. D **71**, 054030 (2005).

[169] J. A. Oller, Nucl. Phys. A **727**, 353 (2003).

[170] A. Martinez Torres, E. J. Garzon, E. Oset and L. R. Dai, Phys. Rev. D **83**, 116002 (2011).

[171] M. Albaladejo and J. A. Oller, Phys. Rev. Lett. **101**, 252002 (2008).

[172] J. A. Oller and E. Oset, Nucl. Phys. A **629**, 739 (1998).

[173] C. Amsler *et al.* [Particle Data Group], Phys. Lett. B **667**, 1 (2008).

[174] G. Bargon, *Introduction to Dispersion Techniques in Field Theory*, W. A. Benjamin, Inc, New York, Amsterdam, 1965.

[175] A. M. Bincer, Phys. Rev. **118**, 855 (1960).

[176] G. Källen and A. S. Wightman, Mat.-fys. Skrifth **1**, 1 (1958).

[177] J. Gegelia, G. S. Japaridze and K. S. Turashvili, Theor. Math. Phys. **101**, 1313 (1994).

[178] M. C. Birse, Z. Phys. A **355**, 231 (1996).